SISSA **ISAS**

SCUOLA INTERNAZIONALE SUPERIORE DI STUDI AVANZATI
INTERNATIONAL SCHOOL FOR ADVANCED STUDIES

Super-massive Black Holes: the missing link in galaxy evolution

Thesis submitted for the degree of
Doctor Philosophiæ

CANDIDATE:
Francesco Shankar

SUPERVISORS:
Prof. Luigi Danese
Prof. Paolo Salucci

October 2005

Table of Contents

Citations to Previously Published Works

Part of the contents of this Thesis has already appeared in the following papers:

Refereed Journals:

- *Supermassive black hole demography: the match between the local and accreted mass functions.*
  Shankar F., Salucci P., Granato G.L., De Zotti G. & Danese L., 2004, MNRAS, **354**, 1020
- *Dynamical and photometric imprints of feedback processes on the formation and evolution of E/S0 galaxies.*
  Cirasuolo M., **Shankar F.**, Granato G.L., De Zotti G. & Danese L., 2005, ApJ, 629, 816
- *The Impact of Energy Feedback on AGN Evolution and SMBH Demography.*
  Vittorini V., **Shankar F.** & Cavaliere A., 2005, MNRAS, accepted

In Preparation:

- *New Relationships between Galaxy Properties and Host Halo Mass, and the Role of Feedbacks in Galaxy Formation.*
  Shankar F., Lapi A., Salucci P., De Zotti G. & Danese L., 2005, ApJ, submitted
- *AGN Luminosity Function from Delayed Black Hole activity.*
  2006

Acknowledgments

My experience here in SISSA has been extraordinary.

First of all I had the chance to work on wonderful and stimulating topics, which are still for many aspects mysterious. For all that I learned here I must thank my supervisor, prof. L. Danese, who has been very active and constant in helping me, in guiding me, even when things were hard to face. He really pushed me to believe in myself.

I thank prof P. Salucci who has always been very nice with me and always had trust in my work. I thank prof. G. Granato, who provided me with the numerical code, and prof. G. De Zotti with whom I had the chance to often work and finally the whole SISSA staff. I thank my friend and collaborator A. Lapi, with whom I have enjoyed and shared experiences inside and outside SISSA.

I also thank my colleagues and friends in SISSA and outside, M. Cirasuolo, P.G. Monaco, D. Marchesini, F. Giovi, S. Tinti, F. Annibali, Z. Bosnjak, I. Musco, B. Giacomazzo, G. Gentile, N. Kawakatu, V. Vittorini, M. Magliocchetti. I then thank all my friends in Trieste: Andrea, Francesca, Pier, Padhu, Enrico, Patrizia, Corrado, Martin, Carlo, Matteo, Luca & Cristina.

I also thank all my friends and relatives in Rome who in these four years have always shown their friendship despite the distance: Davide, Donika, Filippo, Alessandra, Stefano, Alberto, Daniela, Elba, Paolo, Flaminia, Andrea, Elena, Mariapina, Raffaella, Gabriele, Germano, Francesca, Simonetta, Ilaria, Emiliano, Sandro, Fabio, Alberto, Tiziano, Gabriella, Giulia, Alvaro, Adriana & Daniele. I also thank my girlfriend Elisa for her love, care and willingness to follow me in my future life experiences.

Special thanks go to my fantastic family who has always supported me, in every moment of my life!

To my parents

Chapter 1

Introduction

The paradigm that quasars (QSO) and, more generally, Active Galactic Nuclei (AGN) are powered by mass accretion onto a super-massive black hole (SMBH) proposed long ago (Salpeter 1964; Zeldovich & Novikov 1969; Lynden–Bell 1969) has got very strong support from spectroscopic and photometric studies of the stellar and gas dynamics in the very central regions of local spheroidal galaxies and prominent bulges. These studies established that in most, if not all, galaxies observed with high enough sensitivity a central massive dark object (MDO) is present with a well defined relationship between the MDO mass and the mass or the velocity dispersion σ of the host galaxy spheroidal component (Kormendy & Richstone 1995; Magorrian et al. 1998; Gebhardt et al. 2000; Ferrarese & Merritt 2000; Tremaine et al. 2002; Kormendy 2003). A very strong relationship is also present between the MDO and the photometric and dynamical structure of the spheroid host (e.g. Graham et al. 2002, Erwin et al. 2004). Although there is no direct evidence that all MDO are black holes (BH), the evidence for a singularity is actually very tight in the Galaxy (Schödel et al. 2002; Ghez et al. 2003) and alternative explanations are severely constrained in NGC 4258 (Miyoshi et al. 1995; see also e.g. Kormendy 2003). There are also empirical evidences (Ferrarese 2002) that SMBH mass, $M_\bullet$, is also linked with the host Dark Matter (DM) halo mass $M_{\rm vir}$.

How and why SMBH have become so closely linked with their host galaxies and with the whole surrounding DM halo? What role do SMBH play in defining the Hubble

sequence of galaxies? To understand these points we need to insert them in a wider perspective which must include the problem of galaxy evolution and the general processes of structure formation in the Universe.

According to the standard cosmological frame of structure evolution, DM halos have built hierarchically, from smaller to bigger units. Galaxies, in this scenario, have probably formed out of the hierarchical build-up of their host DM halos. However hierarchical models tend to predict substantially fewer massive galaxies at high redshift than are observed (Blain et al. 2002; Scott et al. 2002; Daddi et al. 2003; Tecza et al. 2004; Somerville et al. 2004). Moreover can merging form and preserve the tight correlations between SMBH and their host spheroidal galaxies? On the other hand, the traditional monolithic models, whereby galaxies formed their stars on a timescale shorter than their free-fall time and evolved passively thereafter (Eggen, Lynden-Bell & Sandage 1962), do not fit into a coherent scenario for structure formation from primordial density perturbations, and also tend to over-predict high-redshift galaxies.

In this situation it is essential to look for guidance from observational data. It has long been known that stellar populations in elliptical galaxies are old and essentially coeval (Sandage & Visvanathan 1978; Bernardi et al 1998; Trager et al. 2000; Terlevich & Forbes 2002). A color-magnitude relation is also well established: brighter spheroids are redder (Bower et al. 1992). The widely accepted interpretation is that brighter objects are richer in metals and the spread of their star formation epochs is small enough to avoid smearing of their colors. The slope of this relation does not change with redshift (Ellis et al. 1997; Kodama et al. 1998) supporting this interpretation. The star formation history of spheroidal galaxies is mirrored in the Fundamental Plane (Djorgovski & Davies 1987; Dressler et al. 1987) and in its evolution with redshift. Elliptical galaxies adhere to this plane with a surprisingly low orthogonal scatter ($\sim 15\%$), as expected for a homogeneous family of galaxies. Recent studies (e.g. Treu et al. 2002; van der Wel et al. 2004; Holden et al. 2004, 2005) suggest that ellipticals, both in the field and in clusters, follow this fundamental relation up to $z \sim 1$, consistent with the hypothesis that massive spheroids are old and quiescent.

Direct evidence that massive galaxies with $M \geq 10^{11} M_{\odot}$ were in place at $z \geq 2$,

is provided by recent K-band surveys (Cimatti et al. 2002; Kashikawa et al. 2003; Fontana et al. 2005). The space density of Extremely Red Objects (ERO) at $z \geq 3$ is only a factor $\sim$ 5–10 less than at $z \sim 1$ (Tecza et al. 2004). The submillimeter surveys with SCUBA and MAMBO (e.g. Blain et al. 2002) on the other hand indicate the presence of numerous protogalaxies (with comoving lenght not more than a few kpc scale, see e.g. Greve et al. 2005) with very high star formation rates ($\sim 10^3\, M_\odot \mathrm{yr}^{-1}$) at $z > 2$, most probably already harboring at their center an active central SMBH which is growing parallel to the surrounding spheroid (Alexander et al. 2005).

All these data are at variance with the simple recipe of hierarchical merging and point to a strong co-evolution between the SMBH and the surrounding spheroid, i.e. the *old* stellar component in the galaxy. In fact while the evolution of DM halos is controlled only by gravity, and therefore the underlying physics is simple (even if the evolutionary behavior, especially of subhalos, is complex), processes involving baryons are intricate and may hold the key to reconcile theory with observations. The central problem is to understand *when* the bulk of stars has formed in a galaxy. Large objects may be formed very early by interaction and merging of a hierarchy of primeval *gaseous* "clumps" in a protogalaxy (this is practically equivalent to a monolithic scenario). On the other hand there is no doubt that DM halos do merge and evidence for interacting galaxies is present, especially at low redshift. However it has to be understood how, and *to what extent*, the passively evolving galaxies and the disks are, if at all, modified by such processes.

Also the cosmic density of baryons $\Omega_b = 0.044 \pm 0.004$ has been very precisely determined both through the Cosmic Background Radiation anisotropy and measurements of the primordial abundance of light elements (Cyburt et al. 2001; Olive 2002; Spergel et al. 2003). An important complementary information is that the density of baryons residing in virialized structures and associated to detectable emissions falls short respect to Ω_b. In fact, traced-by-light baryons in stars and in cold gaseous disks in galaxies and in hot gas in clusters amount to a $\Omega_b^G \approx (3-4) \times 10^{-3} \leq 0.1\Omega_b$ (Persic & Salucci 1992, Fugukita et al. 1998, Fukugita & Peebles 2004). On the other hand, in rich galaxy clusters the ratio between the mass of the DM component and the mass of the baryon component, mainly in hot intergalactic gas, practically matches the "universal" ratio Ω_M/Ω_b.

The circumstance that Ω_b is a factor of about 10 larger than $\Omega_{b,\mathrm{lum}}$ puts forth both an observational and a theoretical problem. On one side observations are needed to detect and locate these "missing" baryons (see for a review Stocke, Penton & Shull 2003). On the theoretical side galaxy formation models have to cope with the small amount of baryons presently in gas and stars inside galaxies.

In this thesis we propose solutions to the these basic problems in galaxy evolution, through both theoretical modeling and deep exploration of several pieces of available data. We used the model presented by Granato et al. (2004). The Granato et al. model is rather simple, and physically grounded, based on a set of a few coupled differential equations (see Appendix A). The set of free parameters (see Table A.1 in Appendix A) is rather small compared with the number of physical outputs which it aims to fit.

Basically this model follows the build up with time of the global statistics of virialized DM halos which can host a *single* galaxy. Then trough semi-analytical techniques (SAM), in each of these DM "galactic" halos, the model computes the evolution of the baryon components, divided into hot and cold phases. Stars are formed within the dynamical/cooling times of the host system. Radiation drag, proportional to the actual rate of star formation, feeds a reservoir of low-angular momentum gas which ultimately falls into a central seed SMBH. The kinetic energy injected by Supernovae (SN) is increasingly effective, with decreasing halo mass, in slowing down (and eventually halting) both the star formation and the gas accretion on to the central SMBH. On the contrary, star formation, and BH growth proceed very effectively in the more massive halos, giving rise to the bright SCUBA phase (during which the protogalaxy is obscured by dust) until the energy injected by the AGN in the surrounding interstellar gas unbinds it, thus halting both the star formation and the BH growth and establishing the observed relationships between the BH mass and the stellar velocity dispersion or halo mass. After the AGN shining, the system appears as a luminous optically detectable AGN (QSO phase) and then evolves almost passively (ERO phase). In the whole this model predicts that any spheroid builds up at high redshifts and in a relatively short time, in general $\sim 0.5 \div 1$ Gyr. Such a feature naturally produces numerous, massive galaxies already at very high redshifts.

In particular in this thesis we will characterize the physical links among SMBH,

host galaxy and DM halo. We will show that the stellar and AGN feedbacks played a relevant role in unbinding large amounts of gas and eventually removing them from the galaxy host DM halo (see, e.g., Dekel & Silk 1986; Silk & Rees 1998; Granato et al. 2001, 2004; Hopkins et al. 2005; Lapi et al. 2005) solving the missing baryon problem and setting the correlations observed today in all spheroidal systems. Moreover we will demonstrate that the central SMBH and the surrounding spheroid, i.e. the *old* stellar population in the galaxy, have been built within a short time since the virialization of the host DM halo and therefore galaxies will "keep memory" of the initial conditions in their energy, mass and structure.

In more detail the scheme of the thesis is the following (the expert reader can skip Chapters 2 and 3, which are mainly reviews).

- In Chapter 2 we will sum the most relevant empirical and theoretical aspects regarding the local SMBH population and we will also discuss the main observational results on AGN evolution, statistics and global properties.

- In Chapter 3 we will introduce the main aspects of DM evolution from the primordial inhomogeneities to the properties of virialized DM halos. In particular we will address the fundamental problem of the actual number of DM halos viriliazed at any epoch, and which is the fate of the smaller halos (the sub-halos) when they fall in more massive structures. In the second part of Chapter 3 we will present the details of the physical model by Granato et al. (2004).

- In Chapter 4 we will use local data to compute the SMBH mass distribution, a fundamental tool to understand how these objects have formed. We will test the predictions of the Granato et al. SAM modeling on this observational result.

- In Chapter 5 we will study the match between AGN statistics and SMBH local mass function, to probe the main average properties of accretion. From such a comparison we will define the actual role of merging in building local SMBH. Finally we also compute the AGN visibility timescales, their dependence on SMBH mass and on the survey wavelength.

- In Chapter 6 we will use Granato et al. SAM modeling to reproduce the AGN luminosity functions at all redshifts. We will then compare the predicted activity AGN timescales and SMBH accretion history with the empirical results of the previous Chapter. We will discuss the relationship between high redshift galaxies and AGN statistics. We will then check that our high redshift AGN modeling is able to produce a good fit to the high-redshift galaxies in the K and submillimeter bands as in Granato et al. (2004). Finally we will show that the very low-redshift AGN evolution can be reproduced assuming a self-regulated, supply-limited, accretion onto the already massive SMBH, which are re-activated at very low Eddington regimes.

- In Chapter 7 we will reproduce the dispersion velocity function and the fundamental plane of early-type galaxies, deriving basic properties on the very early stages of the protogalaxy evolution and the effective processes which have dominated galaxy evolution, at least at redshifts above $z = 1.5$.

- In Chapter 8 by comparing the local number density distribution of galaxy luminosity, stellar mass, velocity dispersion and black hole mass with the Mass Function of "galactic" DM halos, we will derive the relationships between these characteristic galaxy properties and the galaxy halo mass. From such relationships we will derive conclusions on the type and efficiency of the main physical processes which govern galaxy evolution and compare these empirical evidences with the model predictions presented in the previous Chapters.

In this thesis we use the following set of cosmological parameters,

$$\begin{aligned} h &= 0.70 \pm 0.04 \text{ Mpc}^{-1} \\ \Omega_M &= 0.27 \pm 0.04 \\ \Omega_\Lambda &= 0.73 \pm 0.05 \\ t_0 &= 13.7 \pm 0.2 \text{ Gyr} \\ \sigma_8 &= 0.84 \pm 0.04 \end{aligned}$$

emerging from a number of observations (the *Concordance Cosmology*, see Spergel et al. 2003).

Chapter 2

SUPERMASSIVE BLACK HOLES: An Overview

2.1 Supermassive Black Holes in the Local Universe

2.1.1 Looking for Supermassive Black Holes

All spheroids, elliptical galaxies and disk galaxy bulges, appear to host a SMBH at their center. In any given galaxy at a distance D and with stellar velocity dispersion σ, a SMBH detection can be roughly quantified in terms of r_G, the radius of the sphere of influence over which the SMBH dominates the gravitational potential of its host galaxy (Barth 2004)

$$r_G = \frac{GM_\bullet}{\sigma^2} = 0.11 \left(\frac{M_\bullet}{10^8\ M_\odot}\right) \left(\frac{200\ \mathrm{km\,s^{-1}}}{\sigma}\right)^2 \left(\frac{20\ \mathrm{Mpc}}{D}\right)\ \mathrm{arcsec} \tag{2.1}$$

where the second equality holds for a telescope measurement projected onto the sky. Therefore a direct SMBH detection, carried out through the analysis of the motion of gravitating bodies embedded in the strong SMBH gravitational field, can be obtained only in nearby galaxies (see Ferrarese & Ford 2004 for a recent review on these topics).

In particular in inactive local galaxies the presence of SMBH in the central region is tested through dispersion velocities of stars, water masers and gas. The mass of the central object is calculated from the collisionless Boltzmann and Poisson equations once the surface

stellar density and galaxy dispersion velocity profiles are measured. The most exciting example is the detection of a SMBH at the center of the Galaxy, which also represents one of the most tightest constraints on the existence of a SMBH. Monitoring has been carried on for about 10 years on 40 stars orbiting around the center of the Galaxy. A few of them have passed the pericenter and Ghez et al. (2003) have measured, from a simultaneous fit to the stars orbit, a central mass of $(4.0 \pm 0.3) \times 10^6\, M_\odot$.

In active galaxies a first attempt to the SMBH mass determination is performed from a direct spectral fitting of the 'Big Blue Bump' (see Section 2.2.3), the optical/UV/soft X-ray continuum thermal emission from an optically thick, geometrically thin accretion disk. More secure mass determinations are performed with the Reverberation Mapping technique. The masses are obtained from the virial theorem $M_\bullet = f\ R_{\rm BLR}\sigma^2/G$, where f accounts for the geometry and kinematics of the system and R_{BLR} is the Broad Line Region (BLR; see section 2.2.3) radius. Such a radius is measured from the delayed response of the BLR emission line flux to variation in the continuum ionizing source flux, caused by the time spent by light traveling from the inner source to the photoionized clouds positioned on a sphere of radius from 10 to 100 times the size of the inner accretion disk. The reverberation mapping technique can probe a radius of about 1000 times the Schwarzschild radius, sampling a region far more inner than the orbits of the nearest stars. The implied measured mass densities, of the order of $10^{10} M_\odot\,{\rm pc}^{-3}$, thus provide a stronger proof to the existence of a very massive collapsed object at the center.

Various authors (Vestergaard 2002; Kaspi et al. 2000) have noted a quite tight correlation between the BLR radius, measured through reverberation mapping, and luminosity of the type:

$$R_{\rm BLR} = (30.2 \pm 5.6) \left[\frac{\lambda L_\lambda(5100\mathring{A})}{10^{44}\,{\rm erg\,s^{-1}}}\right]^{0.66\pm0.09} \text{ lt days}\,. \tag{2.2}$$

Such a correlation, extrapolated to all types of AGN, is used for measuring SMBH masses from the virial theorem. In particular (Vestergaard 2002), using the $CIV\lambda1549$ emission, has calibrated a relation similar to the one in Eq. (2.2), for AGN in the redshift range $1 < z < 5$, where the redshifted UV data are accessible from the ground.

2.1.2 The correlations between SMBH and their host spheroidal galaxies

Kormendy & Richstone (1995) were the first to notice that SMBH masses correlate with the blue luminosity of the surrounding hot stellar component, i.e. bulges for spiral galaxies and the whole galaxy for ellipticals. In particular the authors demonstrated that the scatter of the correlation significantly increases when the SMBH is plotted against the whole mass of spirals (bulge plus disk), clearly indicating that the SMBH mass is tightly linked *only* with the mass of the spheroid.

Ferrarese & Merritt (2000) confirmed such a correlation on a wider sample, claiming a scatter of about 0.6 dex. McLure & Dunlop (2001) then noticed that however the scatter is reduced if only ellipticals are considered. McLure & Dunlop (2002) moreover found that both local inactive and active galaxies, Seyferts and QSO, follow the same $M_\bullet - L_{\rm bulge}$ relation over more than 3 decades in SMBH mass and more than 2.5 decades in bulge luminosity. This strongly supports the conclusion that the host galaxies of powerful QSO are normal massive ellipticals. Contrary to previous claims (Wandel 1999), the authors noticed no systematic offset between the Seyfert 1 and quasar samples, showing that the bulges of Seyfert galaxies and QSO form a continuous sequence, from $M_R \sim -18$ to $M_R \sim -24.5$. McLure & Dunlop (2002) found that the scatter around the best-fitting relation $M_\bullet - L_{\rm bulge}$ for the whole sample is only $\Delta \log M_\bullet = 0.39$ dex, reducing to 0.33 dex if only inactive galaxies are considered. The authors claim that such a reduced scatter, as compared to previous findings, is due to the two-dimensional modeling of the high resolution HST data and to the more accurate, inclination-corrected, SMBH mass estimates provided by their flattened BLR geometrical model (McLure & Dunlop 2002).

It is now clear, from the above studies and ad-hoc near-infrared and high-resolution observations at redshifts below 1, that the hosts of all luminous QSO ($M_V < -23.5$; see Dunlop 2004 for a review) are bright galaxies with $L > L^\star$ (being $L^\star$ the knee of the local galaxy luminosity function, see also Chapter 3, Section 3.4.1). Either Radio-Loud and Radio-Quiet QSO hosts are undoubtedly massive ellipticals (as their light profiles can be very well fitted with a de Vaucouleurs, $r^{1/4}$, profile, see Chapter 3, Section 3.4.1) with negligible disk components. It is clear that a given AGN above a certain luminosity, which

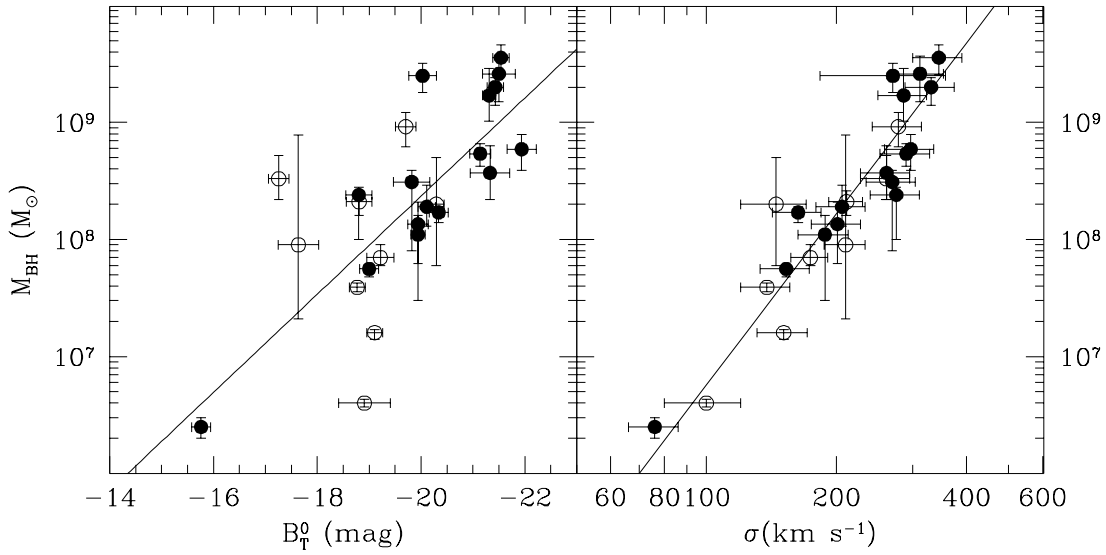

Figure 2.1: Left panel: the relation between SMBH mass and blue luminosity of the galaxy spheroidal component. Right panel: the relation between the SMBH mass and central velocity dispersion of the host galaxy. Filled symbols show ellipticals galaxies, while open symbols show spirals and lenticulars (Figure taken from Ferrarese & Ford 2004).

corresponds to a mass $> 10^8 M_\bullet$, can only be hosted by an elliptical independently of its radio-loudness. In the whole AGN hosts seem to be spheroidal galaxies very similar to their inactive companions.

The AGN hosts moreover seem to be dominated (Dunlop 2004) by old, well-evolved stellar populations (with typically about 1% of mass involved in recent star formation activity). In less luminous AGN the probability of finding a significant disk component in the host galaxy gets stronger (see Fig. 1.3 in Dunlop 2004). Moreover also the fraction of molecular gas, the fuel for star formation, is much higher for lower luminosity AGN.

Kukula et al. (2001) have found, through HST infrared imaging, that the QSO host galaxies at $z \sim 2$, independently of their radio-loudness, have the same structural and photometric properties of local ellipticals and the formation epochs of these sources is consistent with $z > 3$, allowing for passive evolution after that time. The authors argue for a moderate increase in the fuelling efficiency of massive black holes since those redshifts.

Moreover Woo et al. (2004) show that the 15 AGN in their sample lie on the same fundamental plane as non-active galaxies and their $M_{\rm star}/L$ evolution shows a similar

trend to that observed in normal early-type galaxies, consistent with single-burst passive evolution models with formation redshifts $z \geq 1$.

A very tight correlation has been observed (Ferrarese & Merritt 2000; Gebhardt et al. 2000; Tremaine et al. 2002) between SMBH mass and the dispersion velocity of the host spheroidal galaxy $M_\bullet \propto \sigma^\beta$. Its scatter is very small about $\Delta \log M_\bullet \sim 0.3$ at fixed σ. The conclusions of the previous groups are similar even if Gebhardt et al. use a luminosity-weighted line-of-sight dispersion velocity inside the radius R_e, while Ferrarese & Merritt used central velocity dispersions normalized to an aperture of radius equal to 1/8 of the galaxy effective radius R_e. All the group find a similar normalization in the relation and slopes $\beta \sim 4 \div 4.8$.

Marconi & Hunt (2003) point out that the scatter in the above relations gets reduced when the sphere of influence of the SMBH is well resolved and when the galactic luminosity is a good tracer of the old stellar population. Interestingly they also claim an even stronger relation ($\Delta \log M_\bullet \sim 0.25$) between the SMBH mass and the virial bulge mass of the host galaxy $R_e\sigma^2$.

On the same track Graham et al. (2001) found a remarkably tight correlation between SMBH mass and concentration of bulge light, defined as the ratio of fluxes $F(R < 1/3R_e)/F(R < R_e)$. This seems to be a direct consequence of the fact that in ellipticals the brightness profile correlates with galaxy luminosity. Larger and more luminous galaxies have shallower brightness profiles and host more massive BH. Graham (2002) found moreover that the Sersic index n, determined from the $r^{1/n}$ fits to the bulge light profiles, correlates extremely well with the dispersion velocity/SMBH mass. Erwin et al. (2004), through accurate modeling, found that the structure of disk galaxy bulges, as measured by the Sersic index (or by central concentration), is closely related to the central SMBH mass with a scatter comparable to the one found for the SMBH dispersion velocity relation.

Taken together all these empirical evidences point to a global link between the SMBH and the mass, potential and structure of the spheroidal host. We will use these relations, in particular between SMBH mass and its spheroid luminosity/dispersion velocity, to calibrate the SMBH mass local distribution. A more critical analysis of such correlations will then be given in Chapter 4.

In a more general view the SMBH mass is tightly linked with both dynamical and photometric properties of the host galaxies. In fact observationally early type galaxies exhibit a well-defined correlation among their effective radii R_e, luminosities L (or equivalently surface brightness $T \propto L/R_e^2$) and central velocity dispersion σ (i.e. the central SMBH mass). This *Fundamental Plane* (FP) (e.g. Djorgovski & Davis 1987) is often expressed as

$$R_e \propto \sigma^a I^b \tag{2.3}$$

with $a \sim 1.49 \pm 0.05$ and $b = -0.75 \pm 0.01$ as calibrated from 9000 early type galaxies by the SDSS team (Bernardi et al. 2003) and a very small scatter. Projections of the fundamental plane have also been measured independently but such relations present a much larger scatter. In particular it has been found that the radius-luminosity relation is of the type $R_e \propto L^{0.630 \pm 0.025}$ and the Faber-Jackson (1976) relation reads as $\sigma \propto L^{0.250 \pm 0.012}$.

The FP has typically been interpreted as a manifestation of the virial theorem, which relates σ and R_e to the total enclosed (dynamical) mass $M_{\rm dyn}$ and predicts a correlation in the fundamental properties of galaxies:

$$\sigma^2 \propto \frac{M_{\rm dyn}}{R_e} = \left(\frac{M_{\rm dyn}}{L}\right)\left(\frac{L}{R_e^2}\right) R_e \propto \left(\frac{M_{\rm dyn}}{L}\right) I R_e \tag{2.4}$$

giving the relation

$$R_e \propto \sigma^2 I^{-1} \left(\frac{M_{\rm dyn}}{L}\right)^{-1}. \tag{2.5}$$

Clearly this virial theorem expectation is incompatible with the observed fundamental plane in Eq. (7.8) if light traces the dynamical mass. A systematic variation of $M_{\rm dyn}/L$ is assumed to "tilt" the virial theorem scalings into the observed ones (see Boylan-Kolchin et al. 2005). Since

$$\frac{M_{\rm dyn}}{L} = \left(\frac{M_{\rm dyn}}{M_{\rm star}}\right)\left(\frac{M_{\rm star}}{L}\right) \tag{2.6}$$

this tilt could result from increasing $M_{\rm star}/L$ with L due to, for instance, varying the metallicity or stellar population age, or from increasing $M_{\rm dyn}/M_{\rm star}$ with L due to higher dark matter fraction in the central parts of more luminous galaxies.

In literature there are conflicting conclusions on this point. Padmanabhan et al. (2004) claim that modeling ellipticals as a stellar Hernquist profile embedded in an *adiabatically* compressed dark matter halo (see also Chapter 3) the fundamental plane tilt can

be explained with a constant $M_{\rm star}/L$ and an increasing $M_{\rm dyn}/L$ with luminosity. Opposite conclusions are reached instead by Gerhard et al. (2001). We will discuss this issue in Chapter 7.

Moreover the FP of ellipticals is now been observed up to redshift $z \sim 1$ (see Treu 2004 for a review). Data are showing that the FP already at that time has a small scatter, at least for the most massive objects. The FP slope and normalization at $z \sim 1$ indicate moderate differences with respect to the local FP, consistent with passive evolution of the early type-galaxies since that time. Numerical simulations have tried to address the problem of building a fundamental plane at high redshift within the framework of hierarchical models and different authors reach conflicting results (see Boylan-Kolchin et al. 2005): however they agree that mergers of subunits constituted by bulge baryonic systems within dark matter halos usually reproduce a FP with a tilt larger than observed (Dantas et al. 2003) and the FP projections are difficult to preserve (Nipoti et al. 2003).

2.2 The Supermassive Black Hole Paradigm: the AGN phenomenon

AGN are all those extragalactic sources not powered by starlight but most probably powered by a compact central engine made of a SMBH. Such sources in fact produce very high luminosities (up to 10^{48} erg/s, which is 10^4 times the luminosity of a typical galaxy) in a tiny volume. The spatial information is derived from the observed source variability which ranges from a few hours to few light days. Therefore if the radiation, emitted from a region of size R that is moving with speed v, varies at a timescale Δt, then we must have $R \leq c\Delta t/\gamma$. If $\gamma \sim 1$ and $\Delta t \sim 1$ h then $R \leq 10^{14}$ cm, less than the Solar System.

The only process through which it is possible to generate so high powers in such tiny volumes is accretion onto a compact object in which one can easily convert rest-mass energy into radiation with an efficiency of a few percent (just for comparison the nuclear stellar efficiencies are of about 0.008). In fact given a body of mass m that falls from infinity to a distance of, say, $5R_g$, where $R_g = 2GM/c^2$ is the Schwarzschild radius (see Section 2.2.3), from a compact object of mass M, it could radiate an energy equal to up

the potential energy $U = GMm/5R_g = 0.1mc^2$. Accretion onto compact objects, in which M/R is large, is therefore accompanied by the release of large amounts of energy.

2.2.1 The Eddington Limit

The photons released by an accreting object exert a force on the accreting gas: the outward momentum of the photons is thereby transferred to the gas. If $F = L/4\pi r^2$ is the radiative energy flux at a distance r, and k the opacity of the gas (scattering plus absorption), the acceleration due to this force is $g_{\rm rad} = Fk/c$. This force is just balanced by the inward acceleration of gravity $g = GM/r^2$ when the luminosity L has a value called the Eddington limit or Eddington luminosity

$$L_E = \frac{4\pi GMc}{k} = \frac{Mc^2}{t_E} \simeq 1.4 \cdot 10^{38} \left(\frac{M}{M_\odot}\right) \ {\rm erg\,s^{-1}}\,. \tag{2.7}$$

being $t_E = kc/4\pi G = 4 \cdot 10^8$ yr (expressing the opacity in terms of the Thomson optical depth) the Eddington timescale. A steady photon source bound by gravity, cannot have a luminosity significantly exceeding this limit. At a larger luminosity, the atmosphere of the source is blown off by radiation. The value of the Eddington luminosity depends on the opacity of the gas, and thereby on its state of ionization. It depends on the mass of the source but not its size.

If this luminosity is generated by accretion, equating it to the accretion energy defines the Eddington accretion rate

$$\dot{M}_E = \frac{4\pi cR}{k} = \frac{L_E}{c^2} \simeq 1.5 \cdot 10^{17} \left(\frac{M}{M_\odot}\right) \ {\rm g\,s^{-1}}\,. \tag{2.8}$$

If sufficiently strong the radiation pressure building up would prevent further accretion, and the gas would accumulate in an extended atmosphere around the central object. Eq. (2.8) provides at any time during the accretion a proportional link between the accretion rate and central mass which will go exponentially (see Chapter 5).

In the specific case of a black hole (BH) the accretion rate can be much higher than $\dot{M}_E$. An atmosphere surrounding a hole is not supported at its base, but flows in through the horizon. In the process it takes with it the photons trapped in the gas (*photon trapping*). Depending on the density of such an atmosphere, the accretion rate can be arbitrarily high. The luminosity as seen from Earth does not become much higher than L_E however.

Very recently Abramowicz (2004) has shown that the Eddington limit for rotating bodies has to be written as $F_{\rm rad} < F_{\rm eff} = F_{\rm grav} + F_{\rm rot}$, in which the radiation pressure is balanced by the sum of the gravitational plus rotational force. Such a condition can be expressed as

$$L_E^{\rm rot} = L_E[\chi^2_{mass} + \chi^2_{\rm shear} - \chi^2_{\rm vorticity}]\,. \tag{2.9}$$

For rigidly rotating, radiation supported stars the shear is very small and the condition $L_E^{\rm rot} < L_E$ is always fulfilled. For radiation supported accretion disks the shear is always dominant so $L \sim L_E^{\rm rot} > L_E$.

This simple argument suggests that probably the Eddington limit could be easily overcome if the central object is accreting in non-spherical geometry and/or rotating, a condition which data seem to support, as shown by the Soltan argument and extensively discussed in this thesis.

The highest redshift QSO observed is SDSS J1148+5251 at z=6.42 (e.g. Walter et al. 2004) could be a direct evidence of a SMBH accreting at a rate higher than the Eddington limit. It is a very luminous QSO that, if emitting at the Eddington limit, would have a SMBH mass of $\sim 10^9 M_\odot$. Thermal emission from warm dust has been detected at millimeter wavelengths, implying a far-infrared luminosity of $1.3 \cdot 10^{13} L_\odot$ corresponding to about 10% of the bolometric luminosity of the system. If the heating of the dust is dominated by young stars, then the implied star formation rate is $\sim 3000 M_\odot\,{\rm yr}^{-1}$. High-resolution Hubble Space Telescope (HST) imaging does not reveal multiple imaging of the central AGN, implying strong magnification unlikely. Using the Very Large Array (VLA) Walter et al. (2004) from CO emission data have measured a total extrapolated mass for the bounded molecular gas of about $\sim 5.5 \cdot 10^{10} M_\odot$.

The ratio $M_\bullet / M_{\rm star}, \sim\ 1.8 \cdot 10^{-2}$, is much larger than what observed in local galaxies. The authors therefore claim a possibility that in this object there could be no parallel growth between the central SMBH and the stellar system around it, i.e. the SMBH has already grown to its final value while the spheroid is still building up. However it has to be noted that the local proportion between SMBH and spheroid mass could be easily recovered if it is assumed that the SMBH emits at a level slightly higher than the Eddington limit (say a factor $3 \div 4$ above). In this case the central SMBH would have a

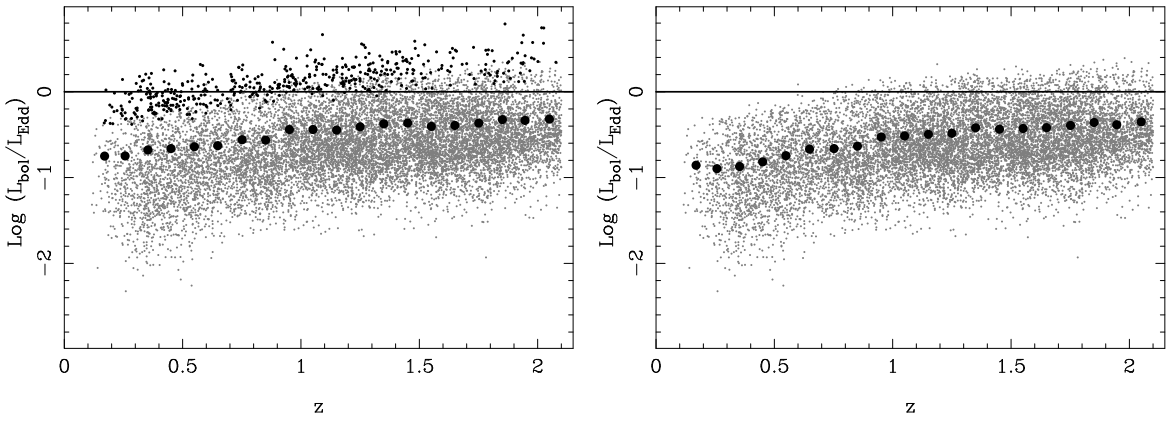

Figure 2.2: Left panel: Eddington ratio as a function of redshift. The gray symbols are broad-line quasars (FHWM $\geq$ 2000 km/s) and the black symbols are narrow-line objects (FHWM $<$ 2000 km/s); the mean values of $L_{\rm bol}/L_{\rm Edd}$ within Δz=0.1 are shown as filled circles. The solid horizontal line marks the Eddington limit. Right panel: same as left one but only broad-line objects have been plotted. (Figure taken from McLure & Dunlop 2004).

mass of $\sim (1 \div 3) \times 10^8 M_\odot$. Indeed in Chapter 6 we will show that super-Eddington emission is one of the most suitable mechanisms for building enough luminous QSO by $z \sim 6$.

Mathur & Grube (2005) investigated the accretion of local Seyfert galaxies showing that these objects are accreting at super-Eddington regimes. It is still yet not clear the amount of parallel star formation which occurs in these galaxies, especially in the central bulges, however these systems seem to rely below the mean $M_\bullet - \sigma$ relation, suggesting that the central SMBH are in the main growth phase. Interestingly as an extreme limit Kawaguchi et al. (2004) (see also Section 2.2.2) discussed that when the accretion is occurring at a rate much larger than the Eddington limit, the accretion is occurring not through a thin (see below) but a "slim" disk, with a cooling time larger than the viscous time, so that the energy is advected towards the SMBH before being radiated. The luminosity can then saturate, and never be larger than a few times L_E.

SMBH masses

$$M_\bullet(t) = \frac{1}{\eta c^2} \int^t dt' L(t') \tag{2.10}$$

keep the archives of the luminous history of AGN sources down to the cosmic time

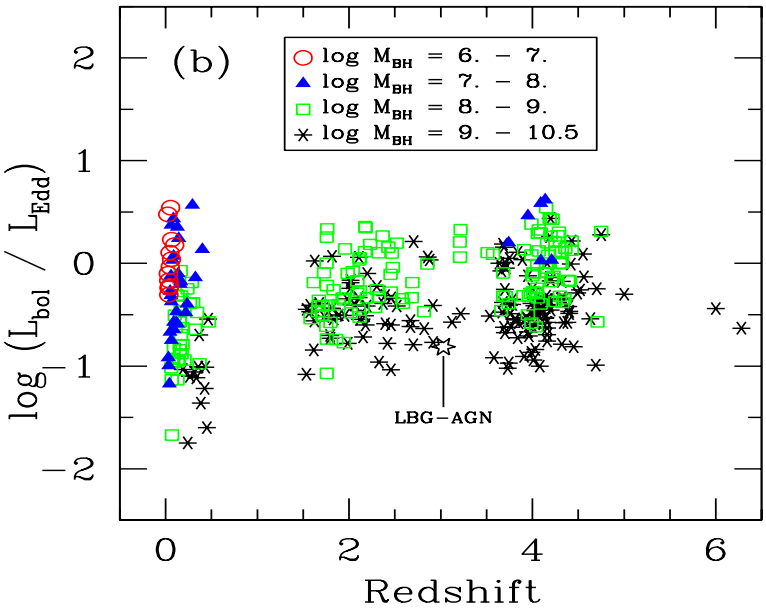

Figure 2.3: Distribution of $L_{\rm bol}/L_{\rm Edd}$ with redshift binned in $M_\bullet$. (Figure taken from Vestergaard 2004).

t. Eq. (2.10) relates the *cumulative* variable $M_\bullet$ to the quantity L which signals *current* source activity. Here $\eta = \epsilon/(1-\epsilon)$, being ϵ the radiative efficiency, represents the actual fraction of the rest mass energy accreted onto the SMBH (see Chapter 4).

The integral nature of Eq. (2.10) allows different activity patterns (as discussed by e.g. Cavaliere & Padovani 1988). For example, the AGN population could be comprised of a number of sources *continuously* active over several Gyrs, but such a trend would accumulate many large masses $M_\bullet(t)$ in excess of $10^{10}\,M_\odot$, at variance with observations in local galaxies (e.g. Tremaine et al. 2002; a similar bound is also found for QSOs shining at higher z see McLure & Dunlop 2004, Vestergaard 2004).

At the other extreme, Eq. (2.10) holds as well during a *single* accretion event of a mass Δm over the time scale τ, much less than the Hubble time, to yield a flash of bolometric luminosity $L \simeq \eta c^2 \Delta m/\tau$. Here each SMBH mass is accreted in one go over a constant τ, so $M_\bullet = \Delta m$ applies and the ratios $L/L_{\rm Edd} \propto L/M_\bullet \sim \epsilon c^2\,/\,\tau$ are closely constant. We will show in Chapter 5 that, through the single-flash approximation, we will

be able to reproduce the local SMBH mass distribution integrating in time the overall AGN statistics. In Chapter 6 we will discuss that only 20-30% of the total relic mass density today can be accounted for through re-activations of already formed SMBH.

As observed up to redshift $z \sim 4$ (see McLure & Dunlop 2004, Vestergaard 2004), the Eddington ratio seems on average to decline significantly only at very low redshift ($z < 1$). At higher redshifts the Eddington ratio is almost constant (see Fig. 2.2 and Fig. 2.3) though with a large scatter, due also to large empirical uncertainties, up to factors of 3-4, in the SMBH mass estimates (Vestergaard 2004). Moreover, as discussed in Section 2.2.5, the break of the AGN luminosity functions, in every band, declines strongly with redshift pointing towards an average decline in luminosity density. If this is the case, over the cosmic time t, new SMBH ought to form continuously, but with, on average, progressively lower masses so as to track the population decline to lower luminosities while retaining nearly constant (or slightly declining) Eddington ratios $L/M_\bullet$. For this to occur, the trend in the hierarchical formation of structures toward ever-growing masses would have to be somehow *reversed* in a closely tuned way for the active SMBH. Therefore even the tight correlations between SMBH and host galaxies, such as the $M_\bullet - \sigma$ relation, would evolve markedly, being progressively extended toward smaller M for decreasing z, still with a narrow scatter.

2.2.2 The Basics of Accretion

The simplest situation for accumulating mass at the center is stationary spherical accretion (Bondi & Hoyle 1944) controlled by the continuity and Euler equations

$$\dot{M} = 4\pi r^2 v \qquad (2.11)$$
$$v\frac{dv}{dr} = -\frac{1}{\rho}\frac{dp}{dr} - \frac{GM}{r^2}\,.$$

In this stage the accretion onto the central object reads as

$$\dot{M}_{\rm Bondi} = \frac{\alpha 4\pi G^2 M_\bullet^2 m_H n}{c_s^3} \qquad (2.12)$$

where α is a dimensionless parameter of order unity and c_s is the sound speed of the gas.

Recently Volonteri & Rees (2005) have shown that the Bondi rate in the initial stages is higher than the Eddington limit and it could have played a crucial role in feeding

the first seeds of the SMBH population (see Section 2.3). Comparing the accretion rates they find

$$\frac{\dot{M}_{\rm Bondi}}{\dot{M}_{\rm Edd}} = 40 M_{\bullet,3} n_3 T_{\rm gas,8000}^{-3/2} \tag{2.13}$$

where the density is in units of $10^4\,{\rm cm}^{-3}$ and the SMBH is normalized to a $10^3 M_\odot$ BH. It is clear that Bondi accretion was probably dominant during accretion in the first high σ-peaks of the density fluctuations in which $T_h > 10^4$ K.

Usually the accretion, as discussed above, will be limited by the central source radiation pressure to be at the level of the Eddington accretion. In this case Bondi/spherical accretion is not the most suitable physical type of accretion for a SMBH. The Bondi recipe has however been implemented in some numerical simulation (e.g. Di Matteo et al. 2005), which have confirmed results of previous Semi Analytical Models (SAM; e.g. Granato et al. 2001, 2004 and the work in this thesis): after a fast growth the SMBH at the galactic center can energetically or dynamically back-react on the Interstellar Medium (ISM) ultimately halting star formation. Granato et al. (2004) in particular (and further analyzed in this thesis) have pointed out that the standard recipe of an Eddington or at most slightly super-Eddington regime, applicable in the case of disk accretion, can still play the role of the fast spherical accretion, letting the SMBH grow substantially within just the host cooling/dynamical time (see Chapter 3), therefore building massive objects at even very high redshifts ($z = 6$).

Mass will generally be accreted from the outer skirts of the host galaxy and the infalling gas will be endowed with substantial angular momentum. In this case accretion onto the central SMBH will proceed through a disk. Following Shakura & Sunyaev (1973) we'll describe the basic process of accretion through a disk. We suppose the simplest geometry of a *thin optically thick disk*, with the vertical thickness H being much smaller than the radius R. This could imply the accretion luminosity L not to be always equal to $L_{\rm Edd}$ as Eq. (2.7) has been derived assuming spherical symmetry.

Vertical support in general requires according to hydrostatic equilibrium

$$\frac{GM}{R^2}\frac{H}{R} = \frac{1}{\rho}\left|\frac{\delta P}{\delta z}\right| \simeq \frac{P_c}{\rho_c H}, \tag{2.14}$$

where P_c and ρ_c are the central density and pressure. Using $v = (GM/R)^{1/2}$ it is possible

to write Eq. (2.14) in the form

$$c_s^2 \simeq \frac{P_c}{\rho_c} \simeq v^2 \frac{H^2}{R^2} \,. \tag{2.15}$$

For the disk to be thin it is necessary to have $H << R$, requiring $c_s^2 << v^2$. In the same limit the radial acceleration due to pressure is given by

$$\frac{1}{\rho}\frac{\delta P}{\delta R} \simeq \frac{P_c}{\rho_c R} \simeq \frac{c_s^2}{R} \simeq \frac{GM}{R^2}\frac{H^2}{R^2} \,, \tag{2.16}$$

which is much smaller than the gravitational acceleration when $H << R$. These arguments simply show that the fluid in a thin disk moves in a Keplerian orbit to a high degree of precision.

In this situation the radial velocity v_R will be much smaller than the azimutal velocity v. The amount of mass crossing any radius R per unit time is $-2\pi R\Sigma v_R$ with

$$\Sigma(R) = 2\int_0^H \rho(R,z)dz \tag{2.17}$$

the surface density of the disk. Being $\Omega(R) = (GM/R^3)^{1/2}$ the Keplerian angular rotation velocity, the specific angular momentum varies as $R^2\Omega \propto R^{1/2}$, which decreases with decreasing R. Therefore accretion through successive Keplerian orbits towards the central mass is possible only if the fluid can constantly loose angular momentum because of some viscous torque.

If we set $F = \nu\Sigma(R\Omega/dR)$ the viscous force per unit length, with ν some unspecified coefficient, the viscous torque will be

$$S(R) = (2\pi RF)R = \nu\Sigma 2\pi R^3 \left(\frac{d\Omega}{dR}\right) \,. \tag{2.18}$$

The direction of the fluid is such that the fluid at a radius less than R (which is rotating more rapidly) feels a backward torque and looses angular momentum whereas the fluid at radius larger than R gains the angular momentum. Therefore the net angular momentum loss due to the torque acting at R and $R + dR$ is, once integrated,

$$\nu\Sigma = \frac{\dot{M}}{3\pi}\left[1 - \left(\frac{R_*}{R}\right)\right] \,, \tag{2.19}$$

where R_* is the inner radius at which the shear vanishes (for a black hole usually R_* is given by the radius of the innermost marginally stable orbit; see below).

The viscous dissipation rate per unit area is given by

$$D(R) = \nu\Sigma \left(R\frac{d\Omega}{dR} \right)^2 = \frac{3G\dot{M}M}{4\pi R^3} \left[1 - \left(\frac{R_*}{R} \right)^{1/2} \right] . \tag{2.20}$$

It is interesting to note that in Eq. (2.20) the rate of radiative energy loss is 3 times the rate of release of binding energy ($GM\dot{M}/R$). This extra energy release is the work done by the torque S, and it derives from the binding energy release at small radii.

The corresponding total luminosity is

$$L = \int_{R_*}^{\infty} D(R) 2\pi R dR = \frac{GM\dot{M}}{2R_*} . \tag{2.21}$$

Note that L is the total gravitational potential energy lost in the drop from infinite distance to R_*. The other half of the potential energy is actually present in the form of kinetic energy of the fluid at R_* and is not available for dissipation as heat.

A thin disk in steady state radiates energy through its top and bottom surfaces. Assuming that the spectrum is a blackbody with surface temperature $T_s(R)$ then we must have $2\sigma T_s^4(R) = D(R)$ (with the factor of 2 arising from the existence of two surfaces) implying that

$$T_s = \left(\frac{3G\dot{M}M}{8\pi R^3 \sigma} \left[1 - \left(\frac{R_*}{R} \right)^{1/2} \right] \right)^{1/4} . \tag{2.22}$$

The results in Eq. (2.21) and Eq. (2.22) are independent of the coefficient of viscosity and can be expressed entirely in terms of $\dot{M}$. However the entire mechanism depends on viscosity. It is worth noticing that the standard fluid viscosity due to molecular scattering, $\nu_{\rm mol} = \lambda_{\rm mfp} c_s$, with $\lambda_{\rm mfp}$ the mean free path and c_s the local sound speed, is inadequate in this context. Infact the Reynold's number

$$Re \approx (Rv/\nu_{\rm mol}) \simeq 2 \cdot 10^9 (M/M_\odot)^{1/2} (R/10^{10}\,{\rm cm})^{1/2} (nT^{-5/2}) , \tag{2.23}$$

is very large for typical values in accretion disks ($n \approx 10^{15}\,{\rm cm}^{-3}$, $T \approx 10^4 K$), showing that molecular viscosity is irrelevant.

Turbulent viscosity could instead be effective with $Re \geq 10^3$. The viscosity in this case is written as $\nu \approx v_{\rm turb} l_{\rm turb}$, where $v_{\rm turb}$ is the velocity associated with turbulent eddies

and $l_{\rm turb}$ is the size of the largest coherent turbulent cell. For a thin accretion disk one can then write, assuming $v_{\rm turb} << c_s$ and $l_{\rm turb} << H$

$$\nu_{\rm turb} \simeq \alpha c_s H \, . \tag{2.24}$$

However accretion which occurs through the simple form of a thin accretion disk could develop in a complicated way due to instabilities usually determined by large-scale magnetic flows or high-degree turbulence. The most general criterion for a thin accretion disk to be stable is to have $d \ln \dot{M}/d \ln \Sigma > 0$. Analytical and numerical studies (Abramowicz & Marsi 1987) have however shown that the $\dot{M}(\Sigma)$ curve has a *S*-shape. Therefore if the accretion rate lies in the instability strip (where the slope of the curve is negative), then stationary accretion is impossible and the system will always "jump" in short periods of time to very different accretion rates.

The physical scenario described above of a thin disk has some limitations. Abramowicz et al. 1980 have calculated that in some accretion regimes the Keplerian motion may break down and for a wide class of non-Keplerian angular momentum distributions the accreting material can form a *toroidal* structure, in some cases resembling a sphere with two deep and narrow funnels along the rotation axis. Indeed observations are more and more suggesting that a gas toroidal structure around the central SMBH could be a very common topology for the AGN population (see Sections 2.2.4 and 2.2.5) .

Following Blandford (2004) we can therefore set $\dot{m} = \dot{M}/\dot{M}_{\rm Edd}$, and distinguish among three main rates of accretion onto a SMBH.

1. Low Mass Supply. When $\dot{m} < \dot{m}_1$, with $\dot{m}_1 \sim 0.3$, the radiative efficiency is very low: being the accretion rate so small the viscous torque are not so effective in heating the electrons and the energy is transported away from the disk by large-scale magnetic fields or is absorbed by the ions, coupled to the electrons by Coulomb scattering. For example in the Galaxy, with about $\dot{m}_1 \sim 0.003$ and, as mentioned before, a rather small central SMBH about $M_\bullet \sim 3 \cdot 10^6 M_\odot$, has a bolometric luminosity of $\sim 10^{36}$ erg/s, which translates into an efficiency of about 10^{-6}. Therefore in such a regime it is possible to ignore cooling and the accretion is adiabatic with the pressure dominated by ions (the specific heat ratio is γ=5/3).

In this adiabatic regime (i.e. no radiative energy losses) the mass and angular momentum conservation equations are unchanged. The energy is advected/convected inward (ADAF, CDAF; see e.g. Narayan & Yi 1994). However the gas is no longer cold and the total energy (kinetic plus gravitational) of the system E must be augmented by the thermal energy. Therefore the net energy flow outwards will include also information on the thermodynamic state of the system, i.e. $F_E = S\Omega - \dot{M}E \rightarrow S\Omega - \dot{M}B$, being B the Bernoulli function $B = L/2R^2 + \Phi + H$, with L the angular momentum, Φ the gravitational energy and H the enthalpy. In adiabatic conditions, $F_E \sim 0$, therefore $B > 0$ implying that the gas has enough energy to escape to infinity with positive kinetic energy. This is been pointed out as a mechanism for producing jets and/or outflows in some classes of AGN (see Narayan & Yi 1994). Instead in the Adiabatic Inflow-Outflow Solutions (ADIOS; Blandford & Begelman 2004) it is proposed that the flow is non-conservative. The energy is still removed in some form of outflow which could be a magneto-hydrodynamic wind with very little mass content.

2. Intermediate mass supply. When $\dot{m}_1 < \dot{m} < \dot{m}_2$, with $\dot{m}_2 \sim 30$, a radiative accretion disk is supposed to form and the physical state is the one described above for a thin Keplerian disk.

3. High mass supply. When $\dot{m}_2 < \dot{m}$, the mass supply is so high that, although there is no difficulty in emitting radiation, the photons are trapped in the gas as it flows inward onto the black hole and cannot escape. Broad absorption-line quasars, and perhaps most radio-quiet quasars are example of this kind of accretion. The flow is mostly adiabatic with γ=4/3 as the gas is radiation dominated.

In the most general case accretion is linked to the geometrical properties of the infalling gas by the equation (Rees 1984)

$$\frac{H}{R} \simeq \left(\frac{kT_{\rm gas}}{m_p c^2}\right)\left(1 + \frac{P_{\rm rad}}{P_{\rm gas}}\right)\left(\frac{R}{R_g}\right). \tag{2.25}$$

As shown in Eq. (2.25) disks become geometrically thick either because radiation pressure becomes competitive with gravity (this is regime 3 above; this is known as "radiative tori")

or because the material is unable to radiate the energy dissipated by viscous friction, which then remains as internal energy (regime 1; called "ion-supported tori").

The shape of a torus depends only on its surface distribution of angular momentum. If the angular velocity is a function of angular momentum, $\Omega(L)$, then the binding energy U is given by $dU/U = \Omega dL/(c^2 - L\Omega^2)$. Therefore where L is minimum, U tends to zero and the tori "puffs up". A self-crossing equipotential surface exists in this case, the Roche lobe, which has the shape of a cusp. The location of such cusp $R = R_{in}$ follows from the condition that the Keplerian angular momentum at R_{in} (given by the gravity of the hole) equals the angular momentum of the rotating matter there. The nonzero thickness of the disk in the cusp implies Roche-lobe overflow and, as in the case of close binaries, dynamical mass loss. The gas lost through the cusp goes towards the central body with roughly free-fall velocity. The cusp can be considered as the inner edge of the disk. The accretion rate through the cusp and the energy loss rate scale as

$$\begin{aligned} \dot{M}_{in} &\sim \Sigma_{in} H_{in} \\ L_{in} &\sim \Sigma_{in} H_{in}^3. \end{aligned} \tag{2.26}$$

For $\dot{M} > \dot{M}_{\rm Edd}$ the cusp goes very very close to the marginally bound orbit. The energy per particle released by the process is the binding energy of the circular orbit located at the cusp. In the extreme case $\dot{M} >> \dot{M}_{\rm Edd}$ the cusp will get closer and closer to the SMBH even over-passing the innermost stable orbit. In such conditions the efficiency of the process tends to zero. It can be shown in particular that the radiated luminosity L grows only logarithmically with the accretion rate for $\dot{M} >> \dot{M}_{\rm Edd}$ and one can therefore conclude that systems with $\dot{M} >> \dot{M}_{\rm Edd}$ have low efficiency compared to standard disks and $L \geq L_{\rm Edd}$.

The thick-disk photosphere emits relatively soft thermal radiation with a spectrum close to a blackbody, characterized by temperatures not very different from the correspond-

ing ones for thin disks. Deep in the funnel one has

$$T_{\max} \sim 10^7 \left(\frac{\dot{M}}{\dot{M}_{\rm Edd}}\right) \left(\frac{M_\bullet}{M_\odot}\right)^{-1/4} \ {\rm K}$$
$$h\nu_{\max} \sim \left(\frac{\dot{M}}{\dot{M}_{\rm Edd}}\right)^{1/4} \left(\frac{M_\bullet}{M_\odot}\right)^{-1/4} \ {\rm keV}\,. \tag{2.27}$$

The interior of the funnel is much hotter than the rest of the disk surface and therefore the same thick disk appears different when observed at different aspect angles. It has been shown that most probably non-accreting perfect fluid tori orbiting a Newtonian center of gravity are subject to violent global nonaxially symmetric instability which could also destroy the tori.

2.2.3 The efficiency and spin of a Supermassive Black Hole

The factor 1/2 in Eq. (2.21) represents an actually non-physical upper limit on the possible extractable energy from a BH as it is correct only for nonrelativistic disks. For a disk around a BH the correct coefficient is the one that corresponds to the binding energy at the marginally stable orbit.

The effective Lagrangian for studying the motion of particles in a spherically symmetric potential can be written as

$$L_{eff} = \frac{1}{2}\left(g_{tt}\dot{t}^2 - g_{rr}\dot{r}^2 - g_{\theta\theta}\dot{\theta}^2 - g_{\phi\phi}\sin^2\theta\dot{\phi}^2\right)\,. \tag{2.28}$$

Because the effective Lagrangian has no explicit dependence on ϕ, the associated canonical momentum p_ϕ along the polar axis is conserved. If the metric is stationary the energy-component of the four-momentum is conserved, which can be interpreted as the energy at infinity E_∞.

In the case of on-rotating time-steady spherical symmetry the metric around a point mass of mass M, i.e. a SMBH, is called the *Schwarzschild* metric and can be written in the matrix form as

$$\begin{pmatrix} (1-2\frac{M}{r}) & 0 & 0 & 0 \\ 0 & (1-2\frac{M}{r}) & 0 & 0 \\ 0 & 0 & -r^2 & 0 \\ 0 & 0 & 0 & -r^2\sin^2\theta \end{pmatrix} \tag{2.29}$$

where we have expressed the Schwarzschild radius as $R_g = 2M$ in units of G=c=1. Using this metric (Krolik 1999) the radial motion equation for particles of nonzero rest mass is

$$\dot{r}^2 = E_\infty^2 - \left(1 - \frac{2M}{r}\right)\left(1 + \frac{L^2}{r^2}\right) . \tag{2.30}$$

Eq. (2.30) can be simply described as the motion of a particle in the relativistic potential $V_{eff}(r) = V_N(r) + 1/2 - ML^2/r^3$, where $V_N = -M/r + L^2/(2r^2)$ is the Newtonian potential. For any given value of the angular momentum L, $V_{eff} = 0$ at $r = 2M$ and then tends toward 1/2 at large r. As L increases the shape of V_{eff} changes from a curve that rises monotonically to one that has both a maximum and a minimum before reaching its asymptotic value. The positions of these extremes are given by

$$r + m = \frac{1}{2}\left(\frac{L}{M}\right)^2 \left[1 \pm \sqrt{1 - 12\left(\frac{M}{L}\right)^2}\right] . \tag{2.31}$$

As for classical dynamics circular orbits occur when the energy exactly matches the value of the effective potential at a place where the effective potential has a minimum. In this case the there are no stable orbits for $L < \sqrt{12}M$, and the smallest radius for which a stable orbit exists, called the *marginally stable* orbit, is r_m=$6M$. For accretion to be maximally efficient the particles should lose as much energy as possible before disappearing into the SMBH. Therefore the maximum accretion efficiency is given by the binding energy at the smallest stable orbit, in this case $V_{eff}(6M)$=$\sqrt{8}/3$. The binding energy is the energy given by the difference between the rest mass of the particle and its energy at infinity: $E_b = 1 - \sqrt{8}/3$=0.057, which is the maximum radiative efficiency of accretion for particles falling into a Schwarzschild SMBH in rest mass units.

If a SMBH has instead an angular momentum $J = aM$ then the metric reads as

$$ds^2 = \left(1 - \frac{2Mr}{\Sigma}\right)dt^2 + \frac{4aMr\sin^2\theta}{\Sigma}dtd\phi - \frac{\Sigma}{\Delta}dr^2 - \Sigma d\theta^2 - \left(r^2 + a^2 + \frac{2Mra^2\sin^2\theta}{\Sigma}\right)\sin^2\theta d\phi^2 \tag{2.32}$$

where $\Sigma \equiv r^2 + a^2 \cos^2\theta$ and $\Delta \equiv r^2 - 2Mr + a^2$, and the polar direction of the coordinates coincides with the direction of the angular momentum. Note that this reduces to the Schwarzschild metric in the limit $a \to 0$. Around a rotating SMBH there is no static observer, the SMBH will "drag" any frame of motion along as it spins. The value of a is limited, it is bounded above by M, because any additional angular momentum would increase the energy of the SMBH and therefore its mass. When accretion occurs through a disk the axis of which does not vary much in time, the angular momentum of the central SMBH builds up rapidly. The marginally bound radius in this case reads as $r_{mb} = 2M \mp a + 2\sqrt{M(M \mp a)}$, and the limiting values are $r_{mb}(a = 0) = 4M$ and $r_{mb}(a = M) = M$ (for prograde orbits). Therefore, being $E_\infty = \sqrt{2V_{eff}(M)} = 1/\sqrt{3}$, the efficiency will increase from $1 - \sqrt{8}/3$ to $1 - 1/\sqrt{3}$=0.42%, as a result of the decrease in the size of the marginally stable orbit from $6M$ to M, and therefore an increase in the release of the maximal efficiency of energy release during the accretion process. It is however worth noticing that in realistic disks, some photons produced in the innermost disk could be captured from the SMBH and this could limit the spin parameter to the value $a \simeq 0.998M$ and therefore diminish the efficiency to $\simeq 30\%$ (Thorne 1974).

A Magnetic HydroDynamic (MHD) simulation has been carried out by Shapiro (2005) of a disk accretion onto a Kerr seed BH. As studied by the author the collapse of a non-rotating Super Massive Star (SMS) (with a mass of $10^4 - 10^5 M_\odot$) could lead to the formation of a Schwarzschild BH. However stars in nature are most likely maximally rotating and simulations have shown that SMS could collapse in Kerr SMBH with $a/M \sim 0.75$, the rest of the mass going into an ambient disk around the hole.

Shapiro (2005) has in more detail investigated the possible evolution in spin and mass of a SMBH originating from POPIII remnant seed in the range $10^2 - 10^3 M_\odot$ (see Section 2.3). The seed is surrounded by a relativistic, magnetized plasma in a torus-like geometry threaded with a poloidal magnetic field. The source of viscosity is MHD turbulence driven by instability. The author finds that limiting the emission at the Eddington limit, the MHD accretion drives the SMBH to the equilibrium value $a/M \sim 0.95$, corresponding to efficiencies ≤ 0.2, which are close to the values we have found in this thesis (Chapter 5), however still below the maximum limit for a Kerr SMBH.

Hughes & Blandford (2003) examine the coevolution of mass and spin in binary merger growth scenarios and find that SMBH are typically spun *down* by mergers. Rapid rotation results only in a few exceptions, i.e. if the binary's larger member already spins quickly and the merger with the smaller hole is consistently near prograde, or if the binary's mass ratio approaches unity. Therefore if most SMBH spin rapidly, and consequently have on average high (≥ 0.1) radiative efficiencies, then this limits the importance of merger scenarios in building up the local SMBH population.

To similar conclusions have recently arrived Volonteri et al. (2005). They studied the distribution of SMBH spins and its evolution with cosmic time in the context of hierarchical galaxy formation theories, finding that the coalescence of comparable-mass holes increases the spin of SMBH, while the capture of smaller companions in randomly oriented orbits acts to spin holes down. As a whole the SMBH spin distribution does not change much with time retaining memory of its initial distribution. However if accretion plays a major role in building the SMBH local population then the SMBH are actually spin up on average with time due to the fact that the disk accretion is usually aligned with the central SMBH spin. Interestingly King et al. (2005) have shown that even if accretion at the beginning occurs in a disk not aligned with the central SMBH spin, torques always act to align the hole's spin with the total angular momentum without changing its magnitude. Volonteri et al. (2005) show that if accretion is via a thin disk, about 70% of all SMBH are maximally rotating having radiative efficiency of about 30%. Even in the case of geometrically thick disk, about 80% of all SMBH have spin parameters a/M >0.8 and accretion efficiencies > 12%.

The hole's spin J could also exponentially decay for the interaction with the torque N of a surrounding magnetic field (associated with the hole itself or with the disk). This process extracts energy E from the hole at a rate $\dot{E} \propto \overrightarrow{J} \cdot \overrightarrow{N}$. This energy extraction of rotational energy has been discussed first by Blandford & Znajek (1977; BZ) and reads as

$$P_{BZ} \simeq g\dot{M}c^2a^2 \tag{2.33}$$

with a the dimensionless spin parameter and g a constant which depends on the geometry of accretion.

2.2.4 AGN Super-Unification Model

According to their spectral properties and luminosity AGN have been classified and divided into various subclasses. This taxonomy may reflect real differences in the physics of these objects but it is commonly accepted that many of the observed differences could be explained by geometric effects (*Unification Models*). However as discussed in the previous sections, a more comprehensive view of AGN physics is now emerging which connects in a *Super*-Unification scheme: accretion rate, spin and mass of the SMBH.

In the standard AGN unification picture (Antonucci 1993), the active galactic nucleus is surrounded by an axisymmetric region (probably a torus) filled with cold and dense (gas and dust) material that intercepts and redistributes in wavelenght and direction a substantial fraction of the primary radiation. The source will be classified as an unobscured (type 1) or obscured (type 2) AGN if its nucleus is observed directly, at a small angle to the axis of symmetry, or through the torus, respectively.

Broad emission lines (FWHM $>$ 2000 km/s) are observed in the optical spectra of Seyfert 1 galaxies, while in Seyfert 2 galaxies are not. According to the Unified Models the nucleus of Seyfert 2 galaxies is seen through the torus and the region where the broad lines are produced (BLR) is completely obscured. Moreover spectropolarimetric observations of various Seyfert 2 galaxies show broad lines in polarized light which points to the fact that radiation of a hidden BLR is scattered towards the line of sight. In X-ray Seyfert 2 show absorbed X-ray spectra (with $N_H \geq 10^{22}\,\mathrm{cm}^{-2}$), while Seyferts 1 do not.

The BLR, within 1 pc from the nucleus, is expected to be formed by dense clouds ($n_e \sim 10^9\,\mathrm{cm}^{-3}$) rotating fast around the nucleus and providing the broad optical emission lines. The obscuring torus should re-emit in the IR band the absorbed optical/UV/X-ray photons. The medium in the Narrow Line Region (NLR), extended on kpc scales, and then visible whatever the torus orientation is, should be photoionized from the central source and produce the forbidden narrow lines observed in the optical.

Radio loud AGN are 100-1000 times more luminous in the radio band than radio quiet AGN with the same optical/UV luminosity and are roughly 10% of the whole AGN population. According to the Unification Schemes for radio loud objects the strong radio

emission is always due to the presence of a relativistic jet extending on kpc-Mpc scales along the torus axis and emitting via synchrotron radiation. In this context BL Lac and Flat Spectrum Radio Loud QSO are those AGN for which the radio jet is pointing towards the observer while the counterparts should be FRI and FRII radio galaxies (respectively), which in the radio maps show extended jets on the plane of the sky.

As discussed in the previous sections accretion and merging could modify the mass and spin of a SMBH. Accretion plays a crucial role in the formation of a disk/torus around the central engine and it could also be linked with spin intensity and with the basic mechanisms of jet production. The *Super*-Unification scheme could in principle explain all the complex AGN taxonomy connecting the jet, the accretion rate and the SMBH mass. In Fig. 2.4 a sketch visualizes the basic properties of a Super-unification scheme for AGN. At high accretion rates and close to maximal spin we find objects with bright accretion disks, strong emission lines and powerful jets. When seen on axis these are the powerful blazars, while at large angles they appear as radio loud QSO or FRII radiogalaxies. At low accretion rates and high spin we find objects with radiatively inefficient accretion disks and therefore little trace of thermal radiation (no emission lines) but still relatively powerful jets. The magnetic field sustaining the BZ effect is determined by the accretion flow (not by its radiation) and possibly profits of a geometrically thick disk. In general radio-loud AGN could just be the high spin tail of an angular momentum distribution and any AGN, in the past, could have been, for some time, possibly radio-active.

The obscuration of an AGN can also be due to the host galaxy itself during major starforming episodes (see also Chapter 3), during which a lot of dust can be produced. Recently Alexander et al. (2005) have clearly shown that large SCUBA surveys have uncovered a large population of massive submillimeter emitting galaxies (SMG) with $f_{850} \geq 4$ mJy at $z \geq 1$ in which a substantial fraction (up to 70%) also harbor intense AGN activity. Martinez-Sansigre et al. (2005) have confirmed that Spitzer Space Telescope, with a sensitivity 10-100 times greater than its ancestors IRAS and ISO, has unveiled Type 2 AGN in the mid-infrared emission at 24-μm, which corresponds to emitted 8 μm. At $z = 2$ in fact dust extinction, unless extreme cases, is negligible at this wavelength and the authors claim that at least half of all the objects in the sample have intrinsic high luminosity obscured

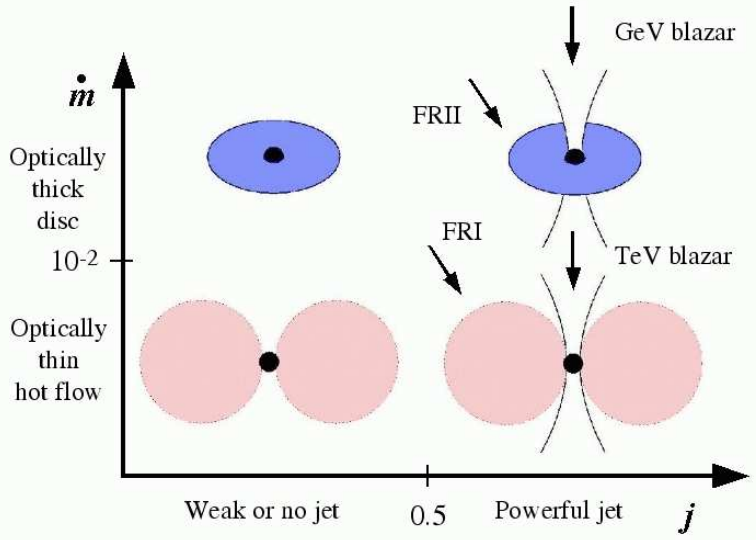

Figure 2.4: Schematic picture of the Super-unification scheme for Active Galactic Nuclei. (Figure taken from Maraschi & Tavecchio 2004)

AGN.

2.2.5 AGN Spectral Energy Distribution

The spectra of AGN extend from radio to γ rays, with a bolometric luminosity ranging from 10^{40} to 10^{48} erg/s.

The spectral region in the 1-20 keV spectra of both radio-quiet and radio-loud type 1 QSO are characterized by a power law with slope $\alpha \approx 0.8$, very similar for local Seyferts and radio galaxies. In addition high energy spectral cut-offs with $E_f \sim 300$ keV have been reported. Therefore the average type 1 AGN hard-Xray spectrum can be represented as $F(E) \propto E^{-0.8} e^{-E/300keV}$. The average obscured AGN spectrum can instead be represented as $F(E)(type2) = F(E)(type1) \int f(N_H) \exp[-\sigma(E) N_H] dN_H$, where $\sigma(E)$ represents the photoelectric absorption cross-section for solar chemical composition (Morrison & McCammon 1983) and N_H is the average hydrogen column density measured along the line of sight. In Fig. 2.5 we show examples of AGN spectra computed numerically assuming various absorbing column densities. It is interesting to notice how the spectra at

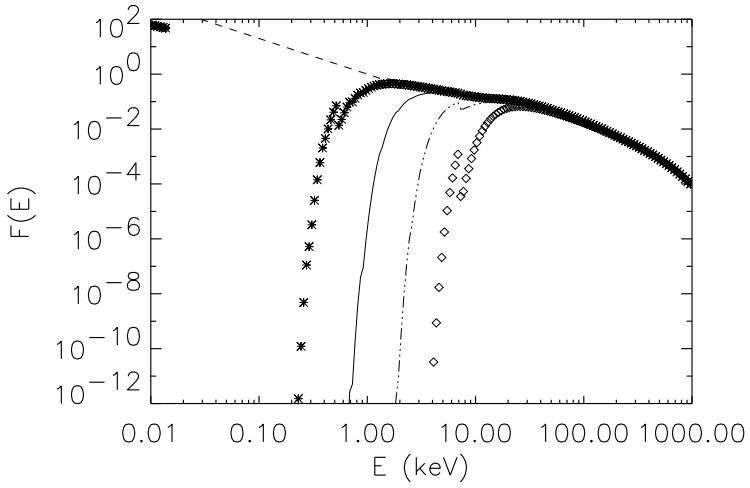

Figure 2.5: Hard X-ray AGN spectra produced with XSPEC for solar metallicity and different Hydrogen column density; the dashed line represents the type 1 AGN spectra; the other lines and symbols are for obscured AGN: from left to right the spectra have been computed using $N_H = 10^{21.5}, 10^{22}, 10^{23.5}, 10^{24.5}\mathrm{cm}^{-2}$

Optical/UV wavelengths are progressively damped due to absorbtion.

The primary power law emission is believed to be produced by a corona of relativistic electrons via inverse Compton on the thermal soft X-ray photons emitted by the accretion disc. Some of the primary radiation is reprocessed via Compton scattering by the accretion disc itself and/or the torus around the nucleus, producing a flattening of the spectral slope above $\sim$ 10 keV. A strong fluorescence iron line at 6.4 keV due to the same reprocessing media is also observed.

Below 1-1.5 keV a radiation excess with respect to the power law emission is detected in a large fraction of Seyferts. This radiation excess is believed to be produced by the high energy tail of the thermal emission from the accretion disc. In the soft X-rays another common component is observed in the X-ray spectra of Seyferts which is believed to be produced by a "warm absorber" (T=10^5 K) on the line of sight (see Fig. 2.6). This gas should be responsible for the OVII and OVIII absorption edges at 0.74 keV and 0.87 keV observed in about 50% of Seyfert 1 galaxies.

QSO and Seyferts seem to have a similar spectrum, even at high redshift. However

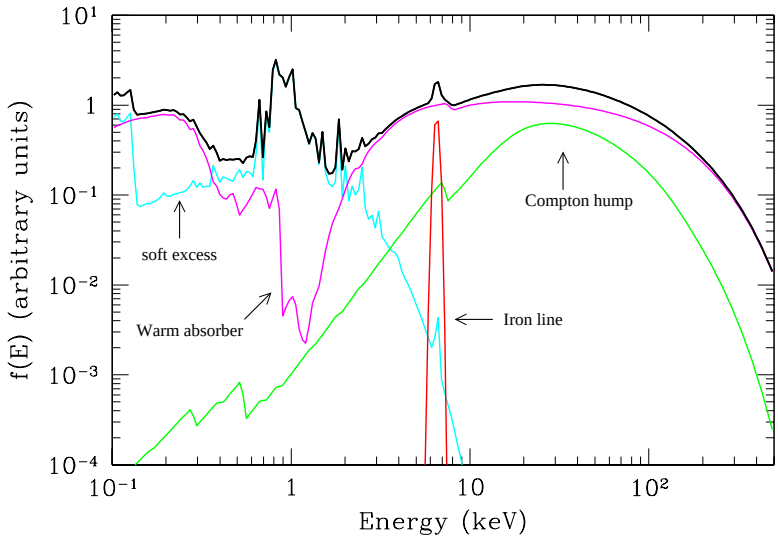

Figure 2.6: Average Hard X-ray spectrum of an AGN; the more the object is obscured the more evident are the reflected components in the spectra. (Figure taken from Risaliti & Elvis 2004)

there are signs of less reflection and iron line features, due to probably higher accretion rates. These are other empirical evidences that accretion rates are actually decreasing on average with time, as discussed in Section 2.2.1. Radio loud QSO are generally harder than radio quiet QSO having an average spectral slope of $\alpha \sim 0.6 - 0.7$. Their harder spectrum is usually ascribed to the presence of an additional X-ray emitting component associated to the radio jet via self-synchro-Compton radiation.

It is believed that the Cosmic X-ray and Gamma-ray background above a few MeV is to a large part a result of blazars. The spectra of blazars is dominated by Doppler-boosted radiation from a relativistic jet pointing close to our line of sight, compared with the quasi isotropic emission from normal quasars. The 30 MeV-10 GeV spectra of most blazars are consistent with being simple power laws with average energy index $\alpha \approx 1.15$.

The optical to UV emission of AGN is characterized by the "Big Blue Bump" (BBB), where the peak of the AGN emission is usually found. The peak energy is around the Lyman Edge (λ=1216Å), and the spectrum can be well approximated with a power law

both at lower and higher frequencies. Interestingly Binnet (2005) has shown that high-z QSO show a break around 1000Å which is not present in local AGN, a clear sign of the strong presence of Crystalline Carbon dust in their environment.

The infrared (IR) emission of AGN (2-200 μm) is, on average, $\sim$ 30% of the bolometric luminosity, with values in single objects ranging from $\sim$ 15% to about 50%. The spectral shape is characterized by a minimum at 1-2 μm, corresponding to the sublimation temperature of dust (between 100 and 2000 K, depending on the composition of the dust grains) an IR bump, typically at 10-30 μm due to the thermal emission of dust, with a temperature range between 50 and 1000 K, and a steep decline ($f_\nu \propto \nu^{-\alpha}$, $\alpha > 3$) at large wavelengths.

An important issue concerning AGN spectra is the estimate of their bolometric corrections, essential for determining the total, bolometric luminosity and, consequently, the mass of the central SMBH which powers the observed emission (Risaliti & Elvis 2004). Given an intrinsic dispersion in the SED of AGN, any flux-limited sample selected in a given spectral band is biased towards high ratios between the flux in the selection band and the bolometric emission. Elvis et al. (1994) estimated from an X-ray selected sample the optical-to-X-ray flux ratio to be $\langle \alpha_{OX} \rangle = -\log(l_0/l_X)/\log(\nu_0/\nu_X) = -1.35$, while Laor et al. (1997) found from a local optically selected sample of PG QSO $\langle \alpha_{OX} \rangle = -1.55$, which amounts to about a factor of 3.3 in flux ratio. Here l_0 and l_X are respectively the monochromatic luminosity at the rest-frame frequency of 2500Å and 2 keV. Moreover many authors have empirically shown that α_{OX} is correlated with the optical luminosity as $l_X \propto l_0^e$, with $e = 0.7 - 0.8$. This would correspond to $\alpha_{OX} \sim 1.4$, for the most luminous objects, which is somewhat in between the two previous estimates. Finally Ueda et al. (2003) showed that if $e = 1$ (constant α_{OX}), the apparent evolution of the Hard-Xray Luminosity Function of X-ray type 1 AGN becomes significantly slower than that of the optical Luminosity Function, whereas their redshift evolution become reasonably consistent (see Fig. 2.8) with each other if $e \simeq 0.7$ consistent with the results for high-z AGN of Vignali et al. (2003).

The optical bolometric correction seems not to have any significant dependence on bolometric luminosity, a clear sign that it is linked with the inner engine, i.e. it is a good

tracer of the inner accretion onto the SMBH. Finally we stress that there is no empirical evidence for any significant variation in the bolometric corrections with redshift (see also Chapter 5, Section 5.1.1).

2.2.6 AGN Evolution: Luminosity Functions

Current constraints on the $z \sim 6$ Quasar Luminosity Function have been given by Fan et al. (2004), but depend strongly on the spectra of their SDSS sample. These authors find the bright-end slope to be consistent with $-4.2 < \beta < -2.2$ and a density for quasars with $M_{1450} < -26.7$ of $(6 \pm 2) \cdot 10^{-10}\,\mathrm{Mpc}^{-3}$ ($H_0 = 65\,\mathrm{km\,s^{-1}\,Mpc^{-1}}$, $\Omega_m = 0.35$, and $\Omega_\Lambda = 0.65$). These QSO are usually detected through photometric techniques.

Constraining the high redshift QSO Luminosity Function (LF) is of fundamental importance for explaining the global re-ionization of the InterGalactic Medium (IGM). It is still controversial but it seems from the analysis of the Gunn-Peterson troughs, i.e. the absence of strong Lyα absorption due to neutral hydrogen, in the spectra of the distant luminous quasars ($z = 4 \div 6$) that a significant fraction of hydrogen is ionized (about $x_{HI} < 10^{-4}$), while there is sign of nearly complete absorption in the spectra of the luminous $z \geq 6$ QSO. Even if the actual numerical limit on the mean mass (volume) weighted neutral fraction is only $x_{HI} > 10^{-2}$, due to the large empirical uncertainties it is still hard to draw any firm conclusion.

However even if such a limit does not directly establish the end of the neutral epoch of the IGM, there is no doubt that the ionizing background emissivity has a steep increase from $z \sim 6$ to $z \sim 5.5$, much steeper than the known galaxy population. Indeed Stiavelli et al. (2004) show analyzing the galaxies in the Hubble Ultra Deep Field and in the Great Observatories Origins Deep Survey (GOODS) that possibly most of the reionization at $z = 6$ could have been caused by galaxies, even if large uncertainties in the UV escape fraction and high redshift galaxy spectra are present in these models.

On the other hand the optical AGN population seems to fall beyond redshift 3, even if X-ray data (see below) indicate a much flatter density evolution. Various studies show that the *extrapolated* number density of the high redshift QSO population falls short of producing enough photons for reionization, however an ad-hoc choice of some parameters

could increase their contribution (see e.g. Meiksin 2005). We will also demonstrate in Chapter 6, that the high redshift QSO could posses activity timescales up to an order of magnitude longer than previously believed, and therefore they could play a more significant role in the Universe reionization at $z \sim 6$, than previously thought.

Fan et al. (2001) confirmed previous observations of Warren et al (1994) and Kennefick et al. (1995) showing that the luminosity function of QSO with redshift $3.6 < z < 5$ and luminosity $-27.5 < M_{1450} < -25.5$ arise by a factor of about 3 per unit redshift from $z \sim 6$ to $z \sim 3$. Moreover they find a flatter slope for the luminosity function at $z \approx 4$. In the redshift range $2.5 < z < 4$, Pei (1995) has shown that the evolution of the Optical QSO LF can be described by a double power law where the characteristic luminosity can be fitted by a Gaussian distribution peaking at a redshift $z \sim 2.8$ and declining at higher redshifts.

For lower redshifts Boyle et al. (2000), Croom et al. (2004) and Richards et al. (2005) have fitted the Optical AGN LF with a double power-law evolution with a faint slope of $-1.5 \div -1.8$, constant in shape, changing through a Pure Luminosity Evolution (PLE) with the break luminosity increasing with redshift. The 2-degree Field (2dF) and SDSS QSO combined survey explored by these groups selected AGN through their UV excess with respect to stars. This selection technique is valid up to $z = 2.2$, the point at which Lyα emission shifts into the observed B band and QSO begin to loose their characteristic UV excess.

Radio loud AGN are only about 10% of the total population. The LF for this population (see Dunlop & Peacock 1990) was separately obtained for steep and flat spectrum sources by means of several samples selected at 2.7 GHz. However this analysis confirmed the presence of a so-called redshift cut-off, similarly to what observed in optical bands, for the all powerful radio sources, QSO and radio galaxies, with a decline in comoving density of a factor ~ 5 between z =2 and 4. The evolution can be described by a PLE but with a negative density evolution at high redshifts.

In the X-ray bands the AGN evolution seems different. In the soft band (0.5-2 keV) Miyaji et al. 2000 have detected a constant AGN comoving density above redshift $z \sim 2$ at variance with optical surveys. Early works on the Hard-Xray LF (2-10 keV) (e.g.

La Franca et al. 2002; Cowie et al. 2003), mainly from *Chandra* surveys, have pointed out a strong AGN evolution. In particular these groups have claimed that lower luminosity AGN seem to peak at lower redshift with respect to higher luminosity AGN. Hasinger et al. (2005) have now collected a sample of about 1000 AGN in the soft band combining *Chandra* and *XMM* deep surveys with *ROSAT* reaching a 95% completeness level. The authors confirm the previous results showing that the space density evolution with redshift changes significantly for different luminosity classes, i.e. a Luminosity Dependent Density Evolution (LDDE). In particular they find a density increase at low redshifts up to a certain redshift and then a flattening.

The most recent work on a complete Hard-Xray AGN LF is by Ueda et al. (2003; but see also the updates by Brandt & Hasinger 2005) from a combination of Hard X-ray surveys above 2 keV performed with *HEAO1*, *ASCA* and *Chandra*, down to a flux level of $3.8 \cdot 10^{-15} \mathrm{erg\,cm^{-2}\,s^{-1}}$ in the luminosity range $41.5 < \log L_X < 46.5$ and redshift $0 < z < 3$. They authors find in this band a strong LDDE AGN evolution (see Fig. 2.7). The Hard-Xray luminosity function is shown in the top of Fig. 2.8.

The level of N_H column density for each AGN is calculated by fitting the observed spectra using the code XSPEC (which we have also used to reproduce Fig. 2.5), which computes the resulting spectra of a Type 1 power-law AGN after absorption (the metallicity and photon index are input model parameters). Ueda et al. (2003) find that the fraction of absorbed AGN decreases with increasing luminosity, while the redshift dependence is not significant (see Fig. 2.11). This result suggests that a modification of a pure geometrical Unification model could be invoked to explain the data. In particular such findings point towards the intuitive possibility that more luminous objects are probably less obscured. This is also evident from the bottom of Fig. 2.8 in which we report the comparison the authors produce between the Hard-Xray LF and the optical LF by Boyle et al. (2000), assuming typical bolometric corrections (see Section 2.2.5). It is interesting to notice that at all redhifts the optically selected AGN match the high-luminosity tail of the Hard-X LF.

Computing the luminosity density in a given luminosity bin as a function of redshift (Fig. 2.9; we will produce the same plot in Chapter 5 for the SMBH mass density) it is possible to infer that most of the luminosity density is contained in objects with luminosity in

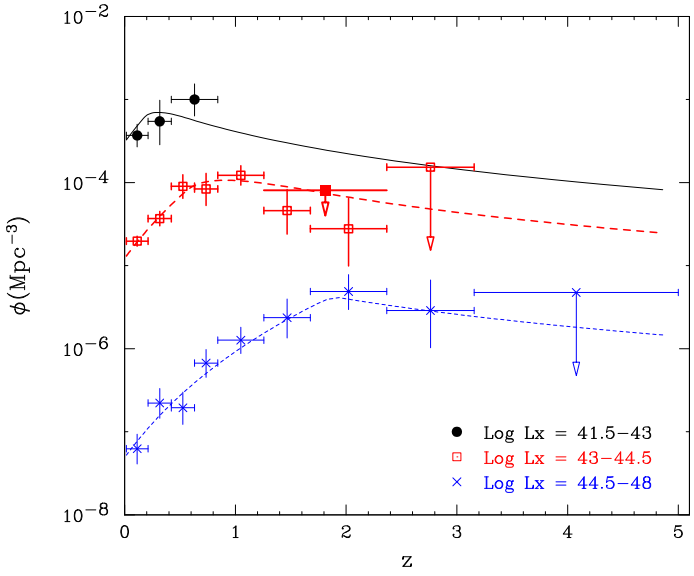

Figure 2.7: AGN comoving spatial density as a function of redshift in three luminosity ranges. (Figure taken from Ueda et al. 2003)

the range $43 < \log L_X < 44.5$ peaking at redshift $z \sim 1$ and with about 50% of the luminous density already emitted by $z \sim 1.5$. However it has to be noted that such luminosity evolution could not imply a proportional mass accretion history for SMBH: the objects could be radiating at very low Eddington ratios and have instead already accumulated high masses or viceversa. We will address such issues in Chapters 5 and 6 showing that indeed theoretical modeling of the AGN accretion history naturally leads to the conclusion that about 60% of the SMBH mass density has been accreted at $z \geq 1$.

Ueda et al. (2003) provide a fit which correlates the luminosity of an object with its hydrogen column density N_H. The authors notice that the recent detected high level of the X-ray Background (XRBG) normalization (see Section 2.2.7, Fig. 2.11) requires some extra obscured AGN populations, not yet detected, with column densities $\log N_H \sim 24.5\,\mathrm{cm}^{-2}$ and $\log N_H \sim 25\,\mathrm{cm}^{-2}$. Moreover the ratio of obscured-to-unobscured AGN must not depend much on redshift and increase for lower luminosities. Such findings have been also confirmed by the recent study of Treister & Urry (2005). In Chapter 5 we will show that the choice of inserting these extra-populations in the Hard-X LF, following the prescriptions by Ueda et

al. (2003), is needed to match the recent empirical constraints on the XRBG normalization (see also Section 2.2.7).

More recently Barger et al. (2005) have used spectroscopically complete deep and wide-area *Chandra* surveys to determine the cosmic evolution of the Hard-X AGN. These authors confirm Ueda et al. (2003) findings that broad-line AGN dominate the number densities at the higher X-ray luminosities, while narrow-line AGN dominate at the lower X-ray luminosities. The broad-line AGN Hard-X LF agrees remarkably well with the optical one which appears to be missing sources at lower luminosities. Barger et al. (2005) also probe the $z \sim 4$ Hard-X LF, finding a pure luminosity evolution from redshift $z \sim 2-3$. In Chapter 6 we will compare the outputs of our theoretical modeling of the AGN luminosity functions with the data sets by Barger et al. (2005) and Ueda et al. (2003).

2.2.7 The X-ray Background

In the Radio band around 100 Mhz, the extragalactic background is about 20-30% of the total background emission and is well explained by superposition of radio galaxies and normal galaxies. In the 1-1000 Ghz frequency range the black body spectrum of the Cosmic Microwave Background (CMB) dominates over any other component, while at higher energies, in the infrared and optical bands, several Galactic components dominate the background emission.

In the γ rays, about 50% of the background emission is due to our Galaxy, where the γ rays are mainly produced by the interactions between the cosmic rays and the interstellar medium. The residual extragalactic γ-ray background can be explained by the integrated emission of unresolved sources (most probably AGN such as Blazars which are thought to produce most of the extragalactic light in the 10 MeV-100 GeV energy range).

Recent SCUBA measurements have resolved most of the non-CMB extragalactic background at 850 μm into single galaxies, whose sub-mm radiation should be produced by dust heated by a starburst event or an AGN. Heated dust in galaxies should also be responsible for the extragalactic IR background. Silva et al. (2004) have shown that exploiting the Ueda et al. (2003) LF, the contribution of AGN to the IR background is negligible ($< 5\%$), implying that the latter is dominated by star formation, however the AGN host galaxies

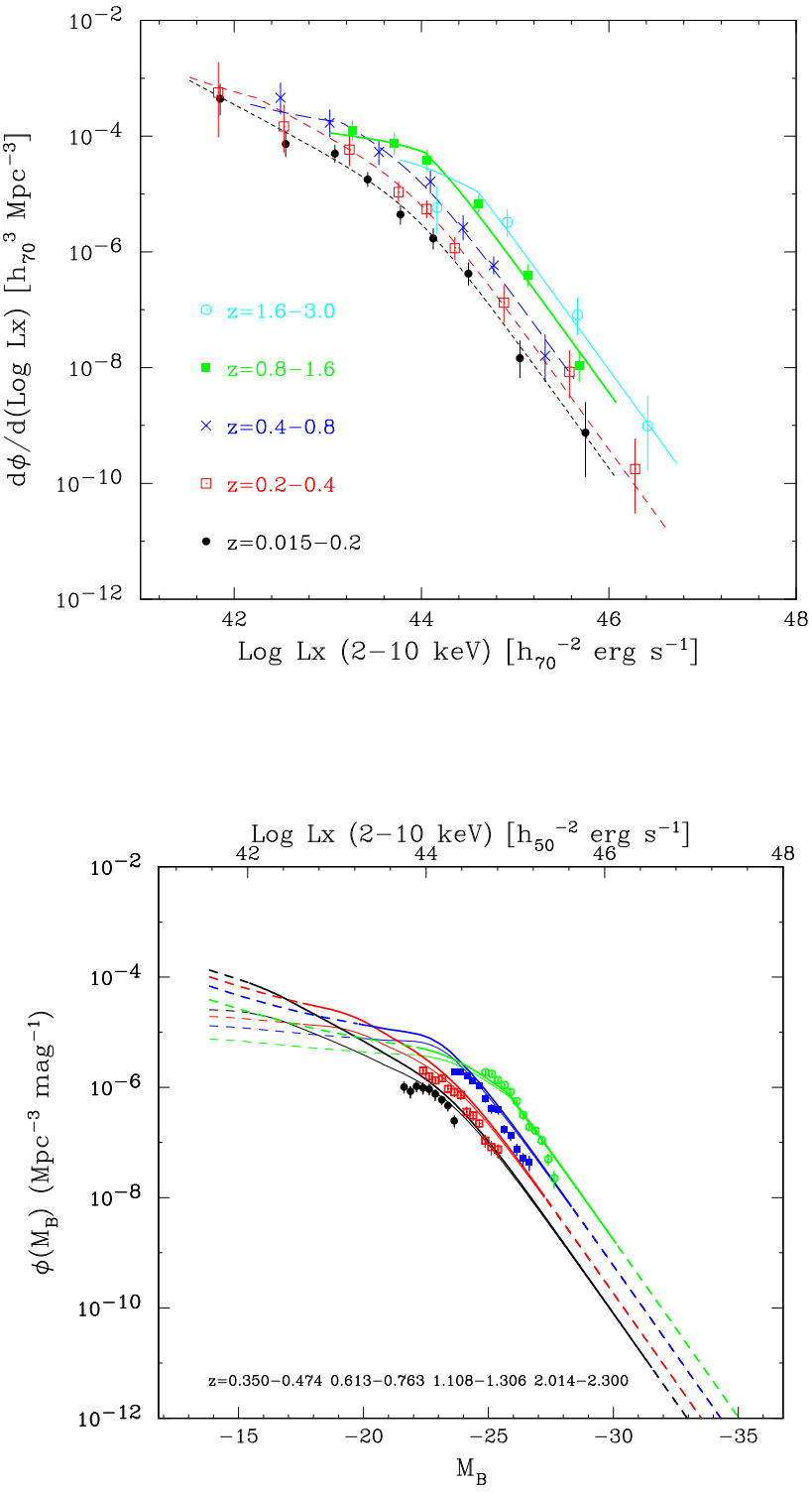

Figure 2.8: Top: Hard-Xray luminosity function up to redshift $z \sim 3$. Bottom: comparison between the optical QSO luminosity function (symbols) by Boyle et al. (2000) and the Ueda et al. 2003 Hard-X LF. (Figures taken from Ueda et al. 2003)

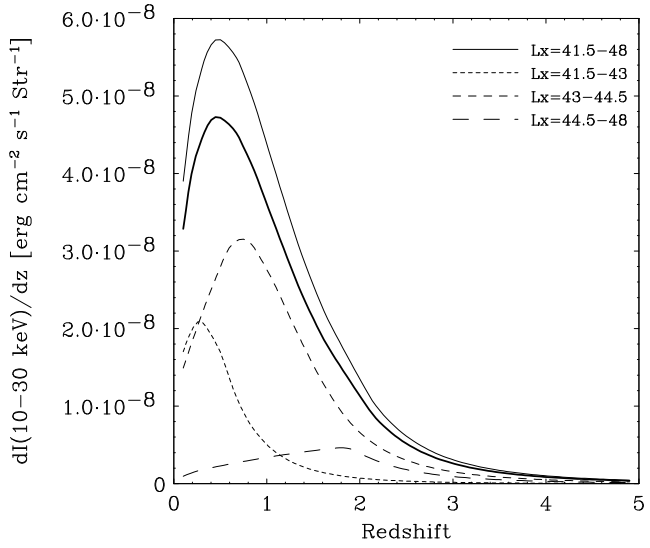

Figure 2.9: Differential contribution of AGN to the 2-10 keV Hard-Xray Background intensity as a function of luminosity and redshift. (Figure taken from Ueda et al. 2003)

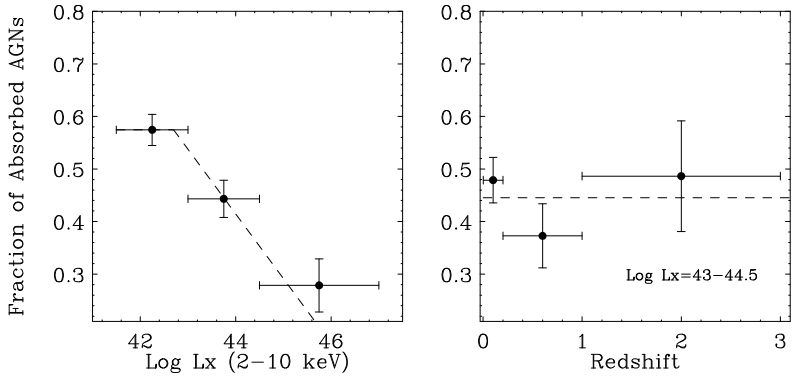

Figure 2.10: Fraction of absorbed AGN with $\log N_H > 22\,\mathrm{cm}^{-2}$ to all AGN with $\log N_H < 24\,\mathrm{cm}^{-2}$ given as a function of luminosity (left panel) and redshift (right panel). Dashed lines represent best-fit to the data. (Figure taken from Ueda et al. 2003)

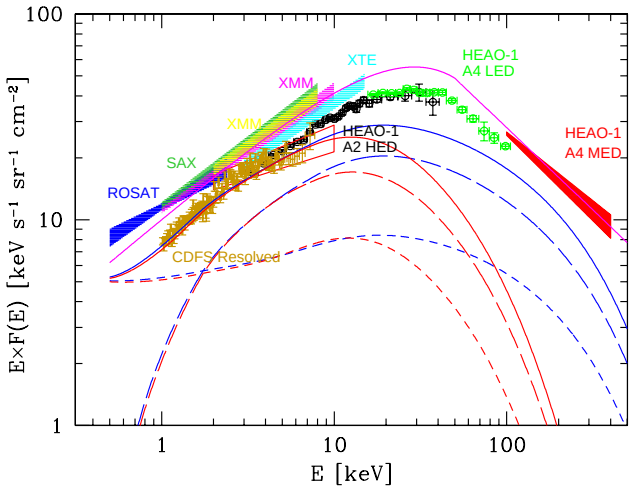

Figure 2.11: A selection of XRBG spectral measurements collected from observations with different satellites as labelled. The solid magenta curve represents the analytical fit of Gruber (1992) renormalized by 30% upwards in order to fit the most recent measurements. The blue and red curves represent the integrated contribution computed through the most recent synthesis models exploiting a Hard-Xray LF non-corrected for very obscured sources. (Figure taken from Comastri 2004)

may contribute significantly to the IR background, up to 20% in the 1-20 μm range. In the optical/UV band, there are no direct estimates of the extragalactic background intensity, which is usually computed by integrating galaxy counts to very faint magnitudes.

The XRBG is a diffuse X-ray glow shining from each sky direction. It was discovered 40 years ago by a rocket flight (see e.g. Giacconi et al. 1967). The first measurement of the XRBG performed by the HEAO-1 satellite covered the energy range from 3 to 60 keV. It was discovered that the XRBG emission, peaking at about 30-40 keV, could be approximated with a bremsstrahlung emission from a very hot plasma with $T \sim 40$ keV. Later on, however, this was proven to be no more than a coincidence, since the bremsstrahlung spectrum vanishes when the contribution of discrete sources is subtracted from the XRBG emission. Even the satellite COBE measured no Compton distortions in the blackbody spectrum of the CMB and this means that no intergalactic gas with $T > 10^8$ K could contribute by more than 0.01% to the hard XRBG intensity. Therefore the origin of the XRBG was completely ascribed to unresolved sources.

In the 0.5-10 keV energy range, where the best X-ray measurements are available, the XRBG is mainly resolved into AGN. Actually the whole XRBG emission up to $\sim$ 300 keV is likely to be produced by AGN. Above 0.5 keV a thermal component is needed to explain the XRBG spectral shape up to $\sim$ 1 keV, which is also featured by strong OVII and OVIII emission lines. The plasma responsible for this radiation is believed to reside in the Galactic halo or among the members of the Local Group.

At about 1-2 keV the Galactic extinction is low and the isotropy level of the XRBG increases. Surveys by *ROSAT* and *Chandra* satellites have shown that at very faint fluxes most of the 1-2 keV XRBG has been resolved into single sources. The major uncertainty in the resolved fraction of the soft extragalactic XRBG resides in the flux of the XRBG itself. Above 2 keV the Galactic clouds are almost transparent to the X-ray and the measured isotropy of the XRBG indicates that its origin is entirely extragalactic.

Setti & Woltjer (1989) were the first to propose that the flat slope of the 2-10 keV XRBG was due to a population of obscured AGN in addition to the bright unobscured AGN with steep spectra. Comastri et al. (1995) then showed that *assuming* for the obscured AGN a distribution of absorbing columns and the same evolution of the unobscured AGN in the Hard-X LF (just increased by a factor of a few at most), it was possible to fit the XRBG spectrum and integral counts. However later Maiolino & Rieke (1995) showed that the local fraction of obscured and unobscured AGN was around $3-4$. Gilli et al. (1999; 2001) then showed that significant additional obscured AGN at higher redshifts are needed to fit the XRBG. It was also proposed that the fast evolving starburst population, with a rapid density evolution up to $z = 0.8$ and then constant, necessary to reproduce the ISO mid-infrared counts, could be responsible for these extra-AGN (Franceschini et al. 2002). However, as clearly shown in Fig. 2.9, most of the obscured sources responsible for the XRBG intensity, are detected at low redshifts, $z \leq 1$.

Up to now the deep pencil-beam and wide-area X-ray surveys (see e.g. Fabian & Worsley 2004 for a review) of the Lockman hole by *XMM-Newton* and the *Chandra* Deep Field North & South (Giacconi et al. 2002; Alexander et al. 2003) have been able to resolve $\sim$ 70-90% of the XRBG up to 10 keV. However this fraction drops significantly to $\sim$ 70% in the 2-4.5 keV band and to $\leq$ 60% for higher bands (according to the Lockman Hole deep

monitoring by *XMM*). Such findings confirm what already stressed by synthesis models: significant additional very obscured AGN sources must be searched for and included in the estimates of the accretion mass density.

2.3 Seed population and Intermediate Mass Black Holes

As it will be discussed more extensively in Chapter 3, DM structure formation is bottom up, with low mass halos condensing first. However a few massive halos of about $10^5 - 10^6 M_\odot$ (at the 3σ level; see Chapter 3) could have formed already out to redshift $z \sim 25$. If baryons fall in their potential well they can further contract being these host halos enough massive to overcome pressure gradients (their "Jeans mass" being $M_J \approx 10^4[(1+z)/11]^{3/2} M_\odot$, see e.g. Haiman & Quataert 2004). In these early structures baryonic clouds could then fragment through molecular H_2 cooling.

At very high z H_2 formation is inhibited as the intermediaries H_2^+ and H^- are dissociated by the CMB. At $z < 100$, when CMB photons are redshifted to lower energies, the intermediaries survive and a sufficiently large fraction ($x_{H_2} \sim 10^{-3}$) of H_2 can accumulate sufficient to cool the baryons in a timescale less than the dynamical one in halos with temperature above ~ 200 K and a density of $n \sim 10^4$ cm^{-3}. In these minihalos of about $10^5 M_\odot$ 3D simulations have shown that the metal-free baryonic gas cannot fragment in clumps below $10^2 - 10^3 M_\odot$, but it rather forms unusually massive stars. Stars with masses between $\sim$ 40-140 $M_\odot$ and above 260 $M_\odot$ collapse directly into a black hole without an explosion, whereas stars in the range $\sim$ 140-260 $M_\odot$ explode without leaving a remnant but polluting the environment with metals. So these first massive stars, Population III (POPIII) stars, could both account for early metal enrichment and for the SMBH seed population.

Volonteri et al. (2003) have discussed that in a Gaussian theory (see Chapter 3), halos more massive than the $\nu - \sigma$ peaks at $z = 20$ contain a complementary error function erfc($\nu/\sqrt{2}$)=(0.00047 for ν=3.5) of the mass of the universe. Therefore the mass density parameter of 3.5σ pregalactic holes is $\Omega_{\nu\sigma} = 0.00047 \Omega_m m_\bullet / 1.1e7 h^{-1} M_\odot > 2 \cdot 10^{-9} h$ being h the Hubble constant in units of 100 km/s. This value is much smaller than the one derived locally in nearby galaxies (see Chapter 4) $\Omega_\bullet = 8.4 \cdot 10^5 M_\odot\,\mathrm{Mpc}^{-3} / 2.8 \cdot 10^{11} M_\odot\,\mathrm{Mpc}^{-3} \approx$

$3 \cdot 10^{-6}$, where the value at the denominator is the critical density today. Therefore if SMBH form out of very rare POPIII BH, the present day mass density of SMBH must have been accumulated during cosmic history via gas accretion, with BH-BH mergers playing a secondary role.

However this is increasingly less true if the seed holes are more numerous and populate higher peaks or halos with smaller masses at higher redshift. As shown by Madau & Rees (2001) and Islam et al. (2004) (see also Koushiappas et al. 2004) if every halo mass at 2 or even 3 σ peaks at $z \sim 24$ forms a 260 $M_{\odot}$ BH, then the density per comoving volume is estimated as $\rho_{\bullet} \sim 3\ M_{\odot}\,\mathrm{Mpc}^{-3}$, already about 70% of the present-day SMBH mass density. It will then be sufficient to add just some gas accretion to grow the BH to the present day mass. The problem at this stage remains the low efficiency of dynamical friction for objects that are still not massive enough. Therefore many BH will keep orbiting around subhalos instead of sinking to the main center. Semi-analytical merger-tree (see Chapter 3) calculations have been carried out, taking into account dynamical friction, tidal disruption and encounters with the galactic disk, to determine the abundance and distribution of SMBH in present-day halos of various masses (Islam et al. 2004): the result is that it is difficult to reproduce the observed SMBH mass distribution with only merging of the initial seeds, and that substantial gas accretion is required.

However the question whether halo/galaxy mergers lead to BH mergers is not yet resolved (e.g. Milosavljevic & Merritt 2004). During galaxy mergers SMBH sink at the center via dynamical friction and form a black hole binary on parsec scale. For the binary to further shrink and coalesce it is necessary to lose its angular momentum which can be transferred to nearby bodies, such as stars, gas or other black holes. In triaxial galaxies it has been claimed (e.g. Yu 2002) that as stellar orbits are chaotic, it is highly probable that the BH binary is surrounded by low angular momentum orbit stars: in this case the decay time for the binary becomes much less than the Hubble time. Successive halo mergers, at a rate much higher than the rate BH binaries can coalesce, can eject the lowest mass SMBH out of the nucleus of the merger remnant. These "wandering" SMBH (Volonteri et al. 2003) can then accrete gas from the surrounding and could in principle be detected, off-set with respect to the galaxy center, as Ultra-Luminous X-ray sources (ULX).

An empirical way of assessing the actual role of SMBH mergers will be via their gravity wave (GW) signature (see e.g. Menou 2003 for a review). It has been shown that with up to 3-year monitoring the *Laser Interferometric Antenna* (LISA), with a signal-to-noise of 5, will be able to monitor hundred of mergers per year mainly due to coalescing SMBH with masses $10^3 < M_\bullet/M_\odot < 10^6$ at high redshifts ($z \geq 5$). However the expected number of event rates will be much less, up to ~ 1 per year, if only deep ($V_c > 100\,\mathrm{km\,s^{-1}}$) potential wells are able to harbor SMBH (Haehnelt 2003). It is worth noticing (Menou et al. 2001) that all the calculations performed on the predicted detectable LISA event rates have been calibrated on the merging events of dark matter halos assuming that the duty-cycle of SMBH formation within them is 1. If such a duty-cycle is much less than the predicted redshift distribution for LISA event rates will peak at much lower redshifts ($z \sim 2$), where the merging rates are higher (see also Chapter 3).

As shown in Section 2.2.6 there are signs in the high redshift AGN spectra that the IGM reionization took place since redshift $z \sim 6$ and before the IGM was much more neutral. However the WMAP satellite has detected a large electron optical depth implying that a significant ionization has already taken place at high redshift $z \sim 15$. There is still debate and uncertainty but the value measured for such optical depth seems to be $\tau = 0.17 \pm 0.04$ (e.g. Kogut et al. 2003). The free electrons produced by an hypothetical "early" reionization in the Universe is detectable also on the CMB spectrum itself, where the damping of temperatures fluctuations at small angular scales, due to photon scattering (see also Chapter 3) boosts the polarization at large angles ($l < 10$; Zaldarriaga 1997). Therefore from the WMAP temperature-polarization angular cross-correlation has been established that the median redshift for reionization is $z = 17 \pm 4$, very close to the value discussed above for the production of the first SMBH seeds. This is a sign that probably the reionization history of the Universe has been quite complicated and it could have developed in two phases.

A population of seeds SMBH, as described above, could have been effective in reionizing the universe so early in time. The first massive stars infact would create HII regions and inhibit further star formation preventing gas cooling as UV photons in the Lyman-Werner bands are able to photo-dissociate the fragile H_2 molecules. At the death

of the first stars the massive black holes can then accrete the surrounding gas and become "miniquasars". Madau et al. (2004; and see Haiman & Quataert 2004 for a comprehensive review on these topics) demonstrated that such sources with their hard spectrum can deposit up to 1/3 of their energy into the surrounding medium, and produce enough electrons to have a positive feedback on the formation of H_2 molecules which in turn could boost cooling and fragmentation of baryons into massive stars. As pointed out by Hui & Haiman (2003) in this scenario normal stars would concurrently heat the IGM and through the overlap of their HII regions keep it fully ionized. In fact Dijkstra et al. (2004) have shown that high redshift QSO which *fully* reionize the IGM would overproduce the soft X-ray background, but a population of miniquasars that only partially ionize the IGM (up to say 50%) is still allowed.

It has also been discussed the possibility of forming massive black holes within a star cluster (see Binney & Tremaine 1987). Infact the self-gravity of a cluster can have a negative heat capacity that makes it vulnerable to the so-called "gravothermal catastrophe": the core collapses on a timescale proportional to the two-body relaxation time and the resulting high central density may lead to BH formation. In clusters with many stars ($N > 10^6 - 10^7$), analytical and numerical methods have highlighted the concrete possibility of forming Supermassive stars or runaway merging of massive stars at the center of the star cluster out of which Intermediate Mass Black Holes (IMBH) of $10^3 - 10^5 M_\odot$ can form which would bridge the gap between the seed massive black holes, remnants of the POPIII stars, and the SMBH in local galaxies.

There have been empirical extrapolations downwards of the $M_\bullet - \sigma$ relation searching for AGN signatures at the center of dwarf galaxies. Filippenko & Ho (2003) have found an upper limit of $10^4 - 10^5 M_\odot$ in NGC4395 radiating much below the Eddington limit. Barth et al. (2004) find a value of about $2 \cdot 10^5 M_\odot$ for Pox 52. Recently Barth et al. (2005) have measured SMBH masses ranging between $10^5 < M_\bullet / M_\odot < 10^7$ and $30 < \sigma / \mathrm{km\,s^{-1}} < 100$, in a local sample of Seyfert 1 galaxies. The most interesting case is M33, for which an upper limit of $10^3 - 10^4 M_\odot$ is measured and seems to be below the extrapolation of the median fit for $M_\bullet - \sigma$ relation (in this thesis we will give physical insights to what conditions could produce such an effect in low-mass systems; see review by van der Marel 2004).

Finally we recall that in the literature it has been proposed that another possible mechanism for primordial BH formation is through the direct collapse of density fluctuations (Carr 1975) even if, in the very beginning, the universe is highly homogeneous and isotropous and the associated Gaussian density fluctuations could be too small to collapse to a BH.

Chapter 3

Evolution of Dark Matter and Baryons: where SMBH fit in

3.1 The cosmological context

To build the metric of the Universe it is usually assumed, based on the observations made on very large scale structures, that the three-dimensional space geometrical properties are the same at all spatial locations and do not single out any special direction in space. Such a three-dimensional space is called *homogeneous* and *isotropic*.

As matter follows geometry, through Einstein equations, it follows that also matter/energy must be homogeneous and isotropic but this is not the case at scales less than 100 Mpc, where we observe filaments, clusters and galaxies.

These matter/geometry considerations can be applied also to entropy. There will be microscopic processes for which entropy will grow linked to some local non thermal conservation (i.e. growth of structures), but such events are overwhelmed by the large scale homogeneity in the thermal conditions, which prevents any large heat flow and therefore keeps the average entropy constant. This is the reason why large-scale evolutions in the Universe can be, in a very first approximation, thought of as "reversible" (i.e. the big bang/big crunch theory).

The full space-time metric with the above assumptions reads as

$$ds^2 = dt^2 - a^2(t)\left[\frac{dr^2}{1-kr^2} + r^2(d\theta^2 + \sin^2\theta d\phi^2)\right] \tag{3.1}$$

expressed in dimensionless coordinates (r, θ, ϕ), i.e. in a 'co-moving' frame in which a given region will always contain the same mass/energy with expansion. The time function $a(t)$ is the *expansion factor* and k $= 0, \pm 1$ indicates the value of the curvature of the three-dimensional space. Both values must be determined through observations.

As $a(t)$ multiplies the spatial coordinates, any proper length $l(t)$ will change in time in proportion to $a(t)$, i.e. $l(t) = l_0 a(t)$, in particular this will be true also for any photon wavelength λ which will be stretched proportionally to the expansion factor causing a red-shift, z, of the spectrum of any light source in the sky, quantified as $1 + z = a_0/a(t)$, where a_0 is the current value of the expansion factor.

Setting in Eq. (3.1)

$$ds^2 = 0 \tag{3.2}$$

we get the equation of a null geodesic and the radius. From an object with intrinsic luminosity L we'll receive a flux $F = dE/\text{Area}\, dt = 1/4\pi a_0^2 r_{\rm em}^2 (1+z)^2 L$, where $r_{\rm em}$ is the solution at the time of emission t_e of Eq. (3.2).

We therefore get the *'luminosity distance'* of an object of luminosity L

$$d_L(z) = \left(\frac{L}{4\pi F}\right) = a_0 r_{em}(1+z) \tag{3.3}$$

Einstein equations express that the space-time geometry is determined by its matter/energy content and viceversa. Using Einstein equations it is possible to derive the equations for the dynamics of the Universe. However it is more intuitive to use the principles of homogeneity and isotropy.

From the first principle of thermodynamics, $dU + pdV = 0$, setting $r = a(t)x$, $U = \rho r^3$, and from the conservation of energy $v^2/2 - GM(r)/r = k$, where $v = (\dot{a}/a)r$, it is straightforward to get the two independent *Friedmann equations*

$$\begin{aligned} \frac{\dot{a}^2 + k}{a^2} &= \frac{8\pi G}{3}\rho \\ \frac{d(\rho a^3)}{da} + 3pa^2 &= 0\,. \end{aligned} \tag{3.4}$$

Eqs. (3.4) combined with the equation of state $p = p(\rho)$ determine completely the the three functions $a(t)$, $\rho(t)$ and $p(t)$. Introducing the critical density $\rho_c(t) \equiv 3H^2(t)/8\pi G$, with $H(t) \equiv \dot{a}/a$, the density parameter $\Omega(t) \equiv \rho/\rho_c$ deriving and rearranging in Eqs. (3.4) one gets

$$\frac{k}{a_0^2} = H_0^2(\Omega - 1) \qquad (3.5)$$
$$\frac{\ddot{a}}{a} = -\frac{4\pi G}{3}(\rho + 3p)$$

which connect the curvature of the Universe with the total 'amount' of matter/energy and the acceleration of the Universe with the 'type' of matter/energy.

For a general equation of state of the type

$$p = w\rho \qquad (3.6)$$

and using the energy conservation equation, $d(\rho a^3) = -pd(a^3)$, one gets from Eqs. (3.5)

$$\rho \propto a^{-3(1+w)}\,. \qquad (3.7)$$

The cross-correlation of different and independent experiments, by the WMAP satellite on the cosmic μwave background, from distant SNa Type Ia, Nucleosynthesis and Clusters of galaxies have now shown that about 23% of the Universe content is made by a still unknown form of matter, called the *Dark Matter* (DM), clustered around galaxies and about 73% of a diffusive form of energy, the *Dark Energy* (DE). Baryons constitute just the 4.4% of the total and other particles, such as neutrinos and photons, contribute less than $1.5 \cdot 10^{-3}$ (see Spergel et al. 2003; see Fig. 3.1).

From such findings, one can write Eqs. (3.5) in a general form. Introducing the matter (DM plus baryons), Ω_m, the dark energy, Ω_Λ, the curvature Ω_V and radiation, Ω_R, parameters one can set

$$\frac{\dot{a}^2}{a^2} + \frac{k}{a^2} = H_0^2\left[\Omega_R\left(\frac{a_0}{a}\right)^4 + \Omega_m\left(\frac{a_0}{a}\right)^3 + \Omega_V\left(\frac{a_0}{a}\right)^2 + \Omega_\Lambda\right]\,. \qquad (3.8)$$

Eq. (3.8) shows how the Universe has passed through various phases during which different components have dominated in the rate of evolution. For pure radiation $w = 1/3$

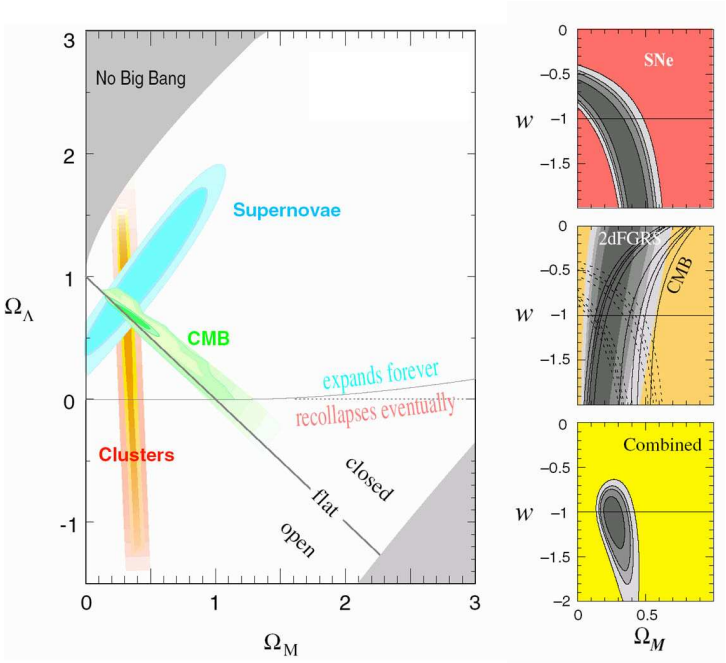

Figure 3.1: Constraints on the cosmological parameters by cross-correlating data on various experiments as labeled. (Figure taken from Knop et al. 2003)

(Eqs. (3.6)), and therefore from Eqs. (3.7), $\rho_{rad} \propto a^{-4}$, while for pure matter $w = 0$ and $\rho_{matter} \propto a^{-3}$.

Combining with $\rho_{rad} \propto T^4$, for thermal radiation, one gets the law of evolution of a plasma energy in an expanding background

$$T(t) \propto \frac{1}{a(t)} \,. \tag{3.9}$$

Therefore in the past the Universe was hotter, denser and dominated by radiation-energy density. In the standard Big Bang model the Universe evolved from an initial singularity, at energies comparable to the Planck scale $(G\hbar/c^3)^{1/2} \simeq 10^{-33}$ cm, to a rapid inflation phase in which it expanded by about 10^{50} times its initial size.

The matter content in the Universe from a hot high-temperature plasma cooled due to the expansion. When the energy scaled down to $k_B T \leq MeV$ the nucleosynthesis of some amount of deuterium, helium and lithium took place. The formation of heavier elements was prevented by the fast evolution of the Universe. Only stars will be able to

synthesize them. This is the reason why the abundances of helium and deuterium are a sensible test for cosmological models.

3.2 Linear theory for Structure Formation

According to Jeans theory, starting from a homogeneous and isotropic 'mean' fluid, small fluctuations in the density, $\delta\rho$, and velocity, δv, can grow in time under the effect of self-gravity.

The gravitational potential that is due to a density perturbation $\delta\rho = \bar{\rho}\delta$ in a region of size R will be $\phi \propto (\delta M/R) \propto \bar{\rho}\delta R^2$. From Eq. (3.8), in the matter dominated epoch, $\bar{\rho} \propto a^{-3}$ and $R \propto a$. The perturbation δ grows then as $\delta \propto a$, making ϕ constant in time. In particular the fluctuations that existed in the Universe at the time when radiation decoupled from matter would have left their imprint on the radiation field. Photons climbing out of a potential well of size ϕ will lose energy and undergo a redshift $(\Delta\nu/\nu) \approx (\phi/c^2)$, creating a temperature anisotropy of the order of $(\Delta T/T) \approx (\Delta\nu/\nu) \approx (\phi/c^2)$. Such imprints have been actually detected by the COBE satellite and confirmed by later missions. The cosmic μwave background radiation is smooth 1 in a part of 10^5. Such very tiny thermal perturbations are considered as the first seeds of structures. For example galaxy clusters have escape velocities of the order $v \approx (GM/R)^{1/2} \sim 1000\,\mathrm{km\,s^{-1}}$ corresponding to a temperature anisotropy of just $\Delta T/T \approx (v/c)^2 = 10^{-5}$.

A simple criterion needed for a fluctuation to grow is that the self-energy of a spherical inhomogeneity of radius λ, $U \sim G\rho\lambda^3/\lambda$, must be grater than the kinetic energy of the gas thermal motion, v^2,i.e.

$$\lambda > \frac{v}{(G\rho)^{1/2}}\,. \tag{3.10}$$

For baryons which is equivalent to say that the free-fall time is less than the hydrodynamical time, i.e. that self-gravity forces are greater than the pressure forces. When such conditions are not satisfied, pressure dominates, the perturbation will propagate like an acoustic wave with wavelength λ at velocity v. For a collisionless fluid, such as DM, the behavior is very similar: when the gravity is not able to sustain the 'pressure', given by the mean square velocity of the particles, these cannot be confined and therefore they undergo *free*

streaming. Fluctuations in this case do not behave like acoustic waves but are smeared out and dissipated.

More quantitatively we perturb a smooth expanding matter background, controlled by the Poisson, Euler and continuity equations

$$\begin{aligned} & a\,\partial_t\delta + \vec{\nabla}_x\left[(1+\delta)\,\vec{u}\right] = 0 \\ & \\ & \partial_t(a\,\vec{u}) + (\vec{u}\cdot\vec{\nabla}_x)\,\vec{u} = -\frac{1}{\rho}\,\vec{\nabla}_x p - \vec{\nabla}_x\phi \\ & \\ & \nabla_x^2\phi = 4\,\pi\,G\,a^2\,\rho\ ; \end{aligned} \tag{3.11}$$

here x is the comoving coordinate, $\vec{u}$ is the peculiar velocity (subtracted from the Hubble flow), and ϕ is the gravitational potential.

Considering only the zero and first order terms, in the approximation that $\delta\rho << \rho$, one finds from Eqs. (3.11)

$$\ddot{\delta} + 2\frac{\dot{a}}{a}\dot{\delta} = 4\pi G\bar{\rho}\delta \tag{3.12}$$

In the static case, $H = \dot{a}/a = 0$, the growth of perturbations is exponential, $\delta \propto exp(i\omega t)$.

In the radiation dominated era recasting Eq. (3.12) in the variable $y = a/a_{eq}$, where a_{eq} is the "matter-radiation" equi-density ($1+z_{eq} \sim 3.9\times10^4(\Omega_m\,h^2)$), the solutions read as $\delta = 1+3/2y$ and $\delta \simeq \ln(4/y)$, showing that in the radiation dominated epoch, perturbations do not grow significantly (as a logarithm of time at the most): they are "frozen" until z_{eq}. This is known as the *Meszaros* effect, which prevents growth of perturbations in the radiation era. It is a direct consequence of the very fast expansion of the background Universe during this epoch.

In a matter dominated Universe ($z < z_{eq}$), of main interest for structure formation, the solution to Eq. (3.12), for a generic set of cosmological parameters, reads as

$$\delta = D(z) \equiv \frac{5}{2}\Omega_m H(a)\int_0^a dx\frac{1}{x^3H(x)^3}\,, \tag{3.13}$$

with $H(x) = [\Omega_m x^{-3} + \Omega_\Lambda]$. An accurate fit to the *growth factor* $D(z)$, used in this thesis,

has been given by Lahav et al. (1991)

$$D(z) \simeq \frac{5}{2}\frac{\Omega_z}{1+z}\left(\frac{1}{70}+\frac{290\Omega_z}{140}-\frac{\Omega_z^2}{140}+\Omega_z^{4/7}\right)^{-1}, \tag{3.14}$$

where

$$\Omega_z = \Omega_m(1+z)^3/[\Omega_\Lambda + (1+z)^3\Omega_m]\,. \tag{3.15}$$

Baryonic perturbations evolve following Eq. (3.16) in which also the term corresponding to Dark Matter gravity is included

$$\ddot{\delta_B} + 2\frac{\dot{a}}{a}\dot{\delta_B} + \left(\frac{c_s^2k^2}{a^2} - 4\pi G\rho\right)\delta_B = 4\pi G\rho\delta\,. \tag{3.16}$$

In an expanding background if gravity overwhelms pressure (the first term in the parenthesis is less than the second term), i.e. $\lambda > \lambda_{Jeans} = c_s(\pi/G\rho)^{1/2}$, then the perturbation can grow. However even those baryonic perturbations which enter the horizon in the matter-dominated epoch (which have a wavelength higher than the Jeans scale) do not grow but oscillate until recombination. In the early hot phase infact, the baryons are in thermal equilibrium with radiation through Thomson/Compton scattering and therefore, supported by the strong radiation pressure, are prevented from collapsing.

When the Universe cools below the hydrogen binding energy, electrons and protons recombine and the radiation decouples from matter. Such a transition occurs at $T_{dec} \simeq 3{\cdot}10^3$ K and $z_{dec} \simeq 1.7 \cdot 10^3$. (The decoupled radiation dominates the background intensity and appears now in the redshifted μwave band (CMB, see Chapter 2, Section 2.2.7) and it is very well fitted by a perfect blackbody spectrum peaking at a temperature of $T = 2.73$ K). After z_{dec} baryonic perturbations are then free to grow within the dominant DM potential wells.

As noted above the Universe is dominated by non-baryonic matter, in principle composed of a variety of particles produced in the early stages and now present as cosmic relics. Such relics are subdivided into *thermal*, produced in thermodynamic equilibrium with the rest of the Universe (neutrinos,...), and *non-thermal*, non in equilibrium (monopoles, cosmic strings...). The first species of particles can be grouped in *hot* matter, which decoupled when it was still relativistic, and *cold* matter which decoupled when it was non-relativistic.

To get some knowledge of the moment of decoupling from thermodynamic equilibrium of a given species of number density n_X one uses the Boltzmann equation

$$\frac{dn_X}{dt} + 3\frac{\dot{a}}{a}n_X + < \sigma_A v > n_X^2 - \Psi = 0, \tag{3.17}$$

where the term $\dot{a}/a$ takes into account the expansion of the Universe, $< \sigma_A v >$ is the rate of collisional annihilation and Ψ denotes the rate of particle creation.

For the collisionless component we can define the *Jean Mass* as

$$M_{JX} = \frac{\pi}{6} m_X n_X \lambda_{JX}^3 \,, \tag{3.18}$$

where $\lambda_{JX} = v_X(\pi/G\rho)^{1/2}$, one finds that at the moment of decoupling for *hot thermal relics*

$$M_{JX} \simeq 3.5 \cdot 10^{15} (\Omega_X h^2)^{-2} \; M_\odot \,. \tag{3.19}$$

Perturbations less than the Jeans mass will be damped. In the relativistic regime, when their velocity is $v_X \simeq c$, the particles will be dispersed from overdense to underdense regions, a process which is partly occurring also in the non-relativistic regime. Moreover perturbations smaller than the *free streaming* scale

$$\lambda_{Xf} \simeq a(t) \int_0^t \frac{v_X}{a(t')} dt' \tag{3.20}$$

will be dissipated due to the natural free motion of particles.

In this *Top-down* scenario, structures evolve through fragmentation from large perturbations, *pancakes*, into smaller units. Therefore small-scale structures emerge very late and this is at odds with observations of high-z proto-galaxies and Quasars (e.g. Fan et al. 2001). In the Cold Dark Matter (CDM) scenario instead the maximum value of M_{JX} is much smaller $\sim 10^5 M_\odot$ and therefore structure formation in this case turns out to be *Bottom up* or *Hierarchical*. However as discussed in the Introduction and in Section 3.4, Hierarchical models are still short in reproducing many observations regarding the High-z galaxy populations.

Before ending this section it is worth noticing that new work has been recently developed on the linear theory of density perturbations. Naoz & Barkana (2005) have added to gravity electron scattering and gas pressure in the evolution of perturbations and

they concluded that the effect is $\geq 10\%$ in the baryonic power spectrum on small scales. Moreover Barkana & Loeb (2005) have proposed that infall of neutral hydrogen in the DM potential wells can imprint acoustic oscillations on the pattern of brightness fluctuation and in principle could be directly detectable through observations of the 21cm fluctuations. Such observations could probe the very first stages of galaxy formation in the range $z \sim$ 20-200.

3.3 Non-linear Evolution: Statistics of Dark Matter Halos

3.3.1 Spherical Collapse

Up to now we have considered the linear evolution of structures, in which we have derived Eq. (3.12) from Eqs. (3.11) in the limit $\delta(x) = (\rho(x) - \bar{\rho})/\bar{\rho} << 1$. For studying the non-linear evolution, when $\delta(x) \sim 1$, we can restrict ourselves to the special case of spherical symmetry, to get the general behavior of a DM halo in this regime. An overdense region will expand more slowly than the rest of the Universe and at a certain *turn around* epoch it will reach a maximum radius, then it will collapse and eventually virialize (i.e. it will reach an energetic-dynamical equilibrium configuration) to form a gravitationally bound object. After this we will then rely on statistical tools to describe the evolution of bound structures in the Universe.

The radius $R(t)$ of such a spherical region will evolve according to

$$\ddot{R} = -\frac{G\,M_{DM}}{R^2} - \frac{4\,\pi\,G}{3}\,\bar{\rho}_\Lambda\,(1 + 3\,w_\Lambda)\,R\ , \tag{3.21}$$

where we have separated the contribution of DM and dark energy.

Let us first quote the solution of the previous equation in a pure matter-dominated Universe, where $\ddot{R} = -G\,M_{DM}/R^2$. The non-linear density contrast as a function of redshift

is implicitly given by (Peebles 1980)

$$(1+z) = \left(\frac{5}{3}\right)\left(\frac{4}{3}\right)^{2/3} \frac{\delta_0}{(\theta-\sin\theta)^{2/3}}$$

$$\delta = \frac{9}{2}\frac{(\theta-\sin\theta)^2}{(1-\cos\theta)^3} - 1 \tag{3.22}$$

where δ_0 is the density contrast at present if it were evolved by the linear approximation. The linear density contrast at a given epoch is in general In pure matter dominated Universe the radius evolution is provided by Peebles (1980)

$$\delta_L = \frac{3}{5}\left(\frac{3}{4}\right)^{2/3} (\theta-\sin\theta)^{2/3} \ . \tag{3.23}$$

Now the evolution of the perturbation is straightforward. The transition to non-linearity ($\delta \approx 1$) occurs for $\theta = 2\,\pi/3$ when $\delta_L \approx 0.57$, i.e., at redshift $1+z_{\rm nl} \approx \delta_0/0.57$; the turn-around occurs when $\delta = 4.6$ and $\delta_L \approx 1.063$, i.e., at redshift $1+z_{\rm ta} \approx \delta_0/1.063$; finally at $\theta = 2\,\pi$ all the mass will be collapsed to a point. However, long before this happens the analysis based on Eq. (3.21) breaks down because the random velocities of DM particles are no longer small. The DM will relax to a virialized configuration in a time which is essentially that corresponding to $\theta = 2\,\pi$. So virialization occurs when $\delta \equiv \Delta_{\rm vir} \approx 18\,\pi^2 \approx 180$ and $\delta_L \equiv \delta_c \approx 1.686$, i.e., at redshift $1+z_{\rm vir} \approx \delta_0/1.686$.

The overdensity at virialization has to be larger than in a matter-dominated Universe owing to the anti-gravitational action of the dark energy that counteracts the collapse. Moreover, it is found that $\Delta_{\rm vir}$ slowly depends on cosmic time; a good fit ($w_\Lambda = -1$), which has been used in this thesis, is provided by Eke et al. (1996)

$$\Delta_{\rm vir}(z) \simeq 18\,\pi^2 + 82\,(\Omega_z - 1) - 39\,(\Omega_z - 1)^2 \ , \tag{3.24}$$

where Ω_z is given in Eq. (3.15).

3.3.2 Gaussian Statistical Field

We can describe the density perturbation in the Universe as a realization of a functional $f(x)\,\epsilon\,[f : {\rm Re}^3 \rightarrow {\rm Re}]$. To each point of the space we associate a scalar, the value

of its density contrast $\delta(x)$, and consider that such a random field has a Gaussian probability distribution function with median zero and σ equal to the square root of the mean square deviation of the density field. Converting in the Fourier space it is straightforward to check that the modes $\tilde{\delta}(k)$ are independent.

The two point correlation function in Fourier space is expressed by the Power Spectrum defined by

$$< \tilde{\delta}(k)\tilde{\delta}(k') >= P(k)\delta_D(k - k') \,. \tag{3.25}$$

$P(k) =< |\tilde{\delta}(k)|^2 >$ expresses on average the amount of power of the perturbation field on the scale $k \sim 1/R$. The power spectrum $P(k)$ contains the complete statistical information of the Gaussian random field and the WMAP data have indicated the initial power spectrum to be nearly scale-free, i.e. of the form

$$P(k) \propto k^n \tag{3.26}$$

with the spectral index $n \approx 0.99 \pm 0.04$. A slight sign of non linearity in the spectrum has been detected. The so-called "running" spectral index, reads as $n = 0.93 + 0.5(-0.03)\log(k/0.05/h)$, which flattens the power on smaller scales.

The evolution until the end of the linear regime for each mode is parameterized as $D(z)\delta_k(z) = T_k\delta_k(z = 0)$, in terms of the transfer function T_k which gives the ratio of the late-time amplitude of a mode to its initial value, where, we remind, $D(z)$ is the linear growth factor between redshift z and the present.

As discussed above, to calculate accurate results for the transfer functions is a technical challenge, mainly because we have a mixture of matter (both collisionless dark particles and baryonic plasma) and relativistic particles (collisionless neutrinos and collisional photons,...) which does not behave as a simple fluid. There are however, as mentioned above, essentially two ways, *Jeans mass* and *damping* effects, in which the power spectrum that existed at early times, detected by WMAP, may differ from the one that emerges at the present.

Bardeen et al. (1986) provide a fitting formula for the power spectrum, which has been used in this thesis. For a CDM model the transfer function reads as

$$T_k = \frac{\ln(1 + 2.34q)}{2.34q}[1 + 3.89q + (16.1q)^2 + (5.46)^3 + (6.71q)^4]^{-1/4} \tag{3.27}$$

with $q = k/\Omega_m h^2\,\mathrm{Mpc}^{-1}$. A non-zero baryonic density lowers the apparent DM density parameter. An apparent shape parameter $\Gamma = \Omega_m h$ has been defined for the transfer function in a model with zero baryon content, for which $q = k/h\Gamma\,\mathrm{Mpc}^{-1}$. The effect of increasing the baryon density Ω_b is to preserve the spectrum shape but to shift it to lower values of Γ. For general models with $\Omega_m \neq 0$ and not too large values of Ω_b Sugiyama (1995) finds

$$\Gamma = \Omega_m h \exp\left[-\Omega_b\left(1+\sqrt{2h}/\Omega_m\right)\right]. \tag{3.28}$$

The effect on the statistics of DM halos (see Chapter 6, Section 6.1) due to the inclusion of baryons in the power spectrum can be significant: the number of halos formed at any time and any mass, especially those in the range $10^{12} \div 10^{13} M_\odot$, diminishes as, according to Eq.(3.28), less power is attributed to a fixed scale.

Once the power spectrum is known the *variance* of the Gaussian fluctuation field, $\sigma \equiv < \delta >^2$, can be computed

$$\sigma^2(R) = \int \frac{dk}{2\pi} k^2 P(k) W(kR) = \int d\ln k \Delta_k^2 W(kR) \tag{3.29}$$

where the result in the integral of Eq. (3.29) depends on the window function W used. This is physically relevant as for Birkhoff's theorem, any scale evolves knowing anything of larger scales therefore through such a filtering only perturbations below R contribute to the density contrast on that scale. Often the window function is expressed as $W(x) = (3/x^3)(\sin x - x\cos x)$ because it allows to simply relate the size of the averaged region to the mass contained within it as $M \equiv (4\pi/3)\bar{\rho}R^3$. Following e.g. Mahmood et al. (2004), one can then write the variance simply as

$$\sigma^2(M) = \int_0^{k_s} dk\, 4\pi k^2 P(k)\, dk \tag{3.30}$$

with $M = 6\pi\rho_0 k_s$, being ρ_0 the mean background density of matter in the Universe. When $\sigma(M) \to 1$, that particular scale characterized by R will go nonlinear and matter at that scale will collapse and form a bound structure.

The evolution with redshift will be that of a *typical* perturbation, i.e. $\sigma(M,z) \propto \sigma(M) \times D(z) \propto a(z)$. Approximating the power spectrum with a power law, $P(k) \sim k^n$, then we can write $\sigma(M,z)^2 \sim \Delta_k^2 \sim P(k)k^3 \sim a^2 M^{-(n+3)}$, which clearly highlights the

characteristic *hierarchical build-up* of DM structures, where smaller masses first achieve non-linearity in time. Infact $\sigma(M) \rightarrow 1$ implicitly defines a "characteristic mass" $M_c(z) = M_{c0}[D(z)/D(0)]^{6/(n+3)}$ that is to collapse at a given epoch, being $M_{c0} \simeq 6 \cdot 10^{14} \Omega_m h^{-1} M_\odot$ the present value and smaller at earlier times ($D(z) \propto a(z)$). In a statistical description we could think of regions having a density contrast of, say, ν times larger than the typical value $\sigma(M,t)$ occurring with a Gaussian probability $P(\nu)$ which will collapse at any redshift for which the condition $\nu a(z)\sigma_0(M) \sim 1$ is satisfied, being $\sigma_0(M)$ the fiducial value of the density fluctuation today.

3.3.3 The Press & Schechter Mass Function

Gravitationally bound objects in the Universe span a large dynamic range in mass. Let $f(M)dM$ be the number density of bound objects in the mass range $M \div M + dM$ and $F(M)$ the number density of objects with masses greater than M. Given a certain realization of the linear density field $\delta(x)$ there will be regions with high density $\delta(x) > \delta_c$, where we are now calling δ_c the linear critic density contrast given in Eq.(3.23). It is reasonable to assume that those regions with a density contrast above the linear critical one at the turnaround point, will eventually condense out as bound objects. Although the dynamics of that region is non-linear, the process of condensation is unlikely to change the mass contained in that region significantly. Therefore if we can estimate the mean number of regions with $\delta(x) > \delta_c$ in a Gaussian random field, we will be able to determine $F(M)$.

The fraction of bound objects with mass greater than M will be in a Gaussian random field

$$F(M) = \frac{1}{\sqrt{2\pi}} \frac{1}{\sigma(M,t)} \int_{\delta_c}^{\infty} exp\left[-\frac{\delta^2}{2\sigma^2(M,t)}\right] . \tag{3.31}$$

Therefore the *Mass Function* $f(M)$ is given by $\partial F/\partial M$ and the comoving number density $N(M,t)$ is found by dividing $f(M)$ by $M/\bar{\rho}$

$$N(M)dM = \sqrt{\frac{2}{\pi}} \frac{\bar{\rho}}{M} \frac{\delta_c}{\sigma^2} \frac{d\sigma}{dM} \exp\left(-\frac{\delta_c^2}{2\sigma^2}\right) dM \tag{3.32}$$

where it has been multiplied by a factor of 2, as outlined in the seminal paper by Press & Schechter (1976; P&S). Infact the integral of $f(M)$ over M gives 1/2, instead of 1, due possibly to the fact that after filtering on a scale R there will be non-zero probability that

those points which have $\delta < \delta_c$ will have $\delta > \delta_c$ when the density field is filtered with a radius $R_1 > R$ ("cloud-in-cloud" problem). Such a problem is a weak point in the P&S formalism and it has been shown that surprisingly, using a sharp k-space filter, the factor of 2 gives the right correction to the mass function, but such a factor is not valid for other filters.

A more refined theoretical approach to calculate the number density of collapsed objects at any redshift has been carried out by Bond et al. (1991). Given a power spectrum and the correspondent field of density perturbations one can filter on a very large R. The corresponding resolution will be $S \equiv \sigma^2(R)$. While lowering the filtering radius, the overdensity δ of the chosen point will determine a random walk $\delta(S)$. At every step ΔS the increment $\Delta\delta$ will be uncorrelated from the previous ones, i.e. $\delta(S)$ will be a Markovian random walk. Now consider an *absorbing barrier* $\delta_c(z) = \delta_c/D(z)$, i.e. when the $\delta(S)$ overpasses $\delta_c(z)$, the object collapses and therefore is removed from the random walk. Such a behavior for the probability of upcrossing at any given step can be described with a diffusion equation from which, after integrating on all trajectories the P&S mass function can be recovered (this is called "excursion set formalism").

Bond et al. (1991) however used a spherical collapse model to determine the barrier height B; in this case the critical overdensity $\delta_c(z)$ required for collapse at z is independent of the mass m of the collapsed region, so it is independent of $\sigma(m)$ therefore since $\nu \equiv \delta_c(z)/\sigma$, then $B(\nu)$ must be the same constant for all ν, i.e. $B(\nu) = \delta_c(z)$. Sheth & Tormen (2002; S&T) have refined this calculation to take into account *ellipsoidal* collapse. An ellipsoidal perturbation is determined by three parameters, eigenvalues of the deformation tensor: the ellipticity e, the prolateness $p < e$, and the density contrast $\delta_e(e, p)$. Regions having a given value of δ/σ will have an ellipticity $e = (\delta/\sigma)/\sqrt{5}$ (Sheth, Mo & Tormen 2001). Therefore to collapse and form a bound object at z, the initial overdensity of such a region must have been $\delta_e(e, z) \sim \delta_c(z)$, which defines a relation between the absorbing barrier and the ellipticity of the object and therefore its mass. Such a connection provides a "moving barrier" which ones integrated hields the following mass function (S&T):

$$N(M, z) = A\frac{\bar{\rho}}{M}\sqrt{\frac{2a}{\pi}}\frac{\delta_c(z)}{\sigma^2}\left[1 + \left(\frac{\sigma^2}{a\delta_c^2(z)}\right)^p\right]\exp\left[-a\frac{\delta_c(z)^2}{2\sigma^2}\right] \tag{3.33}$$

where $A = 0.3222$, $a = 0.707$ and $p = 0.3$. Eq. (3.33) has proved to give a very good fit to high resolution N-body simulations up to redshift $z = 10$ and masses $M \sim 10^{13} M_{\odot}$ at these redshifts (Springel et al. 2005). In this thesis we will always use Eq. (3.33) to describe the mass statistics of DM halos at any redshift.

3.3.4 Structure of a Dark Matter Halo

A universal mass density profile of DM halos was introduced as a result of high N-body simulations performed by Navarro, Frenk & White (1997). These authors found that the density profile can be fitted by a simple formula with only one fitting parameter. This profile (Eq. (3.34)) steepens from r^{-1} near the center of the halo to r^{-3} at large distances, while it has the slope of an isothermal, r^{-2}, in the central parts around the knee

$$\rho(r) = \frac{4\rho_s}{\left(\frac{r}{r_s}\right)\left(1+\frac{r}{r_s}\right)} \tag{3.34}$$

where r_s is a scale radius and ρ_s is the density at this radius. Such a profile has been confirmed in numerical simulations by various groups (e.g. Bullock et al. 1999). However such a profile is just an "initial condition". Recent numerical simulations (Navarro et al. 2004) have however shown considerable scatter in the value of the slope $d\log\rho/d\log r \sim -1$ in the very inner regions. Observationally, spiral galaxies from rotation curve analysis are better fitted in the central regions by a halo core-profile, of the type given by, e.g., Burkert & Salucci (2000), i.e. it is now believed that the profile is not so steep at the center but it rather has a core. The reason for the origin of the core, from an original power-law, as the one shown in simulations, is not yet well understood but, as it will be further discussed in Section 2.4, the DM profile in Eq. (3.34) seems to be preserved during mergers and modified only by the infall of the baryons in the inner regions.

From now on we will call $M_{\rm vir}$, the mass of a halo which has virialized at a given redhsift $z_{\rm vir}$. The proper size of the halo, in this case, is often defined so that the mean density within the halo radius $R_{\rm vir}$ is a factor $\Delta_{\rm vir}$, given in Eq. (3.24), times the mean density of the Universe $\bar{\rho}$ at the redshift z in consideration. The halo mass is then

$$M_{\rm vir} = \frac{4\pi}{3}\bar{\rho}\Delta_{\rm vir}R_{\rm vir}^3\,, \tag{3.35}$$

where *virial radius* is

$$R_{\rm vir} = 31 \left(\frac{M_{\rm vir}}{10^{12} M_\odot}\right)^{1/3} \left(\frac{\Omega_m}{\Omega_m(z)} \frac{\Delta_{\rm vir}}{18\pi}\right)^{-1/3} \left(\frac{1+z}{7}\right)^{-1} {\rm Mpc}\,, \tag{3.36}$$

and the *virial velocity*, i.e. the circular velocity of the virialized halo $V_{\rm vir}$, is

$$V_{\rm vir} = 375 \left(\frac{M_{\rm vir}}{10^{12} M_\odot}\right)^{1/3} \left(\frac{\Omega_m}{\Omega_m(z)} \frac{\Delta_{\rm vir}}{18\pi}\right)^{1/6} \left(\frac{1+z}{7}\right)^{1/2} {\rm km\,s^{-1}}\,, \tag{3.37}$$

being $\Omega_m(z) \equiv \Omega_z$.

Defining the *concentration parameter* as $c = R_{\rm vir}/r_s$ and the function $A(x) = \ln(1+x) - x/(1+x)$ it is straightforward to find

$$\frac{M(s)}{M_{\rm vir}} = \frac{A(cs)}{A(c)} \tag{3.38}$$

where $M(s)$ is the mass enclosed within $s = R/R_{\rm vir}$. Bullock et al. (2001) have found in high-resolution N-body simulations that the c parameter scales with mass and redshift (a dependence that we have taken into account in this thesis in modeling DM halos) as

$$c = \frac{9^{+4.5}_{-3.2}}{1+z} \left(\frac{M_{\rm vir}}{10^{13} h^{-1} M_\odot}\right)^{-0.13}\,. \tag{3.39}$$

The scatter the authors find around the mean relation is $\Delta(\log c_{\rm vir}) = 0.18$ at a given mass. Following Lokas & Mamon (2001) the 1-D velocity dispersion profile can be found on solving the *Jeans equation*

$$\frac{1}{\rho}\frac{d}{dr}(\rho\,\sigma_r^2) + \frac{2}{r}\,(\sigma_r^2 - \sigma_\theta^2) = -\frac{d}{dr}\,\Phi\,, \tag{3.40}$$

supplemented by the boundary condition $\sigma(r) \to 0$ for $s \to \infty$. For isotropic orbits with equal tangential (σ_θ) and radial (σ_r) dispersions, the result is

$$\begin{aligned} \frac{\sigma^2(r)}{v_v^2} &= \frac{1}{2} c^2\, g(c)\, s\, (1+cs)^2 \left[\pi^2 - \ln(cs) - \frac{1}{cs} - \frac{1}{(1+cs)^2} - \frac{6}{1+cs} + \left(1 - \frac{4}{cs} + \right.\right. \\ &+ \left.\left. \frac{1}{c^2\, s^2} - \frac{2}{1+c\,s}\right) \ln(1+cs) + 3\ln^2(1+cs) + 6\,{\rm Li}_2(-cs)\right] \end{aligned} \tag{3.41}$$

in terms of the special function (the dilogarithm)

$${\rm Li}_2(x) = \int_x^0 dt\, \frac{\ln(1-t)}{t}\,. \tag{3.42}$$

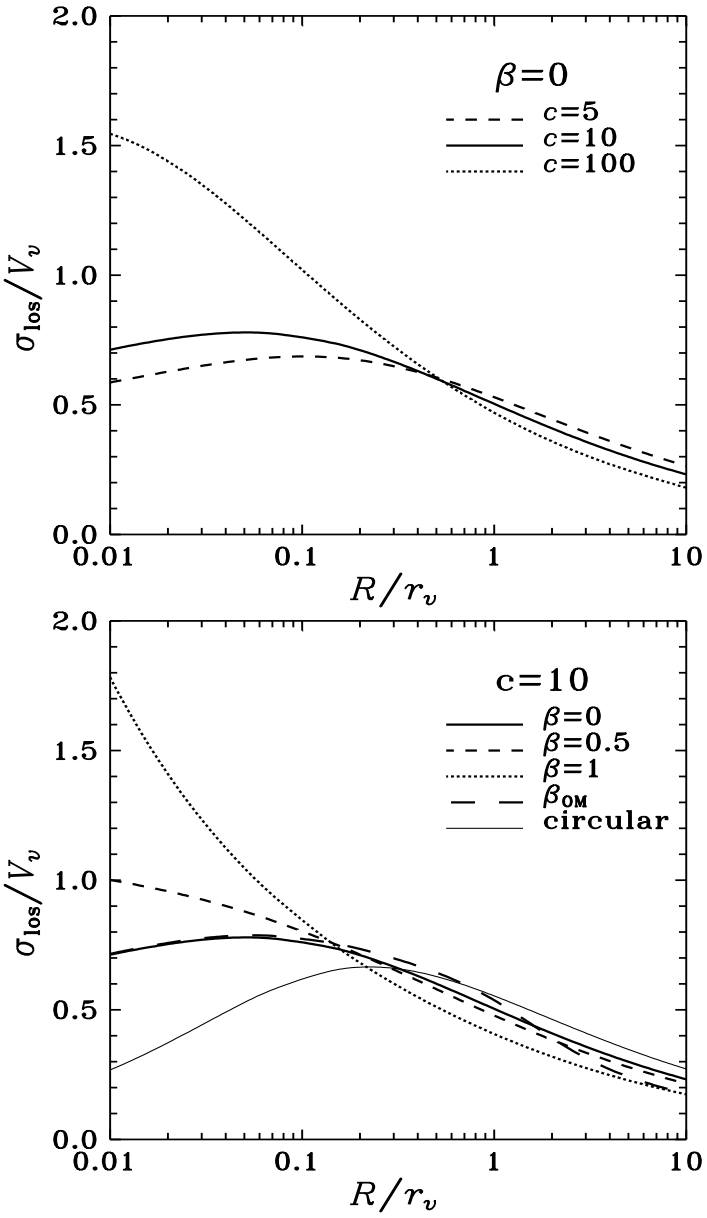

Figure 3.2: Radial velocity dispersion profiles (in units of the circular velocity at the virial radius). Figure taken from Lokas & Mamon (2001)

Eq. (3.41) is reported in Fig. 3.2 in which we can check that the ratio of the dispersion and virial velocities is about $0.55 - 0.6$ at the virial radius. Such findings will be developed and discussed in Section 2.4 and Chapter 7.

As a last point we report also the potential energy associated with the NFW mass distribution

$$W(s) = -\frac{1}{R_{\rm vir}} \int_0^s \frac{GM(s)}{s} \frac{dM(s)}{ds} ds = -W_\infty \left[1 - \frac{1}{(1+cs)^2} - \frac{2\ln(1+cs)}{1+cs} \right] . \qquad (3.43)$$

We will use Eq. (3.43) in Chapters 7 and 8, modified to include baryons.

3.3.5 Halo Formation Rates

The derivative of the P&S mass function is

$$R_{PS}(M,t) = \frac{dN_{PS}(M,t)}{dt} = \left[\frac{\delta_c(t)}{\sigma^2(M)} - \frac{1}{\delta_c(t)} \right] \left[-\frac{d\delta_c(t)}{dt} \right] N_{PS}(M,t) \, . \qquad (3.44)$$

The above expression is positive only for $\sigma(M) < \delta_c(t)$ since $d\delta_c(t)/dt < 0$ (in fact $\dot{\delta_c}(t) = \delta_{c0}/\dot{D} \propto -\alpha\, t^{\alpha-1}$, with $\alpha > 0$). This implies that $R_{PS}(M,t)$ is negative for low-mass objects for almost all realistic power spectra and window functions. The r.h.s of Eq. 3.44 becomes negative for $M < M_c(t)$, where we remind the critical mass $M_c(t)$ is the mass for which $\sigma(M,t) = \delta_c(t)$. $R_{PS}(M,t)$ however must not be interpreted as the formation rate of bound objects. Rather it corresponds to the *net rate of change* in the number density. Infact $R_{PS}(M,t)$ consists of a linear combination of the formation rate $R_{form}(M,t)$ at which objects of a given mass M are formed by mergers of smaller mass objects, and the destruction rate $R_{destr}(M,t)$ at which they are destroyed and/or incorporated in more massive systems:

$$R_{PS}(M,t) \equiv R_{form}(M,t) - R_{destr}(M,t). \qquad (3.45)$$

Merging is one of the most fundamental physical processes for the formation and destruction of halos and formation rates are a fundamental tool for studying galaxy evolution as we will discuss below. Moreover it has to be noted that, once halos merge, not always they lose their identity (see Section 2.3.7): especially in unequal-mass mergers, if the smallest ones are massive/concentrated enough, and/or the halo in which they infall is not so concentrated, they could survive stripping and dynamical friction.

A simple analytical treatment of how to calculate the formation rates has been outlined by Sasaki (1994) who has considered the destruction rate proportional to the P&S mass function $R_{destr} = \Phi(M,t)N_{PS}(M,t)$ where $\Phi(M,t)$ is the efficiency of destruction rate. Supposing such efficiency to have no characteristic mass scale $\Phi(M,t) = \Phi(t)$ one can write

$$\Phi(t) = -\frac{R_{PS}(M,t)}{N_{PS}(M,t)} = \frac{1}{D}\frac{dD}{dt}\left[1 - \frac{\delta_c^2}{\sigma(M)^2 D^2(t)}\right] \tag{3.46}$$

which in the limit $M \to 0$, i.e. $\sigma(M) \to \infty$, if monotonically decreasing with mass, leads to

$$R_{form}(M,t) = \frac{1}{D}\frac{dD}{dt}N_{PS}(M,t)\frac{\delta_c^2}{\sigma^2(M)D^2(t)}. \tag{3.47}$$

From the above formalism, the probability $p(t_1,t_2)$ that an object which exists at t_1 remains at t_2 without merging is given by

$$p(t_1,t_2) = \exp\left[-\int_{t_1}^{t_2}\Phi(t')dt'\right] = \frac{D(t_1)}{D(t_2)}\ (t_2 > t_1) \tag{3.48}$$

and the formation epoch t_f distribution $F(M;t_f,t)$ of bound objects with mass M at t is given by $F(M;t_f,t) = R_{PS}(M,t)\cdot p(t_f,t)$.

Bond et al. (1991), and further Lacey & Cole (1993), Kitayama & Suto (1996) developed more refined analytical methods to treat the process of formation rate and curing the "cloud-in-cloud" problem. Their results are strictly justified only when one adopts the sharp k-space filtering, i.e. the spherical top-hat filtering in k-space, and when $\sigma(M)$ is a monotonically decreasing function of M. The conditional probability that a point resides in an object of mass $M_1 \sim M_1 + dM_1$ at time t_1 provided that it becomes part of a larger object of mass $M_2(> M_1)$ at later time $t_2(> t_1)$ is

$$P_1(M_1,t_1|M_2,t_2) = \frac{1}{\sqrt{2\pi}}\frac{\delta_{c1}-\delta_{c2}}{(\sigma_1^2-\sigma_2^2)^{(3/2)}}\left|\frac{d\sigma_1^2}{dM_1}\right|\exp\left[-\frac{(\delta_{c1}-\delta_{c2})^2}{2(\sigma_1^2-\sigma_2^2)}\right]dM_1 \tag{3.49}$$

where $\sigma_i \equiv \sigma(M_i)$ and $\delta_{ci} \equiv \delta_c(t_i)$. Eq. (3.50), and the corresponding inverse conditional probability $P_2(M_2,t_2|M_1,t_1)$, readily yield instantaneous transition rates from a certain mass to another. Therefore if one weights the number of halos of mass M at a time t with the probability in Eq. (3.49) of having actually formed the objects from smaller subunits of

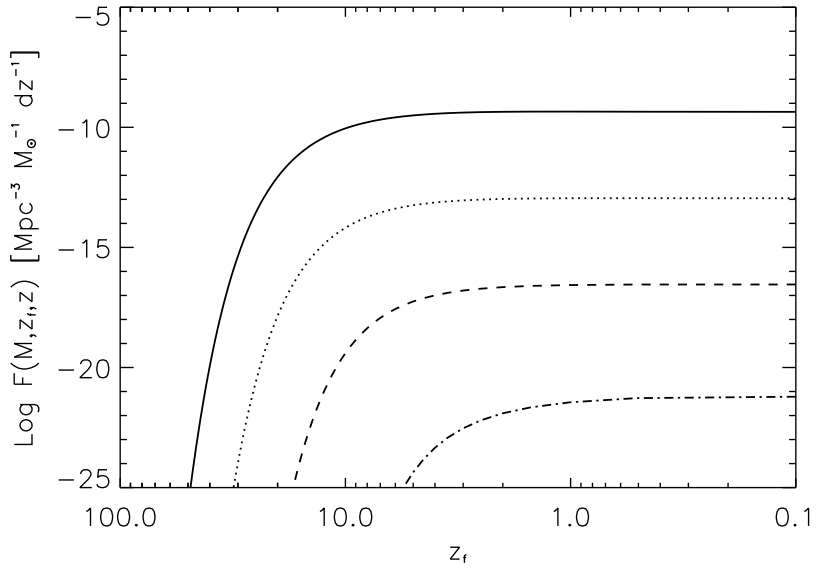

Figure 3.3: Formation Epochs in the Extended Press & Schecther theory in the ΛCDM cosmology; tha various curves are, from top to bottom, for $M = 10^9, 10^{11}, 10^{13}, 10^{15} M_\odot$

mass $M_f < M$, one can set the formation rates as

$$R_{form}(M,t;M_f) = \int_0^{M_f} dM_1 \frac{dP_1(M_1 \to M;t)}{dt} N_{PS}(M,t) = \\ = \sqrt{\frac{2}{\pi}} \frac{1}{\sqrt{\sigma(M_f)^2 - \sigma(M)^2}} \left[-\frac{d\delta_c(t)}{dt} \right] N_{PS}(M,t)\,. \tag{3.50}$$

An object of mass M at the time t could have been formed by the merging of smaller objects of mass from 0 M_f, at a time $t - dt$. The mass M_f is usually set to M/n, with $n = 2$ (see Lacey & Cole 1993), but we have verified that our results are so not sensitive to the exact value of n, as long as $1 < n < 5$. The *survival* probability that an object of mass M at time t_1 remains, without destruction, to have mass less than $2M$ at a later time $t_2 (> t_1)$ is then

$$P_{surv}(M,t_1,t_2) = \int_M^{2M} P_2(M_2,t_2|M,t_1) dM_2. \tag{3.51}$$

In Fig. 3.3 we show the formation rates for different masses. It is readily seen the hierarchical behavior for which big masses are formed later than smaller ones. What reported above, in particular in Eq. (3.50) for the formation of bound objects, is known as the *Extended* Press & Schecther theory (EPS) and is extensively used when comparing results of simulations with theory and in Galaxy formation Semi-Analytical Modeling (SAM), to estimate the number

of baryonic cores formed trough the cosmic epochs. However these methods, EPS and Sasaki's rates, seem to fail in reproducing the results of simulations (see also Benson et al. 2005), being the absolute difference in the rates up to a factor of 2 to 10 varying depending on mass and redshift (Lacey & Cole 1994; Taffoni et al. 2002; Springel et al. 2005). To highlight the problem in Fig. 3.4 we show some results by Taffoni et al. (2003). These authors compare the number of progenitors for a given halo of mass M_0 at $z = 0$ computed from simulations (using the code PINOCCHIO) and the EPS theory. It is straightforward to see the mismatch, up to factor of 10, between the numerical and the analytical results. As commented in Section 2.3.3 the S&T mass function (Eq. (3.33)) is a very good fit to numerical simulations (Springel et al. 2005) and therefore it is expected that its variation with time could better reproduce the rate of production of *virialized* objects at any epoch ($z_{\rm vir} \leq 10$).

In particular, as shown in Fig. 3.5, the total and the positive terms of the S&T mass function derivative coincide for $z \geq 1.5$ and halo masses $10^{12.5} \div 10^{13} M_{\odot}$, which implies that the negative term is negligible in these ranges. In this thesis we have then followed the assumption, used by Granato et al. (2004), that the complete statistics of halos in the range $\sim 10^{12} \div 2 \times 10^{13} M_{\odot}$, which could harbor a galaxy (see Section 2.4), is given by the positive term of the derivative of the S&T mass function that for a mass $M_{\rm vir}$ at time $t_{\rm vir}$ reads as

$$\frac{{\rm d}^2 N_{\rm ST}}{{\rm d}t_{\rm vir}\,{\rm d}M_{\rm vir}} = \left[\frac{a\,\delta_c(t_{\rm vir})}{\sigma^2(M_{\rm vir})} + \frac{2\,p}{\delta_c(t_{\rm vir})}\,\frac{\sigma^{2\,p}(M_{\rm vir})}{\sigma^{2\,p}(M) + a^p\,\delta_c^{2\,p}(t_{\rm vir})}\right] \left|\frac{{\rm d}\delta_c}{{\rm d}t_{\rm vir}}\right| N_{\rm ST}(M_{\rm vir}, t_{\rm vir})\,. \quad (3.52)$$

However, as discussed above, the positive term may not completely represent the formation rates of DM halos: it is still missing a complete *Extended* S&T theory which would need the definition of the survival probabilities (as those in Eq. (3.51) for the P&S mass function), through a "moving barrier" approach (Section 3.3.3). A very first attempt, not yet confirmed, has been pursued by Mahmood & Rajesh (2005) who have implemented a moving barrier model for computing the DM rates using the S&T mass function. Such a method, though analytical, it has to be still numerically solved, with a high computational cost. Anyway their final result is that the *Extended S&T* rates, computed from the survival probabilities, are comparable to the positive term of the S&T mass function derivative

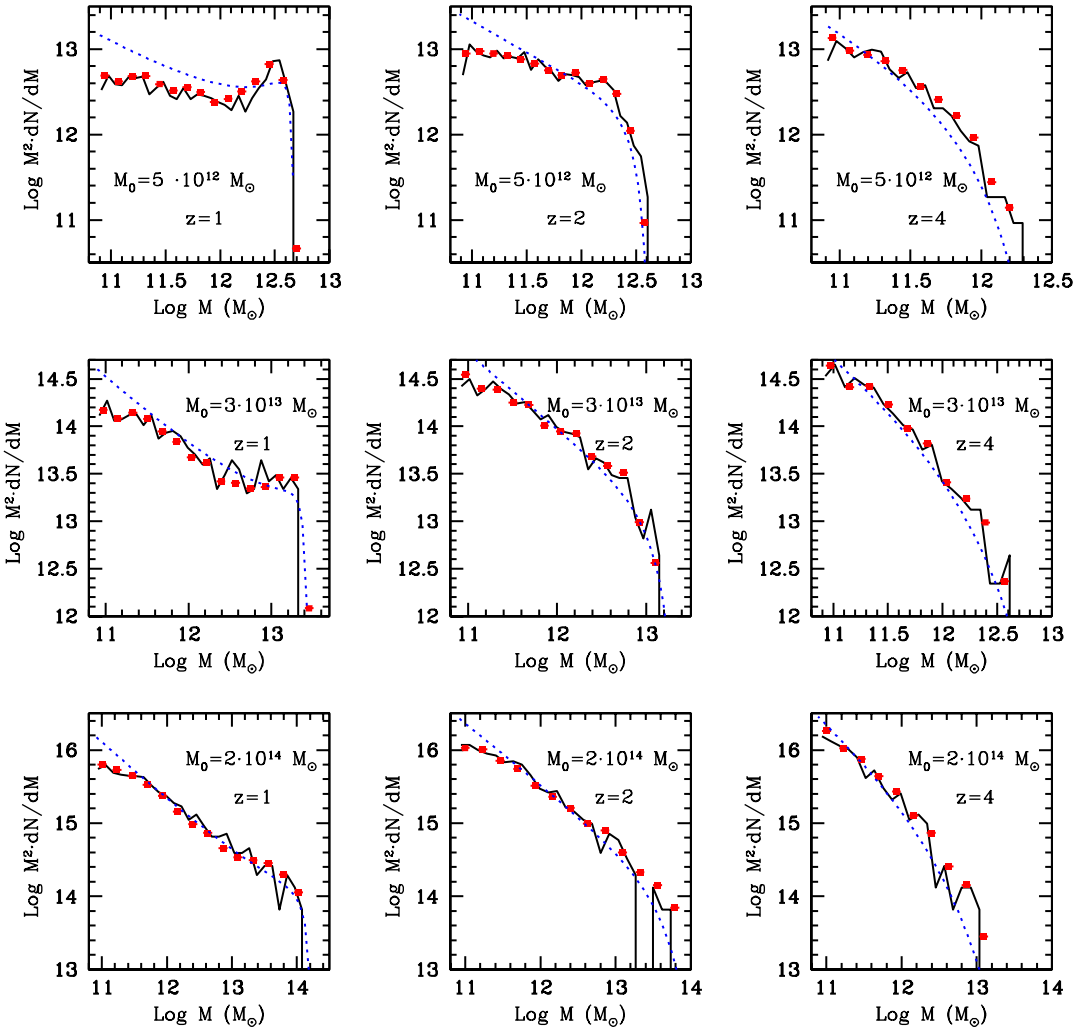

Figure 3.4: Conditional mass functions in the ΛCDM case for parent halos identified at $z = 0$. The points represent the simulation data while the solid lines are the prediction of PINOCCHIO; the dashed lines are the analytical predictions of the EPS. Figure taken from Taffoni et al. (2002)

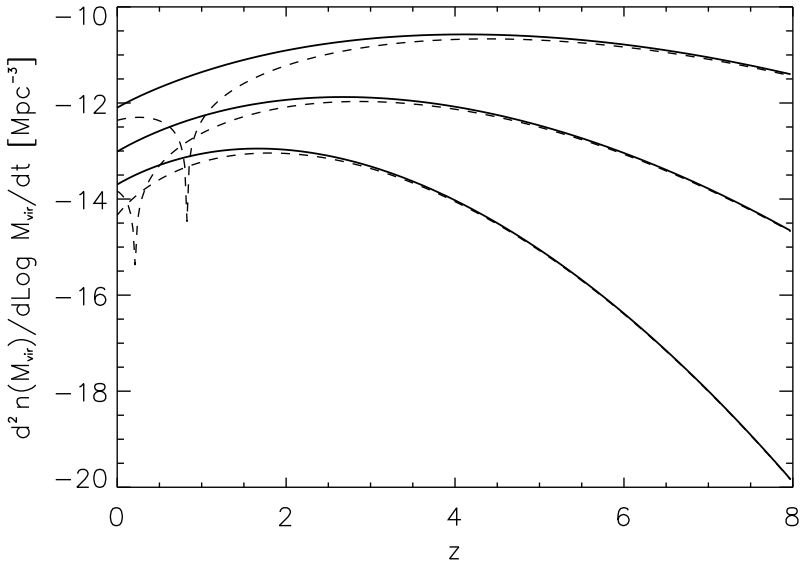

Figure 3.5: Derivative of the S&T mass function. Solid line: only positive term; dashed line: total derivative. From bottom to top the three set of lines are for $M_{\rm vir} = 10^{13} M_{\odot}$, $M_{\rm vir} = 10^{12} M_{\odot}$ and $M_{\rm vir} = 10^{11} M_{\odot}$

(within a factor of 2) in the range of redshift and masses taken into account in this thesis (see their Fig. 11). The most interesting result of this discussion is that the S&T rates seem to be much more accurate than the usual implemented EPS theory, in fitting numerical rates of formation of bound objects as obtained from numerical simulations. Especially at high redshift the number density predicted by the S&T theory for halos of about $10^{13} M_{\odot}$, (which are the halos harboring the powerful high redshift QSO; see Chapter 6) is up to a factor of 10 higher of the EPS rates, but however still more consistent with numerical simulations (Taffoni et al. 2002; see Fig. 3.4). In Fig. 3.6 we show the comparison for the rates computed with S&T and EPS theories for various halo masses as a function of redshift.

3.3.6 The Merger Tree

Given a DM halo at any redshift $z = z_0$ it is possible to build the distribution of the number of progenitors of that halo at any redshift $z > z_0$. This is very useful for building the *halo main progenitor accretion history*, i.e. at any time we can probe the mass

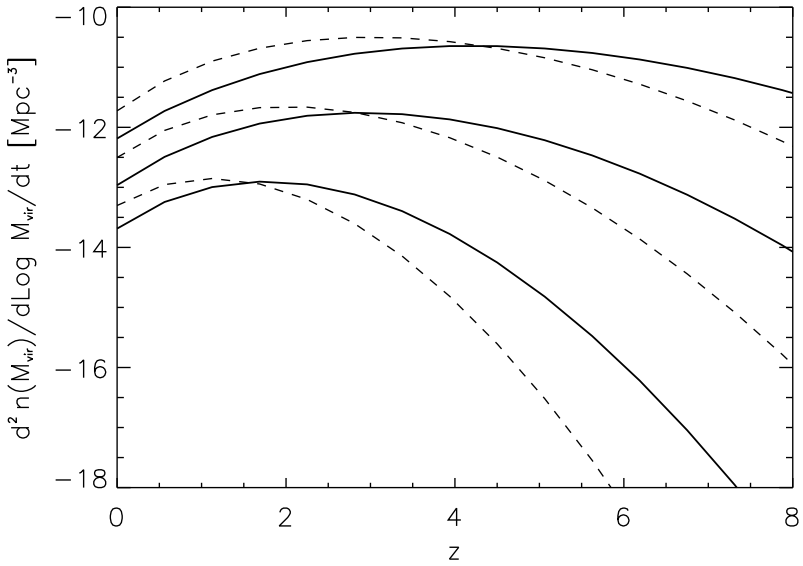

Figure 3.6: Formation Rates in the ΛCDM cosmology. Solid line: computed using the S&T mass function; dashed line: EPS rates. From bottom to top the three set of lines are for $M_{\rm vir} = 10^{13} M_\odot$, $M_{\rm vir} = 10^{12} M_\odot$ and $M_{\rm vir} = 10^{11} M_\odot$

of the most massive "clump" which concurs in building up the final halo mass. In this section we show our results in building a merger tree following the prescriptions by Lacey & Cole (1993). The strongest limitation of this approach is that the statistics is based on the EPS formalism, which we have shown (Section 3.3.5) not to be fully consistent with numerical simulations.

According to EPS, following Eq.(3.50) the fraction of mass in a halo of mass M_0 at redshift z_0, which at an earlier time was in smaller progenitors of mass in the range $M \div M + dM$ is

$$f(M, M_0)dM = \frac{1}{\sqrt{2\pi}} \frac{D}{S^{3/2}} \exp\left(-\frac{D^2}{2S}\right) \frac{d\sigma^2}{dM} dM \,, \tag{3.53}$$

where D is the growth factor (Section 3.2) and $S \equiv \sigma^2(M) - \sigma^2(z_0)$. Integrating this function over the range $0 < M < M_0$ gives unity: all the mass of M_0 was in smaller subclumps at an earlier epoch.

Taking the limit $z \to z_0$ and multiplying by the factor M_0/M to convert from mass weighting to number weighting, Eq.(3.53) gives the number of progenitors dN/dM the more massive halo fragments into when one takes a small step δz back in time. Having

specified the mass resolution M_{res}, one can then compute the mean number of fragments in the range $M_{res} < M < M_0/2$

$$N_p = \int_{M_{res}}^{M_0/2} \frac{dN}{dM} dM \,, \tag{3.54}$$

and the fraction of the accreted mass

$$F_a = \int_0^{M_{res}} \frac{dN}{dM} \frac{M}{M_0} dM \,. \tag{3.55}$$

Following a random normal sequence of numbers below unity (for details see e.g. Volonteri et al. 2003) at any time step the halo mass is fragmented into two smaller subunits out of which also the accreted mass F_a is removed (this technique prevents the formation of too many massive objects at high redshifts as compared to those predicted by the EPS itself, see Lacey & Cole 1993). The merger hierarchy is built up by repeating the same splitting procedure on each subclump at successive time steps. Our results are shown in Fig. 3.7.

In Fig. 3.9 we show the main progenitor accretion histories for a halo masses of $10^{13} M_\odot$, $10^{13} M_\odot$ at $z = 0$. It is interesting to notice that the growth is different: the cluster reaches 1/10 of the mass at $z \sim 1$, while the $10^{13} M_\odot$ halo has gained already 40% of its mass at that time. Moreover it has to be pointed out that if one neglects the accreted mass in Eq. (3.55), as in the original version of Lacey & Cole (1993) at each timestep backwards in time, the growth of the smaller halo is even smoother at low redshift. The average growth of the *total* mass of the DM halo as described by the merger tree, is in very good agreement with the findings by Zhao et al. (2003b) (compare Figs. 3.9 and 3.10).

These authors find that, in high-resolution N-body simulations developed in a ΛCDM cosmology, the build-up of dark halos generally consists of two phases: a first phase of *fast accretion*, where the halo mass increases with time much faster than the expansion rate of the Universe and the circular velocity, i.e. its potential well, increases rapidly with time, and a second phase of *slow accretion*, during which the mass grows at the most linearly with time or by factors of a few while the circular velocity stays almost constant.

The inner properties of the halo, such as r_s, increase rapidly during the fast accretion and stay almost constant or vary slightly in the second phase. It is interesting to notice from Fig. 3.10 that, in particular, even if the mass of the total halo increases with

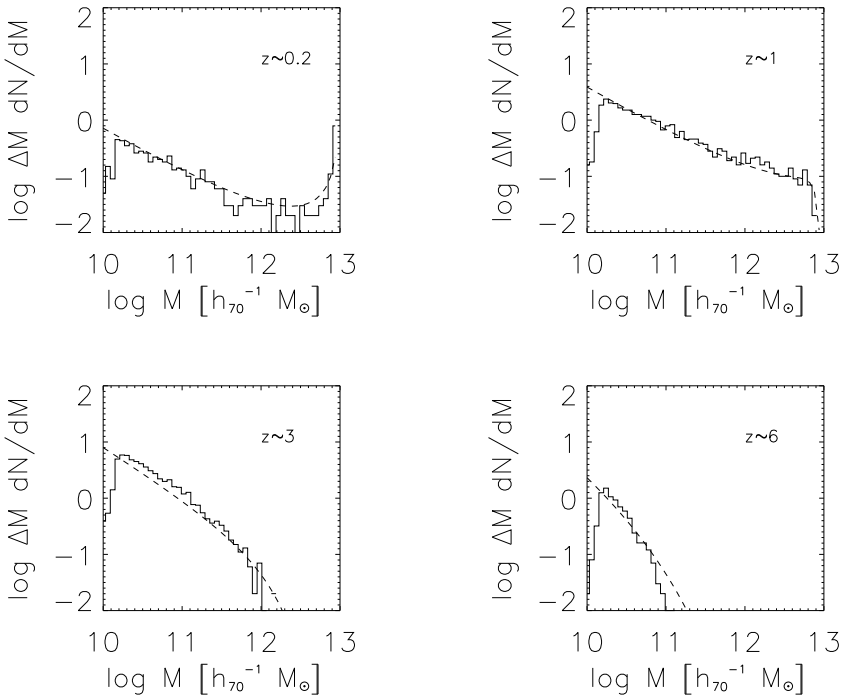

Figure 3.7: Mean number of progenitors with mass M for a $z_0 = 0$, $M_0 = 10^{11} M_\odot$ parent halo at different redshifts as labelled. Dashed lines are the predictions of the EPS theory; histograms show the results for the merger tree (mean of 100 realizations), $M > M_{res} = 10^{-3} \cdot M_0$. Performed by A. Lapi & F.S.

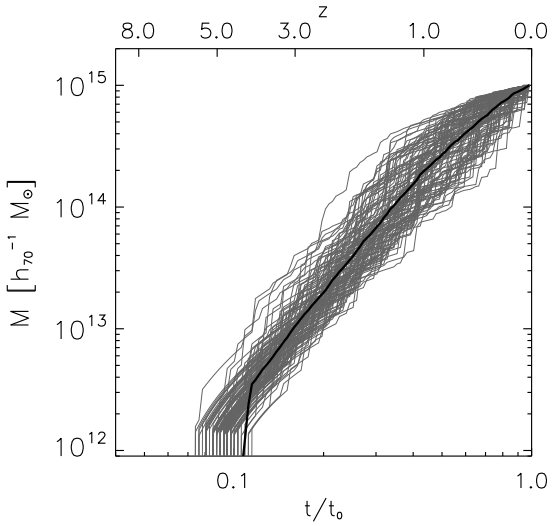

Figure 3.8: Main progenitor halo merger history for a $10^{15} M_\odot$ DM halo. The thick solid line is the average on 100 realizations. Performed by A. Lapi & F.S.

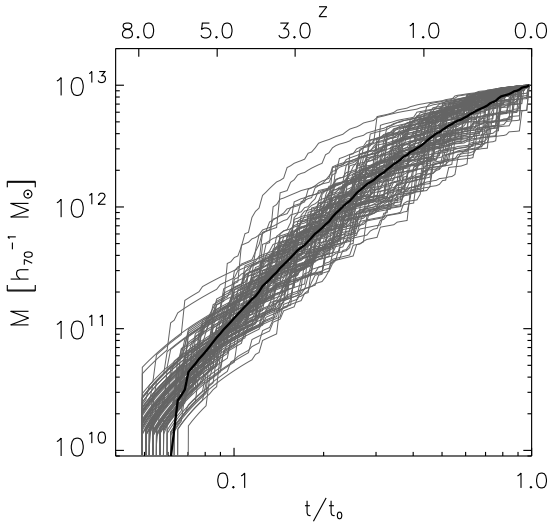

Figure 3.9: Main progenitor halo merger history for a $10^{13} M_\odot$ DM halo. The thick solid line is the average on 100 realizations. Performed by A. Lapi & F.S.

time, the inner mass within r_s, M_s, does not vary significantly, implying that the mass is added in the outer regions (see also Section 3.3.7).

Moreover Wechsler et al. (2002) find c to be intimately linked with the time dependent mass accretion rate onto the halo and in the fast accretion phase, with high mass infall rates, the concentration parameter is related to the background density while stays approximately constant during the slow accretion phase.

3.3.7 Statistics and distribution of Subhalos

During the hierarchical assembly of DM halos the inner regions of early virialized objects often survive accretion onto a larger system, thus giving rise to a population of subhalos. This substructure population evolves in number and mass as it is subjected to the forces that try to dissolve it. Depending on their orbits and their masses these subhalos therefore either merge, are disrupted or survive to the present day.

Such issue is important to fully describe, in a statistical sense, the non-linear distribution of mass in the Universe (galaxies are thought to reside at the centers of DM halos *and* subhalos). According to P&S theory when a region collapses, all its substructure is supposed to be erased at once, while in realistic cases the erasure of substructures is

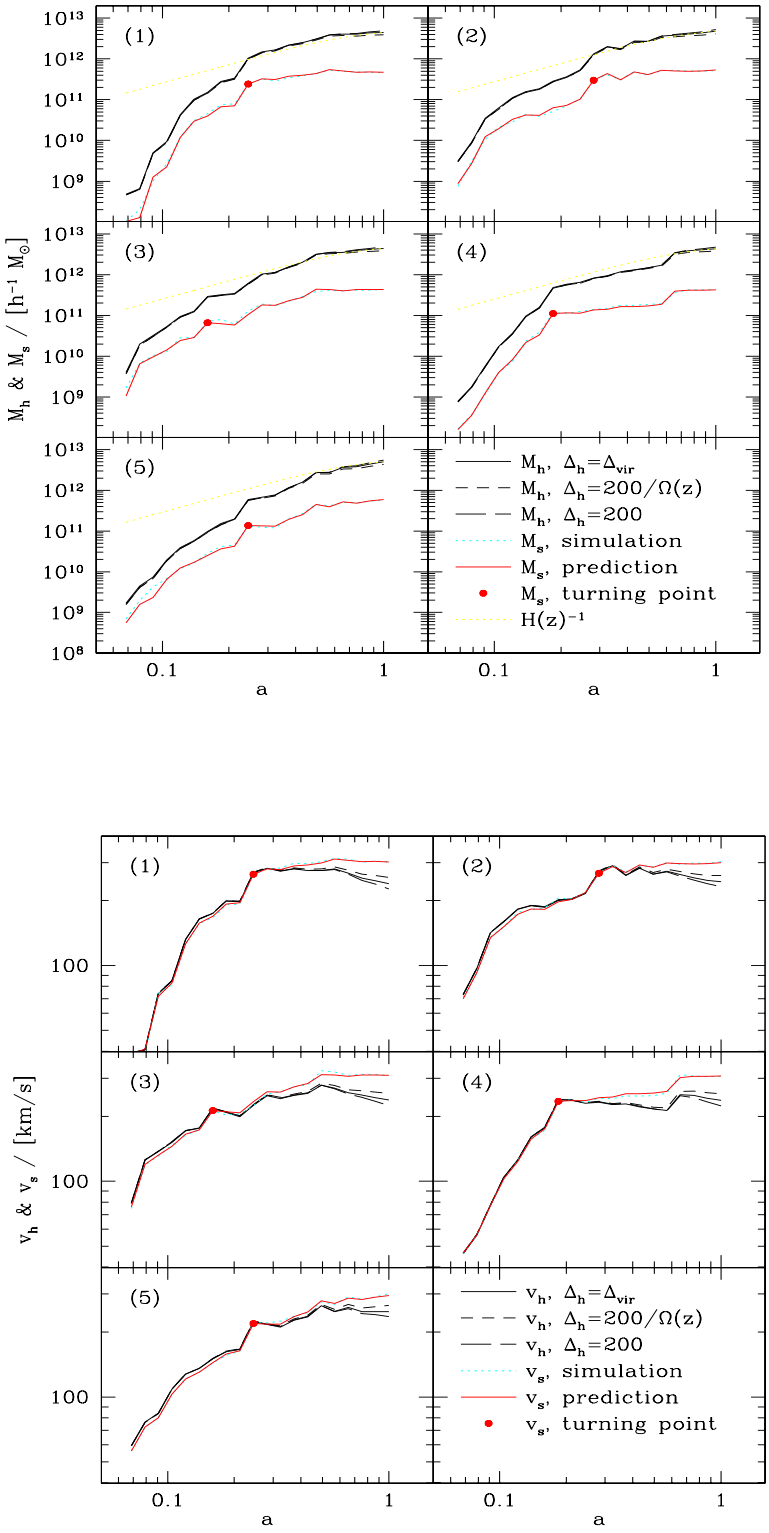

Figure 3.10: Top: mass accretion histories (i.e. the change of the mass of the main progenitor with the scale factor) for five high-resolution halos. M_h defines the total halo mass while M_s just the mass within r_s. Bottom: the evolution of halo circular velocity V_h and inner circular velocity V_s. (Figures taken from Zhao et al. 2003b)

connected to the two-body interaction of already collapsed clumps.

To tackle the problem of how structures evolve, within a hierarchical scenario of DM halos, it has to be taken into account that in unequal mass merger, the smaller halo is dragged inside the bigger halo and its further dynamical evolution is controlled by *dynamical friction*. The orbital decay time caused by dynamical friction is simply $dR/dt = -R/t_{df}$, on the time-scale

$$t_{df} = \frac{1}{2}\left[\frac{\partial \ln M(R)}{\partial \ln R} + 1\right]^{-1} \frac{V_{circ}^3(R)}{4\pi G^2 (\ln\Lambda) M \rho(R) g[V_{circ}(R)/\sqrt{2}\sigma_r]} \tag{3.56}$$

where $\ln\Lambda = 8$, $\sigma_r(x) = f(x)V_{max}^2$, with $f(x)$ a function of the normalized radius (see Oguri & Lee 2004), and $g(\xi) = \mathrm{erf}(\xi) - (2/\sqrt{\pi})\xi \exp(-\xi^2)$. Since the dynamical friction is also proportional to the radius R, the decayed radius R_f of the subhalo during the infalling from an initial radius R_i within the time-interval Δt in the host halo is estimated as $R_f = R_i\left[1 - \frac{\Delta t}{t_{df}}\right]$ and the corresponding stripped mass is $m_f = m_i f[r_t(m_i)]$, where f is a function (Oguri & Lee 2004) of the tidal radius r_t, which is approximately the radius at which gravity balances the tidal force. Beyond this radius the mass m_i will be completely disrupted. This force causes an orbital decay and makes the subhalo more susceptible to strong tidal forces. It is still uncertain from numerical simulations the actual fraction of matter which is stripped away.

Various groups have arrived to similar conclusions exploiting numerical and analytical techniques (see van den Bosch et al. 2005):

- more massive halos have a larger mass fraction of substructures
- the halo-to-halo scatter is large
- the abundance of subhalos per unit parent halo mass is independent of parent halo mass
- the subhalo mass fraction is larger at higher redshifts.

The number of subhalos of mass m for a given parent halo of mass M can be written in the form (Vale & Ostriker 2004)

$$N(m, M)dm = A\left(\frac{m}{x\beta M}\right)^{-\alpha} \exp\left(-\frac{m}{x\beta M}\right)\frac{dm}{x\beta M}\,. \tag{3.57}$$

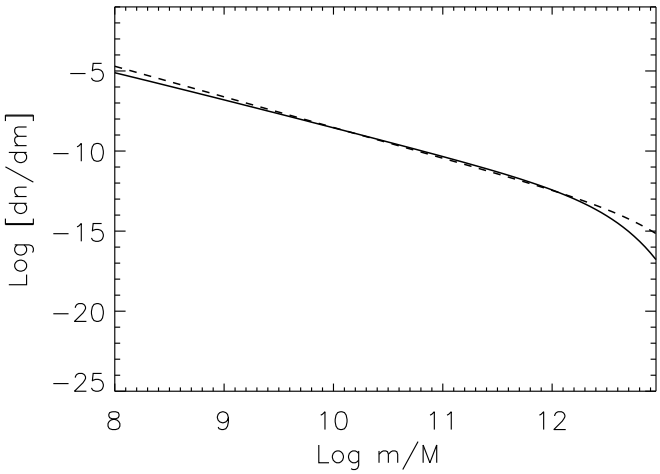

Figure 3.11: Comparison of the subhalo Mass Distribution for a parent halo of mass $M_{halo} = 10^{13} M_{\odot}$: the solid line has been computed following van den Bosch et al. (2005); the dashed line has been computed from Vale & Ostriker (2004).

In Fig. 3.11 we compare the estimates by van den Bosch et al. (2005) and Vale & Ostriker (2004). Their results are very similar. Similar are also the finding, from theoretical modelling, by Oguri & Lee (2004). In this thesis we have used Vale & Ostriker (2004).

In particular van den Bosch et al. (2005),from a detailed study of merging histories, claim that there could be some increase in the number density of subhalos at higher redshift by a factor of 2 to 3 at $z \sim 5$ (see Fig. 3.12).

Lots of numerical effort has been spent in understanding the spatial distribution of subhalos, useful to compare with redshift-dependent clustering of galaxies. Yano et al. (1996) have shown that the problem of statistics *and* spatial distribution of halos can be obtained in a straightforward manner recomputing the P&S mass function setting the variance, which is the Anti-Fourier transform of the two-point correlation function, as

$$\sigma_c(r)^2 = < \delta_{M_2}(r_0)\delta_{M_1}(r_0 + r) > = \frac{V}{2\pi^3} \int_0^{k_c(M_2)} |\delta_k|^2 \frac{\sin kr}{kr} 4\pi k^2 dk. \qquad (3.58)$$

In this picture the halo mass function can be written as (Oguri & Lee 2004)

$$N(m_i|R_i; M, z, z_i) = \sqrt{\frac{2}{\pi}} \frac{M}{m_i} \left| \frac{\partial \sigma(m_i)}{\partial m_i} \right| \left| \frac{\partial \beta}{\partial \sigma(m_i)} \right| e^{-\beta^2/2} dm_i \qquad (3.59)$$

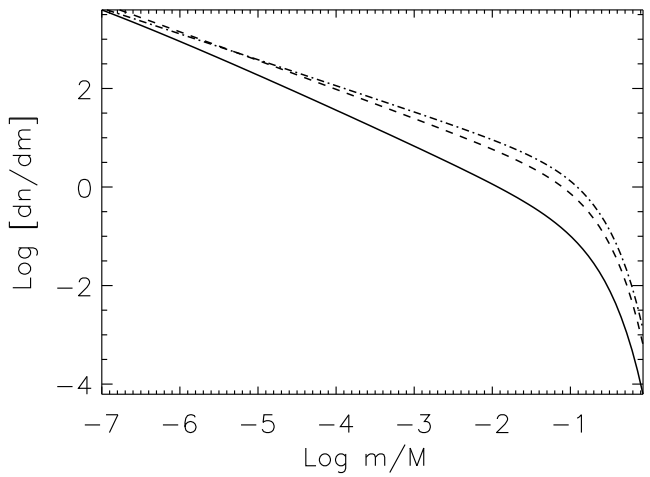

Figure 3.12: Subhalo Mass Distribution for a parent halo of mass $M_{halo} = 10^{13} M_{\odot}$ at various z following van den Bosch et al. (2005): the solid line corresponds to $z = 0$; the dashed line to $z = 2$; the dot-dashed line to $z = 5$.

where $\beta(r) \equiv \frac{\nu_{1c} - \epsilon(r)\nu_{2c}}{\sqrt{1-\epsilon(r)^2}}$. Eq. (3.59) gives the number of subhalos of given mass m_i formed at redshift z_i hosted in a halo of mass M at redshift z located at an orbital radius R_i from the center of the host halo. Assuming then all the bound objects within or near (up to, say, 10 times) the radius of the host halo and on average distributed according to the parent halo density profile one can analytically compute the number of subhalos at each radii in the parent halo.

Following Oguri & Lee (2004), we evolve a system composed of a parent halo (with fixed mass in time) of mass $M = 10^{15} M_{\odot}$ and subhalos of mass m for ~ 0.5 Gyr at redshift $z \sim 1$. As it can be seem in Fig. 3.13 most of subhalos are confined in the outermost regions of the host halo. Then one can suppose that after virialization, i.e. at the end of the *fast* accretion phase, the rest of the mass is accreted almost in the outer regions of the halo, close to or even outer $R_{\rm vir}$.

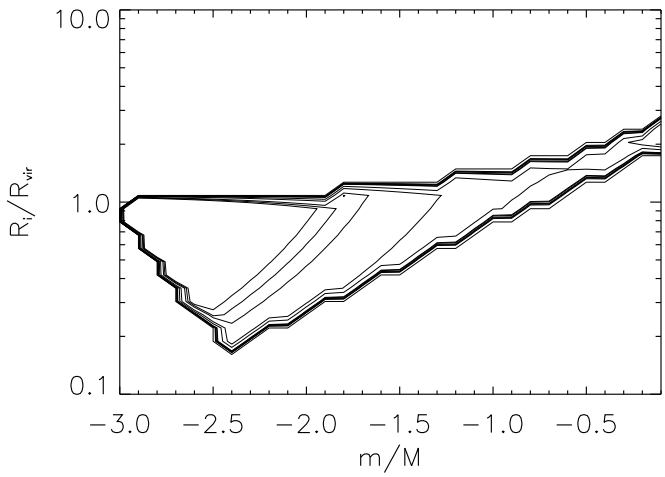

Figure 3.13: Subhalo spatial distribution in a parent halo of mass $M_{halo} = 10^{15} M_{\odot}$ at $z \sim 1$ after evolving the system for ~ 0.5 Gyr following Oguri & Lee (2004).

3.4 Galaxy Evolution

3.4.1 Observational properties of Galaxies

Evidence for Dark Matter

Rotation curves of spiral galaxies, i.e. the rotation velocities V_{rot} as a function of the galactocentric radii r, are one of the traditional tools for detecting DM around galaxies. Such measures are performed via the analysis of the spectra of different gaseous tracers, emitting in the optical (Hα, [NII] lines) and in the radio regime (HI, CO lines).

In the case of a point mass one would expect the rotation velocities to decrease as $r^{-1/2}$ (the Keplerian decline) since $V_{rot}^2 = GM(< r)/r$ and $M(< r)$ is constant. However the observed rotation curves of spiral curves of spiral galaxies have a wide range of shapes (Persic, Salucci & Stel 1996), but in no case the Keplerian decline is observed and the rotation velocity either increases until the last measured point, or it stays approximately flat once the maximum is reached, or it decreases, but always more slowly than the Keplerian decline. This implies that there must be a component of invisible matter that accounts for this kinematics, and its importance increases with increasing radius.

Gravitational lensing provides a powerful tool to probe the mass of galaxies: it allows to measure the mass inside the Einstein ring (in Chapter 8 we will compare our statistical studies of the $M_{\rm vir}/M_{\rm star}$ ratio with lensing determinations of halo masses). For instance Treu & Koopmamns 2002, using also stellar kinematics and mass-to-light ratio constraints, determined that the baryon fraction inside the Einstein ring of PG+1115+080 (corresponding to 1.2 effective radii) is about 65%.

The motion of satellite galaxies around the Milky way and other galaxies show that the actual mass of galaxies is much larger than the luminous one (e.g. Prada et al. 2003). Dark halos are found to extend out to a few hundreds of kpc and the velocity dispersion of the satellites is weakly dependent on luminosity.

Elliptical galaxies can also give an indication of the existence of DM and can be used to test the predictions of cold DM (e.g. Borriello et al. 2003). However, due to the lack of a simple tracer, the situation is more complicated. Different ways to trace the potential as a function of radius have been proposed; the stellar kinematics (e.g. Baes & Dejonghe 2002), the kinematics of planetary nebulae, the kinematics of neutral hydrogen (when present), and the X-ray emitting gas all lead to the conclusion that a substantial amount of DM is present in all galaxies.

All these pieces of observational evidence, combined with the WMAP findings on CMB experiments, are showing that DM exists, dominates the matter content of the Universe and it is mostly clustered around single or grouped galaxies.

Galactic Dichotomy

Galaxies are present in two big families, which reflect distinct morphological, chemical and evolutionary features. Following Kauffmann et al. (2003), Heckman et al. (2004) and Dekel & Birnboim (2005), we can sum up all the observational pieces of evidence on this subject as follows (see Fig. 3.14). There is a gap at $u - r \sim 2$, where galaxies are divided into a blue and red sequence. The former are on average younger, less massive and disky (*late-type* galaxies), while the latter are more massive older and boxy, spheroidal (*early-type* galaxies). Blue, Late-type galaxies dominate the mass function below the knee, $L^\star$, of the Schechter function while red, early-type galaxies take over above $L^\star$ (see Chapter 4). A transition, though with large scatter, seems to occur in the galaxy structural scaling

relations around $M_{crit} \sim 3 \cdot 10^{10} M_{\odot}$ (Fig. 3.14), in particular the mean effective brightness falls below M_{crit}. Local ($z < 0.3$) AGN activity (based on $OIII$), with high accretion rates and high star formation, peaks near M_{crit} with some AGN activity in less massive, younger galaxies, and it is associated with SMBH masses $\leq 10^8 M_{\odot}$ (see also Fig. 3.14). Radio-loud AGN dominate, uncorrelated with $OIII$ luminosity and star formation, in larger halos hosting $\sim 10^8 - 10^9 M_{\odot}$ SMBH (Best et al. 2005).

The Granato et al. model deals only with Ellipticals and bulges of spirals therefore spheroidal galaxies are the main target of this thesis. If the galaxy has virtually no disk it is called Elliptical, defined with the symbol *En*, in which the ratio of the major to the minor axis is given by $b/a = 1 - n/10$. The spheroid brightness profile has a rapid falloff (*Sersic* profile), given by

$$I(R) = I_e \exp\left(s\left[\left(\frac{R}{R_e}\right)^{1/n} - 1\right]\right) \tag{3.60}$$

where R_e is the half-light radius, s is a constant and n is an integer, for $n = 4$ we recover the well-known *de Vaucouleurs* profile. The standard procedure for the analysis of light distribution of an elliptical is to determine curves of constant intensity (*isophotes*). The intensity profile can then be fitted in the form

$$I(\theta) = I_0 + \sum (a_n \cos n\theta + b_n \sin n\theta)\,. \tag{3.61}$$

If $a_n < 0$ then the E-galaxy is *boxy* because the isophotes are somewhat rectangular, show usually flat cores in the central brightness profile and are in general more luminous. On the other side, those with $a_n > 0$, are *disky*, less luminous and with power-law profiles.

There is a remarkable correlation between colors and luminosities of Ellipticals, brighter galaxies being redder. This is called the *color-magnitude* (CM) relation, with a small scatter. The tightness of the CM relation has been confirmed up to $z \sim 1$ (e.g. Stanford et al. 1998). Such a relation is considered to be a relation between the luminosity and the mean metallicity of the stellar population, the metallicity increasing with luminosity. Positive values of the elemental ratio [α/Fe], in particular Mg, have been found, increasing with galactic mass (e.g. Terlevich & Forbes 2002; see Fig. 3.19). Of the same type are the relations found between line-indices and luminosity or dispersion velocity. Bernardi

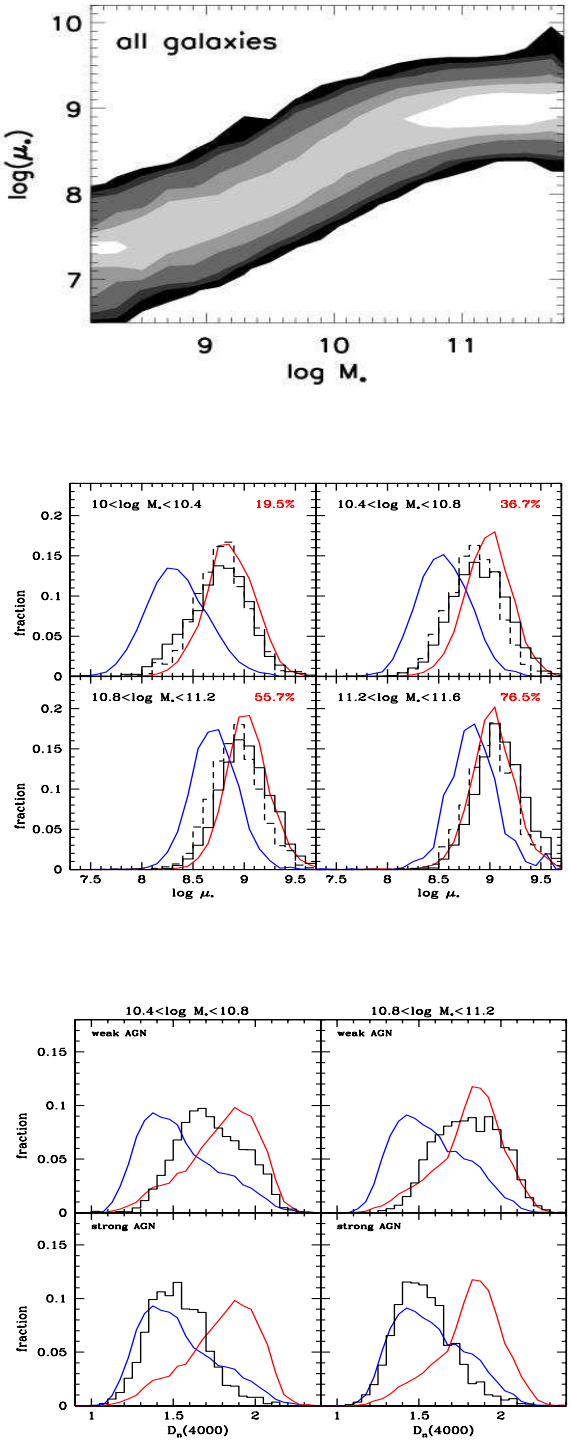

Figure 3.14: Top panel: Surface mass density as a function of stellar mass; Middle panel: Surface mass density distributions of the host galaxies of AGN for early (red) and late (blue) galaxies; the number on the corner is the percentage of E-galaxies. Bottom panel: The D_n distribution for the host galaxies of weak AGN (upper panel) and strong AGN (lower panel). (Figure taken from Kauffmann et al. 2003).

et al. (2003) demonstrated that cluster, group and field early-type galaxies follow almost identical $Mg_2 - \sigma$ relations, the slight zero-point off-sets could be ascribed to almost ~ 1 Gyr difference in the stellar populations of field and cluster galaxies. Another important property of colors and line-indices in Ellipticals is their radial variation. Colors get bluer at large r, metallicity indices become fainter, while Balmer lines become stronger. The modest shift with increasing z found in the zero-point of the FP, $Mg_2 - \sigma$ and CM relations of ellipticals hase led to the conclusion that most of their stars formed at $z \geq 2 \div 3$, in a relatively short burst. Moreover the fact that in early-type galaxies the present rate of SNI, with a long-lived progenitors, is about 10 times higher than the rates of SNII, implies that E-galaxies must be inactive today further supporting a scenario in which for Ellipticals an early, intense star formation phase was followed by a longer, passive evolution stage.

High-redshift Galaxies

Galaxies are found at all redshifts up to ~ 6, but at different epochs they can appear in different morphologies and/or aspect due to their intrinsic evolution. As reviewed by Calzetti & Giavalisco (2000) the Lyman-break technique has highlighted the presence of a substantial number of star-forming galaxies (LBG) at $z > 3$. Their spectra are very similar to those of local UV-bright starbursts, with just more intense interstellar absorption lines due to the distance. Their Star Formation Rates (SFR) are about 10 $M_{\odot}\mathrm{yr}^{-1}\mathrm{kpc}^{-2}$, about 5-10 times larger than those measured in local starbursts. Supposing an average starformation timescale of a few 10^8 yr, by $z = 3$ these systems have formed $\geq 10^{10} M_{\odot}$ or a large fraction of the stellar mass of an $L^{\star}$ galaxy. Shimasaku et al. (2005; see Fig. 3.16, upper panel) have collected all the available secure data on the UV evolution of LBG galaxies. It seems that the comoving number of LBG already at $z \sim 3$ is comparable with the local number density of galaxies with $L \leq L^{\star}$. Moreover Clustering analysis of $z \sim 3-5$ LBG has shown that DM halos hosting bright LBG have a total mass of $10^{12} M_{\odot}$ (e.g. Giavalisco & Dickinson 2001) and their luminous density peaks at $z \sim 3$ (see Fig. 7 in Shimasaku et al. 2005). All these data are reconciled if LBG are hosted in a one-to-one correspondence with halos of mass $\sim 10^{12} M_{\odot}$ with which LBG share similar density evolution (see Fig. 3.6).

Increasing evidence suggests that LBG may account for $\sim 50\%$ of the star formation at $z \geq 2$, with the rest provided by the FIR-bright SCUBA sources. The advent of large-format submm/mm cameras, SCUBA (Holland et al. 1999) and MAMBO (Kreysa et al. 1998), revealed the presence of a significant population of dust-enshrouded galaxies at high redshifts. Several hundred of these sources have been collected up to now (e.g. Scott et al. 2002). SCUBA sources appear similar to the local Ultra Luminous InfraRed Galaxies (ULIRG) undergoing a period of massive star formation at rates $10^2 \div 10^3\, M_\odot\, \mathrm{yr}^{-1}$. Their number density is similar to the local early-type galaxy population, in particular the very luminous Ellipticals, above $(1 \div 2)\, L^\star$. Moreover SCUBA galaxies reside in massive halos, according to lensing (e.g. McKay et al. 2002) and statistical arguments (e.g. Wyithe & Padmanabhan 2005), with mass $\geq 10^{13} M_\odot$ (see also Chapter 8). Interestingly Greve et al. (2004) have shown from CO emission of radio-detected submillimeter galaxies with known redshifts, in the range $1 < z < 3.5$, that such objects could be the result of merging of *gaseous* substructures. In fact they present a total mean molecular gas mass of about $\langle M(H_2) \rangle = (3.0 \pm 1.6) \cdot 10^{10} M_\odot$ within ~ 2 kpc. This is approximately 4 times greater than the most luminous local ultraluminous infrared galaxy but comparable with radio galaxies and QSO. The measured star formation is very high $\geq 700 M_\odot\, \mathrm{yr}^{-1}$. Exploiting the FIR-CO correlation the estimated median dynamical mass is $\langle M_{\mathrm{dyn}} \rangle \sim 10^{11} M_\odot$ within 4 kpc.

The rest-frame near-IR luminosity is a good tracer of the galaxy stellar mass, in particular the K-band (2.2 μm; see also Chapter 4). K-band surveys allow to select galaxies according to their mass up to $z \sim 1.5$ ($\lambda_{\mathrm{rest}} \sim 0.9 \mu$m). At higher redshift, the K-band starts to sample the rest-frame optical and UV regions and space-based observations at $\lambda_{\mathrm{obs}} > 2 \mu$m are needed to cover the rest-frame near-infrared (e.g. *SIRTIF*). Several surveys in this band have been carried out in these years (*ELAIS*, *GOODS*, etc...see Cimatti 2004 for a review).

The results are the following.

- Overall the K20 and other recent near-IR surveys show that galaxies are characterized by little evolution to $z \sim 1$ (see Fig. 3.16), so that the observed properties can be mimicked by a rather constant number density evolution, which is in contrast with the ΛCDM scenario (see below).

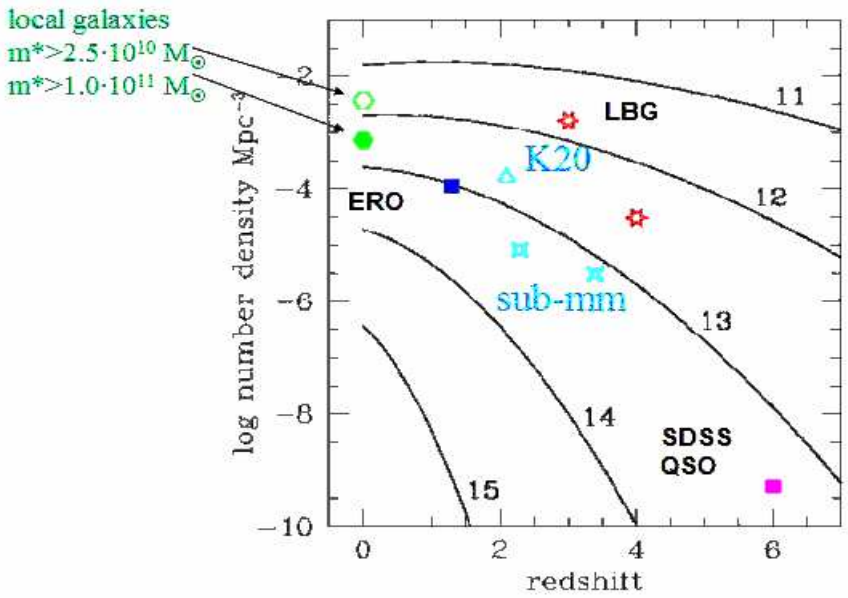

Figure 3.15: Curves show the cumulative number density of DM halos more massive than $10^{11}, 10^{12}, 10^{13}, 10^{14}, 10^{15} M_{\odot}$ from top to bottom as labeled. Points show comoving number densities of several observed populations as labeled. (Figure adapted from Somerville 2004).

- the median redshift in the K20 survey for $N(z)$ is $z_{\rm med} \sim 0.8$ and a high-z tail extended beyond $z \sim 2$. Current hierarchical models do not match the observed redshift distribution (see Fig. 3.20).

- the morphology of old EROs with $K_s < 20$ at $z \sim 1$ (morphology, spectra, luminosities, ages, stellar masses, clustering) imply the existence of a substantial population of old (a few Gyr), passively evolving and fully assembled massive spheroids which requires that major episodes of massive galaxy formation occured at least at $z_{\rm form} \sim 2$. Their number density at $z \sim 1$ is consistent with that of local E/S0 galaxies (see Fig. 3.15).

- A numerous population of star-forming, "dusty" ERO, with disk-like and irregular morphologies emerges at $0.7 < z < 1.7$. These objects are often too faint to be detected in submm surveys due to their inferred far-IR luminosities $< 10^{12} L_{\odot}$.

- "Old" ERO seem to have much stronger clustering than "dusty" ERO, with a comoving r_0 similar to that of present-day luminous ellipticals.

The preceding discussion highlights the importance of understanding the star formation history of different type of galaxies. From UV background constraints, corrected for dust obscuration, it is possible to infer a global, average, Star Formation Rate (SFR; see e.g. Madau et al. 1996). It can be seen that the SFR rises by 1-2 orders of magnitude from redshift $z = 0$ to $z \sim 1.5$ and then stays almost flat (see Chapter 5, Fig. 5.13). Such a behavior, as it will be discussed in Chapters 5 and 6, is similar to the SMBH accretion history, supporting the view of a co-evolution between galaxies and SMBH at all redshifts, as local data on spheroidal galaxies seem to be supporting (Chapter 2). The amount of stars (as discussed in Chapter 8) obtained from direct integration of the SFR is comparable to the local one inferred from the galaxy LF, but still about 1/10 of the density of baryons measured from WMAP and Nucleosynthesis data, an observational evidence which strengthens the *"missing baryon"* problem, already outlined in Fig. 3.18.

3.4.2 The co-evolution model for SuperMassive Black Holes and their Host galaxies

Overview of Galaxy Formation Models

From what we have discussed in the previous sections baryons are thought to fall into the DM potential wells after recombination. However the evolution of baryons in the non-linear phase and after is still not clear.

There are mainly three scenarios for galaxy formation (see Combes 2005 for a basic review).

- *Monolithic collapse.* This idea was initially suggested by Eggen, Lynden-Bell & Sandage (1962). In a halo clouds of cold gas collapse quickly at the center in a relatively short burst ($\leq$ Gyr) of star formation stopped by the Supernova (SN) feedback. A possible disk can then be formed afterwards out of gas falling radially onto the central clump (bulge) of already formed stars. On this basis Eggen et al. (1962) suggested that the old stars in the Mily Way, with low metallicity ([Fe/H]) and low orbital eccentricity e, were probably formed out of gas fallen towards the center in

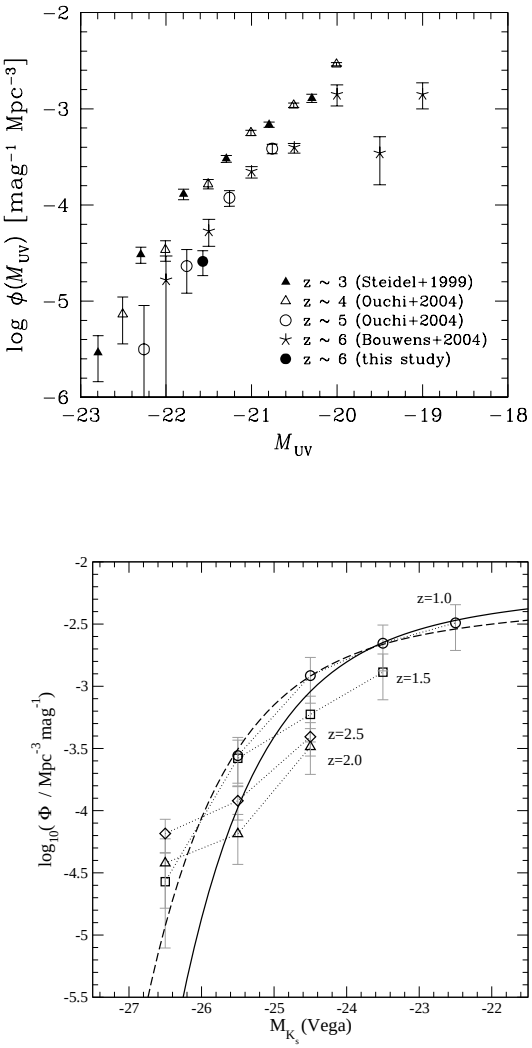

Figure 3.16: Top panel: Far-UV LF of LBG at various redshifts from different groups as labeled. (Figure taken from Shimasaku et al. 2005). Bottom panel: Rest-frame K_s-band LF at various redshifts as indicated. The solid line corresponds to the local K-band LF measured on 2MASS by Kochanek et al. (2001) while the dashed line shows the evolution of the LF at $z = 1$ as estimated by Drory et al. (2003). (Figure taken from Caputi et al. 2005)

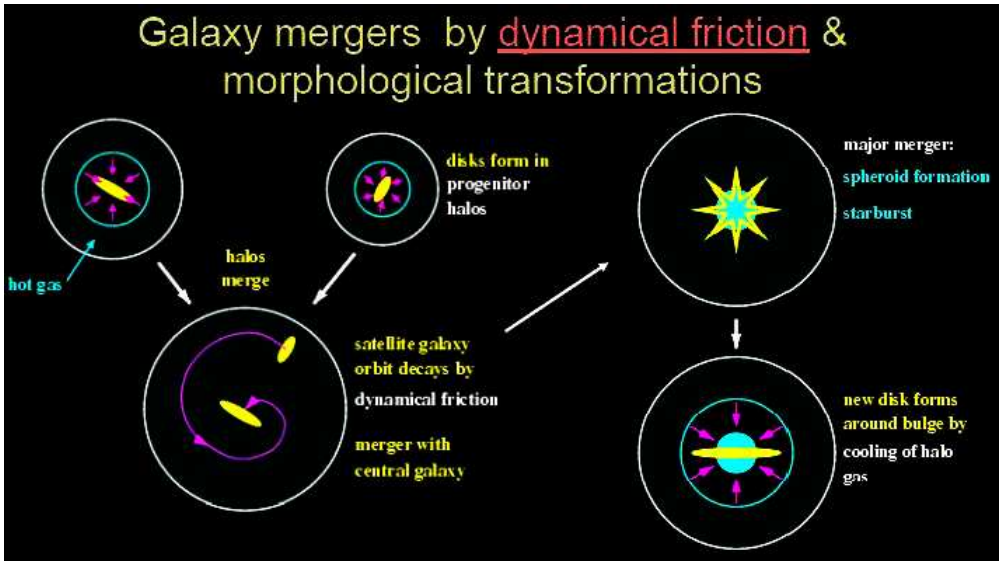

Figure 3.17: Sketch of the Hierarchical scenario: merging of two spirals and formation of a bulge and disk.

radial orbits. In this model the gravitational potential varies slowly and e and angular momentum L are invariants. This second phase of disk formation can have a long star formation phase (of various Gyr).

- *Hierarchical scenario.* A galaxy is formed as the result of the hierarchical assembly of DM building blocks. Gas accumulates within the extended dark halos, dissipates its kinetic energy and settles into the equatorial plane as soon as centrifugal equilibrium is being reached, forming fast rotating disks that subsequently turn into stars. In the merger of two halos their stellar disks, embedded in the extended remnant halo, lose energy and angular momentum due to dynamical friction, sink at the center and finally merge (see Fig. 3.17). Ellipticals in this view are the result of the major merger of two high-redshift stellar disks (Toomre & Toomre 1972). Due to violent relaxation through strong tidal interactions, in this event the stellar systems are destroyed leading to kinematically hot spheroidal stellar remnants (as checked in numerical simulations, e.g. Hernquist 1992). A new disk can finally be formed in the equatorial plane of the stellar remnant due to gas accretion.

- *Secular Evolution.* The bulge component is formed slowly from the disk through the bar action, and the disk can be replenished through continuous external gas accretion. The system is "open", with slow mass growth through time, from external accretion of gas progressively transformed into stars. In the latest disks, the exponential stellar profile, instead of the typical $R^{1/4}$ profile of spheroids, could be a result of secular evolution of a stellar bar.

All these processes must have been at work in building galaxies, probably at different epochs and in different manners as it will be discussed below. For what morphology concern, there have been various attempts in the literature to consider how the two main types, disks and spheroids, could have formed. Among all we will just remind two basic ideas for the origin of such a dichotomy. Susa & Umemura (2000) claim that the dichotomy arises as a consequence of the degree of self-shielding of pregalactic clouds against a UV-background. At high redshift/masses the high rate of cooling makes efficient star-formation and the pregalactic clouds dissipate into a central spheroid. Later the build-up of a UV-background makes a retarded star-formation which prefentially leads to a disk. Dekel & Birnboim (2004) instead address the galactic bimodality to a threshold mass below which disks are built by cold streams regulated by stellar feedback which cause prolonged starformation episodes. Above that mass the cold streams penetrate through hot media and favor massive starbursts.

Up to now Numerical and SAM modeling of galaxy evolution has attempted to evolve baryons in the same manner as DM halos evolve, usually following a standard scheme of disk formation in a halo, merging between halos and their stellar disk cores, and subsequent formation of spheroids (basically the *Hierarchical model*). However several problems have arisen through this approach. A direct way to show this is reported in Fig. 3.18 which compares the local mass/galaxy luminosity function with the DM halo mass function. Fig. 3.18 by Somerville & Primack (1999) clearly highlights the fact that the simple hierarchical formation structures is not enough to account for the population of galaxies: extra-physics needs to be taken into account for galaxy modeling, even if some limitations due to the still poor resolution of Numerical simulations for studying baryonic physics does play a significant role (e.g. Governato et al. 1996).

The most striking difficulties which a CDM model faces in reproducing the prop-

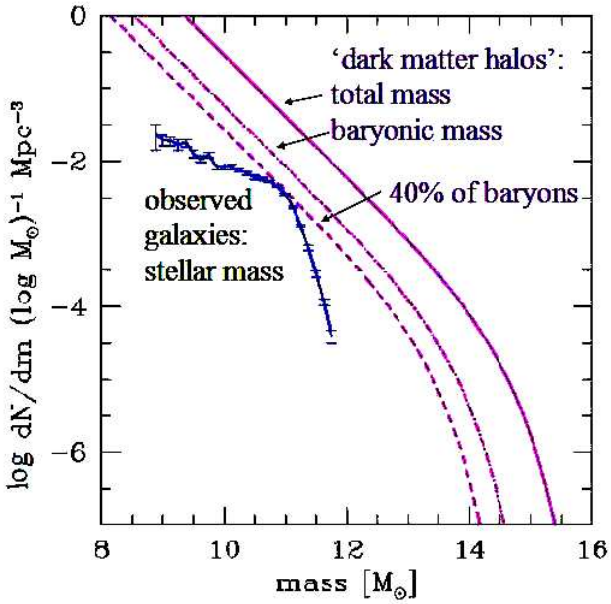

Figure 3.18: Solid line: mass function of DM halos at $z = 0$ predicted by the P&S theory; dotted line: P&S mass function rescaled in masses by the cosmological value of 0.16; dashed line: P&S mass function rescaled by the cosmological factor plus a factor equal to 0.4. The blue line with error bars shows the local mass function of galaxies. (Figure from Somerville 2004).

erties of galaxies are the following.

- There has been substantial mass loss: the baryons locked up in galaxies are just about1/10 of the total $\sim 4\%$ measured by WMAP;

- Numerical simulations have shown that the proto-galaxy which forms inside a DM halo is smaller than observed (e.g. Navarro & White 1993). Gas cools too quickly ('overcooling' problem, e.g. see e.g. Maller & Dekel 2002) turning completely into stars at the present epoch.

- Too concentrated substructures are observed in N-body simulations as compared to the visible substructure in the local group. This is the reason why, for example, the Tully-Fischer relation for disks, $L \propto V_c^{\alpha}$, with $\alpha \sim 3 \div 4$, is well reproduced by numerical simulations in slope but not in the zero-point (see e.g. Mo & Mao 2004).

- The number of faint galactic objects are much less than the number of low-mass halos.

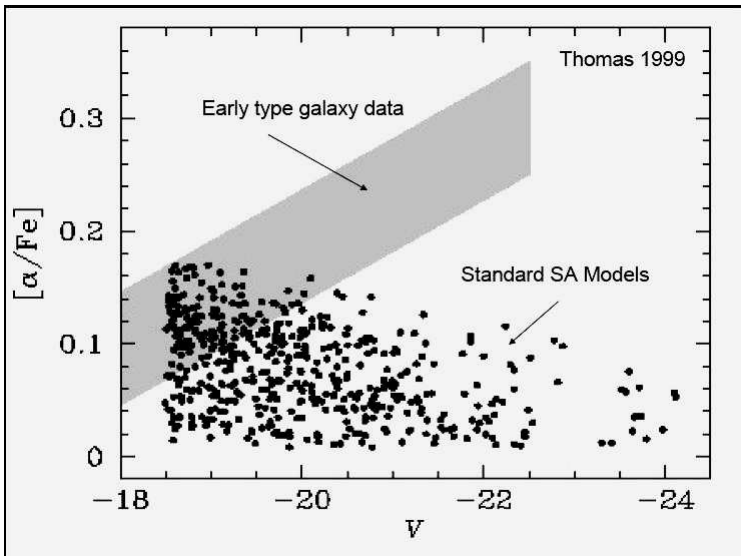

Figure 3.19: α-enhancement in Early-type galaxies compared with hierarchical predictions. (Figure adapted from Thomas 1999).

- The baryonic mass function has an exponential fall-off instead DM halos have a power-law distribution up to $\sim 10^{14} M_{\odot}$.

- The number of high redshift galaxies predicted by hierarchical theories are much less than the ones actually observed (see Fig. 3.20).

- It could be that the merging galaxies contain SMBH. It is not easy for the binary (or multiple) SMBH to shrink and merge. Moreover, in the limit that no gas accretion from the ongoing surrounding star formation is at work, there must be a very stringent fine-tuning at work which forces the merging end-product SMBH to be tightly linked with the stellar bulge of the resulting spheroid (see Chapter 1).

- The fast metal enrichment of high-redshift galaxies and QSO and the radial and mass metal gradients found in early-type galaxies.

- The short visible timescales for AGN activity at high redhsift. QSO, according to merging models (e.g. Wyithe & Loeb 2003), are activated during galaxy mergers on

time-scales proportional to the dynamical time, i.e. $\tau_{\rm vis} \leq$ a few 10^6 yr, much shorter, for $z \geq 3$, than the e-folding time for SMBH growth (see Chapters 5 and 6)

However some progress in hierarchical models has been carried out in the last years, which improves the match with the data, but relying on "ad-hoc" prescriptions. For example in Fig. 3.21 we report the result by Baugh et al. (2004) in which the authors are able to reproduce the high-redshift number counts of submm sources and LBG in a ΛCDM cosmology assuming a top-heavy IMF for the stars formed in bursts. However such a prescription could cause the formation of too many massive stars which would finally end up in BH or Supernova (SN). Thus such a prescription could indeed not produce enough stars to account for the local galaxy LF. Menci et al. (2004) instead propose to increase the formation of stars at high redshift through the implementation of galaxy-interactions, added to halo-merging, which can increase star formation in the galaxy perturbing the host potential well (see Fig. 3.20 and below).

The Antihierarchical Baryon Collapse Model

Here we present the details of the galaxy formation scenario followed in this thesis.

First of all our treatment of DM merging relies on the use of the S&T rates given in Eq. (3.52). As discussed in the previous sections the S&T mass function provides a better fit to numerical simulations at all scales relevant for galaxy formation up to very high redshift. The EPS theory falls short in reproducing numerical simulations redshifts above 3 (see Fig. 3.4). For $z \geq 1.5$, most of the mass function time variation, at all masses in the range $\sim 10^{12} \leq M_{\rm vir}/M_{\odot} \leq 10^{13.2}$, is controlled by the positive term in the time derivative, being the negative one negligible (see Fig. 3.6 and Fig. 3.5). Therefore in our model we have considered that merging rate, i.e. *the rate of production of virialized halos*, is controlled by the $\dot{n}^{+}_{S\&T}$, within a factor of 2 of precision (see discussion in Section 3.3.5). In any virialized halo we consider the formation of a single galaxy, a spheroid. Further evolution involving the host DM halo will not affect the inner baryonic region (as discussed in Section 3.3.6, see Fig. 3.10). As described in our development of the merging tree of a

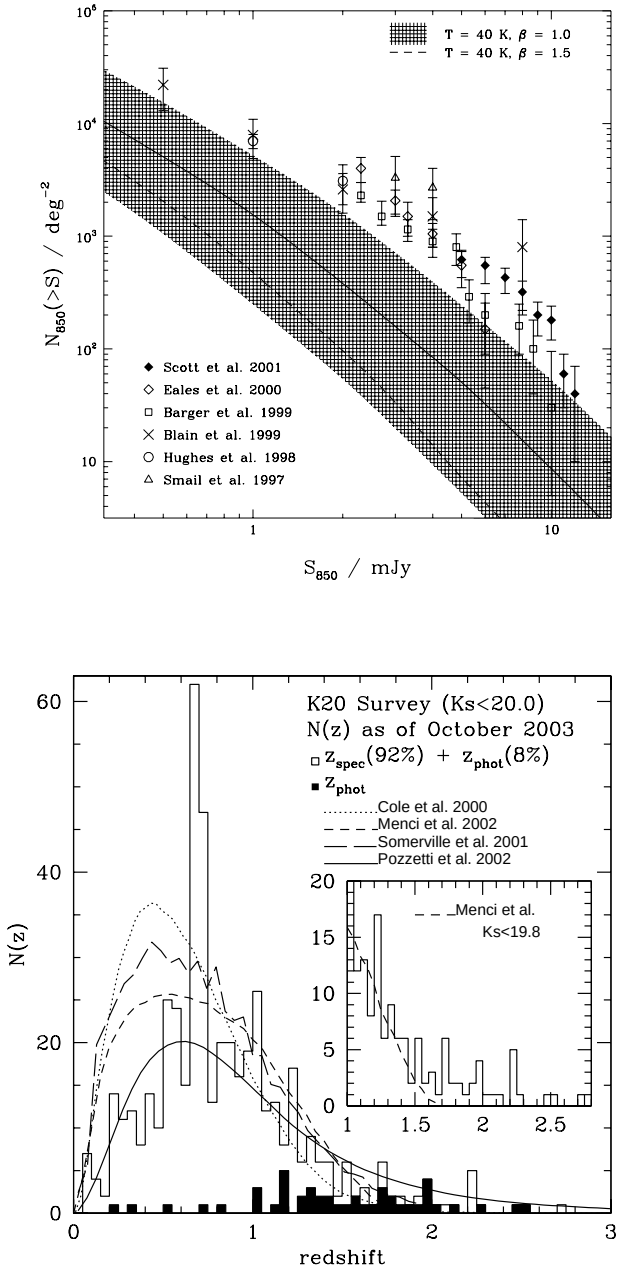

Figure 3.20: Top panel: Integral number counts at $\lambda = 850\mu$m data compared with hierarchical models predictions using a hot SED for the starburst. (Figure taken from Kaviani et al. 2004). Bottom panel: The K20 survey $N(z)$ ($K_s < 20$) compared with predictions of several hierarchical models. (Figure taken from Cimatti 2004).

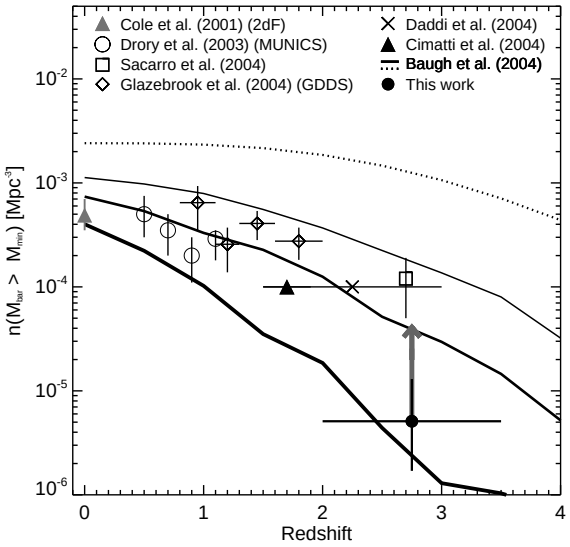

Figure 3.21: Data points: comoving number density of galaxies with visible masses $\sim 6 \cdot 10^{10} M_{\odot}$ as derived from CO observations of Submm Galaxies (from several groups as labeled). Solid line: predictions from the Baugh et al. (2005) model. Dotted curve: total baryonic matter content available in $\geq 10^{11} M_{\odot}$ DM halos, obtained scaling the abundance of dark halos by 0.16. (Figure taken from Combes 2005).

$10^{13}\, M_{\odot}$ halo (see Fig. 3.9), and confirmed in numerical simulations of Zhao et al. (2003b), the evolution of the host DM halo is fast at the beginning, while a successive rather smooth accretion occurs, which increases the mass up to a factor of $2 \div 3$ and deposits mass mostly in the outer region (see also Fig. 3.11).

At any redshift $z \geq 1.5$ for any halo which virializes, we assume the following evolutionary scheme (see Mo & Mao 2004).

- The first step is the DM host halo virialization. The formation of a potential well is established through a fast-accretion phase (Zhao et al. 2003b; see Section 3.3.4) of DM clumps (i.e. a *major merger*) after which the halo reaches dynamical equilibrium with a circular velocity equal to $V_{\rm vir}$ (see Fig. 3.10).

- The baryons (mostly in the form of H and He) in the infall will develop shocks and stabilize in hydrostatic equilibrium, at the halo virial temperature (White & Rees 1978). In these first stages the baryons are expected to be on average distributed almost like the DM component (which we suppose to follow Eq. (3.34)). However

baryons are expected to locally condense in cold clouds, *clumps*, due to the high power on small perturbation scales, and to the fact that the cooling time is very short at high redshift. Maller & Bullock (2004) claim that several galaxy properties could be accounted for if baryons are condensed in pressure-supported clouds during infall.

- The baryon clouds will then spiral in the parent halo, just as shown in Fig. 3.17, with the only difference being that these clouds are mostly still in the gaseous form, instead of being stellar disks. Such gas clouds in fact, even during the infall, do not condense much stars: Kennicut 1998 in fact has shown that the efficiency of star formation is just a few percent in a spiral typical rotation time which is comparable, at high redshift, with the cloud dynamical collapse time.

- During infall the dissipation through cloud-cloud collision is negligible, as shown by simulations (e.g. Barnes 1992), but becomes important only when such clouds have sunk to the center of the halo. Moreover energy and angular momentum loss could occur through dynamical friction. Due to the progressive steepness of the host halo density profile and the mass dimension relative to the host, most of the energy is lost in the inner regions, at $R \sim 0.1 R_{\rm vir}$: here (Eq. 3.66) the loss of energy is comparable to the DM binding energy.

- The loss of orbital energy of dense clouds increases the kinetic energy of the DM in the inner region which expands (thereby reducing the halo concentration), possibly removing the initial inner cusp in the density profile and leaving a core, i.e. the region becomes baryon-dominated (Borriello et 2003 and see Chapter 7). Indeed El-Zant et al. (2004) find in numerical simulations that the infalling massive clumps spiral towards the central region and, being progressively disrupted, they tend to lose energy causing a sensible flattening of the NFW cusp.

- The baryons which have collapsed will then "take the place" of the inner DM particles, with their same orbital energy. We will check in Chapter 7 that in fact baryons collapsed, today locked up in stars, have a binding energy per unit mass comparable to that of DM.

- Once in the halo center the baryons will start feeding a strong starburst. Such a picture is very well consistent with what is observed in SCUBA and Starburst galaxies, in which the strong star formation episode is confined in a limited region of a few kpc (Greve et al. 2005) and lasts for less than a Gyr.

- The starburst may drive a large amount of gas out of the halo, leaving just a small fraction of the initial baryons locked up in present-day galaxies. Baryons will also be removed from the host halo during the infall due to stripping and ongoing star formation.

- A disk can later be formed in the equatorial plane of the already present stellar spheroid due to gas successive infall/cooling of the previously heated gas (e.g. "fountain effect").

Let's now discuss the baryons evolution in a more quantitative way. Initially the baryons reach a temperature of the order of the halo virial temperature

$$kT_{\rm vir} = \frac{1}{2}\mu m_p V_{\rm vir}^2 \tag{3.62}$$

with m_p the proton mass and μm_p the mean molecular weight.

The baryonic infall timescale is given by the dynamical time

$$t_{\rm dyn}(r) = \left[\frac{3\pi}{32G\rho(r)}\right]^{1/2}. \tag{3.63}$$

For a spherical top-hat fluctuation (see Section 3.3.1) the dynamical time is comparable to $t_{\rm coll}/2$, the time a spherical fluctuation takes to collapse after turnaround. The clouds, displaced all over the halo with a NFW profile density, will spiral in and *could* lose energy in favor of the background DM. The dynamical friction timescale, expressed in units of the number and mass of clouds, is

$$t_{\rm dynfr} \sim 0.3 t_{\rm coll} f(\epsilon) \frac{M_{\rm vir}}{M} \frac{1}{\ln \frac{M_{\rm vir}}{M}} \tag{3.64}$$

being M the mass of a given cloud and $f(\epsilon) \sim \epsilon^{0.78} \sim 0.5$ (Lacey & Cole 1993), the dependence on orbit eccentricity. Eq. (3.64) highlights the fact that the clouds in the mass range $(2 \div 20) \cdot M_{\rm vir}$ have $t_{\rm dynfr} \sim t_{\rm coll}/2 \sim t_{\rm dyn}$, therefore they will be not much affected

by dynamical friction during their spiralling down the halo, especially the smaller ones, but these clouds will lose energy just in the final stages of their infall when they are close to the center of the halo.

Assuming that the energy loss of the gas cloud at radius r is deposited in a spherical shell with radius r it can be written (Mo & Mao 2004)

$$\varepsilon \propto \frac{\dot{E}}{4\pi r^2 \rho(r)} \frac{dt}{dr} \propto \frac{M}{r} G(r) = \frac{M}{r} \frac{\rho(\bar{<} r)}{\rho(r)} \left(1 + \frac{d \ln V_c(r)}{d \ln r}\right), \tag{3.65}$$

with $\rho(\bar{<} r)$ the mean density of DM within radius r and $V_c(r) = [GM_{vir}(< r)/r]^{1/2}$. The energy gain per unit mass by the DM at radius r is therefore

$$\varepsilon \sim \varepsilon_{\rm orb} \frac{M}{M_{\rm vir}} \frac{r_s}{r}, \tag{3.66}$$

with $\varepsilon_{\rm orb}$ the orbital energy per unit mass.

Such an estimate is in line with the so-called *"Dynamical Attractor-Hypothesis"* (Loeb & Peebles 2003 and Gao et al. 2004). Supposing the clouds to be on average of order 1/10 of the halo mass, the baryons which fall in the inner regions of $0.1 r_{\rm s}$, according to Eq. (3.66), will start releasing energy, and such gravitational energy loss will be sufficient to let the DM present in that region to expand. The clouds will then *replace* the DM particles keeping the same binding energy. The system will finally act as a *collisionless mixture of stars and DM* (Gao et al. 2004).

In the absence of a such an effect, the usual *adiabatic contraction* (in which the product of length and velocity scales is conserved; Blumenthal et al. 1986) would tend to make the central mass density run even steeper than the original DM profile model, leading to problems. As outlined in Loeb & Peebles (2003), setting $\eta = M_{\rm star}/M_{\rm vir}$, in the adiabatic approximation the addition of stellar mass in a region that contains DM will produce an increase of the inner mass and velocity $M_f = (1+\eta)M_i$, $\sigma_f = (1+\eta)\sigma_i$ and a proportional decrease in radius $R_f = R_i/(1+\eta)$. Such results are in contradiction with data: as it will be shown in Chapter 7, the adiabatic model produces too small effective radii and too large dispersion velocities to fit the spheroidal galaxies fundamental plane and local dispersion velocity function.

Now we will describe the different physical processes taken into account in the

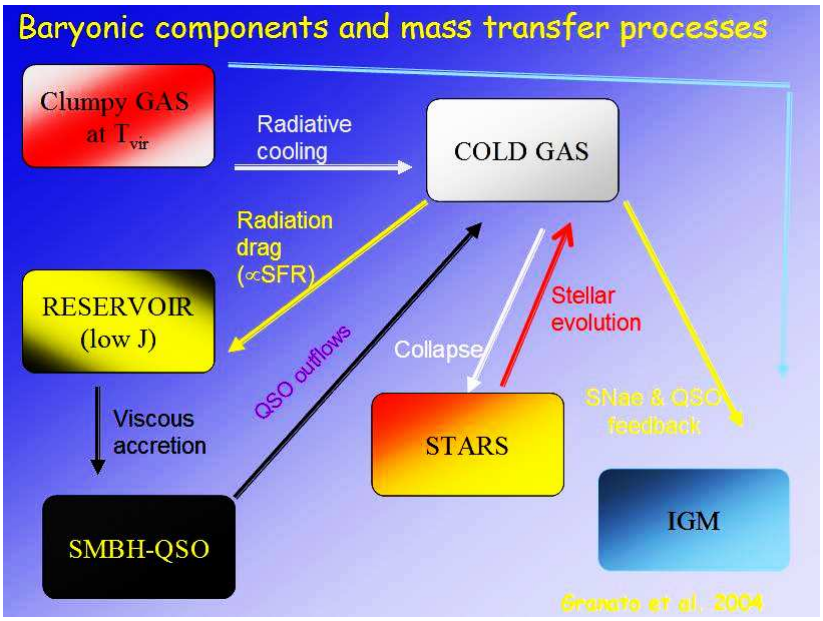

Figure 3.22: Scheme of the baryonic components included in the model (*boxes*) and of the corresponding mass transfer processes (*arrows*). (Figure adapted from Granato et al. (2004).

model developed by Granato et al. (2004), which govern the evolution of a spheroidal galaxy (see Fig. 3.22 for a scheme and Appendix A for a basic summary of the model).

At the moment of virialization it is assumed that $M_{\rm inf}(t_{\rm vir}) = f_b M_{\rm vir}$ with $f_b = 0.16$, the universal ratio of baryons to DM. The *diffuse gas* in the outer regions, with mass $M_{\rm inf}(t)$, will infall on a timescale given by the maximum between the dynamical time Eq. (3.63) (which is a lower limit as it neglects angular momentum) and the cooling time. In fact the necessary condition for a gas cloud to cool is that its cooling time is less than the dynamical time but even if the gas can cool, it will not fragment until it has accumulated in a region small enough for its local density to dominate that of the background halo. The infalling gas, initially at the equilibrium temperature in the DM potential well, is therefore transferred to the cool star-forming phase at a rate

$$\dot{M}_{\rm cold}(t) = \frac{M_{\rm inf(t)}}{\max[t_{\rm cool(r_{vir})}, t_{\rm dyn}(r_{\rm vir})]} \tag{3.67}$$

There are various important processes by which gas can cool in halos (see Silk &

Bouwens 2001 for a review).

- *Compton Cooling*: low-energy photons passing through a gas of non-relativistic electrons scatter the electrons slowing them down in the direction of motion.

- *free-free emission (Bremsstrahlung)*: it is dominant for high temperatures ($10^6 - 10^7 K$) (e.g. primordial gases, intracluster medium, etc...) when matter is almost entirely ionized. The dominant cooling mechanism is due to the acceleration of electrons off the bare H^+ and He^{2+} nuclei.

- *Recombination and collisional ionization*: these processes are dominant at much lower temperatures ($10^4 - 10^5$ K).

Summing up the previous physical processes it is possible to express the cooling time as

$$\begin{aligned} t_{\rm cool}(r) &= \frac{3}{2}\frac{\rho_{\rm gas}(r)}{\mu m_p}\frac{kT}{Cn_e^2(r)\Lambda(T)} \\ &\simeq \frac{10^6}{C_8}\left(\frac{n_e}{1\,cm^{-3}}\right)^{-1}\left[\left(\frac{T}{10^6{\rm K}}\right)^{-1/2} + 1.5\left(\frac{T}{10^6{\rm K}}\right)^{-3/2}\right]^{-1} {\rm yr}\,, \end{aligned} \tag{3.68}$$

where the last equality holds for a H-He plasma with primordial abundances (Padmanabhan 2003). $\Lambda(T)$ is the cooling function computed by Sutherland & Dopita (1993), followed in this thesis, which takes into account also the dependence on metal abundance, $C = \left\langle n_e^2(r)\right\rangle / \left\langle n_e(r)\right\rangle^2$ is the clumping factor and μ is the mean molecular weight. The increase of the cooling time in Eq. (3.68) due to the dilution of the hot gas as the cold gas drops out should be taken into account. However this effect is minimum as the cold phase is always less than 50% and can therefore be ignored.

Following Padmanabhan (2003) we can compare the dynamical and cooling times as

$$R = \frac{t_{\rm cool}}{t_{\rm dyn}} \approx \frac{M_{\rm baryons}}{9\cdot 10^{11} M_\odot} \simeq \frac{R}{80\,{\rm kpc}}\,. \tag{3.69}$$

Eq. (3.69) shows that galaxies have a "cooling cut-off": it is not physically plausible to form galaxies with mass higher than $10^{12} M_\odot$ (compare with Fig. 3.18) and with dimensions greater than 80 kpc.

The time derivative of the cold, star forming gas is given by

$$\dot{M}_{\rm cold}(t) = \frac{M_{\rm inf}(t)}{t_c} - \psi(t) + R\,\psi(t) - \alpha\,\psi(t)\ , \tag{3.70}$$

where $\psi(t) \equiv \dot{M}_{\rm star}$ is the Star Formation Rate (SFR), R is the fraction of mass returned by evolved stars ($R \approx 0.3$ for Salpeter IMF) and α is the effective efficiency for the removal of cold gas by the stellar feedback. In Granato et al. SAM it is assumed that the cold gas distribution still follows the DM distribution,

$$\psi(t) = \int_0^{r_{\rm vir}} \frac{1}{\max[t_{\rm cool}(r), t_{\rm dyn}(r)]} \frac{dM_{\rm cold}(r,t)}{dr} dr\,. \tag{3.71}$$

The quantity α is

$$\alpha = \frac{N_{SN}\,\epsilon_{SN}\,E_{SN}}{E_B}\ , \tag{3.72}$$

N_{SN} being the number of SNe per unit mass of condensed stars, $\epsilon_{SN}\,E_{SN}$ is the energy per SN used to remove cold gas, and E_B is the binding energy per unit gas mass within the DM halo. We can now highlight the dependence of the SN feedback on halo mass and virialization redshift. Following Zhao et al. (2003b) and Mo & Mao (2004), the latter quantity can be written as

$$E_B = \frac{1}{2}\,V_{\rm vir}^2\,f(c)\,(1 + f_{\rm cosm})\ , \tag{3.73}$$

where $f(c) \approx 1$ is a weak function of the concentration c and $f_{\rm cosm} \sim 0.16 - 0.18$ is the universal ratio of baryonic-to-dark matter mass in a halo (see also Chapter 8). By properly including the dependence of $V_{\rm vir}$ on the halo mass and redshift, we get

$$E_B \approx 2.7 \times 10^{14} \left(\frac{1+z}{4}\right)^{0.86} \left(\frac{M_{\rm vir}}{10^{12}\,M_\odot}\right)^{2/3} {\rm cm}^2\,{\rm s}^{-2}\ . \tag{3.74}$$

The effective efficiency is then well approximated by

$$\alpha \approx 1.0 \left(\frac{\epsilon_{SN}}{0.1}\right) \left(\frac{N_{SN}}{8 \times 10^{-3}}\right) \left(\frac{1+z}{4}\right)^{-0.86} \left(\frac{M_{\rm vir}}{10^{12}\ M_\odot}\right)^{-2/3}\ , \tag{3.75}$$

where we set $E_{SN} = 10^{51}$ ergs. Eq. (3.72) highlights the intuitive behavior for which SN feedback is more powerful in less deep halo potential wells.

As expressed in Eq.(3.70) the numerical code by Granato et al. (2004) the feedback due to SN explosions, as also be taken into account. At any time since virialization in the halo, a mass fraction of the cold phase is removed as

$$\dot{M}_{\rm cold}^{SN} \sim -\psi(t)\epsilon_{\rm SN}\frac{N_{\rm SN}E_{SN}}{V_{\rm vir}^2}\frac{M_{\rm cold}}{M_{\rm gas}}\,. \tag{3.76}$$

We have also checked that SN feedback on the infalling gas,

$$\dot{M}_{\rm inf}^{SN} \sim -\psi(t)\epsilon_{\rm SN}\frac{N_{\rm SN}E_{SN}}{V_{\rm vir}^2}\frac{M_{\rm inf}}{M_{\rm gas}}\,, \tag{3.77}$$

must be negligible. Such kind of feedback in fact halts star formation too early in less massive halos producing too few stars. Moreover it significantly diminishes the iron abundance in less massive spheroids, canceling out the α-enhancement (see discussion after Eq. (3.102)).

It is interesting to stress, following by Granato et al. (2004), that in the whole the SFR has an inverse dependence on the host halo mass, yielding a natural anti-hierarchical growth of spheroids, i.e. an Anti-hierarchical Baryon Collapse (ABC) trend. Such an anti-hierarchy is on average to be intended as *statistical*: at high redshifts, the numerical fraction of more massive spheroids with respect to the number at $z = 0$, is higher than that of lower mass galaxies. This behavior is compatible with what observed in the galaxy luminosity function itself, see Fig. 3.16 (lower panel), where most of the massive systems are already in place by $z \sim 1.5$. Such an evolutionary mode is also a direct consequence of the fact that at higher redshifts most of the deepest (with higher virial velocity) DM potential wells are already established being the Universe denser (see Chapter 7, Fig. 7.1).

The cooling time dependence on virialization redshift and halo mass is, for a pure hydrogen plasma (see Granato et al. 2004),

$$t_{\rm cool} \simeq 1.6\cdot 10^{11}(1+z_{\rm vir})^{-5/2}h^{1/3}\left(\frac{M_{\rm vir}}{10.^{12}M_\odot}\right)^{1/3}\left(\frac{M_{\rm vir}/M_{\rm gas}}{1/0.16}\right)^{1/2}C^{-1}\,{\rm yr}\,. \tag{3.78}$$

As discussed by Romano et al. (2002) and as it will be further discussed in Chapter 8, the halo-to-star mass ratio is inversely proportional to the stellar or halo mass, $M_{\rm vir}/M_{\rm star} \propto M_{\rm star}^{-\zeta}$, with $\zeta \geq 0.3$. Such a behavior is usually ascribed to SN feedback that (see also Eq. (3.75)) is progressively more efficient in shallower potential wells. Therefore, being the star mass proportional to the gas mass, the cooling time will be very weakly dependent on halo mass ($\propto M_{\rm vir}^{1/12}$).

Moreover since the mean density within the virial radius is $\simeq (100 \div 200)\,\rho_{\rm crit}$, the mean value of $t_{\rm dyn}$ is about a factor of 10 shorter than the expansion timescale at all redshifts, independently of halo mass. Therefore, following Eq. (3.71), the SFR will be $\psi \propto M_{\rm vir}^{3/2}$, pointing to the fact that more massive halos, with deeper potential wells, will create more stars and faster.

We can also get an analytical estimate of the total amount of energy injected by the SN in a DM halo since virialization. To do this we need a rough estimate of the total amount of stars formed in the halo. With the assumption that the star formation occurs on a timescale $t_{\rm star}$, we get

$$\psi(t) = \frac{M_{\rm cold}(t)}{t_{\rm star}} \; ; \tag{3.79}$$

the equation for the mass $M_{\rm star}$ cycled through stars can be easily solved to yield

$$M_{\rm star}(t) = \frac{M_{\rm inf}(0)}{\gamma}\left[1 - \frac{s\gamma}{s\gamma - 1}\,\exp(-t/t_c) + \frac{1}{s\gamma - 1}\,\exp(-s\gamma t/t_c)\right] \; , \tag{3.80}$$

where $\gamma = 1 - R + \alpha$ and $t_c = \max[t_{\rm cool}(r_{\rm vir}), t_{\rm dyn}(r_{\rm vir})]$. In the above formula $s = t_c/t_{\rm star} \gg 1$, since we expect that in more central and knotty regions the cooling and dynamical times are shorter than t_c, which is estimated at the virial radius. The total starburst timescale in Granato et al. model is set by the AGN feedback (see below and Chapter 6, Fig. 6.5).

The mass in stars at present time obtainable from Eq. (3.80) only includes the fraction $f_{\rm surv}$ of stars survived until now $M_{\rm star}^{\rm now} = f_{\rm surv}\, M_{\rm star}(t_{\rm now})$. The survived fraction depends on the IMF and on the history of star formation. As a reference, for a Salpeter IMF after about 10 Gyr from a burst, we have $f_{\rm surv} \approx 0.6$. If we assume that most of the stellar feedback derives from SN explosions, then the total energy injected into the gas is given by

$$E_{\rm star} = \epsilon_{SN}\, E_{SN}\, N_{SN}\, M_{\rm star} \approx 8 \times 10^{58} \left(\frac{\epsilon_{SN}}{0.1}\right) \left(\frac{N_{SN}}{8 \times 10^{-3}}\right) \frac{M_{\rm star}}{10^{11}\, M_\odot}\,{\rm erg} \; . \tag{3.81}$$

During the first stage a large amount of dust is produced by SN. According to Nozawa et al. (2003) each SN can produce an amount of dust of about $0.5\,M_\odot$, depending on progenitor metallicity and mass. In a kpc scale (see Murray et al. 2005) an optical depth for dust $\tau_{\rm dust}$ of order unity can be reached with about 10^6 SN that can be generated within 10^8 yr for a SN rate of 10^{-2}/yr. For the large star formation rates of about $100-1000 M_\odot$/yr,

typical of SCUBA galaxies at $z > 2$ (e.g. Aretxaga et al. 2003) $\tau_{\rm dust} \sim 1$ would be reached in just 10^6 yr or even less (*SCUBA phase*).

Dwek (2004) has discussed that the dust produced by SN, essentially composed of silicates, are substantially less opaque, by an order of magnitude, than the carbon dust produced by Asymptotic Giant Branch (AGB) stars. The AGB dust production however is delayed by a few 10^8 yr with respect to the SN one. Dwek has calculated that for a luminous IR galaxy to become opaque through carbon dust it takes about $5 \cdot 10^7$ yr (which is however still much shorter than the average timescale of the starburst in our model, about 5×10^8 yr, see Fig. 6.5). For this reason we could expect that before complete obscuration of the galaxy, a *pre-SCUBA phase* could occur (very short indeed!), during which, being the SMBH still small, the spheroid may appear as an optically bright, non-active proto-galaxy. However a constraint on the time-length of a possible pre-SCUBA phase is given by the AGN luminosity functions (see Chapter 6). In this thesis we have assumed however that there is enough dust mass from SN to obscure in a relatively short time, the entire galaxy.

In Granato et al. (2004) the SED of the galaxy is computed by the code GRASIL (Silva et al. 1998) which computes the time-dependent ultraviolet to radio galaxy SED, given their star formation (Eq. (3.71)) and chemical enrichment (Eq. (3.102)). It has been included (see also Silva et al. 2005) a differential extinction of stellar populations (younger stellar generations are more affected by dust obscuration), because of the fact that stars form in a denser than average environment, the molecular clouds (MC), and progressively get rid of them. GRASIL takes into account the size of MC, the MC optical depth, the escape timescale of newly born stars from MC, and the different distribution of the various dust components. In Chapter 6 we will provide the fit to the SCUBA and K-band counts with their dependence on redshift and we will highlight their connection with the high-redshift AGN population.

As discussed above observational data point to a tight relation between the spheroid and its central SMBH. Moreover these two systems seem to grow proportionally during time as observed in the global SFR (see Chapter 5, Fig. 5.13). One mechanism which can create a tight link between the SFR and the SMBH growth is provided by the *radiation drag* (Kawakatu & Umemura 2002). This mechanism will create a low angular momentum gas

reservoir which will settle around a seed SMBH, left over by a possible high redshift POPIII population and/or from primordial black holes (see Chapter 1, Section 2.3). This seed will eventually grow into a SMBH powering a kinetic wind which will remove most of the dust and gas in the galaxy quenching star formation (*QSO phase*).

After the QSO shining the galaxy will proceed with an almost passive evolution towards redder colors (*ERO phase*). The intermediate- and low-mass systems, with virial masses around $10^{12} M_{\odot}$ instead will show up as LBG, with much less star formation, $\leq 100 M_{\odot} \mathrm{yr}^{-1}$, peaking at $z \sim 2-3$, in full agreement with Fig. 3.15.

Kawakatu, Umemura & Mori (2003) have demonstrated that in the central regions of protogalaxies the drag due to stellar radiation may result in a loss of angular momentum of the gas at a rate that in a clumpy medium is well approximated by

$$\frac{d \ln J}{dt} \simeq \frac{L_{\mathrm{sph}}}{c^2 M_{\mathrm{gas}}} (1 - e^{-\tau}) \tag{3.82}$$

where L_{sph} is the global luminosity and τ is the effective optical depth of the spheroid which can be expresses as $\tau = \bar{\tau} N_{int}$, where $\bar{\tau}$ is the average optical depth of single clouds and N_{int} is the average number of clouds intersected by a light ray over a typical galactic path. To get an idea of the physical basis of radiation drag one can think of the simple process of matter-photon interaction. A mass m_0 traveling at the speed v_0 in the laboratory frame, after photon absorption, will decrease its speed to v, given, through the conservation laws, by $mv = m_0 v_0$, with $m > m_0$ as $m = m_0 + h\nu/c^2$. The photon re-emission will be anisotropic and boosted towards the direction of motion. Therefore after re-emission the mass will be reduced again to the initial value $m_0 c^2 = mc^2 - h\nu$ but the final momentum has definitely reduced to $mv = m_0 v_{\mathrm{fin}} + h\nu v/c^2$. Being $mv = m_0 v_0$, we have $v_{\mathrm{fin}} = v_0 - h\nu v/c^2 m_0$ i.e. $v_{\mathrm{fin}} < v_0$. From the last equation it is evident that radiation drag will be more effective when more mass is present and/or the stellar radiation is more energetic. Moreover differentiating one gets $dv/dt = -(h\nu v)/(m_0\, c^2) \Rightarrow v(t) = v_0(exp(-h\nu t)/(m_0\, c^2))$ from which one can estimate the average drag timescale.

The gas can then flow toward the center, feeding a mass reservoir around the SMBH at a rate

$$\dot{M}_{\mathrm{inflow}} \simeq -M_{gas} \frac{d \ln J}{dt} \simeq \left(\frac{L_{\mathrm{sph}}}{c^2} \right) (1 - e^{-\tau})\, M_{\odot} \mathrm{yr}^{-1}\,. \tag{3.83}$$

During the early evolutionary stages the luminosity is dominated by massive main-sequence stars, $M \geq 5M_{\odot}$ and is thus proportional to the SFR $\psi(t)$. We then have

$$\dot{M}_{\rm inflow} \propto 10^{-3}\psi(t)(1-e^{-\tau})\, M_{\odot}{\rm yr}^{-1}\,, \tag{3.84}$$

where the proportionality constant actually depends on the implemented IMF but in the code is left as a free parameter (see Appendix A).

Firstly material accumulates in a circumnuclear mass reservoir. As discussed in Chapter 2, the existence of a mass reservoir, possibly in a toroidal structure which can obscure the active source along the line of sight, has now been empirically proved. The material then flows towards the SMBH on a timescale depending on the viscous drag.The reservoir will accumulate at the net rate

$$\dot{M}_{\rm res} = \dot{M}_{\rm inflow} - \dot{M}_{\bullet} - \dot{M}_{\rm feedback}\,, \tag{3.85}$$

where we also allow SMBH feedback to remove some of the reservoir mass. However it has to be noted that such an effect is a minor one: the AGN feedback onto the reservoir is weighted as $\dot{M}_{\rm feedback} \propto L_h M_{\rm res}/M_{\rm gas}$, and therefore, being $M_{\rm res} << M_{\rm gas}$, it is orders of magnitudes less intense than the feedback on the other gas components (see Eq. (3.99) and Eq. (3.98)).

The actual accretion onto the central SMBH is given by

$$\dot{M}_{\bullet} = \min[\lambda\dot{M}_{\rm Edd}\,, \dot{M}_{\rm visc}]\,, \tag{3.86}$$

where we allow for some super-Eddington accretion up to a factor $\lambda \sim$ a few (see Chapter 6 for more details). Following Duschl et al. (2000) and Burkert & Silk (2001), the viscosity reads as $\nu = Re^{-1}\nu_r$, where $Re_{\rm crit} = 100-1000$ is the critical Reynolds number for the onset of turbulence (see Chapter 1). With these assumptions the viscous time can be expressed as $\tau_{\rm visc} = \tau_{\bullet}^{\rm dyn} Re_{\rm crit}$, where $\tau_{\bullet}^{\rm dyn}$ is the dynamical time referred to the system "SMBH plus reservoir", $\tau_{\bullet}^{\rm dyn} = (3\pi/32G\rho_s)^{1/2}$ which is usually much shorter than all the other relevant timescales taken into account. Therefore the SMBH growth is mostly limited to the Eddington accretion. As most of the mass in the reservoir is ultimately accreted onto the central BH, then we expect at the end of the accretion phase

$$M_{\bullet} \approx 10^{-3}\, M_{\rm star}\,(1-e^{-\tau})\ . \tag{3.87}$$

From Eq. (3.87) we predict that the ratio $M_\bullet/M_{\rm star}$ could present a downturn at small halo/spheroid masses. In Granato et al. (2004) it has been assumed that the effective optical depth depends on the cold gas metallicity and mass $\tau \propto Z\, M_{\rm gas}^{1/3}$ (see also Appendix A). The outcomes of the numerical code yield on the average $Z \propto M_{\rm vir}^{0.3}$ in the mass range $10^{11} \leq M_{\rm vir} \leq 3 \times 10^{13}\ M_\odot$. Since $M_{\rm gas} \sim f_{\rm cosm}\, M_{\rm vir}$, one then gets

$$\tau \propto M_{\rm vir}^{2/3}\ . \tag{3.88}$$

As already anticipated the Granato et al. SAM modeling includes AGN Feedback which has major effects on galactic evolution. Recent *XMM-Newton* observations of bright QSO (Pounds et al. 2003) give strong evidence for intense outflows from the nucleus, with mass rates $\dot{M}_{\rm out} \sim 1\, M_\odot\, {\rm yr}^{-1}$ and velocity $v \sim 0.1c$ in the form of blue-shifted X-ray absorbtion lines. As it will be shown in Chapter 5 almost all galaxies must have undergone an active phase in their past and probably the most massive SMBH must have "tilted" the observed local correlations (see Chapters 2, 7 and 8) among spheroid, SMBH and DM halo. AGN feedback must have also modulated, together with cooling, the exponential cut-off of the local galaxy luminosity/mass function (see Chapter 7). As discussed by Benson et al. (2003), the absence of *superwinds* would create too many "monster galaxies". However, as the authors recognize, the total energy budget required to obtain a good match to the galaxy luminosity function greatly exceeds the energy available from SN explosions (see Chapter 8). It has also been shown that the large energy injection from SMBH plays crucial roles in the thermal outflow and dynamical blowout of baryons from group of galaxies, causing the steepening of the $L_X - T$ relation at small temperatures, and may also play some role in preheating scenarios for larger structures, in Clusters (see e.g. Lapi et al. 2003). The efficiency of the kinetic energy feedback also depends on the structure and nature of the medium in which it is deposited.

Sazonov et al. (2004) have claimed that the AGN radiative heating can effectively perturb the ISM and in particular the runaway heating due to the QSO can heat and evaporate large part of the cold phase. The "hot phase" equilibrium temperature is close to the temperature at which Compton cooling balances inverse Compton cooling, $T_{IC} \sim 10^{6\div7}$ K.

The timescales for the gas to become "hot" could be however long and radiation pressure, in general, will have minor dynamical effects, and therefore it could be difficult to understand how most of the baryons are actually removed from the DM halo. Models of UV resonance-line acceleration for O-star winds have rather been adopted to explain the fast ($v \rightarrow 0.1c$) outflows in BAL QSO. In fact electron scattering has a cross section of $< \sigma/H > \sim 7 \times 10^{-25} x\,\mathrm{cm}^2$ per hydrogen atom (with x the ionized fraction) while the effective cross section through scattering in UV resonance lines (Begelman 2004) is about *seven* orders of magnitude larger, therefore the impact on galaxy environment is much faster and stronger with this kind of feedback.

Lamers & Cassinelli (1999) have developed a theory for stellar winds which has been applied to AGN by Murray et al (1995). Following Murray et al. (1995) the approximate solution for the wind velocity produced by line acceleration as a function of the radius is

$$v = v_\infty \left(1 - \frac{r_f}{r}\right)^{2.35} , \tag{3.89}$$

where r_f is the radius at which the wind is launched. The asymptotic speed is

$$v_\infty \sim \left(\gamma \frac{GM_\bullet}{r_f}\right)^{1/2} . \tag{3.90}$$

Setting $\gamma \simeq 3.5$ and using the Eddington limit one gets (see Granato et al. 2004)

$$\frac{v_\infty}{c} \sim 6.2 \cdot 10^{-2} \left(\frac{r_f}{10^{16}\,\mathrm{cm}}\right)^{-1/2} L_{\mathrm{Edd},46}^{1/2} . \tag{3.91}$$

The asymptotic speed is reached at $r \geq 40 r_f$, setting f_c as the covering factor and assuming that the system is surrounded by a Hydrogen column density N_H, from mass conservation, one derives $\dot{M}_{\mathrm{wind}} = 4\pi r^2 \rho(r) v_r \sim 4\pi f_c m_H N_H 40 r_f v_\infty$ and finally

$$L_K = \frac{1}{2}\dot{M}_{\mathrm{wind}} v_\infty^2 \simeq 3.6 \times 10^{44}\, f_c N_{22} L_{\mathrm{Edd},46}^{3/2} \mathrm{erg\,s}^{-1} . \tag{3.92}$$

The speed of a shock or sound wave propagating through a medium with a "cloudy" phase structure will be highest in the phase with the lowest density. The wind or hot bubble emanating from the central AGN will tend to follow the "path of least resistance". To parameterize such effects we set $L_h = f_h \cdot L_K$, by denoting with f_h the actual fraction of the kinetic energy transferred to the diffuse gas in the galactic halos. Since studies of Broad

Absorption Line (BAL) QSO suggest $N_{22} \geq 30$ and $f_c \geq 0.1$ (see e.g. Chartas et al. 2002; Chartas, Brandt & Gallagher 2003) and $f_h \geq 0.3$ (see e.g. Inoue & Sasaki 2001; Nath & Roychowdhury 2002), their product can be assumed $f_h\, f_c\, N_{22} \approx 1$.

The wind from the central SMBH will sweep up the surrounding gas into a shell, bounded by an inner shock in which the wind velocity is thermalized and an outer shock in which the surrounding gas is heated and compressed by the wind. These two regions are separated by a contact discontinuity. The shell velocity depends on whether the shocked wind gas is able to cool (*"momentum-driven"* flow) or not (*"energy driven"* flow).

Compton cooling must have been very effective in the very first stages. Fabian (1999) has discussed that this type of momentum-driven feedback, in the initial galaxy evolution phase, when it is enshrouded by dust, could regulate the self-feeding of the high-z SMBH at the center of obscured protogalaxies. In particular the outward force resulting from an AGN wind acting on a column of matter at a radius r of total mass $N_H 4\pi r^2 m_p$, is $L_{\rm wind} = 2v^4 f v_m/G$, being f a geometrical factor.

The dynamics of the wind in this regime will be dominated by momentum conservation and the shell's equation of motion will then be $d[M(R)\dot{R}]/dR = 4\pi R^2 \rho v^2 = \dot{M}_{out} v = L_{Edd}/c$, which integrated twice gives $R^2 = G L_{Edd} t^2/2 f_g \sigma^2 c$, neglecting integration constants for large t (King 2003). In the snowplow phase the shell will then move with constant velocity $v_m = R/t \propto M_\bullet$. Therefore the SMBH mass reads as

$$M_\bullet = \frac{\Omega_b \kappa}{\Omega_m 2\pi G^2}\sigma^4 \simeq 1.5 \times 10^8 \left(\frac{\sigma}{200 {\rm kms}^{-1}}\right)^4 M_\odot\,. \tag{3.93}$$

However King (2003) reports that the Compton cooling time is of the order of $t_{\rm Compton} \simeq 10^5 R^2_{\rm kpc}(c/v)^2 b M_8^{-1}$ yr and that the energy-driven feedback will be dominating just after a time $t_{\rm flow} \sim R/v_s \sim 8 \cdot 10^6 R_{\rm kpc}\sigma_{200} M_8^{-1/2}$ yr, where v_s is the shell velocity. It is straightforward to check that $t_{\rm flow} \sim 10^7$ yr at the most if, in the initial stages, $R_{\rm kpc} \sim r_f$ and the SMBH seed is about $10^2 - 10^3 M_\odot$. Therefore very soon the energy-driven condition for the evolution of the wind will be dominant (the momentum-conserving AGN feedback could still play some, minor, role in the last evolutionary stages when radiative cooling becomes effective; Begelman & Nath 2005). Same conclusions have been reached by Wyithe & Loeb (2003) who claim that in the first stages of the proto-galaxy evolution cooling is always

much longer than the typical AGN timescales ($10^7 - 10^8$ yr). These authors moreover from an analysis of several local data (Wyithe & Loeb 2005) argue that the energy conserving regime is probably the most suitable physical treatment for AGN feedback.

The energy-driven limit feedback constrains the final SMBH mass. The simplest way to show this is to impose that the host halo gravitational attraction balances the AGN energetic output. The accretion onto the central SMBH will then be limited by (following Silk & Rees 1998)

$$f_{\rm wind} L_h t_{\rm wind} \leq \frac{G M_{\rm vir} m_{\rm bar}}{R_{\rm vir}}, \tag{3.94}$$

which implies that the SMBH mass is limited

$$M_\bullet \leq \frac{2.5 \cdot 10^5}{f_{\rm wind}} \left(\frac{\sigma}{200\,{\rm km s^{-1}}} \right)^5 M_\odot \,, \tag{3.95}$$

where $f_{\rm wind} \sim v/2c \sim 5 \times 10^{-2}$, $t_{\rm wind} \sim R/\sigma \sim 10^8$ yr and $m_{\rm bar} \sim 0.16 M_{\rm vir}$. A straightforward way to estimate the possible efficiency of AGN activity on the surrounding medium is given by the particle-photon energy ratio (Lapi et al. 2003)

$$f_{wind} = \frac{E_p}{E_\gamma} = \frac{p_p}{2 m_p} \frac{1}{p_\gamma c} = \frac{p_p}{2 m_p c} = \frac{m_p v}{2 m_p c} = \frac{v}{2c} \sim 0.05 \,. \tag{3.96}$$

where the last equality derives from the observational data on BAL QSO (for which $v \sim 0.1c$).

The feedback relation expressed in Eq. (3.95) however produces too small SMBH masses with respect to local estimates (see e.g. Fig. 2.1, right panel) if the activity time scale related to the *final* SMBH mass is $t_{\rm wind} \geq 10^8$ yr. Eq. (3.95) however produces the right SMBH masses to fit the $M_\bullet - \sigma$ relation if the time associated with the final growth of the SMBH is one order of magnitude less (see Chapters 5 and 6). In the Granato et al. model $t_{\rm wind}$ is the time when the energy injected by the AGN in the Inter-Stellar Medium (ISM) equals the binding energy of the gas

$$\int_0^{t_{\rm wind}} f_{\rm wind} L_h dt = M_{\rm gas} V_{\rm vir}^2 \,. \tag{3.97}$$

The timescale $t_{\rm wind}$ is about the time the protogalaxy spends in the SCUBA phase in Granato et al. model: in fact the spheroid is obscured for nearly the whole time before the peak of AGN activity, until when the central SMBH becomes sufficiently massive to remove

most of the gas/dust and let the AGN shine as a luminous dust-free QSO (see Chapter 6, Fig. 6.5). We will discuss in this thesis that the time needed for the SMBH to unbind the gas and dust in the galaxy and finally halt star formation, is of the order of the last e-folding time of its exponential growth (see also discussion after Eq. (3.99)).

The physical model sketched in Eq. (3.97) is also in line with recent detections. In fact this model predicts that the AGN in the SCUBA phase is optically invisible but still detectable in less absorbed wavelengths, such as in Hard X-rays. Alexander et al. (2005) have shown that in the deep SCUBA survey at $z \geq 1$ and fluxes $f_{850\,\mu m} \geq 4$mJy, combined with ultra-deep X-ray observations with *Chandra*, the majority ($\approx 70\%$) of the submm sources host substantial AGN activity ($L_X \sim 10^{42} \div 10^{44.5}\mathrm{erg\,s^{-1}}$) and are on average heavily obscured ($N_H \geq 10^{23}\mathrm{cm^{-2}}$). It is found that intense star-formation activity (of order $\sim 1000 M_\odot\,\mathrm{yr}^{-1}$) however dominates the bolometric output of these sources. Such findings reveal also the actual presence of a *delay* (Monaco et al. 2000; Granato et al. 2001) between the virialization of the host DM halo and the shining of the QSO during which the SMBH significantly increases its mass, at variance with previous models (e.g. Wyithe & Lobe 2003 and Chapter 6).

Moreover Borys et al. (2005) analyzed deep X-ray, optical and mid-infrared *Spitzer* observations of the *Chandra Deep Field North and South* and *GOODS* of a submillimeter galaxy sample with a median redshift of $z = 2.2$. They find a power-law correlation between the estimated stellar and nuclear X-ray luminosity, implying that SMBH masses are correlated to their host stellar masses. The median stellar mass they measured is about $10^{11} M_\odot$. From the estimated X-ray luminosity, under the assumption of Eddington limited accretion, the SMBH masses appear to be 1-2 orders of magnitude smaller than in local galaxies of same stellar mass. Such empirical findings are in agreement with Eq. (3.97), see Chapter 6 (Fig. 6.5). Granato et al. predict in fact that, during the initial proto-galactic evolutionary stages, the SFR is already significantly high, while the SMBH is still growing from a small seed. Therefore the SMBH-to-stellar mass ratio is predicted to be much smaller than the final one, at the peak of the AGN activity.

Similarly to SN, in the Granato et al. (2004) code the AGN feedback at each

timestep removes mass from the cold to the hot gas phase

$$\dot{M}_{\rm cold}^{QSO} \sim -\frac{L_h}{V_{\rm vir}^2}\frac{M_{\rm cold}}{M_{\rm gas}} \tag{3.98}$$

and from the infalling gas (following the energy conserving recipe of Eq. (3.97)

$$\dot{M}_{\rm inf}^{QSO} \sim -\frac{L_h}{V_{\rm vir}^2}\frac{M_{\rm inf}}{M_{\rm gas}}\,. \tag{3.99}$$

If we assume that the BH mass is growing at around the Eddington rate, most of the kinetic energy in winds is then emitted when the SMBH reaches its maximum mass, i.e. $E_K \approx (2/3)\, t_{ef}\, L_K$. The action of the AGN therefore occurs on very short timescales, the e-folding timescale t_{ef} (see Chapter 5, Eq. (5.17)). Then, using Eq. (5.17), AGN activity transfers to the gas a total energy amount

$$E_{AGN} = f_h\, E_K \approx 3.6\times 10^{60}\, f_h\, f_c N_{22}\, \left(\frac{\epsilon}{1-\epsilon}\right)\left(\frac{t_E}{4\times 10^8\,{\rm yr}}\right)\left(\frac{M_{BH}}{10^8\ M_\odot}\right)^{1.5}\ {\rm ergs}\ . \tag{3.100}$$

Note that the energy is *super*-linear with SMBH mass, i.e. more AGN energy is generated in more massive systems, which naturally explains the exponential cut-off in the galaxy luminosity function (see also Chapter 8).

This overall energy input discharged into the ISM can be easily compared to the total energy gained from accretion $E_{\rm acc} = 1.8\times 10^{62}\,(\epsilon/1-\epsilon)\,(M_{BH}/10^8\,M_\odot)$ ergs, to obtain

$$E_{AGN} \approx 2\times 10^{-2}\, E_{\rm acc}\, \left(\frac{M_{BH}}{10^8\,M_\odot}\right)^{0.5}\ . \tag{3.101}$$

Here we indicate with ϵ the radiative efficiency.

At each time step in the numerical code Granato et al. (2004), following Romano et al. (2002), also estimate the amount of metals produced in the galaxy. The fundamental equation of the chemical evolution is given by

$$\frac{dG_i(t)}{dt} = -X_i(t)\psi(t) + R_i(t) + \left(\frac{dG_i}{dt}\right)_{\rm inf} - \left(\frac{dG_i}{dt}\right)_{\rm reh}\ . \tag{3.102}$$

$G_i(t) = X_i(t) M_{\rm cold}(t)$ is the cold gas mass in the form of the element i. The quantity $X_i(t)$ represents the abundance by mass of the element i. $R_i(t)$ represents all the rates at which SNI and SNII as well as single low- and intermediate-mass stars restore their processed and unprocessed material to the ISM. The infalling term in Eq. (3.102) is the primordial

chemical composition of the infalling gas while the reheating term gives the amount of cold gas which is heated and subtracted to further stellar processing.

In the Granato et al. model the α-enhancement in early-type galaxies (see Fig. 3.19) is a natural consequence of the more rapid spheroid formation in more massive systems. Being the SFR proportional to the host virial mass, the spheroid and the central SMBH grow faster, and therefore the AGN shines earlier halting the SFR earlier and preventing the SNIa to enrich the ISM with Fe.

To end this section we point out that the adopted IMF in the code is the following

$$\begin{aligned} \Phi(M) &\propto M^{-0.4} \text{ for } M \leq 1\, M_{\odot} \\ &\propto M^{-1.25} \text{ for } 1\, M_{\odot} < M \leq 100\, M_{\odot}\,. \end{aligned} \tag{3.103}$$

The choice of the IMF could slightly alter some predictions on the final chemical abundances, however the basic results are invariant. Especially the predictions on the galaxy luminosity function (Chapter 7) is not modified by the choice of the IMF, while the amount of the total stars produced could be altered by at most 30% (see also Chapter 8).

3.4.3 The SMBH fueling problem: low-redshift SMBH evolution

It is believed that the angular momentum in DM halos is generated by the tidal torque associated with the growth of density fluctuations in the linear regime. In the Zel'dovich approximation for which the motion of particles is studied through Lagrangian coordinates $r(q,t) = a(t)x(q,t)$, the angular momentum of the material which makes up a protogalaxy is written as

$$J = \bar{\rho} a^5 \int_{V_L} (x - x_G) \times v d^3 q\,. \tag{3.104}$$

Expanding Eq. 3.104 up to the first order and then converting from an integration in the volume to an integration on the surface we get

$$J = -\bar{\rho} a^5 \dot{D}(z) \int_{\Sigma_L} \phi(L)(q)(q - q_G) \times dS\,. \tag{3.105}$$

Hence J vanishes to first order if Σ_L is spherical or is an equipotential of ϕ. In practice the angular momentum gain can occur due to non-symmetry. Moreover in linear theory J increases with time proportionally to the growth factor $D(z)$.

At the end of the linear stage the final angular momentum of a Dark Matter halo can be quantitatively defined with the dimensionless spin parameter

$$\lambda_J = \frac{J|E|^{1/2}}{GM^{5/2}} \tag{3.106}$$

where E and M are the total energy and mass. For random Gaussian fields this expression has been evaluated integrating from the linear stage to the non-linear one (e.g. Bullock et al. 2001). It is found that the average value is $\lambda_J \sim 0.05$, and recently it has been shown (e.g. D'Onghia & Bullock 2001) that systems which have not undergone any major merger since $z = 3$ have spin parameters about a factor of 2 lower on average. The value of λ_J is almost independent of the initial density fluctuation and is roughly equivalent to v_ϕ/σ, the ratio between the azimuthal velocity and the dispersion velocity of the system. N-body simulations have shown that the λ_J-distribution of virialized halos turned out to be well described by a log-normal.

Assuming that the baryonic gas system in the collapsed DM halo will retain its specific angular momentum, the exponential disk scale lenght R_d can be determined, adopting a flat rotation curve with velocity v_c, as $j_d = 2R_d v_c = \sqrt{2}\lambda_J V_{\rm vir} R_{\rm vir}$. For this magnitude of the angular momentum, the *centrifugal barrier* which a baryonic particle matter must overcome to settle in the center of the protogalaxy is

$$R_{\rm barr} = \frac{j_{\rm max}(z)}{GM_b} \approx 2 \left(\frac{M_b}{10^8 M_\odot}\right)^{1/3} \left(\frac{1+z}{5}\right)^{-1} \left(\frac{\lambda_J}{0.05}\right)^2 \left(\frac{\Omega_b}{0.05}\right)^{-4/3} h_{70}^{2/3}\,{\rm kpc}\,. \tag{3.107}$$

Compared $R_{\rm barr}$ with the Schwarzschild radius R_g, the ratio is given by

$$\frac{R_{\rm barr}}{R_g} \approx 10^8 \left(\frac{1+z}{5}\right)^{-1)} \left(\frac{\lambda_J}{0.05}\right)^2 \left(\frac{\Omega_b}{0.05}\right)^{-4/3} h_{70}^{2/3}\,. \tag{3.108}$$

Therefore from this kind of reasoning it is clear that it is not easy to make a galactic system lose its angular momentum letting mass accrete in the central regions and especially in the very central SMBH. Strong, large scale mechanisms must be invoked to destabilize the potential field of the baryonic system.

As shown in the previous section, radiation drag could be very efficient in driving the first stages of SMBH evolution during the massive early formation of the spheroids at high redshifts. Other dynamical fueling processes however could be effective at lower redshift, in groups of galaxies or disk systems.

In the non-linear stage protogalaxies have formed as separate systems and have moved away from each other. The interaction among galaxies will create torques which can in principle destabilize the central potential of the host galaxy and induce star formation and probably also accretion onto the central SMBH.

The relative loss of angular momentum $\Delta J/J$ of the gas in the host galaxy due to an instability, for example an interaction with a companion galaxy (but equivalently the same order-of-magnitude effect could be obtained through a bar instability), can be simply calculated as follows. Consider a galaxy with a SMBH at its center. If $M(< r)$ is the mass within r around which an annulus of gas mass m of the same radius r orbits, the energy potential distortion due to a "fly-by" of a nearby galaxy at a distance R, with velocity V and impact parameter b is $\delta E_p \simeq m\mu G\,[1/(R-r) - 1/(R+r)] \simeq 2m\mu Gr/R^2$. The torque will then be

$$T = \frac{\partial E_p}{\partial \phi} \approx \frac{\delta E_p}{\delta \phi} = \frac{2m\mu Gr}{\pi R^2} \tag{3.109}$$

with $\delta\phi = \pi$ and $R^2 = b^2 + (Vt)^2$.

Therefore the angular momentum variation of the gaseous annulus will be

$$\Delta j = \int_{-\infty}^{\infty} T\,dt \sim 2\,\frac{\mu Grm}{Vb}\,. \tag{3.110}$$

Simulations have shown that $\Delta j/j$ could be about 30% or more (e.g. Barnes & Hernquist 1998). Such accretion episodes could be considered as minor accretion events for the SMBH, as probably they are not determinant for its main mass growth. Such processes could just induce some *re-activation* of the dormant central engine usually at sub-Eddington regimes. The duration of the activity in this case is set by the fly-by timescale which is of the order of the host galaxy dynamical time $\tau \sim 2R_g/V \simeq 10^{-1}$Gyr.

Triaxial perturbations of the central potential efficiently transport gas inwards (e.g. Shlosman et al. 1990). Bars of gas and of stars form at various radii within a given AGN host galaxy ("bars within bars"), with each bar playing a distinct role in the funneling of gas towards the central regions. If the potential is non-spherical the accretion in the central region, and most probably onto the SMBH, increases by an order of magnitude. As discussed recently by Wyse (2004) the physical condition necessary for the onset of bar-instability in disks can be set as a pure surface density criterion. Such a value is indeed

very close to the surface density critical value found by the SDSS team (Kauffman et al. 2003) to divide galaxies into bulge-dominated, AGN-bright and disks dominated galaxies. A simple criterion for a disk to be unstable is that its maximum rotational velocity v_M is less than the circular velocity GM/R, or equivalently that the (Mo et al. 1998) disk to halo mass ratio m_d is larger than the disk spin momentum parameter λ_J; in terms of surface density this can be rewritten as (Wyse 2004) $\mu \geq \mu_0 \propto v_m^4/G^2 M_d \sim 10^8 M_\odot/\mathrm{kpc}^2$. Such a relation naturally leads to the Tully-Fischer relation in spirals.

Any perturbation in the potential promotes turbulence in the galactic structure and possibly fueling in the central parts (the so-called "starburst-AGN connection"). Wada & Norman (2002) have computed numerical simulations of a gas and stellar disk evolving in a fixed DM halo potential well. In particular they clearly show that gravitational/thermal instabilities and SN exploding uniformly in the structure could make the ISM highly turbulent and inhomogeneous causing the formation of a torus in the inner 30 pc in a few dynamical times. The scale height of the torus will be proportional to the $(SFR/M_\bullet)^{1/2}$ and an average accretion rate of 0.3 $M_\odot/yr$ will feed the central SMBH.

In Chapter 6 we will present a possible scheme for SMBH evolution at low redshifts ($z \leq 1.5$) driven by re-activations induced by de-stabilizations of the host potential well. We will show that this mechanism induces a progressive depletion of the cold gas available for accretion onto the central SMBH naturally accounting for both the strong AGN LF negative luminosity evolution and the very rapid drop of the Eddington limit (see Chapter 1).

Another proposed mechanism for SMBH fueling is direct capture of solar-type stars which is possible if the angular momentum of the stars is smaller than some critical value (Frank & Rees 1976). This value is given by $J_{cap} \leq lGM_\bullet/c$, where $l = 4$ for a Schwarzschild black hole, and for a Kerr one $l > 4$ for an incoming particle retrograde to the spin of the hole, and < 4 for a direct particle. For SMBH smaller than $10^8 M_\odot$ solar-type stars with angular momentum smaller than $\sqrt{2GM_\bullet r_{disr}}$ will be tidally disrupted before they reach the horizon at a radius $r_{disr} = (M_\bullet/M_{disr})^{-2/3} R_g$, the "loss cone" of stars with sufficiently small angular momentum is larger than that for direct capture. Consider a SMBH (Zhao et al. 2002) embedded in an isothermal stellar cusp ($\rho \propto r^{-2}$). For an isotropic Gaussian

velocity distribution a fraction

$$f_{cap}(r) = \left(\frac{J_{cap}}{2\sigma_{star} r}\right)^2 = \frac{2R_g r_\bullet}{r^2} = 4\frac{\sigma_{star}^2}{c^2}\left(\frac{r_\bullet}{r}\right)^2 \tag{3.111}$$

of the stars at radius r has sufficiently low angular momentum and will be captured within a dynamical time ($r_\bullet = GM_\bullet/c^2$ is the radius of the SMBH sphere of influence). For a singular isothermal cusp we can now write the rate at which the "loss cone" of stars with low angular momentum is depleted given a mass accretion rate of stars captured from radius r. Outside $r_\bullet$ this stars accretion is given by

$$\dot{M}_{cap}(r) = 4\pi\rho(r) r^2 \sigma_{star} f_{cap} = 8\,\frac{\sigma_{star}^5}{Gc^2}\left(\frac{r_\bullet}{r}\right)^2 \tag{3.112}$$

which once integrated in time yields

$$M_\bullet \approx 10^8 \left(\frac{\sigma_{star}}{200\mathrm{kms}^{-1}}\right)^5 \left(\frac{t_0}{14\,\mathrm{Gyr}}\right) . \tag{3.113}$$

Such a process presents some weak points. It does reproduce the observed $M_\bullet - \sigma$ relation, but in the hypothesis that the "loss cone" stays full and for a very long time which contrasts with the presence of very massive SMBH at high z. In fact dynamical relaxation makes stars wander in angular momentum space and fill the loss cone on a timescale $t_{fill} \sim f_{cap} t_{relax}$, where $t_{relax} = (N_{star}/8 \ln N_{star}) t_{dyn}(r_\bullet) \sim 10(\sigma_{star}/150\,\mathrm{kms}^{-1})^{6.6}\,\mathrm{Gyr}$.

A very interesting improvement in these kind of models was carried out by Miralda-Escude & Kollmeier (2005). They claim that stars after repeated crossing are finally captured by the thin accretion disk, with a higher cross section than the central SMBH itself, and this can shorten the time required for the SMBH to grow. In this way the disk will be continuously replenished with matter from plunging stars. This scenario can also partly answer to the problem of matter transportation to the central regions. However such a model predicts that much of the initial stellar mass in the central region could be depleted soon. Therefore for producing massive SMBH a significant amount of the relic SMBH mass must be added through gas accretion.

Chapter 4

SMBH Demography

In this Chapter the local SMBH Mass Function (MF), including the contribution from the spheroidal components of late-type galaxies, is estimated exploiting and extending the technique outlined by Salucci et al. (1999) and later presented by Shankar et al. (2003). In Section 4.1 we critically discuss the relationships, presented in Chapter 2, among luminosity, mass, and velocity dispersion of the spheroidal components of galaxies ($L_{\rm sph}$, $M_{\rm sph}$, and σ), and $M_\bullet$. In Section 4.2 we present and discuss two estimates of the local SMBH MF, derived via the velocity dispersion distribution function (VDF) and the LF, respectively.

4.1 Correlations among SMBH mass, galaxy luminosity and velocity dispersion

The SMBH MF can be derived coupling the statistical information on local LF of galaxies with relationships among luminosity (or related quantities, such as stellar mass and velocity dispersion) and the central BH mass (see e.g. Salucci et al. 1999).

Since the BH mass correlates with luminosity and velocity dispersion of the bulge stellar population, we need separate LF for different morphological types (which have different bulge to total luminosity ratios), and it is convenient to use galaxy LF derived in bands *as red as possible*, where the old bulge stellar populations are more prominent.

4.1.1 Bulge luminosity versus black hole mass

McLure & Dunlop (2002) analyzing a sample of 72 active and 20 inactive galaxies found that the central BH mass and the total R-band magnitude, M_R, of the bulge are strictly related. In particular, considering only inactive elliptical galaxies with accurate measurements of BH mass, the relation, converted to $H_0 = 70$, reads

$$\log\left(\frac{M_\bullet}{M_\odot}\right) = -0.50(\pm0.05)M_R - 2.69(\pm1.04)\ , \tag{4.1}$$

with a scatter of $\Delta\log(M_\bullet) = 0.33$. It is worth noticing that the relationship has been derived using B-band magnitudes, translated to R-band assuming an average color (B-R)=1.57. A larger scatter $\Delta\log(M_\bullet) \simeq 0.45$ was found by Kormendy & Gebhardt (2001), who used a sample including also lenticular and spiral galaxies.

For galaxies observed with a spatial resolution high enough to resolve the BH sphere of influence, Marconi & Hunt (2003) report a tight relation between the SMBH mass and the host galaxy bulge K-band luminosity

$$\log\left(\frac{M_\bullet}{M_\odot}\right) = 1.13(\pm0.12)\left[\log(\frac{L_K}{L_{K_\odot}}) - 10.9\right] + 8.21(\pm0.07) \tag{4.2}$$

with a scatter $\Delta\log M_\bullet = 0.31$. Translating Eq. (4.1) to the K-band using the colour $R-K = 2.6$ (Kochanek et al. 2001, with $K - K_{20} = -0.2$), it is apparent that the Marconi & Hunt (2003) relationship yields higher BH masses at fixed luminosity. Correspondingly, the derived SMBH mass density is up to a factor of 2 higher than obtained from Eq. (4.1). A closer analysis shows that most of the discrepancy is due to SMBH in spiral galaxies (see Section 4.3) and can be ascribed to the uncertainty in the evaluation of their bulge component. Since most of the local mass density is contributed by BHs in E and S0 galaxies, we decided to exploit the relationship reported in Eq. (4.1).

As pointed out by McLure & Dunlop (2002), their $M_R - \log M_\bullet$ relation is compatible with a linear relation between BH and spheroidal mass, $M_{\rm sph}$. Indeed, inserting the result found by Borriello et al. (2003), $M_{\rm sph}/L_R \propto L_R^{0.21\pm0.03}$, we get $M_\bullet \propto M_{\rm sph}^{1.03\pm0.12}$.

4.1.2 Velocity dispersion versus BH mass

While the presence of a strong correlation between BH mass and velocity dispersion of the stellar spheroid, $M_\bullet - \sigma$, is undisputed (Ferrarese & Merritt 2000; Gebhardt et al. 2000), the value of its slope is still debated. A detailed analysis of the available data by Tremaine et al. (2002) yields

$$\log\left(M_\bullet \frac{80}{H_0}\right) = 4.02(\pm 0.32)\log(\sigma_{200}) + 8.13(\pm 0.06)\ , \tag{4.3}$$

σ_{200} being the line-of-sight velocity dispersion in units of $200\,\mathrm{km\,s^{-1}}$. The slope is in reasonable agreement with the findings of Ferrarese (2002), $M_\bullet \propto \sigma^{4.58\pm0.52}$. It should also be noted that the velocity dispersions used by Tremaine et al. (2002) refer to a slit aperture $2r_e$, while those reported by Ferrarese refer to $r_e/8$. The scatter around the mean relationship is small, $\Delta \log M_\bullet = 0.3$, possibly consistent with pure measurement errors.

The low mass and low velocity dispersion regime is quite difficult to investigate. The analysis of M33 by Gebhardt et al. (2001) yields an upper limit on the BH mass ($\sim 1500 M_\odot$) more than 10 times below the central value predicted by Eq. (4.3). However the larger upper limit ($\sim 3000 M_\odot$) claimed by Merritt, Ferrarese & Joseph (2001) is consistent with the steeper $M_{BH} - \sigma$ relation found by Ferrarese (2002). Filippenko & Ho's (2003) estimate of the mass of the central BH in the least luminous type 1 Seyfert galaxy known, NGC 4395, ($M_\bullet \simeq 10^4$– $10^5\,M_\odot$) is not inconsistent with Eq. (4.3). However it should be also mentioned that the BH mass in this case has been estimated using indirect, rather than dynamical arguments. The efforts to detect the so called intermediate mass BHs ($10^3\,M_\odot \leq M_\bullet \leq 10^6\,M_\odot$) in galactic centers and therefore to constrain the very low σ ($< 50\,\mathrm{km\,s^{-1}}$) end of the $M_\bullet$–σ relation have been recently reviewed by van der Marel (2003; see also Chapter 1, end of Section 2.3 and Chapter 7).

It is worth noticing that the $M_\bullet$–σ relationship needs not to keep a power-law shape down to low $M_\bullet$ or σ values. On the contrary, in the model by Granato et al. (2004) we have presented in Chapter 3, Section 3.4.2, for the coevolution of QSOs and their spheroidal hosts, in the least massive bulges, the SMBH growth is increasingly slowed down by supernova heating of the ISM as the bulge mass (hence σ) decreases. As a result, $M_\bullet$ is expected to fall steeply with decreasing σ, for $\log[\sigma(\mathrm{km\,s^{-1}})] \leq 2.1$. This model also

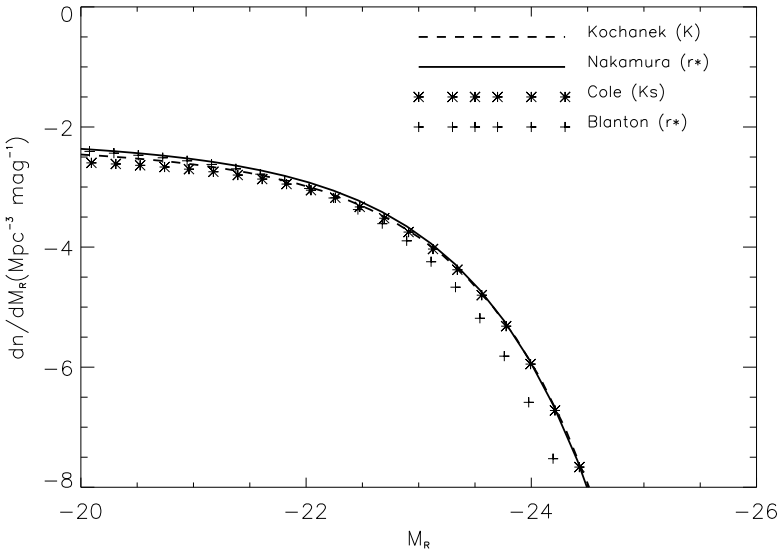

Figure 4.1: Galaxy luminosity function estimates converted to R-band total magnitudes as described in the text.

predicts that the observed spread around the mean relationship is a natural one, deriving mainly from the different virialization redshifts of host halos (see Chapter 7 for details).

4.2 The local SMBH Mass Function

The local SMBH MF can be estimated either from the local LF or from the local velocity dispersion function (VDF) of spheroidal galaxies and galaxy bulges, through the $M_\bullet$–$L_{\rm sph}$ or the $M_\bullet$–σ relation, respectively. Previous studies (Yu & Tremaine 2002; Aller & Richstone 2002) have shown that the two methods may yield estimates of the local mass density of SMBHs differing by a factor of $\simeq 2$. On the other hand Ferrarese (2002), McLure & Dunlop (2003) and Marconi et al. (2004) found very good agreement among the results of the two methods.

4.2.1 Local luminosity functions of spheroids and bulges

The LFs best suited for our purpose are those in red and IR bands, which are more directly linked to the mass in old stars. Moreover, we need separate LFs for the various

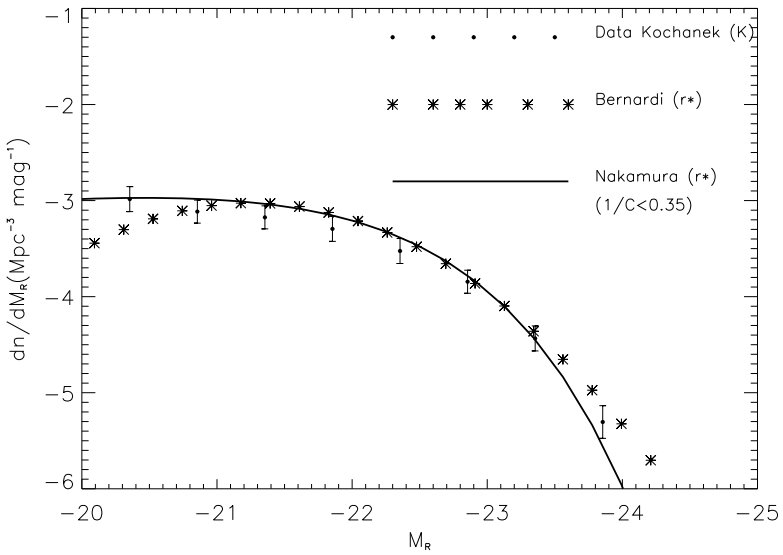

Figure 4.2: R-band luminosity function estimates for early-type galaxies. Data points from Kochanek et al. (2001).

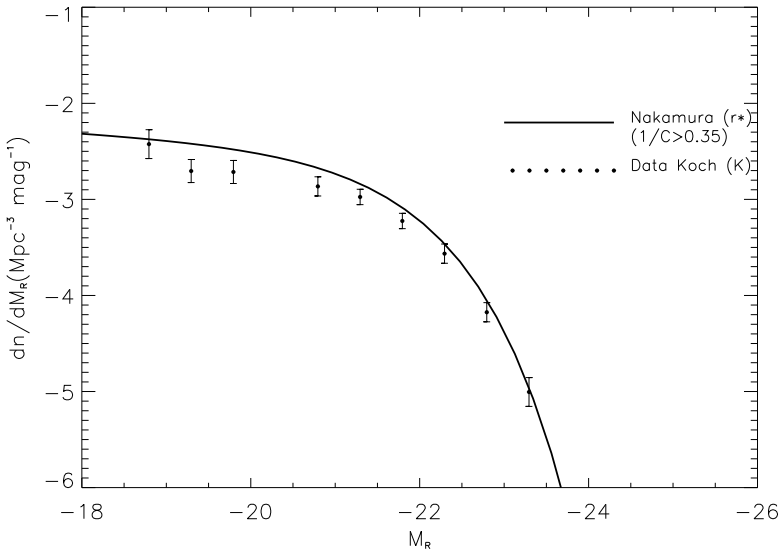

Figure 4.3: R-band local luminosity functions estimates for late-type galaxies.

morphological types with different bulge to total luminosity ratios. We will use the K-band LF by Kochanek et al. (2001), the K_s-band LF by Cole et al. (2001), the r^* band LF by Blanton et al. (2001, 2003), Nakamura et al. (2002), and Bernardi et al. (2003). To compare LFs defined in different bands we must set up a common definition of the total magnitude/luminosity and of average colours.

Since we are interested in the total luminosity of spheroidal components of galaxies, we adopt as total magnitudes those obtained with a de Vaucouleurs profile. We have therefore corrected by -0.2 the surface brightness limited magnitudes, K_{20}, of the 2MASS sample and the Petrosian magnitudes, used by Blanton et al. (2001; 2003) and by Nakamura et al. (2002). Both magnitude systems in fact are defined for apertures which contain $\sim 80\%$ of the total flux for the adopted profile. For the Kron magnitudes of Cole et al. (2001), in the K_s band, we used a brightening of -0.11, which is required to convert them to an $r^{1/4}$ luminosity profile.

Magnitudes were converted to the R-band using the mean colours $R - K_s = 2.51$ and $R - r^\star = -0.11$ (Blanton et al. 2001). We assume an error of 0.1 mag. on colours and include it in our estimate of the final errors on the SMBH MF.

As illustrated by Fig. 4.1, the different estimates of the LF are in very good agreement with each other, except for that by Blanton et al. (2003), which is low at bright magnitudes (by a factor $\simeq 4$ at $M_R < -24$). Indeed the Schechter function adopted by the latter authors falls below their own data points at $M_{r^*} - 5\log(H_0/100) = -23$ (cfr. their Fig. 5). The classification by Kochanek et al. (2001) allows a clear cut distinction between early and late type galaxies. A similar classification has also been proposed by Nakamura et al. (2002). Figures 4.2 and 4.3 show that the agreement is quite satisfactory also for early and late types separately, although the early-type LF by Bernardi et al. (2003) misses objects fainter than $M_R \simeq -21$ because of their velocity dispersion criterion ($\sigma > 70\,\mathrm{km\,s^{-1}}$ and $S/N > 10$).

4.2.2 From the local luminosity function to the SMBH mass function

Based on Table 1 of Fukugita, Hogan & Peebles (1998), to obtain the LF of the spheroidal components we adopt the average R-band bulge-to-total luminosity ratios

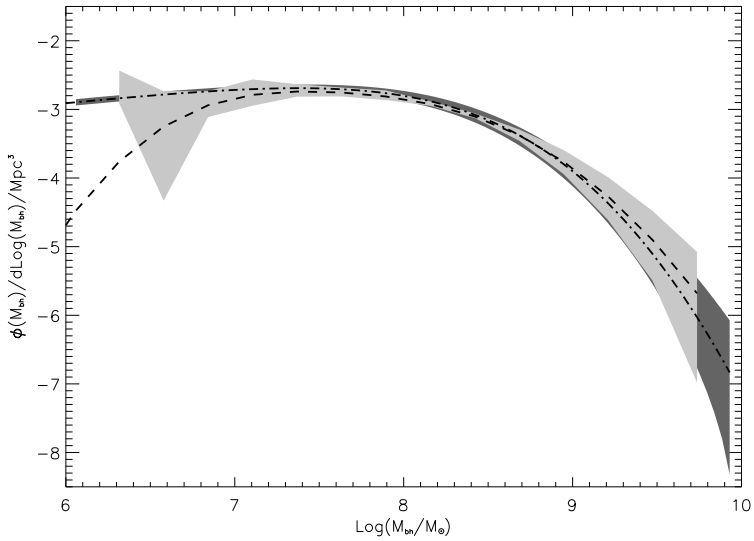

Figure 4.4: Local mass function of SMBHs hosted by early-type galaxies. The dot-dashed line shows the estimate obtained from the r^*-band LF (Nakamura et al. 2002) coupled with the $M_\bullet$–$L_{\rm bulge}$ relation (see text); the dark gray area shows the estimated errors. The dashed line and light gray area refer the MF derived using the bivariate dispersion velocity distribution (cfr. Fig. 4.7).

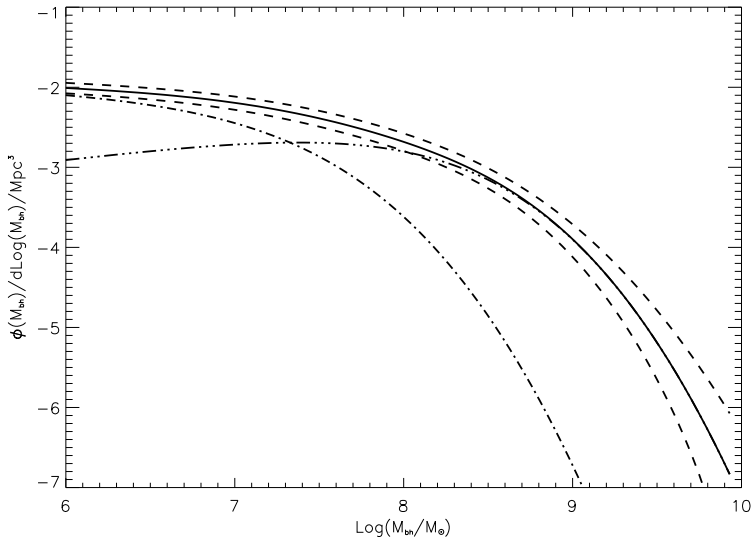

Figure 4.5: Global SMBH mass function (solid line) and its uncertainties (dashed lines). The three dots-dashed and the dot-dashed lines show the contributions from SMBHs hosted by early- and late-type galaxies, respectively.

$f_{\rm sph}^{\rm early} = 0.85 \pm 0.05$ for early-type galaxies and $f_{\rm sph}^{\rm late} = 0.30 \pm 0.05$ for late-type galaxies.

The SMBH mass function was then computed convolving the LF with the $M_\bullet$–$L_{\rm sph}$ relation by McLure & Dunlop (2002) [see Eq. (4.1)], assuming a Gaussian distribution around the mean with a dispersion $\Delta \log(M_\bullet) = 0.33^{+0.07}_{-0.05}$. These uncertainties encompass most of the values quoted in the recent literature (see Sect. 2.2). The errors on the SMBH MF include the overall uncertainties on the LF, on the bulge fractions, on the $M_\bullet$–$L_{\rm sph}$ relation and its scatter. The uncertainties on the LF, including those on colours, contribute about 70% of the error budget.

The SMBH MF in early type galaxies, shown in Fig. 4.4, has been estimated using the LF of Nakamura et al. (2002), converted to R-band, and Eq. (4.1). The match with the MF computed via the VDF and the $M_\bullet$–σ relation (see below) is very good. The corresponding SMBH mass density amounts to $\rho_\bullet^0(E) = 3.1^{+0.9}_{-0.8} \times 10^5 M_\odot/{\rm Mpc}^3$, in excellent agreement with the findings of McLure & Dunlop (2003) and Marconi et al. (2004), and 30% higher than the estimate by Yu & Tremaine (2002) and Aller & Richstone (2002).

The MF of SMBH hosted by spiral bulges was computed in the same way, using the LF for late-type galaxies by Nakamura et al. (2002). Their local mass density is $\rho_\bullet^0(Sp) = (1.1 \pm 0.5) \times 10^5 M_\odot/{\rm Mpc}^3$, bringing the overall mass density to $\rho_\bullet^0 = (4.2 \pm 1.1) \times 10^5 M_\odot/{\rm Mpc}^3$. The local number density of SMBHs with $M_\bullet > 10^7\, M_\odot$ is $n_{\rm SMBH} \simeq (1.3 \pm 0.25) \times 10^{-2}$ Mpc^{-3}. As illustrated by Fig. 4.5 the main contribution to the global mass density comes from the range $2 \times 10^7 < M_\bullet < 1 \times 10^9 M_\odot$, mostly populated by SMBH in early-type galaxies, while less massive BHs are preferentially hosted in late type objects.

Our determination is very close to the result by Marconi et al. (2004), who used a methodology similar to ours. As suggested by Aller & Richstone (2002) the MF can be well represented by a four parameter function, which for our determination (per unit $d \log M_\bullet$) takes the form:

$$\Phi(M_\bullet) = \Phi_* \left(\frac{M_\bullet}{M_*}\right)^{\alpha+1} \exp\left[-\left(\frac{M_\bullet}{M_*}\right)^{\beta}\right], \tag{4.4}$$

with $\Phi_* = 7.7(\pm 0.3) \cdot 10^{-3}$ Mpc^{-3}, $M_* = 6.4(\pm 1.1) \cdot 10^7\ M_\odot$, $\alpha = -1.11(\pm 0.02)$ and $\beta = 0.49(\pm 0.02)$ ($H_0 = 70\,{\rm km\,s^{-1}\,Mpc^{-1}}$). The formula holds in the range $10^6 \leq M_\bullet/M_\odot \leq 5 \times 10^9$.

Table 4.1: Local SMBH mass densities

Method	$\rho_\bullet^0(10^5 M_\odot \mathrm{Mpc}^{-3} h_{70}^2)$
Early Type Galaxies	
r^*+$M_\bullet - L_{\mathrm{bulge}}$	$3.1^{+0.9}_{-0.8}$
bivariate VDF + ($M_\bullet$–σ)	$3.0^{+1.0}_{-0.6}$
Sheth VDF + ($M_\bullet$–σ)	2.8
Late Type Galaxies	
r^* + ($M_\bullet$–L_{bulge})	1.1 ± 0.5

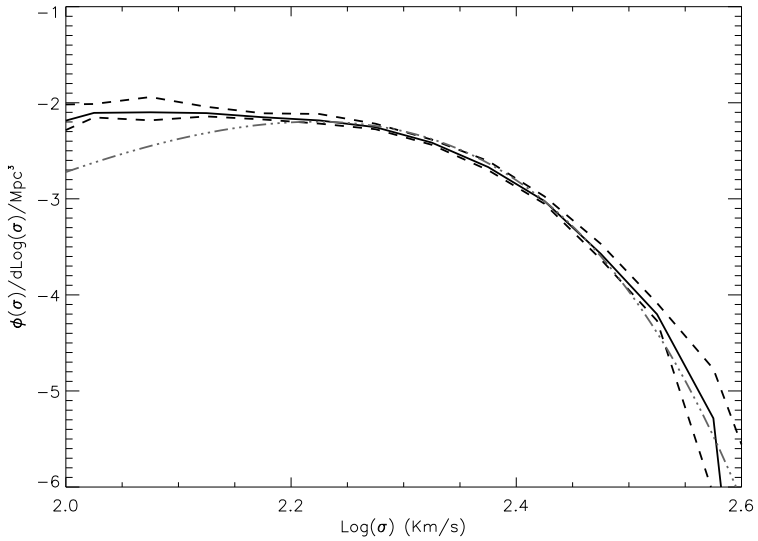

Figure 4.6: Velocity dispersion function. The solid line is the estimate obtained from the Nakamura et al. (2002) LF coupled with the bivariate (luminosity, σ) distribution derived from the SDSS data in the r^*-band; its uncertainty region is shown by the dashed lines. The three dots-dashed line is the estimate by Sheth et al. (2003).

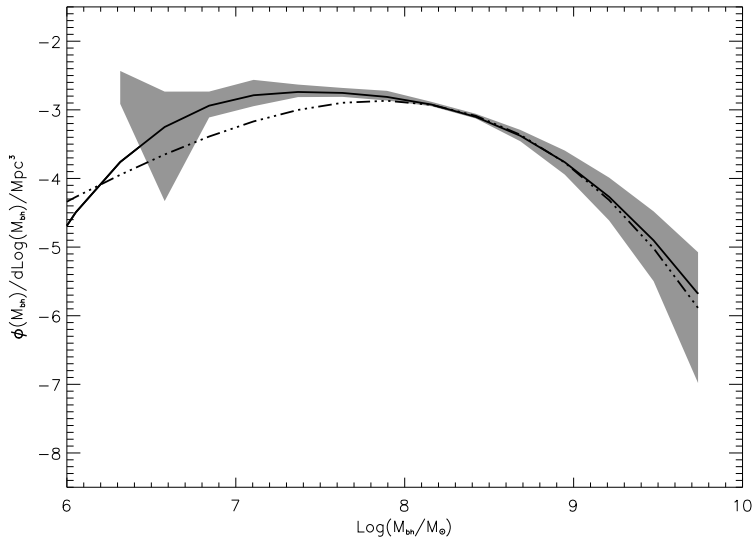

Figure 4.7: Estimates of the local mass function of SMBH hosted by early type galaxies, derived from the velocity dispersion functions in Fig. 4.6 coupled with the $M_\bullet$–σ relation by Tremaine et al. (2002). The gray area represents the uncertainties on the estimate based on the bivariate (luminosity, σ) distribution.

4.2.3 The local velocity dispersion function

The local VDF can be derived from the local galaxy LF exploiting the luminosity–σ relation (Gonzalez et al. 2000; Sheth et al. 2003), well established for spheroidal galaxies (Faber & Jackson 1976). The analysis of a sample of 86 nearby E and S0 galaxies, yields (de Vaucouleurs & Olson 1982; Gonzalez et al. 2000):

$$M_{B_T} = (-19.71 \pm 0.08) - (7.7 \pm 0.7) \log \sigma_{200} + 5 \log h, \tag{4.5}$$

with $h = H_0/100\,\mathrm{km\,s^{-1}\,Mpc^{-1}}$. However, data for larger samples suggest a steeper relation. Bernardi et al. (2003), using about 9000 early type galaxies selected from the Sloan Digital Sky Survey (SDSS), found $L_{r^*} \propto \sigma^{3.91}$, where σ refers to a $r_e/8$ aperture. The VDF of the SDSS has been actually obtained with a fixed aperture of 1.″5 and then converted to the $r_e/8$ aperture following the conversion suggested by Jørgensen, Franx & Kjaergaard (1995).

Estimates of the local VDF have been derived by Shimasaku (1993) and Gonzalez et al. (2000) (see Kochanek 2001 for a comprehensive review), and more recently, by Sheth

et al. (2003) who were the first to allow for the distribution (assumed Gaussian with a luminosity dependent width) of data points around the best fit relationship.

To make a fuller exploitation of the data by Bernardi et al. (2003) we have used them to derive the bivariate distribution $p_{ij} = p(L_i, \sigma_j)$, yielding the fraction of objects in the r^*-luminosity bin centered at L_i and in velocity dispersion bin centered at σ_j. The 9000 objects in the samples, covering an absolute magnitude range $-18 \leq M_{r^*} \leq -27$ and a velocity dispersion range $1.8 \leq \log(\sigma) \leq 2.7$ (σ in km/s), have been subdivided in bins of width 0.05 both in M_{r^*} (19 bins) and in $\log(\sigma)$ (170 bins). The VDF is then estimated as:

$$n(\sigma_j) = \sum_i p_{ij} n_i, \tag{4.6}$$

$n_i = n(L_i)$ being the r^*-band LF for early type galaxies by Nakamura et al. (2002; Fig. 4.2). The resulting VDF is shown in Fig. 4.6 with its errors, computed using the formula for the propagation of errors in a multivariate function with independent random errors in each variable. The uncertainties are bigger towards the two extremes, where the number of sampled objects decreases, and smaller around the knee of the function. We have checked that our results are independent of the bin size.

Using the K-band LF (Kochanek et al. 2001) converted to the r^*-band adopting a colour $K - r^* = -2.73$, appropriate for early-type galaxies (Blanton et al. 2001; Kochanek et al. 2001) we find differences in the VDF of at most 0.15 dex. From Fig. 4.6 it is apparent that our estimate is very close to that by Sheth et al. (2003), apart for the more rapid decline at low velocity dispersions, due to the selection criteria adopted by Bernardi et al. (2003), as noted above.

It is interesting to show, following Sheth et al. (2003), that there is no well defined "Faber-Jackson" relation. The exponent in the relation $L \propto \sigma^\alpha$, depends on how the correlation is computed (see Fig. 4.8). Computing the $L - \sigma$ relation as $L_i = \sum_k p_{ik}\, \sigma_k$, yields $L \propto \sigma^4$, while computing the $\sigma - L$ relation as $\sigma_j = \sum_k p_{kj} L_k$, yields $L \propto \sigma^{2.8}$. As it will be discussed in Chapter 8 to convert the VDF to a LF and viceversa, the bisector correlation is needed, i.e. $L \propto \sigma^3$. Therefore in our view, there is no physical meaning for the "slope" of the Faber-Jackson relation, however, as discussed in Chapter 7, the locus of the data points on the $L - \sigma$ plane constraints the efficiency of AGN and SN feedbacks.

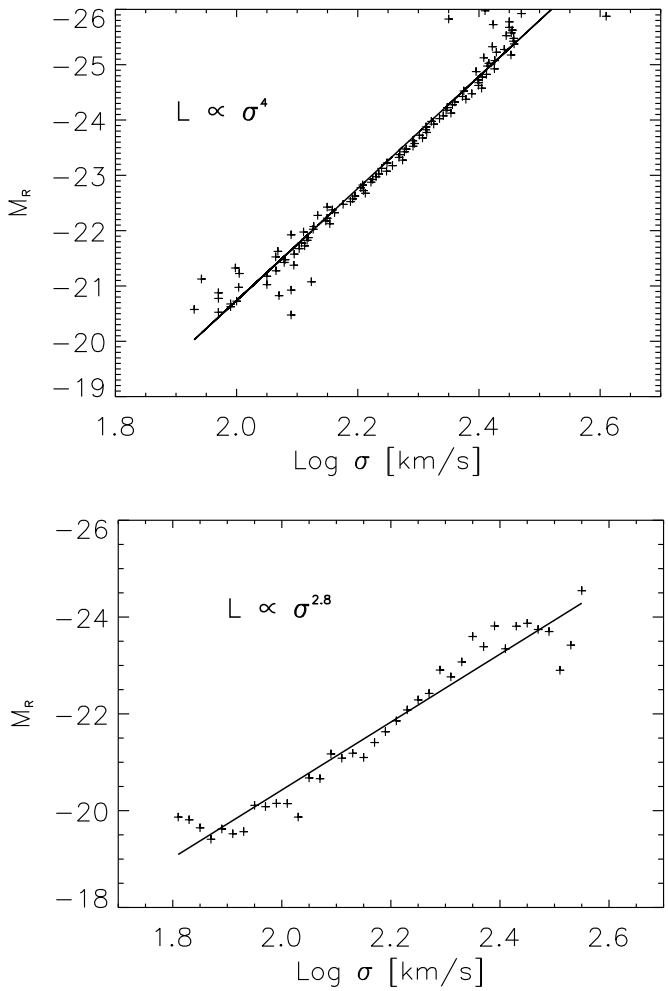

Figure 4.8: The Faber Jackson relation. Upper panel: computed at fixed luminosity bin. Bottom panel: computed at fixed $\log \sigma$ bin.

The contribution from late type galaxy bulges to the VDF is rather difficult to assess. In fact, the bulge-to-disk mass ratios depend more on morphology than on luminosity and on rotational velocity. Although for a given morphological type a correlation between the bulge velocity dispersion and the maximum rotational velocity may be expected, the use of the Tully-Fisher relation (among luminosity and rotation velocity) to infer the velocity dispersion is rather unsafe (see discussions of Sheth et al. 2003 and Ferrarese 2002).

4.2.4 From the VDF to the SMBH MF

In order to get an estimate of the local mass function of SMBHs, the local VDF for early-type galaxies can be convolved with the $M_\bullet$–σ relation of Tremaine et al. (2002). The SDSS velocity dispersions (Bernardi et al. 2003) given for an aperture of $r_e/8$, have been converted to $2r_e$ aperture using Eq. (16) of Tremaine et al. (2002), since the $M_{BH}-\sigma$ relation of Tremaine et al (2002) has been estimated with velocity dispersions taken within an aperture corresponding to $2r_e$. We assume a Gaussian distribution of BH masses at constant σ, with a dispersion $\Delta = 0.30^{+0.07}_{-0.03}$ dex.

The SMBH MF estimates derived from the VDF obtained through the bivariate probability distribution and from the VDF by Sheth et al. (2003) are shown in Fig. 4.7. The shaded area shows the uncertainties on the former estimate, including the contributions from errors on both the VDF and Δ. Again, the decline for $M_\bullet \leq 10^7\,M_\odot$ is due to the incompleteness of the SDSS sample at low velocity dispersions. The integrated mass density of SMBH in early-type galaxies is $\rho^0_\bullet = 2.8 \times 10^5 M_\odot/\mathrm{Mpc}^3$ or $\rho^0_\bullet = 3.0^{+1.0}_{-0.6} \times 10^5 M_\odot/\mathrm{Mpc}^3$ if we use the VDF by Sheth et al. (2003) or that obtained through the bivariate probability function, respectively. As noted above, the evaluation of the contribution of SMBHs hosted by late-type galaxies through this method is hampered by the poor knowledge of the local VDF for their bulges. Adopting the temptative estimate by Sheth et al. (2003) for the late type galaxy contribution to the VDF, coupled with Eq. (4.3), with the same scatter $\Delta = 0.3$, we get $\rho^0_{BH} = 1.2 \times 10^5\ M_\odot/\mathrm{Mpc}^3$, nicely consistent with the estimate derived from the LF.

Wyithe & Loeb (2003) obtained a lower estimate of the total mass density mainly because they neglected the scatter Δ of the $M_{BH}-\sigma$ relationship.

4.3 More on the determination of the SMBH Mass Function

SMBH Mass Function from the $M_\bullet - P_{\rm radio}$ relation

Following Salucci et al. (1999) and Sadler (2004) we can estimate the SMBH MF using the relation which links the SMBH mass and radio power. Franceschini, Vercellone & Fabian (1998) found a quite tight relationship between the radio power of the galaxy and the mass of the central SMBH

$$\log M_\bullet = 0.376 \log P_{1.4}(\mathrm{WH\,z^{-1}}) + 0.173 \tag{4.7}$$

implying that the total radio power emitted by a galaxy could be a tracer of the presence of a SMBH and an estimator of its mass. It is however to be kept in mind that clearly radio luminosity is not the only physical quantity linked to the SMBH mass (see also Chapter 2, Section 2.2.4), most probably also the accretion rate must be linked with the other two variables forming a "fundamental plane" (see e.g. Lacy et al. 2001; Merloni et al. 2003). Later analysis by Laor (2000) and Ho (2002) found in fact a much larger scatter for the $M_\bullet - P_{\rm radio}$ relation but using a mixture of galaxy types (including spirals). Snellen et al. (2003) found that a large sample of nearby optically selected elliptical galaxies with stellar velocity dispersions measured by Faber et al. (1989) follow the $M_\bullet - P_{\rm radio}$ relation.

We have verified that the Sadler et al. (1989) radio LF is in perfect agreement with the one derived by Magliocchetti et al. (2002) from a larger sample in the 2dF survey including Ellipticals and AGN galaxies. The space density of radio-emitting AGN is extremely close to a simple power-law of the form $\Phi(P) \propto P_{1.4}^{-0.62\pm0.03}$ over almost five decades in luminosity from $10^{20.5}$ to 10^{25} WHz^{-1}, before turning down above 10^{25} WHz^{-1}.

Exploiting Eq. (4.7) and the radio LF by Sadler et al. (2002) it is in principle possible to derive the SMBH mass function. The result is shown in Fig. 4.9, where we have shown the match with the accreted SMBH mass function obtained from optical data. This again suggests that the radio loudness could be linked with the most massive most luminous AGN, mostly QSO, being probably a transient phase in their evolution. As noted by Salucci et al. (1999) probably a more refined treatment should take into account the *core* radio power instead of the total radio luminosity of the galaxy, but minor changes are produced once also the scatter in the $P_{\rm tot} - P_{\rm core}$ relation is included (Sadler 1989).

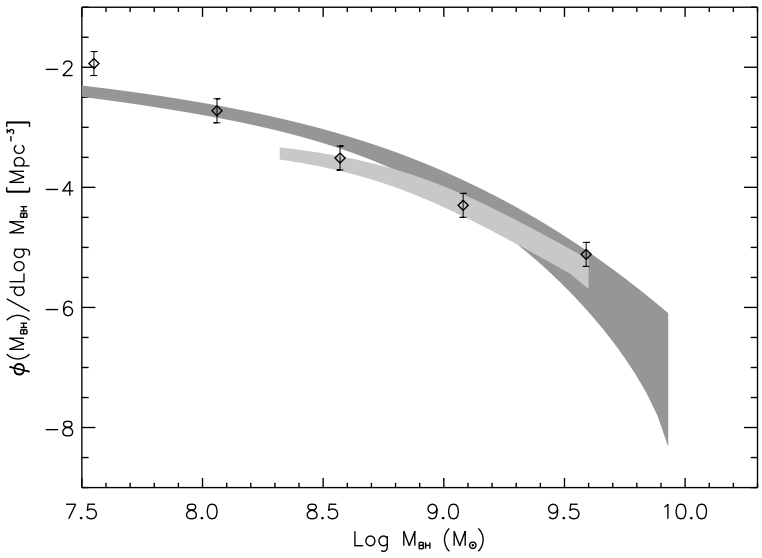

Figure 4.9: Diamonds: estimates of the local mass function of SMBH hosted by early type galaxies derived from the $M_\bullet$–$P_{\rm radio}$ relation by Franceschini et al. (1998) at 1.4 Ghz. The gray area represents the uncertainties on the estimate based on the $M_\bullet$–$L_{\rm bulge}$ relation. Also shown the contribution to the SMBH accreted mass function from Optically selected AGN (light gray area).

An alternative method to derive the SMBH Mass Function

It is now interesting to compare the results in this chapter with those found by other authors. To derive the SMBH MF from the $M_\bullet - L_{\rm bulge}$ relation Yu & Tremaine (2002), followed by Marconi et al. (2004), adopt the following relation

$$\phi_{\rm bulge}(M_\bullet) = \frac{f_{S0}}{f_E + f_{S0}}\phi(m - \delta m_{S0}) + \frac{f_E}{f_E + f_{S0}}\phi(m - \delta m_E) \tag{4.8}$$

to estimate the bulge luminosity function of SO/Sa galaxies, where f_i represents the fraction of i-type of galaxy and δm is the light bulge correction. This approximation, rather uncertain, provides anyway $\sim 20\%$ less in the final SMBH mass density than what we find with our method. This can be seen in Fig. 4.10 where we have compared the galaxy bulge luminosity functions obtained in Section 2.3.2, with an average correction of $L_{\rm sph}/L_{\rm tot} = 0.85$ for Early type galaxies, and the one obtained from Eq. (4.8) using $f_{S0} = 0.21$, $f_E = 0.11$, $\delta m_{\rm S0} = -0.3$ and $\delta m_E = 0$ (Fukugita, Hogan & Peebles 1998).

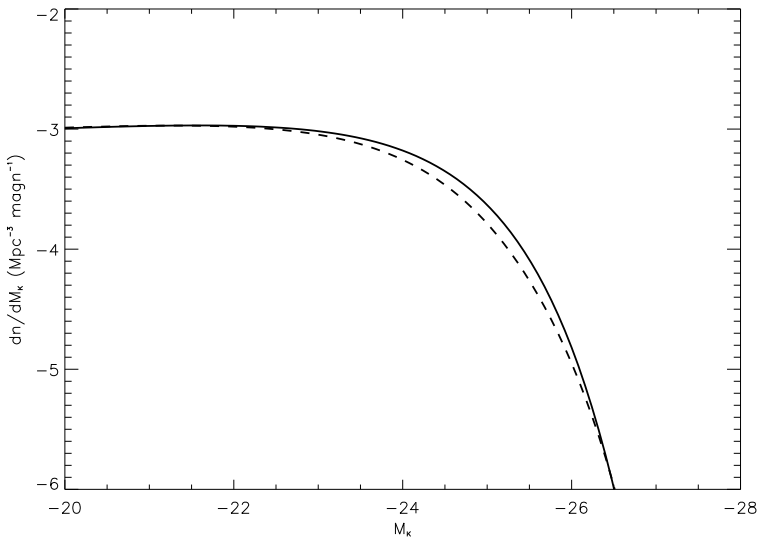

Figure 4.10: Estimate of the early type spheroidal galaxy LF. Solid line: estimate using the fraction of SO and E galaxies as given in Eq. (4.8). Dashed line: estimate using an average bulge correction of $L_{\rm sph}/L_{\rm tot} = 0.85$.

Chapter 5

SMBH Accretion History

Soltan (1982) showed that, in the framework of the AGN paradigm, the total accreted mass density can be inferred from the observed QSO/AGN counts. The basic ingredients of the calculation are *i)* the bolometric correction $k_{\rm bol}$, *ii)* the effective redshift and the corresponding K-correction, and *iii)* the mass to radiation conversion efficiency ϵ. When more precise luminosity functions of QSO/AGN became available, Chokshi & Turner (1992) presented a first estimate of the accreted mass density and derived constraints on the corresponding mass function (MF).

In this Chapter we compute the total accreted mass density and mass function and, through the comparison with the local estimate, constrain the mean accretion properties and evolutionary trends of the SMBH population.

5.1 The accreted mass density

Following Soltan (1982) the total mass density accumulated by accretion on BHs powering QSOs can be deduced from QSO counts, under quite simple assumptions. If ϵ is the mass to radiation conversion efficiency, the bolometric luminosity is

$$L_{\rm bol} = \epsilon \dot{M}_{\rm acc} c^2 \tag{5.1}$$

and the mass accretion rate reads

$$\dot{M}_\bullet = (1-\epsilon)\dot{M}_{\rm acc}. \tag{5.2}$$

The conversion of luminosities measured in a given band to bolometric luminosities requires the knowledge of bolometric corrections $k_{\rm bol}$ (see, e.g., Elvis et al 1994), which may depend on luminosity and/or redshift. The mass accreted up to the present time by all AGNs brighter than L can be written as

$$\rho_{\rm acc}(>L) = \frac{1-\epsilon}{\epsilon c^2}\int_0^{z_{\rm max}} dz \frac{dt}{dz} \int_L^{L_{\rm max}} dL' k_{\rm bol}(L',z) n(L',z) L'. \tag{5.3}$$

where $n(L',z)$ is the *comoving* luminosity function. As noted by Soltan (1982), $\rho_{\rm acc}$ is independent of H_0 and of the QSO lifetime.

The most complete AGN surveys are those at X-ray (hard and soft), optical, and radio wavelengths (see Chapter 2, Section 2.2.6). The latter selection is however rather inefficient, since only $\sim 10\%$ of AGNs are radio loud.

The meaning of Eq. (5.3) can be readily understood converting it in number counts. In fact setting

$$n(S,z)dSdz = \Phi(L,z)dL\frac{dV}{dz}dz \tag{5.4}$$

and using the definition of luminosity distance (Eq. (3.3)) and comoving volume (Eq. (5.8), one gets

$$\rho_{\rm acc} = \frac{1-\epsilon}{\epsilon c^2}\int_0^{z_{\rm max}} dz(1+z) \int_{S_{\rm min}}^{S_{\rm max}} dS' \frac{4\pi}{c} k_{\rm bol} S' n(S',z)$$

which clearly shows that the accreted mass density is given by the sum of all the number counts contributions at various redshift, the result being independent of the cosmological parameters. The factor $(1+z)$ is necessary since photons lose energy in the Universe expansion but mass is conserved (unless there is energy dissipation as, for example, in gravitational waves).

5.1.1 Mass accreted on optically selected QSOs

The 2dF survey (Boyle 2000; Croom et al. 2003), as anticipated in Chapter 2, Section 2.2.5, has provided an accurate determination of the redshift-dependent LF of optically selected AGNs with $M_B < -22.5$ and $z < 2.2$. Croom et al. (2003) showed that the data are consistent with PLE of the form $L_B(z) = L_B(0) \times 10^{0.21z(5.476-z)}$ (for a ΛCDM model with $\Omega_m = 0.3$), peaking at $z_p \simeq 2.74$ and exponentially declining at higher redshifts. Although

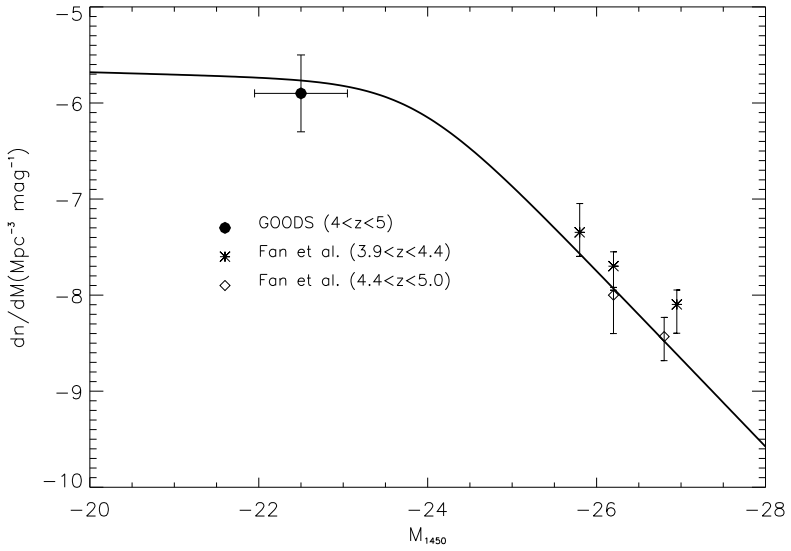

Figure 5.1: Optical AGN LF at high-z. Data from the SDSS (Fan et al. 2001) and GOODS survey (Cristiani et al. 2004). The solid line shows the Croom et al. (2003) power-law model at $z = 4.5$.

the luminosity function is poorly known for $z > 2.4$, there is strong evidence (see Fan et al. 2001 and Osmer 2003 for a recent review), for a rapid decrease with increasing redshift of the space density of bright QSO for $z \geq 3$. More recently, very deep X-ray (Barger et al. 2003) and optical (Cristiani et al. 2004) surveys have provided strong constraints on the space density of less luminous QSOs at high redshift. As illustrated by Fig. 5.1, the Croom et al. (2003) power-law model provides a sufficiently accurate description also of the data at $z \geq 4$.

Inserting such model in Eq. (5.3), and integrating it up to $z = 6$, we get, for $k^B_{\rm bol} = 11.8$, appropriate for $L_B = (L_\nu \nu)_B$ with $\nu_B = 6.8 \times 10^{14}$ Hz (Elvis et al. 1994) and $\epsilon = 0.1$:

$$\rho^{\rm opt}_{\rm acc} = 1.4 \times 10^5 \frac{k_{\rm bol}}{11.8} M_\odot/{\rm Mpc}^3 \ . \tag{5.5}$$

with objects at $z \leq 2.2$ contributing $\rho^{\rm opt}_{\rm acc} = 0.8 \times 10^5 M_\odot/{\rm Mpc}^3$. Using the Boyle et al. (2000) LF, which is however inconsistent with high redshift data, $\rho^{\rm opt}_{\rm acc}$ increases by 20%. Thus the mass density accreted on BHs powering the optical QSO emission is a factor $\simeq 3$ lower than the estimated local SMBH mass density.

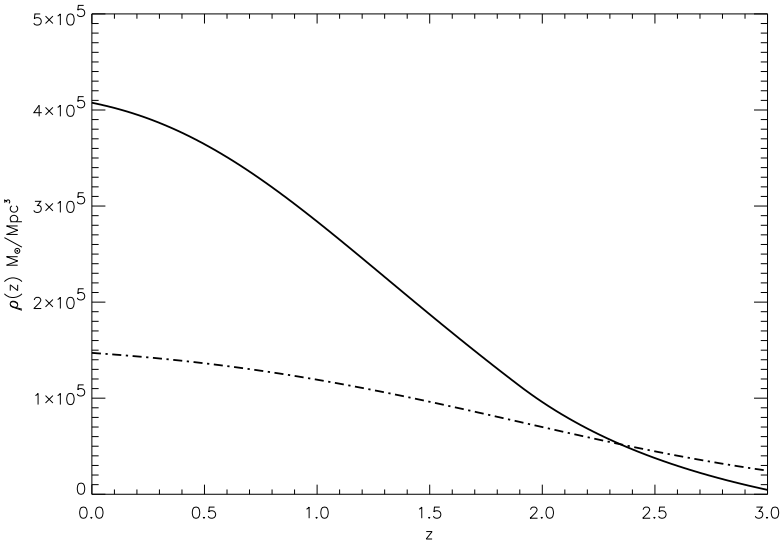

Figure 5.2: Accreted mass density as a function of redshift. The solid and the dot-dashed lines show the increase, with decreasing redshift, of the comoving accreted mass density as inferred from the epoch-dependent hard X-ray luminosity function by Ueda et al. (2003), with a luminosity dependent bolometric correction (see text), and from the optical luminosity function by Croom et al. (2003), respectively.

The estimate of $\rho_{\rm acc}^{\rm opt}$ is affected by uncertainties on $k_{\rm bol}^B$ and on ϵ. An upper limit of $k_{\rm bol}^B = 16$ can be derived from the Elvis et al. (1994) sample. On the other hand, recent data point to a lower bolometric correction than used in Eq. (5.5). For instance, McLure & Dunlop (2003) find $k_{\rm bol}^B \sim 8$, and Vestergaard (2003) finds $k_{\rm bol}^B = 9.7$ for higher redshift QSOs. On the whole we attribute to $k_{\rm bol}^B$ an uncertainty of about 30%. It is worth noticing that no dependence of the optical bolometric correction on optical luminosity has been reported.

The efficiency ϵ of conversion of accreted mass into outgoing photons can be as high as $\simeq 0.4$ for extreme-Kerr BHs. On the other hand, no firm lower limit to ϵ can be set; in extreme cases a BH can grow without radiating any photon at all. However, the low predicted value of $\rho_{\rm acc}^{\rm opt}$ does not necessarily imply a low value of ϵ, since an additional important contribution to the local BH mass density is expected from highly absorbed hard X-ray selected AGNs, contributing a large fraction of the X-ray background energy density, but only marginally represented in optical surveys.

5.1.2 Mass accreted on X-ray selected AGNs

As reviewed in Chapter 2, Section 2.2.7, most of the XRBG intensity can be considered as "luminosity" due to accretion onto SMBH. The equation $E = Mc^2$ can be rewritten in terms of radiation and mass densities as

$$U(1+\bar{z}) = \frac{\epsilon}{1-\epsilon} c^2 \rho_\bullet \tag{5.6}$$

where U is the XRBG energy density. However as summarized by Gilli (2003) there is a systematic problem with the normalization of the XRBG between 2 and 10 KeV (while the slope has been by now established to have a photon index $\Gamma \simeq 1.4$). Such uncertainty in the normalization can be up to 40 %. The lowest value is 8 given by Marshall et al. (1980) and the highest is 11.5 by Vecchi et al. (1999), in units of keVs^{-1}sr^{-1}cm^{-2}keV^{-1}.

As already anticipated in Chapter 2, the high-energy spectrum of the XRBG has been resolved up to 50% at the most and probably the rest of the emission is produced by a still unveiled population of Compton-thick sources.

As shown in Chapter 2, Section 2.2.6, a comprehensive study of the redshift-dependent hard X-ray AGN LF, including the distribution of the absorption column density N_H, has been recently carried out by Ueda et al. (2003; U03 from now on). In the following we will refer to their LDDE model, with the additional fraction of AGN with $24 < \log(N_H) \leq 25$ required in order to fit the XRB with the most recent normalizations (Vecchi et al. 1999; Barcons et al 2000; Gilli 2003). The additional AGN fraction implies an increase of the mass density by 25%.

We have firstly computed the actual contribution of the very Compton thick sources ($\log(N_H) = 24.5$) to the XRBG and number counts in the $2-10$ keV, using the U03 LF and their prescriptions for the inclusion of obscured sources. In a Friedmann Universe the intensity of the XRBG $F(E)$ at the energy E, produced by all the AGN in the redshift range $0 - z_{\max}$ and in the luminosity range $L_{\min} - L_{\max}$ can be written as

$$F(E) = \frac{1}{4\pi} \int_0^{z_{\max}} \frac{1+z}{4\pi d_L^2} \frac{dV}{dz} dz \int_{L_{\min}(z)}^{L_{\max}(z)} f[E(1+z)] \rho[L(z), z] dL(z)\,, \tag{5.7}$$

where

$$\frac{dV}{dz} = 4\pi d_L^2 \left(\frac{c}{H_0}\right) \frac{1}{(1+z)^3 \sqrt{1+2q_0 z}} \tag{5.8}$$

and d_L is the luminosity distance (Eq. (3.3)), H_0 and q_0 are the Hubble constant and deceleration parameter, respectively; $\rho[L(z), z]$ is the comoving AGN X-ray luminosity function in a given energy band $E_1 - E_2$; $f[E(1+z)]$ is the source flux at the energy $E(1+z)$ divided by the source flux in the energy band $E_1 - E_2$.

The number of AGN per steradian with a flux $S > S_{\rm lim}$ in the energy band $E_1 - E_2$ is given by

$$N(> S_{\rm lim}) = \frac{1}{4\pi} \int_0^{z_{\rm max}} \frac{dV}{dz} dz \int_{max[l_{\rm min}(S_{\rm lim},z), L_{\rm min}(z)]}^{L_{\rm max}} \rho[L(z), z] dL(z) \tag{5.9}$$

where

$$l_{\rm lim}(S_{\rm lim}, z) = 4\pi d_L^2 \frac{S_{\rm lim}(E_1, E_2)}{K(z, E_1, E_2)} \tag{5.10}$$

and $K(z, E_1, E_2)$ is the K-correction term given by

$$K(z, E_1, E_2) = \frac{\int_{E_1(1+z)}^{E_2(1+z)} f(E) dE}{\int_{E_1}^{E_2} f(E) dE}. \tag{5.11}$$

The redshift distribution of the AGN in a sample with limiting flux $S_{\rm lim}$ in the $E_1 - E_2$ energy band is simply given by the argument of the redshift integral in Eq. (5.9).

Our results are shown in Fig. 5.3 and Fig. 5.4 in which we show that the additive family of very obscured Compton-thick AGN better fits the latest data on the normalization of the XRBG spectrum and number counts.

Unfortunately the available information on the overall spectral energy distribution of hard X-ray selected objects (and particularly of the faint ones, which are the most relevant to estimate the low mass end of the MF) is scanty, so that estimates of the bolometric corrections are difficult. The bolometric correction, $k_{\rm bol}^{2-10} \simeq 32$, derived by Elvis et al. (1994), refers to optically bright quasars. Evidences for an increase of the hard X-ray to optical luminosity ratio, $L_{HX}/L_{\rm opt}$ with decreasing optical luminosity have been reported by Vignali et al. (2003) and bolometric corrections, $k_{\rm bol}^{2-10} \simeq 12 - 18$, substantially smaller than the Elvis et al. (1994) value, have been estimated at least for a few Seyfert galaxies (Fabian 2003). Moreover, in order to match the optical LF of Boyle et al. (2000) starting from the hard X-ray LF, U03 had to assume that $L_{2\ keV} \propto L_{2500A}^{0.7}$ in close agreement with the observational data by Vignali et al. (2003).

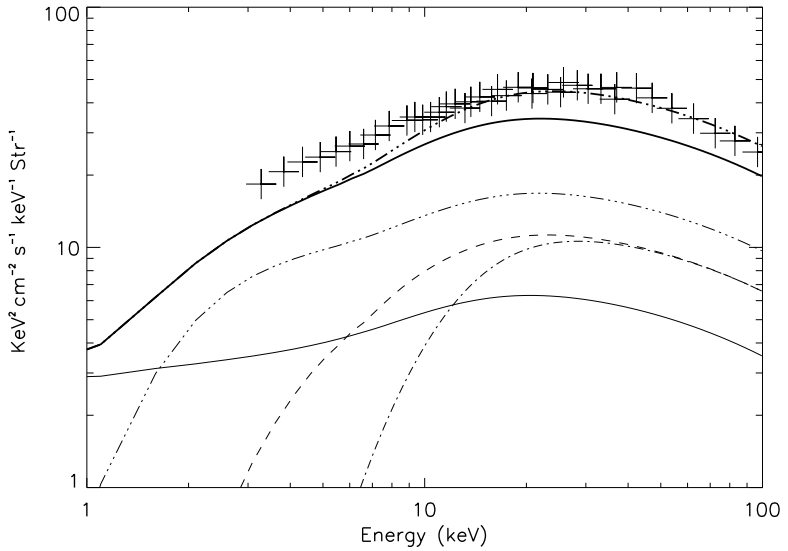

Figure 5.3: Synthesis model to fit the XRBG spectrum using several families of obscured AGN. Thick solid line: total computed emission without the extra family of Compton-thick AGN. Triple dot-dashed line: total emission inserting Compton-thick AGN with $\log(N_H) = 24.5$. Thin solid line: $\log(N_H) = 21.5$, triple dot-dashed line: $\log(N_H) = 22.5$, dashed line: $\log(N_H) = 23.5$ and dot-dashed line: $\log(N_H) = 24.5$. Crosses: re-normalized data by Gruber et al. (1999) to fit the upper normalization of the XRBG (see Fig. 2.11).

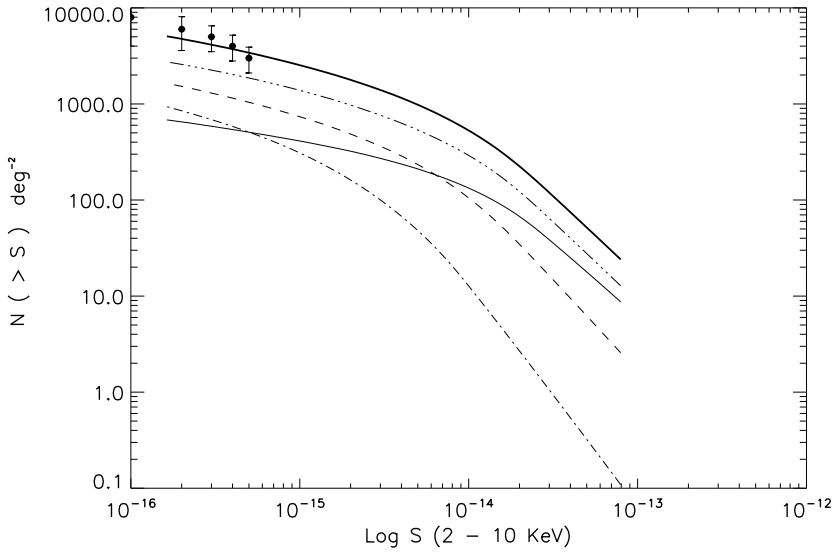

Figure 5.4: Synthesis model to fit the XRBG number counts. Thick solid line: total number counts including extra Compton-thick AGN with $\log(N_H) = 24.5$. Thin solid line: $\log(N_H) = 21.5$, triple dot-dashed line: $\log(N_H) = 22.5$, dashed line: $\log(N_H) = 23.5$ and dot-dashed line: $\log(N_H) = 24.5$. Data by Brandt & Hasinger (2005).

If the optical/UV bolometric correction is independent of luminosity, the U03 relationship between UV and X-ray luminosity implies:

$$k_{\rm bol}^{2-10} = 17 \left(\frac{L_{2-10}}{10^{43} {\rm erg\,s^{-1}}} \right)^{0.43} . \tag{5.12}$$

Inserting Eq. (5.12) in Eq. (5.3), assuming $\epsilon/(1-\epsilon) = 0.1$, and integrating over the luminosity and redshift intervals ($41.5 \leq \log(L_{2-10{\rm keV}}) \leq 46.5$ and $z \leq 3$) investigated by Ueda et al. (2003), we find

$$\rho_{\rm acc}^{HX} \simeq 4.1 \times 10^5 M_\odot/{\rm Mpc}^3 . \tag{5.13}$$

If we extrapolate the LF up to $z = 6$, we get a mass density larger by 15%.

As a consistency check, we have subtracted the contribution of Type 2 AGNs, following the prescriptions given by U03, in order to get the contribution to the local mass density of Type 1 objects only. We find:

$$\rho_{\rm acc}^{\rm Type\,1} \simeq 1.5 \times 10^5 M_\odot/{\rm Mpc}^3 , \tag{5.14}$$

in close agreement with the result obtained using the optical LF [Eq. (5.5)]. The relatively large contribution of the optically selected AGNs to the local BH mass density ($> 30\%$), despite their small ($< 20\%$) contribution to the intensity of the HXRB, reflects their lower X-ray to optical luminosity ratio. Since $\rho_{\rm acc}^{\rm Type\,1} \propto [(1-\epsilon)/\epsilon] k_{\rm bol}^{2-10}$ and $\rho_{\rm acc}^{\rm opt} \propto [(1-\epsilon)/\epsilon] k_{\rm bol}^{B}$, from the agreement between the two estimates we can conclude that the uncertainty on $k_{\rm bol}^{2-10}$ is similar to that on $k_{\rm bol}^{B}$, i.e. $\simeq 30\%$.

The mass accretion history is illustrated by Fig. 5.2 showing the increase with decreasing redshift of the comoving accreted mass density, $\rho_{\rm acc}(z)$, as inferred from the optical (dot-dashed line) and from the hard X-ray (solid line) epoch dependent comoving luminosity function $n(L, z)$:

$$\rho_{\rm acc}(z) = \frac{1-\epsilon}{\epsilon c^2} \int_z^{z_{\rm max}} dz' \frac{dt}{dz'} \int_{L_{\rm min}}^{L_{\rm max}} dL'\, k_{\rm bol} L'\, n(L', z), \tag{5.15}$$

where the X-ray (but not the optical) bolometric correction is a function of luminosity, as discussed above. As shown by Fig. 5.2, most of the accretion occurs at $z > 1.5$ for optically selected AGNs, and at $z < 1.5$ for hard X-ray selected AGNs.

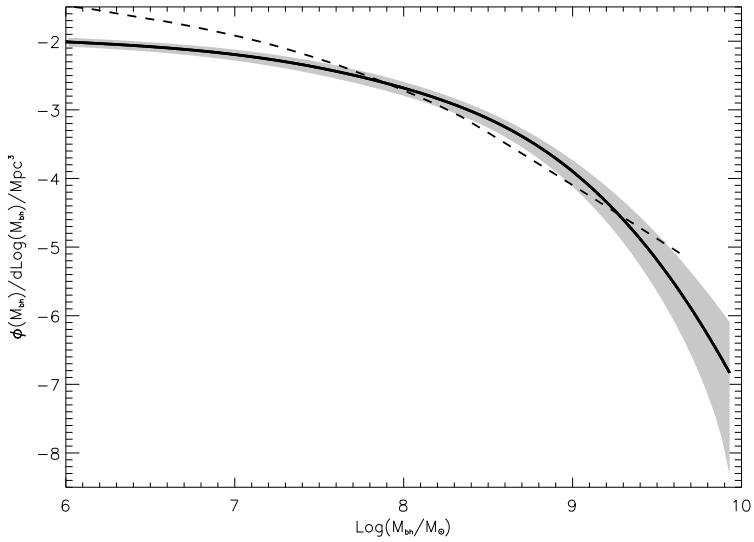

Figure 5.5: Local SMBH MF (solid line), including SMBHs hosted by both early- and late-type galaxies, with its 1σ uncertainty (shaded area), compared with the accreted MF (dashed line) estimated from the X-ray LF by U03, using a luminosity dependent bolometric correction. Such estimate is obtained by differentiating the integral mass function [Eq. (5.19)] with $\lambda = L/L_{\rm Edd} = 1$.

The close correspondence of the accreted mass density inferred from the hard X-ray LF with the local SMBH mass density $\rho_\bullet \simeq 4.2 \pm 1.0 \times 10^5\, M_\odot/{\rm Mpc}^3$ (see Table 4.1) for $\epsilon/(1-\epsilon) = 0.1$ shows that *there is no much room for really "dark" accretion* (i.e. for accretion with radiative efficiency $\epsilon \ll 0.1$), confirming the findings by Salucci et al. (1999) and of Marconi et al. (2004), unless the luminous phases of the AGNs are characterized by radiative efficiencies much higher than the usually adopted value. But even if ϵ is close to the maximum allowed values ($\simeq$ 0.3–0.4; Thorne 1974) the accreted mass accounts for $\geq$ 25–30% of the local SMBH mass density, and one would be left with the problem of accounting for the correlations between $M_\bullet$ and the bulge mass or velocity dispersion which arise naturally as a consequence of feedback associated to radiative accretion (Silk & Rees 1998; Cavaliere et al. 2002; King 2003; Granato et al. 2004; see also next Chapters).

A more explicit test of the role of accretion is obviously the comparison, presented in the next Section, of the resulting MF with the local SMBH MF.

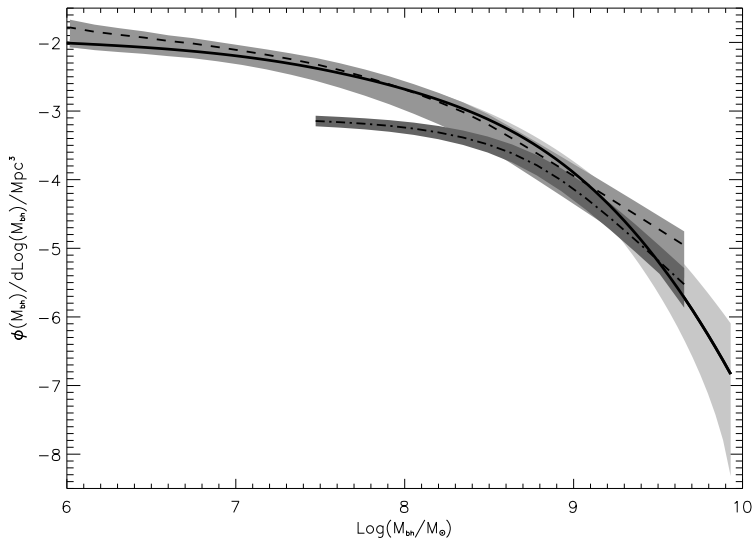

Figure 5.6: Comparison of the accreted MF (dashed line) computed as in Fig. 5.5, but for λ given by Eq. (5.24) with the local SMBH MF (solid line, with 1σ uncertainties represented by the shaded area). The dot-dashed line shows the accreted MF of optically selected QSOs ($M_B < -22.5$).

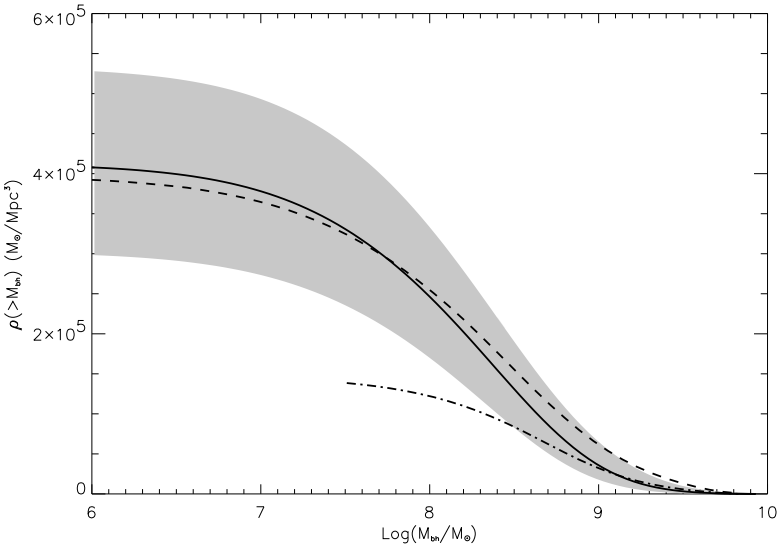

Figure 5.7: Cumulative local SMBH MF (dashed line) with its 1σ uncertainties, compared with the cumulative MF of optically selected QSOs ($M_B < -22.5$; dot-dashed line) plus X-ray selected Type 2 AGNs.

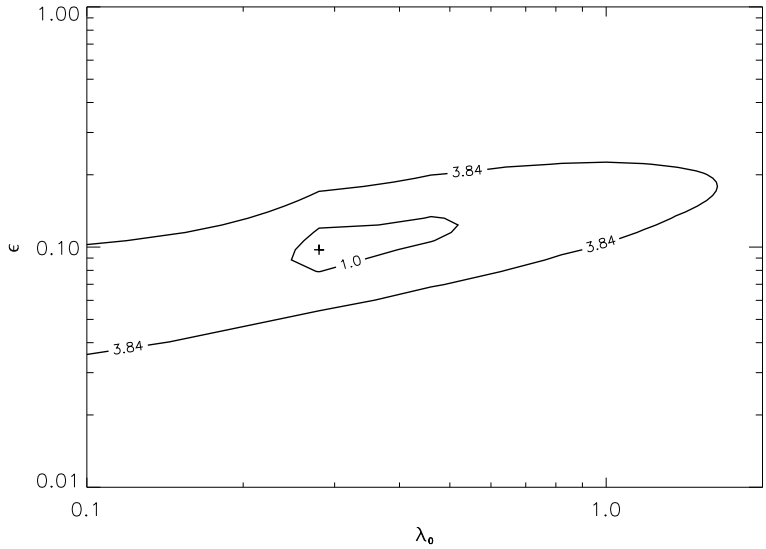

Figure 5.8: Iso-χ^2 contours in the ϵ–λ_0 plane for the match between the accreted and the local SMBH MFs. The contours are labelled with their value of $\Delta\chi^2$. The projections of the $\Delta\chi^2 = 1$ and $\Delta\chi^2 = 3.84$ contours on the axis corresponding to a parameter give the 68% and 95% confidence intervals, respectively, for such parameter.

5.2 The local accreted mass function

The AMF can be derived from the AGN LF once a relationship between luminosity and BH mass is established (Chokshi & Turner 1992). Salucci et al. (1999) compared, under plausible assumptions, the accreted MF with the local SMBH MF to infer information on the accretion history. This point has been recently reexamined by a number of authors (e.g. Yu & Tremaine 2002; Aller & Richstone 2002; McLure & Dunlop 2003; Yu & Lu 2004; Marconi et al. 2004), who reached different conclusions.

Let us assume that the local SMBH mass is mostly due to radiative accretion and that the accretion rate $\dot{M}_\bullet$ is proportional to $M_\bullet$ (see e.g. Small & Blandford 1992; Cavaliere & Vittorini 2002; Marconi et al. 2004), at least during the main accretion phases. A recent analysis of SDSS quasars suggests that the two quantities are correlated (McLure & Dunlop 2003), although with a huge scatter, at least partly due to the uncertainties in BH mass estimates. An almost constant $\dot{M}_\bullet/M_\bullet$ is also expected, according to the physical model of Granato et al (2004), during the fast growth of the SMBHs and up to the bright

quasar phase.

If $\dot{M}_\bullet/M_\bullet$ is constant, the bolometric luminosity grows exponentially (as does the BH mass):

$$\begin{aligned} L_{\rm bol}(t) &= \epsilon \dot{M}_{\rm acc} c^2 = \frac{\epsilon}{1-\epsilon}\dot{M}_\bullet c^2 \\ &= \frac{\lambda c^2}{t_E} M_\bullet(t_i) \exp\left[\frac{(t-t_i)}{t_{ef}}\right], \end{aligned} \tag{5.16}$$

with e-folding time

$$t_{ef} = \frac{\epsilon t_E}{(1-\epsilon)\lambda}, \tag{5.17}$$

where λ is the average ratio $L/L_{\rm Edd}$, t_E is the Eddington time and t_i is the time when the growth starts. The e-folding time equals the Salpeter time if $\lambda = 1$.

The growth stops when the SMBH reaches its maximum mass, set equal to its present-day mass $M_\bullet^0$, i.e. we neglect the mass increase during the declining phase of the light curve (see Yu & Lu 2004). The maximum bolometric luminosity is then:

$$L_{\rm bol,max}(M_\bullet^0) = \lambda \frac{M_\bullet^0}{t_E} c^2. \tag{5.18}$$

Under these assumptions, the local SMBH MF is related to the epoch-dependent LF in a given observational band by the energy balance equation:

$$\begin{aligned} &\frac{1-\epsilon}{\epsilon c^2}\int_0^{t_0} dt \int_{\bar{L}}^{\infty} dL k_{\rm bol} L n(L,t) = \\ &= \int_{\bar{M}_\bullet^0}^{\infty} dM_\bullet^0 n(M_\bullet^0)\left[M_\bullet^0 - \bar{M}_\bullet^0\right], \end{aligned} \tag{5.19}$$

where $\bar{L} = L_{\rm max}(\bar{M}_\bullet^0)$. The local MF $n(M_\bullet^0)$ is straightforwardly obtained differentiating Eq. (5.19) with respect to $\bar{M}_\bullet^0$.

Eq. (5.19) is derived from the continuity equation (see Yu & Lu 2004). The luminosity/mass continuity equation (Small & Blandford 1995; Cavaliere & Vittorini 2002; Murali et al 2002; Steed & Weinberg 2004) describes the evolution of the mass function and yields hints on the relation between the local mass function of inactive SMBHs and the past history of accretion or merging of BHs. Following Yu & Lu (2004), continuity equation reads

$$\frac{\partial n(L,t)}{\partial t} + \frac{\partial(<\dot{L}> n(L,t))}{\partial L} = S(L,t), \tag{5.20}$$

where $n(L,t)$ is the luminosity function at time t, contributed by SMBHs of any present-day mass $M_\bullet^0$, turned on at any time $t_i \leq t$, $< \dot{L} >$ is the luminosity derivative averaged over initial times t_i and present-day mass $M_\bullet^0$ and $S(L,t)$ is the source term.

If the accreted mass is most of the relic mass in local BHs, it follows that the initial seeds have $M_\bullet^i \ll M_\bullet^0$. We want to explore the case in which most of the present day mass of SMBHs has been accumulated in accretion episodes traced by light, hereafter denoted as the luminous accretion case. In this framework we can assume that the seeds are 'in place' and that the source term can be neglected in the continuity equation. Yu & Lu (2004) have shown that for the luminous accretion case the observed AGN luminosity function $n(L,t)$ is related to the present day SMBH MF by

$$\frac{1-\epsilon}{\epsilon c^2}\int_0^{t_0} dt \int_{\bar{L}}^{\infty} dL k_{\rm bol} L n(L,t) = \int_0^{\infty} dM_\bullet^0 \times$$

$$n(M_\bullet^0)\int_{\bar{L}}^{\infty} dL \dot{M}_\bullet \tau_{\rm vis}(M_\bullet^0) P(L \mid M_\bullet^0)\,, \tag{5.21}$$

where $n(M_\bullet^0)$ is the local number density of SMBHs with present day mass $M_\bullet^0$. The luminosity $L_{\rm min}$ is the minimum luminosity required for an AGN to be included in the LF , and the time $\tau_{\rm vis} = \tau(L \geq L_{\rm min} \mid M_\bullet^0)$ is the total visibility time $\tau_{\rm vis}$, *i.e. the total time spent by the SMBH in the active, visible phase with* $L \geq L_{\rm min}$. $P(L \mid M_\bullet^0)dL$ is the fraction of the active, visible phase with luminosity in the range $L \rightarrow L + dL$ (Yu and Lu 2004). $\bar{M}_\bullet^0$ is the present day BH mass of an AGN that had a maximum luminosity $\bar{L}$. Notice that l.h.s. of Eq. (5.21) is just the r.h.s. of Eq. (5.3). This equation represents the conservation of mass. In the same framework, conservation in number can be written as

$$\int_0^{t_0} dt \int_{\bar{L}}^{\infty} dL n(L,t) = \int_0^{\infty} dM_\bullet^0 \times$$

$$n(M_\bullet^0)\int_{\bar{L}}^{\infty} dL \tau_{\rm vis}(M_\bullet^0) P(L \mid M_\bullet^0)\,. \tag{5.22}$$

In the limit of $\bar{L}$ and $\bar{M}_\bullet^0$ vanishing, the innermost integrals in r.h.s. of Eq. (5.21) and Eq. (5.22) will reduce to $M_\bullet^0$ and to $\tau_{\rm vis}(M_\bullet^0)$ respectively.

If we want to exploit the luminosity and mass dependence of Eq. (5.21) and Eq. (5.22), we have to specify the relationship between mass and luminosity during the

luminous accretion. Following Eq. (5.1) we get

$$P(L \mid M_\bullet^0)dL = \frac{dL/\dot{L}}{\int_{L_{\rm min}}^{L_{\rm max}} dL/\dot{L}} = \frac{dL/\dot{L}}{\tau_{\rm vis}(M_\bullet^0)}\,. \tag{5.23}$$

where the maximum bolometric luminosity is reached at some fiducial time $t_{\rm max}$, after an interval $\tau_{\rm vis}$, during which the AGN is included in the LF since $L_{\rm min} \leq L \leq L_{\rm max}$. We remind that in Eq. (5.21) and Eq. (5.22) $\bar{L}$ is the maximum luminosity reached during the active phase by a BH of present day mass $\bar{M}_\bullet^0$. Inserting Eq. (5.23) in Eq. (5.21) we then recover Eq. (5.19) (see Yu & Lu 2004 for details).

In Fig. 5.5 the estimated AMF derived from the epoch-dependent X-ray LF by U03, assuming Eddington limited accretion ($\lambda = 1$), is compared with the local SMBH MF (including SMBHs hosted by both early- and late-type galaxies). Although the two curves are rather close to each other, their shapes differ. The fact that the assumption of Eddington limited accretion leads to an AMF exceeding the SMBH MF in some mass range shows that it cannot be true for all epochs and/or luminosities. Indeed, as discussed in Chapter 2, Section 2.2.1, low-z/low luminosity AGNs are known to be radiating well below the Eddington limit (Wandel et al. 1999), as recent estimates (Chapter 2) suggest for quasars up to $z \simeq 2$ (McLure & Dunlop 2004; Vestergaard 2004).

The match between the AMF and the local SMBH MF indeed improves significantly (Fig. 5.6) if we adopt a redshift dependent Eddington ratio of the form:

$$\begin{aligned} \lambda(z) &= \lambda_0 & \text{if } z \geq 3 \\ &= \lambda_0[(1+z)/4]^\alpha & \text{if } z < 3 \end{aligned} \tag{5.24}$$

with $\lambda_0 = 1$ and $\alpha = 1.4$. The discrepancy at $M_\bullet \geq 10^9\ M_\odot$ is only marginally significant being slightly more than 1σ level. On the other hand, the generally higher AMF estimate derived from the X-ray, compared to that from the optical, LF (see Fig. 5.6), reflects the strong luminosity dependence of the fraction of Type 2 AGNs, which are represented in the X-ray, but not in the optical, LF. X-ray surveys (see, e.g., Hasinger 2003) have shown that the Type 2 fraction increases from $\simeq 30\%$ at high luminosities ($L_{2-10\,\rm keV} \geq 10^{44}\,\rm erg\,s^{-1}$) to $\simeq$ 70–80% at low luminosities ($L_{2-10\,\rm keV} \leq 3 \times 10^{42}\,\rm erg\,s^{-1}$), consistent with the results of optical spectroscopic surveys of complete samples of nearby galaxies, without pre-selection

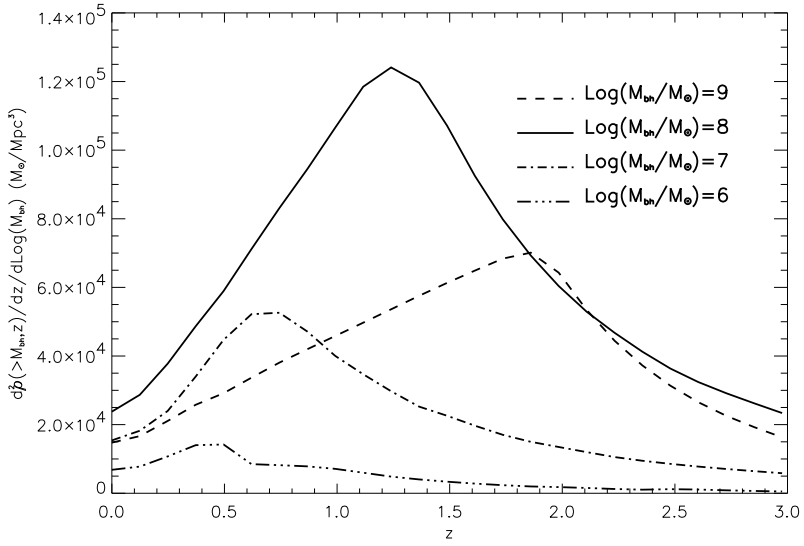

Figure 5.9: Contributions to the local SMBH MF as a function of redshift, for several values of $M_\bullet^0$.

(Huchra & Burg 1992; Ho et al. 1997). As a check, we have computed and plotted in Fig. 5.7 the cumulative accreted mass density function obtained by summing the contribution of the optically selected QSOs to that of Type 2 X-ray selected AGNs; again, the agreement with the local SMBH mass density function is very good. We checked that a dependence of λ on luminosity, as suggested by Salucci et al. (1999), rather than on redshift, yields an equally good fit.

Requiring that the AMF matches the local SMBH MF we obtain constraints on the radiative efficiency and on the maximum value of the Eddington ratio [Eq. (5.24)]. A minimum χ^2 analysis yields $\epsilon \simeq 0.09\,(+0.04, -0.03)$ and $\lambda_0 \simeq 0.3\,(+0.3, -0.1)$ (68% confidence errors; see Fig. 5.8). The constraints on the parameter α ruling the evolution of the Eddington ratio [Eq. (5.24)] are rather loose ($0.3 \leq \alpha \leq 3.5$).

5.3 Accretion history and AGN visibility times

Replacing t_0 with t in Eq. (5.19) and differentiating with respect to z and $\bar{M}_\bullet^0$ we get the contributions to the $n(M_\bullet^0)$ from different cosmic epochs, shown for several values

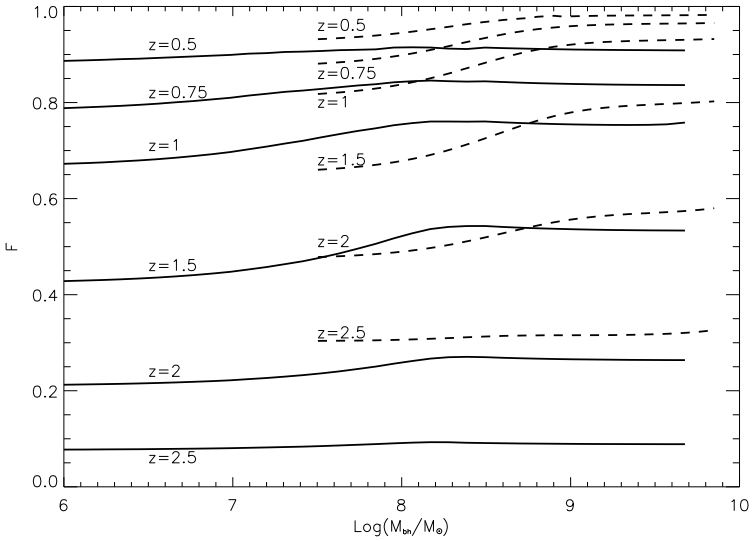

Figure 5.10: Fraction of the final accreted mass as function of mass and redshift. Solid and dashed lines refer to accretion evaluated exploiting Hard X-ray LF of AGN and optical LF of QSOs respectively.

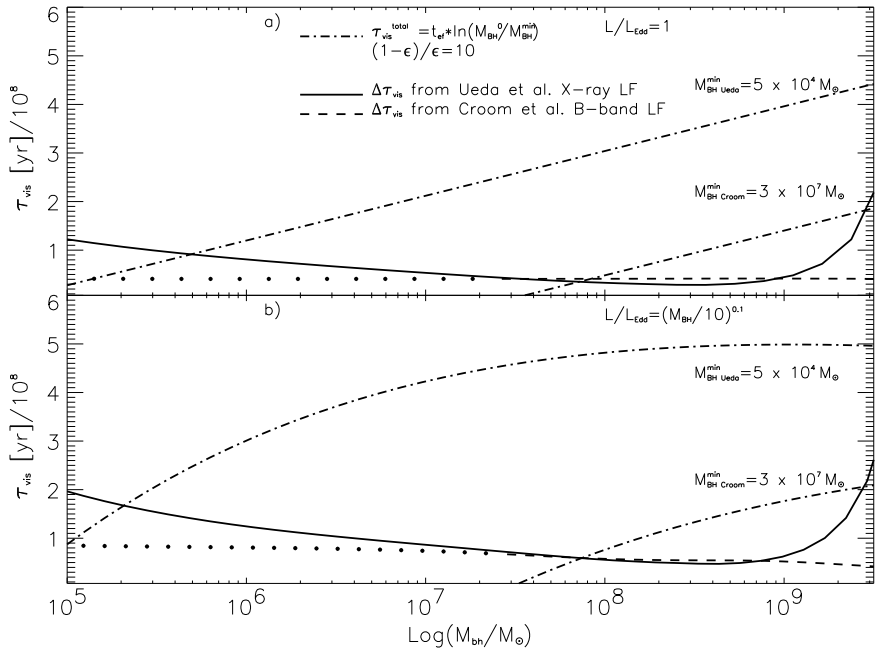

Figure 5.11: Lower and upper limits to the visibility time scales using a constant $\lambda = 1$ (panel *a*) and using a non-constant $\lambda = (M_\bullet/10^{10}M_\odot)^{0.1}$ (panel *b*). The dotted line indicates the extrapolation of the optical AGN luminosity function to magnitudes fainter than $M_B = -22.5$.

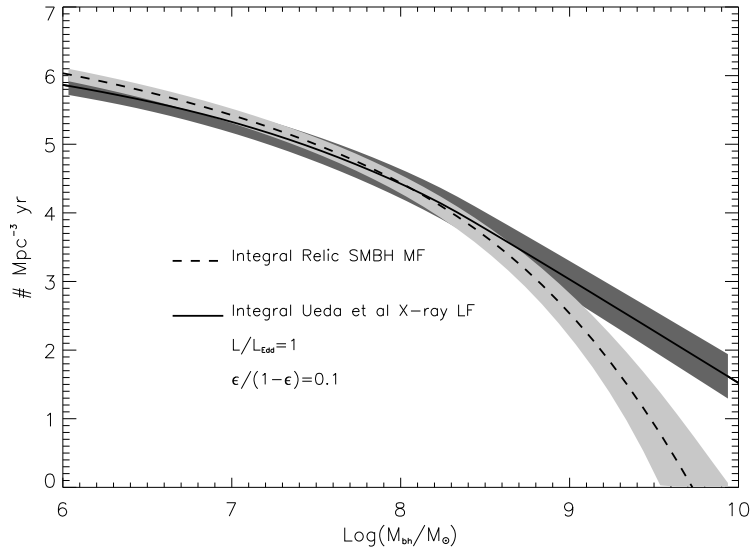

Figure 5.12: Comparison between the cumulative number of AGN and the relic SMBH population under the hypothesis of an exponential growth light curve.

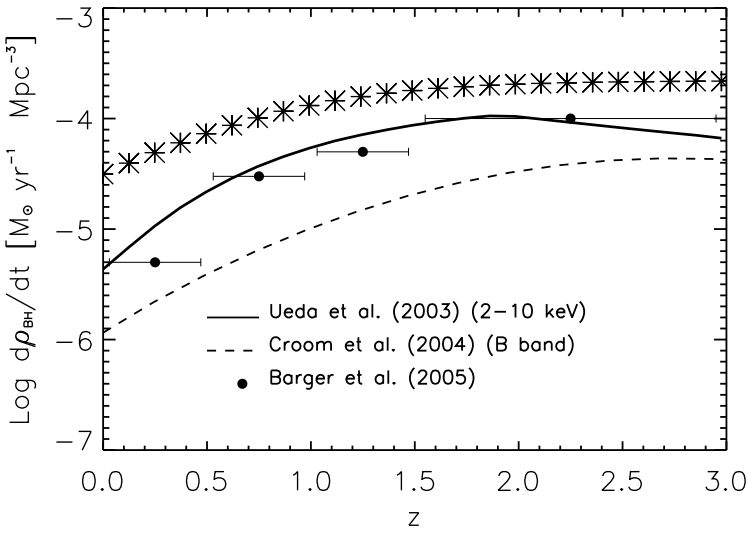

Figure 5.13: Comparison between the SMBH Accretion Rate Density computed with the Ueda et al. (2003) HXLF and with optical LF and the data by Barger et al. (2005). Stars: SFR divided by the factor $2 \cdot 10^{-3}$, equal to the observed ratio $M_\bullet - M_{\rm sph}$.

of $\bar{M}^0_\bullet$ in Fig. 5.9, which evidences that mass is accreted earlier and more rapidly by the more massive BHs.

From Eq. (5.3) we can get the time dependence of the mass accumulated in BHs with $M > \bar{M}^0_\bullet$

$$\rho_{\rm acc}(> \bar{M}^0_\bullet, t) = \frac{1-\epsilon}{\epsilon c^2} \int_0^t dt' \int_{\bar{L}}^\infty dL k_{\rm bol} L n(L, t'), \tag{5.25}$$

with $\bar{L} = \lambda \bar{M}^0_\bullet c^2 / k_{\rm bol} t_E$. In Fig. 5.10 the ratio

$$F = \frac{\rho_{\rm acc}(> \bar{M}^0_\bullet, t)}{\rho_{\rm acc}(> \bar{M}^0_\bullet, t_0)}, \tag{5.26}$$

is shown as function of mass for the Hard X-ray LF and for the optically selected QSOs. F is independent of ϵ, but, due to the dependence on luminosity $\bar{L}$ it depends, though weakly, on $k_{\rm bol}$ and λ. It is apparent that the accretion on X-ray selected AGN is occurring in the redshift interval $0.5 \leq z \leq 2$, while for optically selected QSOs most of the mass is already in place at $z \simeq 1.5$. The mass dependence of the ratio F shows that mass is more rapidly accumulated in more massive BHs.

The inner integral of the l.h.s. of Eq. (5.22) represents the time interval during which a BH of present day mass $M^0_\bullet$ exhibit a luminosity $L > \bar{L}$. In fact using Eq. (5.23) we can write

$$\int_{\bar{L}}^\infty dL \tau_{\rm vis}(M^0_\bullet) P(L \mid M^0_\bullet) = \int_{\bar{L}}^\infty \frac{dL}{\dot{L}} = \tau_{\rm lum}(L \geq \bar{L} | M^0_\bullet)\,. \tag{5.27}$$

Therefore the average time spent by a SMBH with $L \geq \bar{L}$ reads as

$$\langle \tau_{\rm lum} \rangle = \frac{\int_0^{t_0} dt \int_{\bar{L}}^\infty dL \Phi(L,t)}{\int_{\bar{M}^0_\bullet}^\infty dM^0_\bullet n(M^0_\bullet)}. \tag{5.28}$$

In the limit $\bar{L} \to L_{\rm min}$ we get $\langle \tau_{\rm lum} \rangle = \langle \tau_{\rm vis} \rangle$. The equation states that $\langle \tau_{\rm lum} \rangle$ is independent of the efficiency, as noted by Yu and Tremaine (2002), but it depends on $k_{\rm bol}$ and λ. Also it may vary with the e.m. band in which the LF has been defined, since, for instance, the amount of absorption significantly depends on the observational wavelengths. This lower limit, computed using the U03 LF and the best estimate of the Local MF, is very weakly dependent on the BH mass, except at $M_\bullet > 10^9 M_\odot$, where the X-ray LF predicts a MF of the accreted mass larger than the local MF (see Fig. 5.11).

We have also estimated the same limit only for optically selected QSOs (Fig. 5.11; dashed lines). The two limits are very similar for $M_\bullet > 10^7\ M_\odot$. This result depends on the relationship between the present-day mass of a BH and the corresponding maximum luminosity, which in turn depends on the assumption $\dot{M}/M_\bullet$ =constant.

Adopting the U03 LF, we find $\langle \tau_{\rm lum} \rangle \simeq 1.5{\times}10^8$ yr if we adopt a redshift-dependent Eddington ratio [Eq. (5.24)] and $\simeq 8 \times 10^7$ yr if we keep $\lambda = \lambda_0$.

We stress that this is however a lower limit to the time interval $\tau_{\rm vis}$, spent at $L \geq L_{\rm min}$. If $\dot{M}/M_\bullet = {\rm const}$, the duration of the visible phase is simply:

$$\tau_{\rm vis}(M_\bullet^0) = t_{ef} \ln \left[\frac{L_{\rm max}(M_\bullet^0)}{L_{\rm min}} \right] = t_{ef} \ln \left[\frac{M_\bullet^0}{M_\bullet^{\rm min}} \right], \tag{5.29}$$

where $M_\bullet^{\rm min}$ is the BH mass when radiative accretion yields luminosity $L \geq L_{\rm min}$ (Fig. 5.11; dot-dashed lines). In the case of the X-ray LF of U03, the minimum 2–10 keV luminosity included at $z \simeq 0.8$, where the contribution to the X-ray background peaks, is $\log(L_{\rm min}) \simeq$ 42–42.4. With the bolometric correction given by Eq. (5.12), the corresponding minimum BH mass is:

$$M_\bullet^{\rm min} = \frac{5 \times 10^4}{\lambda} \frac{L_{\rm min}}{10^{42} {\rm erg\,s^{-1}}}\ M_\odot. \tag{5.30}$$

The minimum BH mass contributing to the LF of optically selected QSOs for the bolometric correction by Elvis et al. (1994) is :

$$M_\bullet^{\rm min} = \frac{3 \times 10^7}{\lambda} 10^{-0.4(22.5+M_B^{\rm max})}\ M_\odot, \tag{5.31}$$

where $M_B^{\rm max} \simeq -22.5$ (Boyle et al. 2000; Croom et al. 2003).

Using Eq. (5.27) and Eq. (5.29) the number conservation expressed in Eq. (5.22) can be written as

$$\begin{aligned} &\int_0^{t_0} dt \int_{\bar{L}}^{\infty} dL n(L,t) \\ &= \ t_{ef} \int_0^{\infty} dM_\bullet^0 n(M_\bullet^0) \ln \left(\frac{M_\bullet^0}{\bar{M}_\bullet^0} \right), \end{aligned} \tag{5.32}$$

which adds further, independent constraints on ϵ and λ_0 (see Fig. 5.12). Using the U03 LF and assuming a 30% uncertainty on the bolometric correction for X-ray luminosities, we find an allowed range for ϵ pretty similar to that following from the match between the

AMF and the local SMBH mass function ($0.06 \leq \epsilon \leq 0.13$) while the constraints on the Eddington ratio are looser ($0.5 \leq \lambda_0 \leq 2$).

To conclude the section we have also estimated the redshift dependent Accretion Rate Density (ARD) $d\rho_\bullet/dz$, i.e. the total mass density accreted at any time. In Fig. 5.13 we compare the ARD with the $SFR(z)\cdot(2\cdot10^{-3})$, rescaled by the observed ratio $M_\bullet - M_{\rm sph}$. It is straightforward to check the close link in time evolution of the stars and SMBH accretion histories. At $z \leq 1$ the ARD starts dropping more rapidly than the SFR, due to the fact that the latter is dominated by star formation in disks at these redshifts (see also Chapter 8).

5.4 Comparison with previous works

The formalism developed in Eq. (5.21), Eq. (5.22) and Eq. (5.23) simply converts the *source-free* (i.e. with negligible creation/destruction of SMBH) continuity equation into Eq. (5.19). Small & Blandford (1985) and Marconi et al. (2004) use the mass continuity equation written in Eq. (5.20) in terms of mass as

$$\frac{\partial n(M,t)}{\partial t} + \frac{\partial(< \dot{M}(M,t) > n(M,t))}{\partial M} = S(M,t), \tag{5.33}$$

where now with M we indicate the *current* SMBH mass at the time t. The "average" accretion rate $< \dot{M}(M,t) >$ is then converted to an *instantaneous* accretion rate, $\dot{M} = L_{\rm bol}(1-\epsilon)/\epsilon\, c^2$, as

$$< \dot{M}(M,t) >= \frac{M}{t} = \frac{M}{\tau_{\rm lum}}\frac{\tau_{\rm lum}}{t} = \delta(M,t)\dot{M}, \tag{5.34}$$

where $\delta(M,t)$ is the duty cycle, in principle dependent on mass/luminosity and time. Therefore the number of comoving AGN per luminosity bin can be set to $\Phi(L,t)d\ln L = \delta(M,t)N(M,t)dM$, here $\delta(M,t)$ indicating the fraction of active SMBH of mass M at time t. Eq. (5.33) can then be rewritten as

$$\begin{aligned} n(M,t) < \dot{M}(M,t) >&= \frac{\lambda(1-\epsilon)}{\epsilon t_E}[\Phi(L,t)]_{L=\lambda\frac{Mc^2}{t_E}} \\ \frac{\partial n(M,t)}{\partial t} &= -\frac{c^2\lambda^2(1-\epsilon)}{\epsilon t_E^2}\left[\frac{\partial\Phi(L,t)}{\partial L}\right]_{L=\lambda\frac{Mc^2}{t_E}} . \end{aligned} \tag{5.35}$$

As shown by Marconi et al. (2004) the solution is almost independent of the initial condition, fixed at high redshift. Merloni (2004) instead follows the SMBH evolution backwards setting the boundary at $z = 0$ $n(M, t_0)dM = n(M_\bullet)dM_\bullet$, where $n(M_\bullet)$ is the SMBH relic MF.

However, to describe the *average* drift of the $n(M, t)$ function in the time step δt, the average accretion rate should be calculated at a given time t averaged over the whole SMBH population at that time (Merloni 2004; Steed & Weinberg 2004; Yu & Lu 2004):

$$< \dot{M}(M,t) >= \frac{\int_M^\infty n(M,t)\dot{M}(M,t)dM}{\int_M^\infty n(M,t)dM}\,. \tag{5.36}$$

Eq. (5.34) can be considered as a sufficient approximation of Eq. (5.36) only in special conditions, i.e. when the accretion rate does not significantly depend on mass $\dot{M}(M,t) \sim \dot{M}(t)$. Moreover if one adopts Eq. (5.16) as the reference light curve for SMBH growth, then the instantaneous accretion rate $\dot{M}(t)$ rises exponentially. Therefore one expects the instantaneous accretion rate $\dot{M}(t)$ being significantly different from the accretion rate M/t averaged over the elapsed time t, being the discrepancy even stronger within the last e-folding times, relevant for SMBH shining, when the rise in $\dot{M}(t)$ becomes even steeper.

Moreover in this Chapter we have found a lower limit to the average visible time, $\langle \tau_{\rm lum} \rangle \geq (4 - 10) \times 10^7$ yr, through the statistical comparison between AGN and SMBH demography, a computation which is independent of the radiative efficiency. Another way to probe the AGN luminous timescales is to use *clustering* analysis. Martini & Weinberg (2001) find a visible time $\tau_{\rm lum} \sim 10^7$ yr for a clustering length for optical QSO of $r_1 \sim 10h^{-1}$ Mpc. There are several uncertainties in this method (Martini 2004), such as the presence of a scatter between halo mass and QSO luminosity/SMBH mass (which might be present, as it will be discussed in Chapter 6), which could produce systematic off-sets in the results.

However the latest studies on the topic have confirmed (and actually increased!), the result by Martini & Weinberg (2001), finding an average value $\tau_{\rm lum} \sim$ a few 10^7 yr (e.g. Porciani et al. 2004). Clustering results seem to be therefore very close to the findings of this Chapter (cfr. Fig. 5.11).

As stated above, we find that the visible time gets longer to about $\tau_{\rm lum} \sim 10^8$ yr for the visible X-ray selected AGN and ongoing analysis of *Chandra* data on the clustering of X-ray selected sources will probably confirm such results (see Gilli et al. 2005). The

longer visible timescales for X-ray AGN is due to the fact that X-rays are less absorbed and the visible objects in the hard electromagnetic bands shine longer. In Chapter 6 we'll get deeper into the analysis and physical meaning of the AGN visible and total timescales exploiting the match between the S&T MF and the AGN LF.

Chapter 6

Fitting Active Galactic Nuclei Luminosity Function

In the previous chapter we have analyzed AGN statistics to infer global properties on the SMBH accretion history. Through the statistical match with local data, we have been able to set lower limits on the AGN *visible* times which we find to be $\geq 4 \times 10^7$ yr, the SMBH growth e-folding time. Within the framework of the Granato et al. co-evolution model, in this chapter we work out the AGN visible duty-cycle needed to reproduce the observed AGN statistics in the optical and Hard-Xray bands, and we discuss the physical meaning of such timescales, comparing them with the previous results.

6.1 Previous models

Fitting AGN LF has proven a real challenge for galaxy evolution models. The usual method followed is to set a link between the SMBH mass and the halo mass, as given by, e.g. a feedback relation (see Chapter 3, Section 3.4.2) or a constant ratio (Haiman & Loeb 1998). In particular Wyithe & Loeb (2003; WL hereafter) provide the *feedback constrained* relation

$$M_\bullet(M_{\rm vir}, z) = \epsilon M_{\rm vir} = \epsilon_0 M_{\rm vir} \left(\frac{M_{\rm vir}}{10^{12}\, M_\odot}\right)^{2/3} [\xi(z)]^{5/6}\, (1+z)^{5/2}\,, \qquad (6.1)$$

where the constant ϵ_0 is fixed from the fit to the $M_\bullet - \sigma$ relation, which can be recovered from Eq. (6.1) imposing that the total energy released by the AGN overcomes the DM potential well (see Eq. (3.95) in Chapter 3).

The comoving number of AGN/SMBH at any redshift is then provided by the DM halo rate of formation according to the equation

$$\Phi(L,z) = \int_z^\infty dz \int_0^\infty dL \frac{dM_\bullet}{dL} \frac{dM_{\rm vir}}{dM_\bullet} R(M_{\rm vir}, z') \delta[L - M_\bullet f(z,z')] \,. \tag{6.2}$$

The δ function limits the integration to only those AGN which formed at any redshift $z' \geq z$ that shine at z with luminosity L following the growth of the *light curve* $f(z,z')$. Here for $R(M_{\rm vir}, z)$ (see discussion Chapter 3, Section 3.3.5) we define the formation rate of virial objects which host an AGN.

However, as shown e.g. by Granato et al. (2001) and WL, Eq. (6.2) can be further simplified considering the duty-cycle for AGN activity, $t_{\rm vis}$ much shorter than the cosmological time at all redshifts $z \leq 6$, as shown by statistical and clustering techniques (Chapter 5). Thus one can write

$$\Phi(L,z) \simeq t_{\rm vis} R(M_{\rm vir}, z) \frac{dM_{\rm vir}}{dM_\bullet} \frac{dM_\bullet}{dL} \,. \tag{6.3}$$

WL and Mahmood et al. (2004; M04 hereafter) in particular have followed Eq. (6.3) aiming at fitting both the AGN LF at all redshifts and the local SMBH mass function.

Haehnelt et al. (1998) have shown that an equally good fit to the high redshift AGN LF could be gained either by using a $M_\bullet - M_{\rm vir}$ relation very similar to Eq. (6.1) with a visible timescale of a few 10^7 yr, or with a simple $M_\bullet \sim 10^{-4}\, M_{\rm vir}$ proportion with a few 10^5 yr as duty-cycle. However, as shown in Chapter 5, any model which aims at reproducing the overall AGN statistics at all redshifts and at the same time reproduce the local SMBH mass function through accretion episodes, must account for a radiative efficiency of the order $\epsilon \sim 0.1 - 0.15$, which corresponds to an e-folding time $t_{\rm ef} \sim 4 \cdot 10^7$yr and a luminous time $\tau_{\rm lum} \geq 4 \cdot 10^7$ yr (see Eq. 5.28). WL and M04 have however found that the best fit for the model defined in Eq. (6.3) is obtained if one sets

$$t_{\rm vis} = 0.035 t_{\rm dyn} = 0.035 \frac{R_{\rm vir}}{V_{\rm vir}} = 0.035 \cdot 1.5 \cdot 10^9 \left[\frac{\Omega_m}{\Omega_z} \frac{\Delta_{\rm vir}(z)}{18\pi^2} \right] \,, \tag{6.4}$$

where $\Delta_{\rm vir}(z)$ has been defined in Eq. (3.24) and Ω_z in Eq. (3.15). The proportionality constant is derived assuming that the cold gas of the AGN host galaxy is located in a disk with a characteristic radius $(\lambda/\sqrt{2})R_{\rm vir} \sim 0.035 R_{\rm vir}$ (with $\lambda \sim 0.05$ and supposing conservation of angular momentum; see Chapter 3, Section 3.4.3).

However it is easy to check that for $z \geq 4$, $t_{\rm vis} \leq 10^7$ yr, approaching $(1/10) \times t_{ef}$ for $z = 6$. Such models can hardly explain, in light of the Soltan's argument discussed in Chapter 5, how these high-redshift ultra-luminous AGN, being active for a so short timescale, have been able to accumulate so much mass to become the most massive SMBH in the Universe. Moreover Eq. (6.1) predicts too massive SMBH with respect to observations, of the order of $10^{11}\, M_\odot$, at $z \sim 6$.

We compute the relic SMBH MF as implied by the AGN LF exploiting the duty cycle in Eq. (6.4)

$$\frac{dn}{dM_\bullet} = \int_0^\infty \frac{t_H(z)}{t_{\rm vis}(z)} \frac{dL}{dM_\bullet} \Phi(L, z) dz \,. \tag{6.5}$$

In Fig. 6.1 we show the total AMF as given by Eq. (6.5) using the Pei (1995) LF. The result is about a factor of 2 higher than the local estimate at the level of $\sim 10^8\, M_\odot$, up to a factor of 3-4 at $M_\bullet \sim 10^7\, M_\odot$. This result is a direct consequence of the short visible timescales in Eq. (6.4), which in turn implies a low radiative efficiency and more mass accreted (see Chapter 5, Eq. 5.17 and Eq. 5.3).

The model expressed in Eq. (6.3) is highly dependent on the type of Cosmological model used for describing the DM halo evolution. Firstly for a fixed $M_\bullet - M_{\rm vir}$ relation, the AGN statistics in Eq. (6.3) is fixed by the product of the number of newly formed halos and the visible time. The result found by WL in Eq. (6.4), was obtained by using the EPS theory for the DM rates. However after the discussion in Chapter 3 (Section 3.3.5), the $\dot{n}^+_{S\&T}$, which provides a number of new virilized halos up to a factor of 10 higher than the EPS, provides a better fit to N-body numerical simulations. Therefore inserting the $\dot{n}^+_{S\&T}$ in Eq. (6.3), one would find even shorter visible timescales to recover the fit to the AGN LF. As an example in Fig. 6.2 we show that using the S&T rates the best fit to the data at $z = 4.3$ is obtained using the timescale in Eq. (6.4) divided by a factor 3, which means $t_{\rm vis} \sim 3 \times 10^6$yr. Even shorter timescales, approaching $\sim 10^5$ yr, would be needed at higher redshifts. The choice of a different matter density power spectrum also has significant

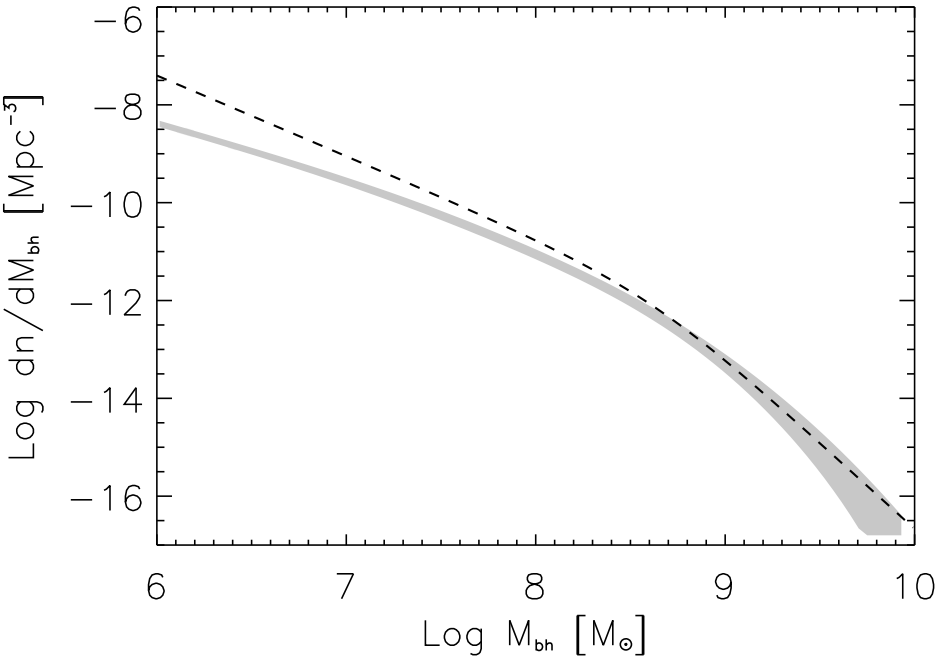

Figure 6.1: Dashed line: the predicted SMBH relic Mass Function as computed by the model in Eq. (6.5) given the duty-cycle in Eq. (6.4). The gray area is the 1-σ uncertainty region of the SMBH mass function computed in Chapter 4.

effects on the statistics of DM halos. WL and M04 use a simple power spectrum without correction for baryons which instead (see Chapter 3, Eq. (3.27) and Eq. (3.28)) decreases the number of halos in the S&T MF of about a factor from 2 to 3 at $z = 4.3$, and up to a factor of 10 at $z \sim 6$ at halo masses of about $10^{13}\,M_{\odot}$, relevant for luminous AGN. Such a property, providing a lower number of DM halos at any given redshift, allows for a mild/strong increase of the AGN visible timescale (see Eq. (6.3)).

A similar, but minor, effect on the number density at high masses is played by the cosmological parameter σ_8, the normalization of the field mass variance (see Eq. (3.30)), which however we have set equal to the most recent estimate from the WMAP released data. Increasing its value, increases the number of massive halos, as σ_8 provides the power at big scales ($R = 8\,\mathrm{h}^{-1}\mathrm{Mpc}$).

As reported in Granato et al. (2004) and in Chapter 3, we extend our galaxy evolution code to halos with mass $\log(M_{\rm vir}/M_{\odot}) \leq 13.2$. This limit in the DM halo mass which can host a single galaxy provides the best fit to the galaxy LF and to the dispersion velocity

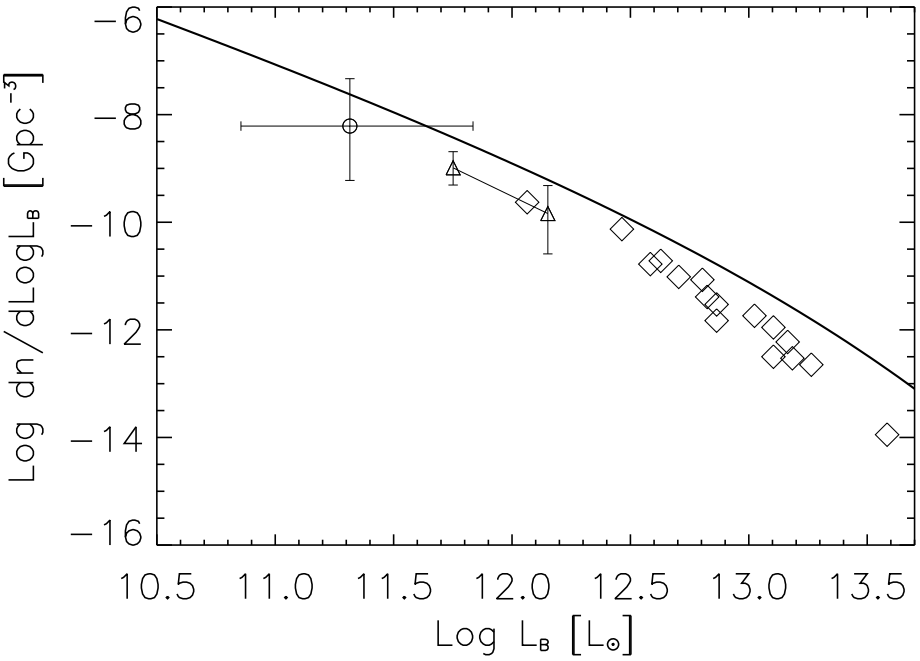

Figure 6.2: The predicted AGN optical LF at $z = 4.3$ following Eq. (6.3), Eq. (6.1) and Eq. (6.4) using $\dot{n}^{+}_{S\&T}$. The best fit is obtained by dividing the visibility $t_{\rm vis}$ by a factor of 3. Squares: data by Fan et al. (2001) and (2003), and by Kennefick et al. (1995); triangles: data by COMBO-17 (Wolf et al. 2001); circle: data by GOODS (Cristiani et al. 2004).

function of local galaxies (see Chapter 7). Such a limit is also supported by observational evidence from lensing (Kleinheinrich et al. 2004) and statistical analysis (see Chapter 8).

If we take into account such a cut-off and using Eq. (6.4), we find that using the model in Eq. (6.3) the optical AGN LF at $z = 3$ is reproduced only at luminosities below $\log(L_B/L_\odot) = 13.1$ (see Fig. 6.3). To have a global fit to the data, we need to extend the model beyond $\log(M_{\rm vir}/M_\odot) \geq 13.2$. At lower redshifts in particular the model presented in Eqs. (6.3) and (6.4) is able to fit the overall AGN LF only if we allow DM halos of mass $M_{\rm vir} \sim 10^{14}\, M_\odot$ to harbor AGN. However DM halos of such masses are known to usually host group of galaxies (see Chapter 8, Figs. 8.2 and 8.3), as their long cooling times prevent the formation of single galactic cores. To solve this problem M04 have limited the creation of AGN in halos of mass $\log(M_{\rm vir}/M_\odot) \leq 13.2$ and have empirically inserted a lorentzian tail beyond this limit. Through such a device the authors can extend the fit to the bright tail of the AGN LF.

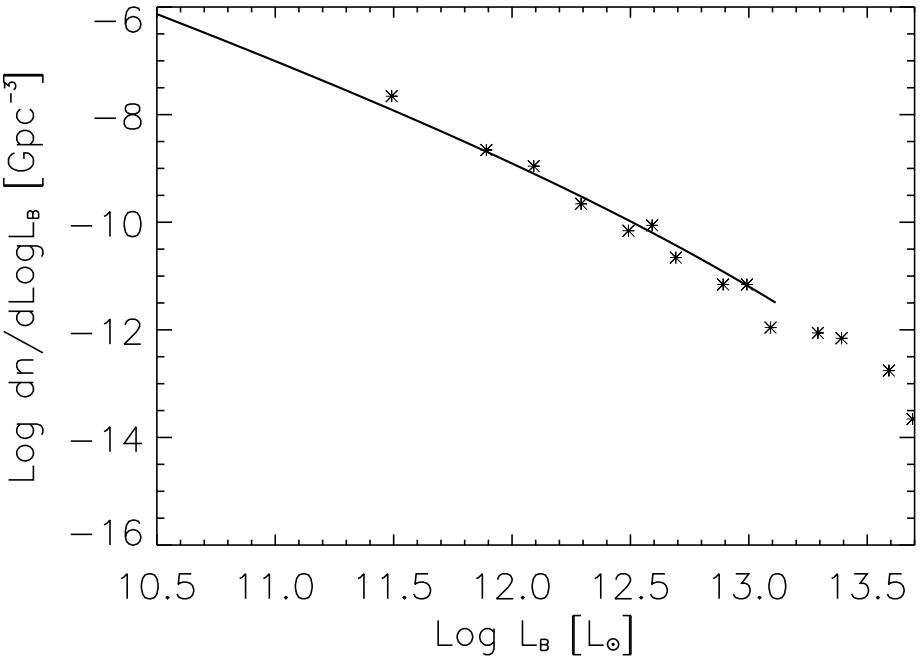

Figure 6.3: AGN Luminosity Function computed at $z = 3$ through Eq. (6.3) and Eq. (6.4); stars: data from Pei (1995).

In our model instead we consider a scatter of about 0.3 dex in $\log M_\bullet$ at fixed halo mass $M_{\rm vir}$ and virialization redshift $z_{\rm vir}$ which can effectively produce a gaussian tail in the SMBH MF, and therefore in the AGN LF, beyond the limit of $2 \times 10^{13}\, M_\odot$. Within the framework of the Granato et al. model, between the spheroid and the central SMBH we expect a negligible scatter. In fact the growth of the stellar component and of the central BH are strictly symbiotic, double tied by the positive effect of the photon drag, proportional to the star formation rate, favoring the inflow toward the reservoir around the central BH, and by the negative effect of the BH growth, powering outflows (see Chapter 3 and Chapter 7, Fig. 7.6). Instead plausibly a larger dispersion between the host DM halo and the SMBH mass could occur, due to the fact that the feedback in this case is unilateral, from the SMBH to the surrounding DM and therefore the latter relation could be not as tight as the former one.

6.2 AGN LF from delayed Black Hole activity

Our target is to compute the AGN LF improving on previous assumptions and inserting new elements regarding the physiics of baryons. In particular we assume, following Monaco et al. (2000) and Granato et al. (2001), the peak of the AGN activity delayed by a time interval $t_{\rm delay}$ with respect to the host DM halo virialization epoch at $t_{\rm vir}$.

Following Chapter 3, Section 3.4.2 (in particular Eqs. (3.84), (3.85) and (3.86)) the light curve built in our model is characterized by two phases (see also Figs. 6.5 and 6.6).

1. Initially the BH starts growing at $t_{\rm vir}$, from an initial seed which we suppose already in place at the galactic center with $M_{\rm seed} \sim 10^2\, M_\odot$ (Chapter 3, Section 2.3). The BH accretes at a fraction $\lambda = \dot{M}/\dot{M}_{\rm Edd}$ of the Eddington rate, and reaches a final mass $M_{\rm peak}$ (at the shining time $t_{\rm sh} = t_{\rm vir} + t_{\rm delay}$). In this phase, the star formation is very high (see Fig. 6.5 right panel) and therefore the consequent reservoir mass growth is very rapid (Eq. (3.85)). The condition in Eq. (3.86) then favors an Eddington-limited accretion, being the accretion rate high enough to sustain the pressure-supported accretion limit (see Chapter 2, Section 2.2.1). The AGN during the main growth phase before the peak of activity is obscured by the surrounding dust in the galaxy, therefore it could possibly be detected only in the Hard-Xrays and the proto-galaxy will appear as a submillimeter source (see Chapter 3). It is worth recalling that detections of Hard-Xray AGN activity have been claimed in the majority ($\sim 70\%$) in the sample of SCUBA galaxies by Alexander et al. (2005).

2. After a time $t_{\rm delay}$, when the central SMBH will be enough massive and luminous to remove most of the gas and dust from the surroundings, the galaxy system will shine as an optical AGN, i.e. $t_{\rm delay} \sim t_{\rm wind}$ (Chapter 3, Eq. (3.97)). Due to the delay, following Eq. (6.2), the computation of the AGN LF, $\Phi(L, t_{\rm sh})$, is done associating to it a lower numeric weight of DM rates, i.e. the one at the time $t_{\rm vir} < t_{\rm sh}$, which in turn enables us to increase the visibility time $t_{\rm vis}$ to recover the fit. The optical AGN LF and the bright part of the Hard-Xray AGN LF, provide constraints on the actual height of the peak in the AGN light curve. In fact most of the luminous tail in the AGN LF is

produced, as shown in Fig. 6.4, within a time $t_{\rm vis}$, around the peak in the $\dot{M}_\bullet$ curve. This is also the time when most of the AGN feedback energy is transmitted to the surrounding medium (see Chapter 3, comments before Eq. (3.100)). We expect that $t_{\rm vis}$ will depend on the wavelength in which we compute the AGN LF. In particular it will be longer for Hard-Xray AGN, being photon-absorption less strong in these bands. In our model, as it is clear from Figs. 6.5 and 6.6, the delay time is not much affected by the halo mass or virialization redshift. Instead being the SMBH growth exponential, the shorter is the Eddington ratio λ, the longer is the e-folding time (see Eq. (5.17)), and therefore the longer is the delay. From our code we get that for $\lambda \sim 3$, $t_{\rm delay} \sim (3-5)\times 10^8$ yr, while it increases to about a Gyr for $\lambda \sim 1$. This point highlights the need for higher Eddington ratios at higher redshifts in order to produce enough massive BH and luminous AGN by $z \sim 6$. In our model we set $\lambda \sim 3-4$ for $z_{\rm vir} \geq 5$ and $\lambda \sim 1-2$ for lower redshifts (see Appendix A).

3. After the peak, if the SFR drops by orders of magnitude (as in the right panel of Fig. 6.5) the subsequent infall onto the reservoir is negligible and the SMBH does not grow significantly anymore, therefore $M_{\rm relic} \sim M_{\rm peak}$. If instead the SFR is still substantial after the AGN blowout, the SMBH can still grow by factors of a few. Such a descendant phase could last for Gyr (cfr. Fig. 6.6, left panel). In this stage the SMBH grows at low accretion levels, from 10^{-5} to, maximum $10^{-1}\,M_\odot\,{\rm yr}^{-1}$ in the most massive halos. However it must be noted that the AGN LF faint-end and Hard-Xray number counts set a strong constraint on the actual descendent phase. As it will be shown more in detail below, this second accretion phase must not be very prolonged or at least it must occur at very radiative inefficient regimes (e.g. ADAF, see Chapter 2) as otherwise it would create too many faint objects with respect to observations. In the following we will only use the model shown in Fig. 6.5 which better reproduces the data. Such a result is in line with what discussed also by Yu & Lu (2004) through SMBH/AGN demographic comparisons.

In more detail we base our findings on the following assumptions.

- The formation rates of DM halos with mass $M_{\rm vir}$ at time $t_{\rm vir}$ are given by the

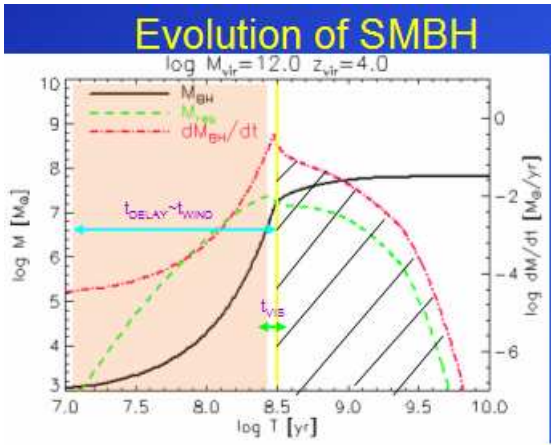

Figure 6.4: Light curve of an AGN as output of the numerical code for a $M_{\rm vir} = 10^{12}\,M_\odot$ at $z_{\rm vir} = 4$. The lines represent the growth of the SMBH mass (solid), of the reservoir mass (dashed) and the light-curve (dot-dashed). The dark area, delimited by the arrow marked as $t_{\rm delay} \sim t_{\rm wind}$, represents the time when the system, obscured by dust, appears as a SCUBA galaxy. The visibility time in the figure is about $t_{\rm vis} \sim 4 \times 10^7$ yr. The striped area represents an eventual descendant phase in the light curve.

positive term in the time derivative of the S&T MF (see Eq. (3.52)). We remind that we set the cutoff parameters to the fiducial values $z_- \approx 1.5$, $M_- \approx 10^{11.4}\,M_\odot$ and $M_+ \approx 10^{13.2}\,M_\odot$ therefore we force the formation rates to vanish outside these ranges in mass and redshift, but we include a gaussian dispersion of about 0.3 dex around the mean $M_\bullet - M_{\rm vir}$ at any redshift.

• The computation of the SMBH light curve is the output of the code by Granato et al. (2004) and it is the result, at each instant, of $\dot{M}_\bullet(t)$ given in Eq. (3.86) as a result of the set of differential equations exposed in Chapter 3, Section 3.4.2 and Appendix A. However during the exponential SMBH growth before the peak, it is possible to analytically express the AGN light curve produced by the code as in Eq. (6.6) to derive the main physical trends. The light curve can then be modeled as

$$L(t) = \frac{\lambda\, M_\bullet\, c^2}{t_{\rm Edd}}\, e^{(t - t_{\rm vir} - t_{\rm delay})/\tau_+}\, \theta_H\big(t_{\rm vir} + t_{\rm delay} - t_{\rm vis} \le t \le t_{\rm vir} + t_{\rm delay}\big)\ . \qquad (6.6)$$

Here $t_{\rm Edd} \approx 4 \times 10^8$ yr is the Eddington timescale, and here we call $\tau_+ \approx \epsilon\, t_{\rm Edd}/(1-\epsilon)\,\lambda$ the e-folding time (see Chapter 5) in terms of the BH mass-energy conversion efficiency

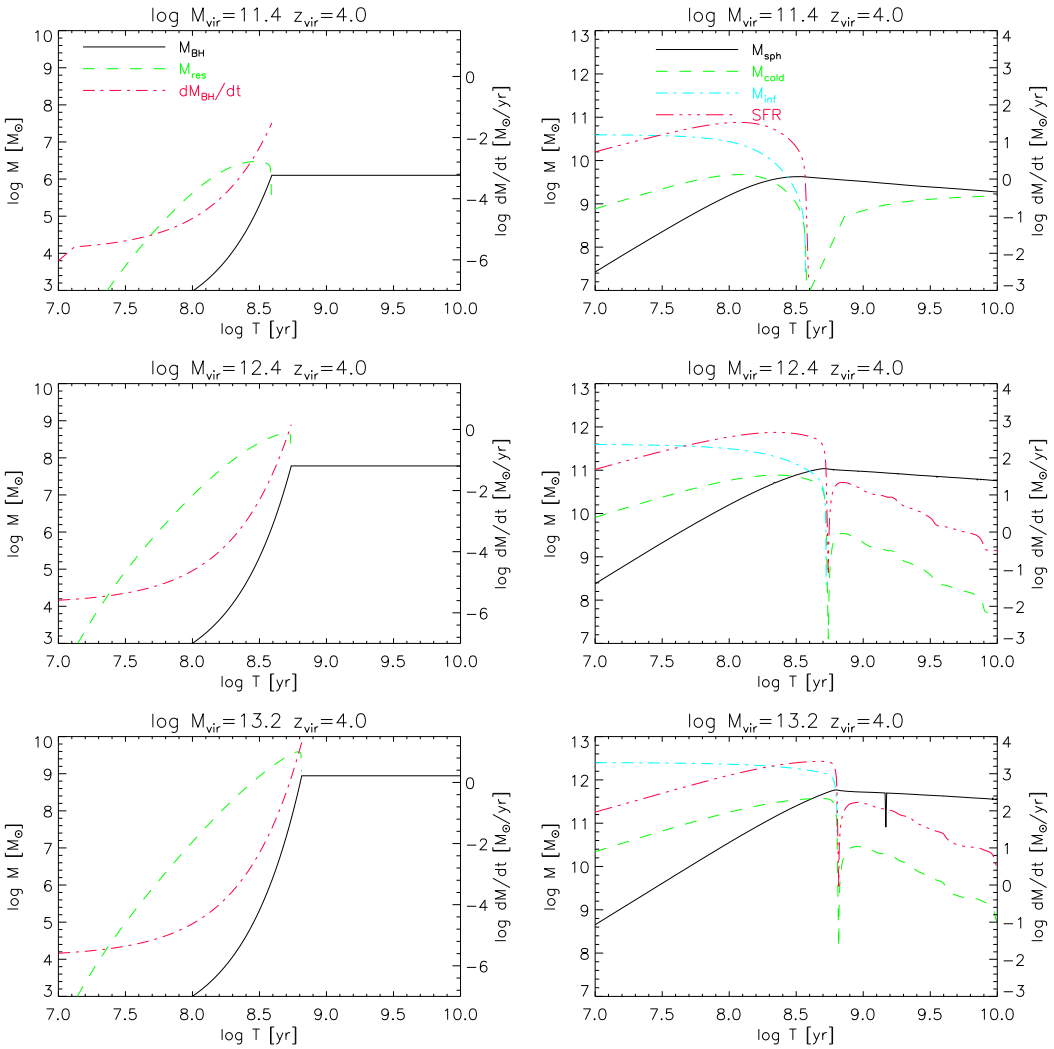

Figure 6.5: Left panel. Light curves as output of the numerical model. Right panel. Star Formation rate and evolution of the several baryonic components in the galaxy. All the curves are as labeled.

$\epsilon \approx 0.15$; in addition, the Heaviside function[1] θ_H specifies that the AGN shines unobscured only during the time interval $t_{\rm vis}$ before the peak of its light curve (see Fig. 6.4). Eq. (6.6) shows that if one includes obscuration in the AGN light curve, the total AGN duty-cycle, that the model predicts to be about $0.3 \div 1$ Gyr (see Figs. 6.4 and 6.5), reduces to the visible time, $\sim (0.4 \div 1) \times 10^8$ yr, i.e. it is reduced by about 1 order of magnitude.

[1]Recall that the Heaviside function θ_H is defined by

$$\theta_H(x) = \begin{cases} 1, & \text{if } x \text{ is true;} \\ 0, & \text{otherwise.} \end{cases} .$$

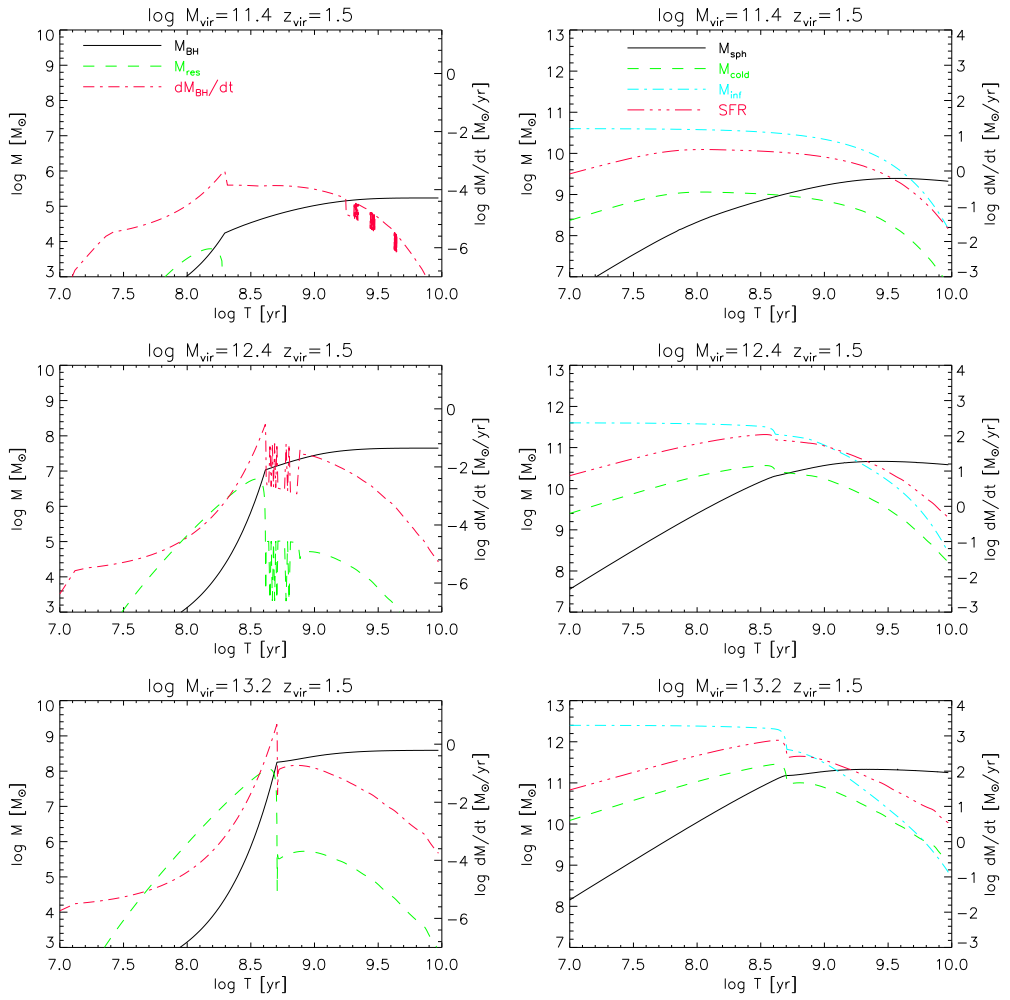

Figure 6.6: Left panel. Light curves as output of the numerical model. Right panel. Star Formation rate and evolution of the several baryonic components in the galaxy. All the curves are as labeled. Slightly different parameters are used in this plot as compared to the ones used in Fig. 6.5 in order to enhance the descendant phase.

• The computation of the AGN LF at a time t and luminosity L is computed numerically summing up the contribution of all the sources which virialize at any time $t' < t$ and have the right delay to shine at the time t with luminosity $L = (\epsilon/1-\epsilon)\dot{M_\bullet}(t)c^2$. We can express such a computation analytically as

$$\Phi(L,t) = \int_{t-t_{\rm delay}}^{t-t_{\rm delay}+t_{\rm vis}} {\rm d}t_{\rm vir} \int_{M_-}^{M_+} {\rm d}M_{\rm vir} \, \frac{{\rm d}^2 N_{\rm S\&T}}{{\rm d}t_{\rm vir}\,{\rm d}M_{\rm vir}} \, \delta_D\left(L - \frac{\lambda\, M_\bullet\, c^2}{t_{\rm Edd}}\, e^{(t-t_{\rm vir}-t_{\rm delay})/\tau_+}\right) ,$$

where δ_D indicates the Dirac delta function. Following the output of our model in Fig. 6.5, we can approximate the time delay to be almost independent of the BH mass, therefore we

can explicitly perform the inner integration in Eq. (6.7). The result comes to

$$\Phi(L,t) = \frac{1}{L}\int_{t-t_{\rm delay}}^{t-t_{\rm delay}+t_{\rm vis}} {\rm d}t_{\rm vir} \quad \left|\frac{{\rm d}M_{\rm vir}}{{\rm d}\ln M_\bullet}\right|_{\bar{M}_\bullet} \quad \frac{{\rm d}^2 N_{\rm S\&T}}{{\rm d}t_{\rm vir}\,{\rm d}M_{\rm vir}}\Big|_{M_{\rm vir}(\bar{M}_\bullet)} \quad , \tag{6.7}$$

$$\text{with} \quad \bar{M}_\bullet \equiv \frac{L\,t_{\rm Edd}}{\lambda\,c^2}\,e^{(t_{\rm vir}+t_{\rm delay}-t)/\tau_+} \quad .$$

which is very similar to Eq. (6.2).

If one includes the declining phase of the AGN light curve we can generalize Eq. (6.2) as

$$\Phi(L,t) = \frac{1}{L}\int_{t-t_{\rm delay}-\chi\,\tau_-}^{t-t_{\rm delay}+t_{\rm vis}} {\rm d}t_{\rm vir} \quad \left|\frac{{\rm d}M_{\rm vir}}{{\rm d}\ln M_\bullet}\right|_{\bar{M}_\bullet} \quad \frac{{\rm d}^2 N_{\rm S\&T}}{{\rm d}t_{\rm vir}\,{\rm d}M_{\rm vir}}\Big|_{M_{\rm vir}(\bar{M}_\bullet)} \quad , \tag{6.8}$$

$$\text{with} \quad \bar{M}_\bullet \equiv \frac{L\,t_{\rm Edd}}{\lambda\,c^2}\left(1+\frac{\tau_-}{\tau_+}\right)\Big[e^{(t-t_{\rm vir}-t_{\rm delay})/\tau_-}\,\theta_H\big(t-t_{\rm delay}-\chi\,\tau_- \le t_{\rm vir} \le t-t_{\rm delay}\big) +$$

$$+\, e^{(t_{\rm vir}+t_{\rm delay}-t)/\tau_+}\,\theta_H\big(t-t_{\rm delay} \le t_{\rm vir} \le t-t_{\rm delay}+t_{\rm vis}\big)\Big] \quad .$$

Here τ_- is the characteristic timescale of the AGN light curve in the declining phase, and we consider the AGN as dead after a time lapse $\chi\,\tau_-$. However a close check to the overall set of empirical data has proven that the condition $\tau_- << t_{\rm delay}$ must hold. The latter result matches with the findings in Chapter 5, where a good match was found between the AMF and relic SMBH MF, assuming a negligible accretion phase beyond the SMBH peak of activity (cf. Eq. (5.16)).

To compare our results with the data, the bolometric AGN luminosity function computed above has to be converted in the optical and hard X-ray bands through the appropriate bolometric corrections. For the optical band we use $L_B = f_B\,L$ with $f_B \approx 0.1$. For the hard X-ray band (between 2 and 10 keV) we use $L_X = f_X\,L$ with $f_X \approx k_X^{-1/(\beta_X+1)}\,(L/10^{43}\,{\rm erg\ s^{-1}})^{-\beta_X/(\beta_X+1)}$; here we adopt $k_X \approx 17$ and $\beta_X \approx 0.43 \div 0.73$, as proposed by Ueda et al. (2003) and adopted in Chapter 5.

• We also compute the BH mass function as

$$\Psi(M_\bullet,t) = \int_0^t {\rm d}t_{\rm vir} \quad \left|\frac{{\rm d}M_{\rm vir}}{{\rm d}M_\bullet}\right| \quad \frac{{\rm d}^2 N_{\rm S\&T}}{{\rm d}t_{\rm vir}\,{\rm d}M_{\rm vir}} \quad . \tag{6.9}$$

6.3 Results

Our model in general provides a very good fit to the optical and Hard-X AGN LF up to the cut-off redshift $z_{\rm vir} = 1.5$. The best fit is obtained using a visibility time in the range $t_{\rm vis} \sim (2 \div 6) \times 10^7$ yr for optical data (see Figs. 6.9, 6.10, 6.11, 6.14 and 6.16) and $(3 \div 8) \times 10^7$ yr for X-ray data (see Figs. 6.12, 6.15 and 6.17). For computing the AGN LF we have used a slightly descendant Eddington ratio of the type $\lambda = 1$ for $z_{\rm vir} \leq 3$, $\lambda = 1.7$ for $3 \leq z_{\rm vir} \leq 5$ and $\lambda \sim 3 - 4$ for higher redshifts.

Such visibility times do not have any particular trend with redshift, they are quite constant at the most slightly increasing at low redshift. This clearly shows that they are not linked to any large-scale evolution (such as disk cooling as in Eq. (6.4)) but just to the local physics of dust obscuration. It is interesting in this sense that we find a higher visible time for Hard-X ray LF approaching $\sim 10^8$ yr for the very faint low-redshift sources (see Fig. 6.17). Such visibility times are in very good agreement with the findings in Chapter 5 (see Section 5.4). Moreover our model is able to reproduce the Hard-X LF data increased, according to the prescriptions by Ueda et al. (2003), to account for the very obscured AGN with $\log N_H \geq 25$, which are needed to fit the more recent, higher XRBG normalization data (see Chapters 2 and 5; dark areas in Figs. 6.12, 6.15 and 6.17) and very recently confirmed by La Franca et al. (2005). In particular the comparison between Fig. 6.15 and Fig. 6.17 shows that the visible time, at fixed redshift, depends on luminosity, being close to the e-folding time, $t_{\rm vis} \sim 4 \times 10^7$ yr, for the high-luminosity Hard-X and optical AGN, approaching $\sim 10^8$ yr for the less luminous Hard-X AGN, supporting a scenario for which the less luminous AGN are also the most obscured ones (compare Fig. 2.11). It is interesting to notice that if in building the predicted Hard-X ray LF at $z_{\rm sh} = 2.6$, one includes the whole theoretical AGN light-curve produced in the model (i.e. without any cut given by the Heaviside function in Eq. (6.6)) the number of predicted AGN is at least a factor of $2 - 4$ above the data especially at faint luminosities (see Fig. 6.13).

The corresponding accreted mass function in our model (see Fig. 6.7) is compatible with the Soltan argument. We have redone the calculations as in Chapter 5, differentiating the energy balance equation in Eq. (5.19) and adopting the above Eddington ratios,

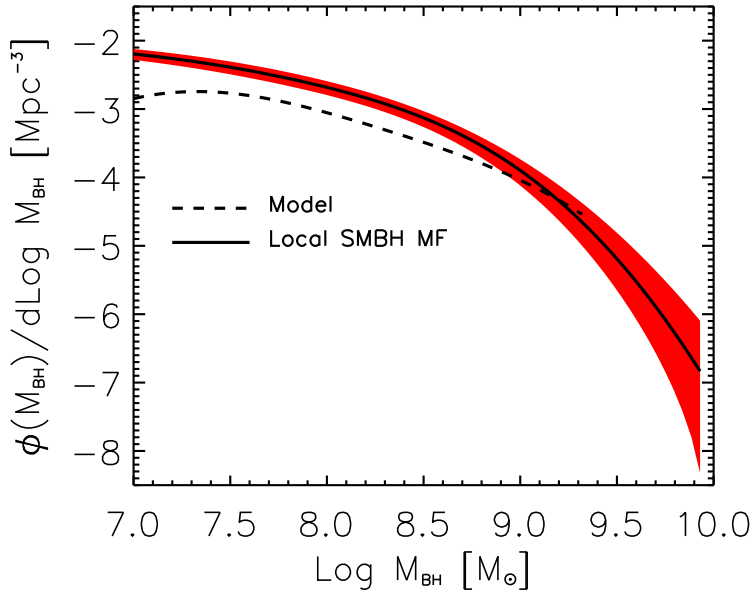

Figure 6.7: Predicted SMBH Mass Function for $z_{\rm vir} \geq 1.5$. Solid line: SMBH computed in Chapter 4 with its 1-σ uncertainty region (dark region).

exploiting the Ueda et al. (2003) LF, corrected for very obscured sources (see Fig. 6.8). The two mass functions in Figs. 6.7 and 6.8 are well in agreement, showing that the for $z \geq 1.5$ about 60% of the relic SMBH mass density (Chapter 4) is in place. This also agrees with the estimate done by Ueda et al. (2003) on the redshift distribution of the luminosity density of Hard-X ray selected AGN (see Chapter 2, Fig. 2.9). The rest of the mass will be accreted at later times and it will build up the bulk of the X-ray background (see Chapter 2, Section 2.2.7 and Section 6.4).

In large galactic halos the SFR turns out to be very high at high redshift, yielding a quick increase of the metallicity and of dust mass. The latter, as discussed in Chapter 3, Section 3.4.2, is computed by GRASIL (Silva et al. 1998). GRASIL, following the chemical evolution code basically described in Chapter 3, Eq. (3.102), computes the photometric evolution of galaxies in which the effects of a dusty interstellar medium, including dust from AGB stars, have been included. The fraction of gas is divided into two phases: the star-forming molecular clouds and the diffuse medium. Granato et al. (2004) have calculated the dust mass as proportional to the product of the gas mass by its metallicity, with a coefficient determined by the condition of a gas-to-dust ratio of 110 for solar metallicity.

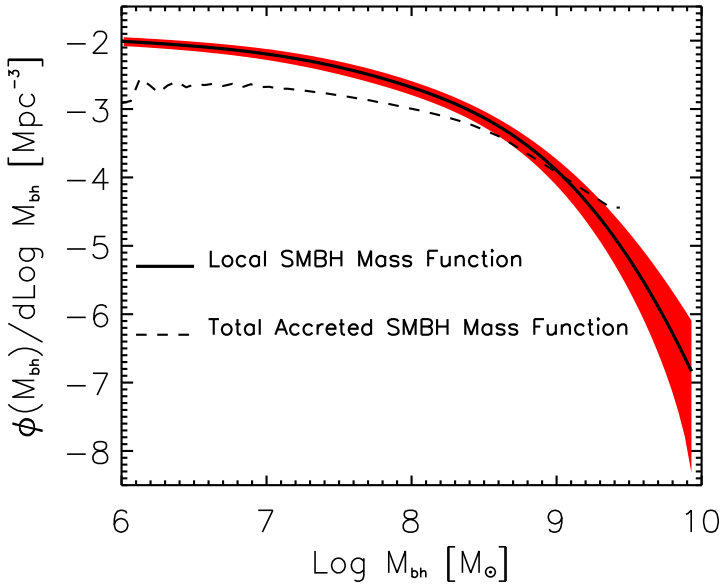

Figure 6.8: Dashed line: Accreted SMBH Mass Function using Ueda et al. (2003) LF for $z \geq 1.5$ with Eddington ratios as given in the text. Solid line: SMBH computed in Chapter 4 with its 1-σ uncertainty region (dark region).

Thus most of the star formation occurs in a dusty environment, so that these galaxies are powerful far-IR/submillimeter sources, highly obscured in the visual and near-IR bands. In Fig. 6.19 (upper panels) we have plotted the model predictions at 850 μm against the SCUBA counts (upper left panel). In particular for a flux density limit of 5 mJy the model predicts a median redshift of 2.4 (upper right panel), to be compared with the $z_{\rm median} = 2.4$ found for the sample of Chapman et al. (2003).

During the obscured phase the total luminosity of the galaxy is dominated by the star formation in the very first stages but a significant contribution of the AGN can be visible especially in the most massive objects (see Fig. 6.18). Alexander et al. (2005) have observed that a substantial fraction $\approx 75\%$ of bright (≥ 4 mJy) SCUBA sources at $z \geq 1$ host AGN activity with $L_X \geq 10^{42}\,{\rm erg\,s^{-1}}$, being the majority of the sources $\approx 80\%$ heavily obscured with $N_H \geq 10^{23}\,{\rm cm^{-2}}$. In Fig. 6.21 we show that in our model almost all the sources with accretion rates $\dot{M}_\bullet \geq 2 \times 10^{-3}\,M_\odot {\rm yr}^{-1}$, for which $L_X \geq 10^{42}\,{\rm erg\,s^{-1}}$, make up almost all the SCUBA counts at the level of 5 mJy. Moreover we predict (see Fig. 6.20) that the cumulative Hard-X number counts corresponding to very faint fluxes, about $3 \times 10^{-16}\,{\rm erg\,cm^{-2}\,s^{-1}}$, is only a minor fraction of the sources which make the X-ray

background, the limit of which is $N(> 3 \times 10^{-16}\,\mathrm{erg\,cm^{-2}\,s^{-1}}) \sim 4000$ (see Chapter 5, Fig. 5.4).

After the ISM has been swept out, galaxies evolve passively. The combination of redshift and aging soon makes them extremely red. We computed the expected contribution to the extragalactic K-band counts of spheroidal galaxies in this phase. A comparison (Fig. 6.19; middle and lower panels) of the predicted with the observed redshift distribution of galaxies with $K \leq 20$ (Cimatti et al. 2002) shows that they fully saturate the high-redshift tail of the distribution.

As outlined in Chapter 3, Section 3.4.1, Cimatti et al. (2002) selected a complete sample of extremely red objects (EROs) $[(R_s - K \geq 5)]$ with $K \leq 19.2$. More than 60% of the objects have redshift, mostly spectroscopic. On the basis of the spectra, the sample has been subdivided into dusty and nondusty ERO. Their data suggest that there is a significant number of old dust-free ellipticals galaxies place at $z \geq 1$. This results is confirmed by the subsequent analysis by Pozzetti et al. (2003), who found that the bright end of the K-band LF at $z \geq 1$ is dominated by red/early-type galaxies. Our model is consistent with these results (see Fig. 6.22).

Finally we show that this model, based on very rapid and massive bursts of star formation, provides also spheroids with an average metallicity about solar and more, in less than a Gyr, consistent with the high-redshift data from QSO environments (see Hamann & Ferland 1999). The metallicity also increases with stellar mass (see Fig. 6.23) which can solve, as shown in Romano et al. (2002) and Granato et al. (2004), the problem of the α-enhancement in elliptical galaxies (see Chapter 3).

6.4 Low-redshift AGN Evolution

In this section we investigate a possible physical model to describe how accretion episodes onto massive BH power AGN at $z \leq 1.5$. We implement a simple analytic approach to compute the trend and the stochastic component of the trigger to accretion.

As outlined in Chapter 3, Section 3.4.3, large-galaxy scale events, as galaxy-galaxy interactions in groups and/or bar/disks instabilities, could effectively perturb the gravita-

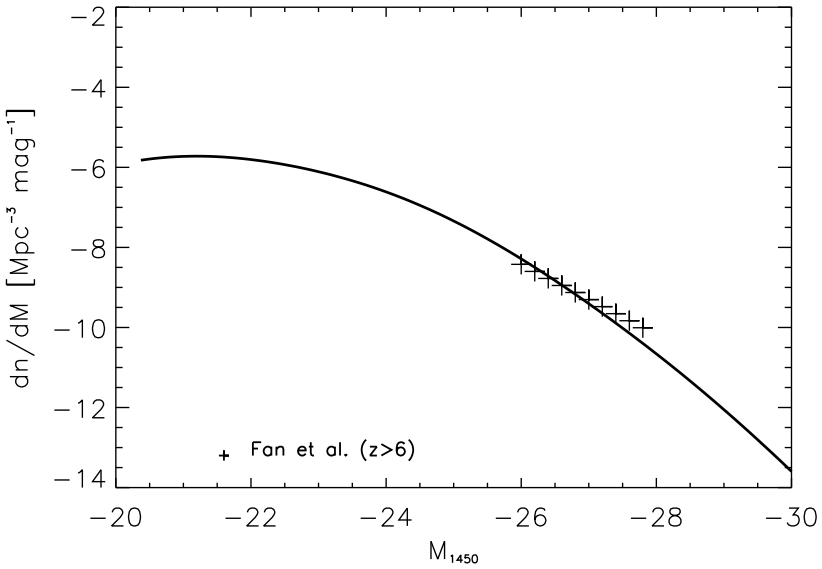

Figure 6.9: Optical AGN LF at $z_{\rm sh} = 6$. The visibility time is $\tau_{\rm vis} = 4 \times 10^7$ yr. Data are as labeled.

tional equilibrium of the gas reservoir in the host galaxy and trigger recurrent starburst episodes and gas accretion onto SMBH. If the central SMBH is already massive, the accretion will most probably occur in a *sub*-Eddington regime. The gas mass $m(z)$ in the hosts in fact is consumed with no fresh gas imports provided by gas-mergers. So the accretion becomes *supply-limited* and it can be easily *sub*-Eddington. We find that downward of $z \simeq 1.5$ the Eddington ratios related to still emitting, most massive holes drift below unity on average, with a widening scatter (see Fig. 6.25). We also include the later, generally smaller events triggered in the field by interactions of gas-rich galaxies and by capture of satellite galaxies. Thus we compute the quasar luminosity functions falling and dimming toward $z \simeq 0$ (see Fig. 6.24).

The interactions in groups outnumber the bound mergers for $z < 1.5$, consume more gas and decay faster, so speeding up the QSO evolution (see Menci et al. 2003). Direct evidences of activity connected with clearly interacting galaxies are given by Rifatto et al. (2001), Komossa et al. (2003), Ballo et al. (2004), and Guainazzi et al. (2005), who report AGN hosted in both galaxies of the interacting systems ESO 202-G23, NGC 6240, Arp 299, and ESO509-IG066, respectively. These findings complement the large, long known body of evidence indicating that some 30% QSO and strong AGN hosts have close companions

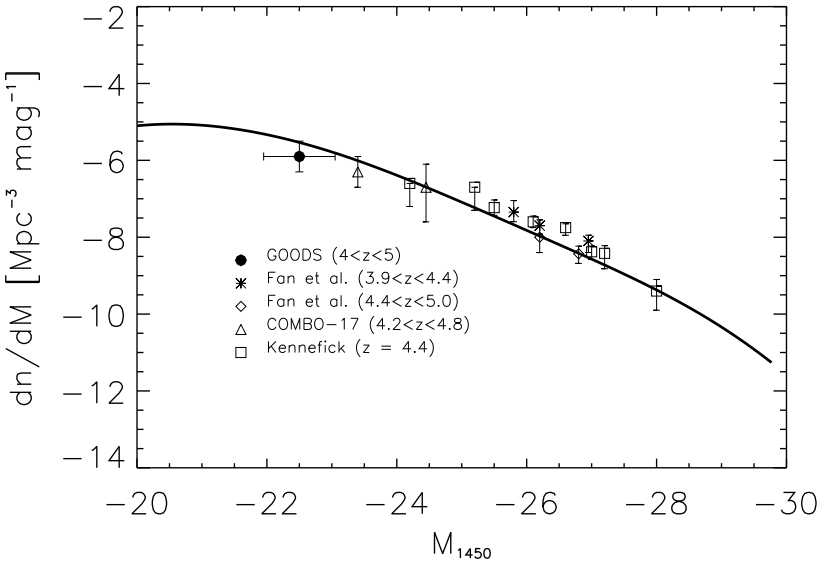

Figure 6.10: Optical AGN LF at $z_{\rm sh} = 4.7$. The visibility time is $\tau_{\rm vis} = 4 \times 10^7$ yr. Data are as labeled.

or show signs of ongoing interactions (see also the statistics by Bahcall et al. 1997 and Kauffmann et al. 2003). Other "field" processes like interactions of gas-rich hosts, satellite cannibalism and bar/disks instabilities are also significant fueling modes at low redshifts.

We let all these dynamical events, with their overall *trend* and their *stochastic* component, to form or rekindle the BHs as they may. Any of the above mechanism acting on the galactic potential will destabilize on average a fraction f of the cold gas mass m in the host from its equilibrium at $r \sim$ kpc from the center. The amount $f\,m$ funneled to the galaxy center ends up in part into circumnuclear starbursts, and in a smaller part trickles down onto a central BH. When the main integral governing the gas equilibrium is the angular momentum j, the fraction f has been computed in Cavaliere & Vittorini (2000) to read (see also Chapter 3, Section 3.4.3)

$$f \simeq |\frac{\Delta j}{j}| \tag{6.10}$$

This may attain a maximum close to 1/2, as expected from mass inflow vs. outflow. A fraction around $\sim 1/10$ of the inflow reaches the BH rather than ending into circumnuclear starbursts, as indicated by the statistics of the energy sources that heat up the dust in bright IR galaxies (see Franceschini, Braito & Fadda 2002). So $\Delta m = f m \,/\, 10$ is the mass made available by an interaction for actual accretion, while the rest ends up into stars or

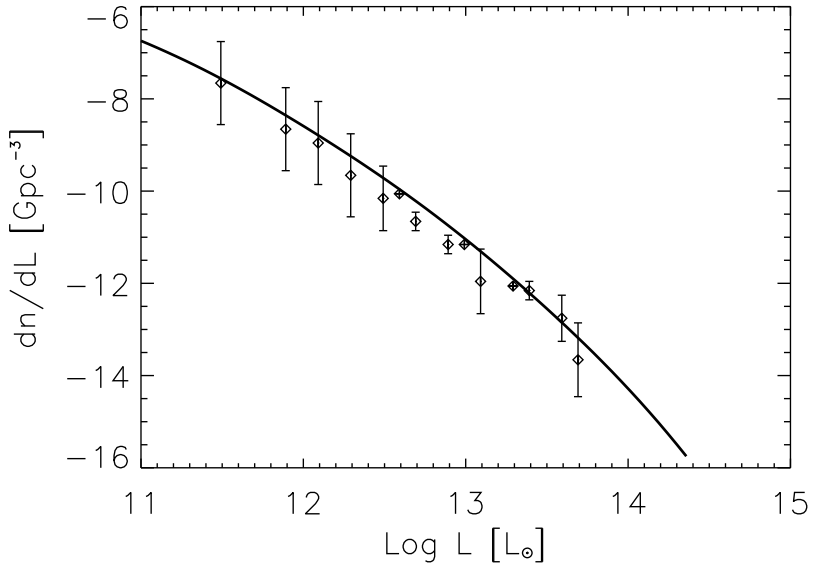

Figure 6.11: Optical AGN LF at $z_{\rm sh} = 3.1$. The visibility time is $\tau_{\rm vis} = 4 \times 10^7$ yr. Data are from Pei (1995).

is dispersed. The process of fueling takes times of order t_d, the host dynamical time, and covers a few Salpeter times.

Corresponding to larger galaxies being more resistant to gravitational distortion f will scale as σ^{-1}. Recurrent interactions will iteratively *exhaust* the initial gas mass m_{in} in the host. We stress that the luminosity $L \propto \Delta m$ attained in an accretion event no longer is in a fixed relation to the current BH mass $M_\bullet$. This is because the accreted mass Δm depends on the *stochastic* process that increases $M_\bullet$ at given σ.

Denoting by M the *current* SMBH mass at a general time t, the stochastic process is ruled by the equation

$$\partial_t N(M,\sigma,t) = -\frac{\alpha}{\tau_r} N(M,\sigma,t) + \frac{\alpha}{\tau_r} \int d\Delta m \; p(\Delta m \,|\, \sigma)\, N(M-\Delta m,\sigma,t) \;, \qquad (6.11)$$

proposed by Cavaliere & Vittorini (2002) which generalizes the continuity equation given in Eq. 5.33. The evolutionary rate $\partial_t N$ is contributed by two terms. The first describes the BHs which interact and thereby increase their initial mass M, so depleting the number $N(M,t)\,dM$ in the mass range $(M \; - \; M + dM)$. The second describes the number of BHs which start from a lower mass $M - \Delta m$ and accrete a gas amount Δm, with probability $p(\Delta m, \sigma)$ (for details see Vittorini et al. 2006). The fraction α of bright galaxies which resides in groups with membership ≥ 3 locally attains 20% (Ramella et al. 1999), while the

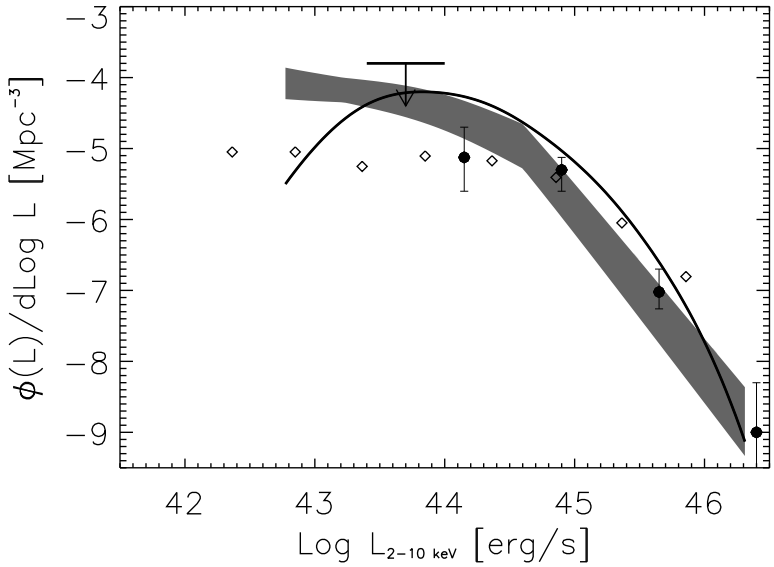

Figure 6.12: Hard-X AGN LF at $z_{\rm sh} = 2.6$. The visibility time is $\tau_{\rm vis} = 3 \times 10^7$ yr. Dots: data by Ueda et al. (2003); diamonds: data from Barger et al. (2005); arrow: upper limit on AGN number density at $z = 3$ from Ueda et al. (2003). Gray area: Hard-X LF with its uncertainty region from Ueda et al. (2003) including AGN with $\log N_H \geq 25$.

timescale τ_r is the average time between two SMBH (re)activations. In the above equation the number of BHs is conserved, while they are re-distributed toward larger masses.

To capture the evolutionary trends given by Eq. (6.11) it is convenient to consider at first small accretion events with $\Delta m/M << 1$, and to Taylor expand to second order. So, we end up with the approximate equation

$$\partial_t N(M,\sigma,t) \simeq -\frac{\alpha\langle\Delta m\rangle}{\tau_r}\,\partial_M N(M,\sigma,t) + \frac{\alpha\langle\Delta m^2\rangle}{2\tau_r}\,\partial_M^2 N(M,\sigma,t)\,. \qquad (6.12)$$

This is similar to a Fokker-Planck equation, actually one based on the probability distribution $p(\Delta m\,|\,\sigma)$. The coefficient of the first order derivative $C(M,t) \equiv \langle\Delta m\rangle\,/\,\tau_r$ represents the average upward *drift* of the mass under accretion, while the coefficient of the second derivative $D(M,t) \equiv \langle\Delta m^2\rangle\,/\,2\tau_r$ plays the role of a *diffusion* coefficient; the averages are computed by using the probability distribution $p(\Delta m\,|\,\sigma)$.

The above components can be brought together to yield the LF, upon using the formalism of the continuity equation along the L axis, as originally proposed by Cavaliere, Morrison & Wood (1971). This takes on the form

$$\partial_t N(L,\sigma,t) + \dot{L}\,\partial_L N(L,\sigma,t) = \alpha\;\frac{N_{bh}(\sigma,t)\;p(L\,|\,\sigma,t)}{\tau_r(t)}\;, \qquad (6.13)$$

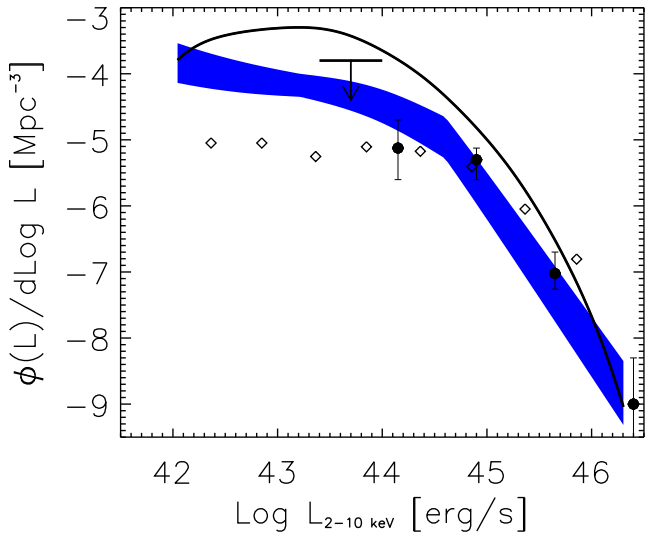

Figure 6.13: Hard-X AGN LF at $z_{\rm sh} = 2.6$. Including the whole light curve. Dots: data by Ueda et al. (2003); diamonds: data from Barger et al. (2005); arrow: upper limit on AGN number density at $z = 3$ from Ueda et al. (2003). Gray area: Hard-X LF with its uncertainty region from Ueda et al. (2003) including AGN with $\log N_H \geq 25$.

considering for simplicity light curves equal and monotonically decreasing on the scale τ. The solution is given by

$$N(L,\sigma,t) = \frac{\alpha}{\dot{L}} \int_L^\infty dL' \, \frac{N_{bh}(\sigma,t') \; p(L' \,|\, \sigma,t')}{\tau_r(t')} \; ; \tag{6.14}$$

for numerical computations we use the specific values $\dot{L} = -L/\tau$ with $\tau \simeq t_d = 10^{-1}$ Gyr, and $\alpha = 0.2$.

Upon convolving over σ, we obtain the bolometric LF; this is converted to optical luminosity L_B on using the standard bolometric correction of 10. The results are plotted in Fig. 6.24 where we compare them with the data of Boyle et al. 2000 and Grazian et al. 2000.

Decreasing luminosities and increasing masses produce Eddington ratios λ_E declining on average. In fact, the luminosities of the sources when re-activated are lower due to gas exhaustion. Fig. 6.25 illustrates our numerical results. The figure shows the complex behavior of λ_E at low redshifts is very similar to what found by McLure & Dunlop (2004) and Vestergaard (2004) (see Chapter 2, Figs. 2.2 and 2.2). The overall decline is due to the average dimming of all luminosities, more rapid in hosts with smaller σ; these undergo relatively faster gas consumption due to the scaling $\langle f \rangle \propto \sigma^{-1}$ discussed above.

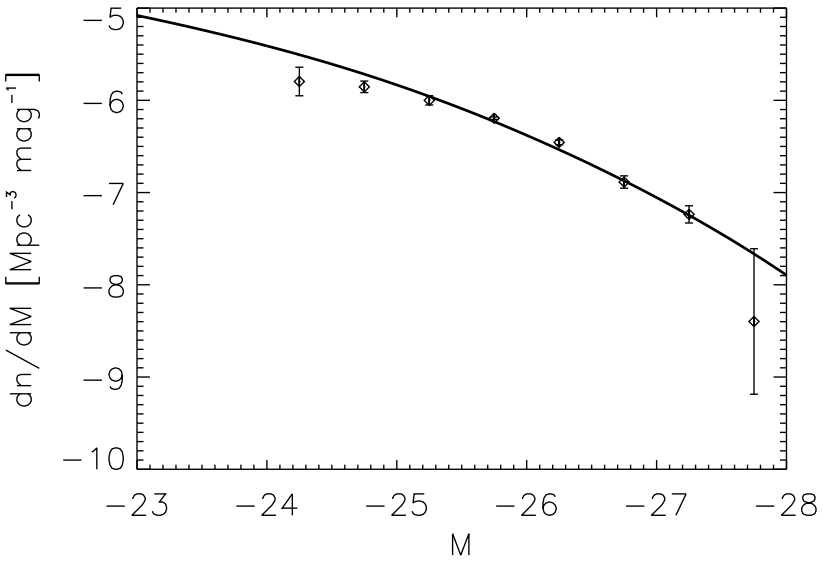

Figure 6.14: Optical AGN LF at $z_{\rm sh} = 1.9$. The visibility time is $\tau_{\rm vis} = 6 \times 10^7$ yr. Data are from Croom et al. (2004).

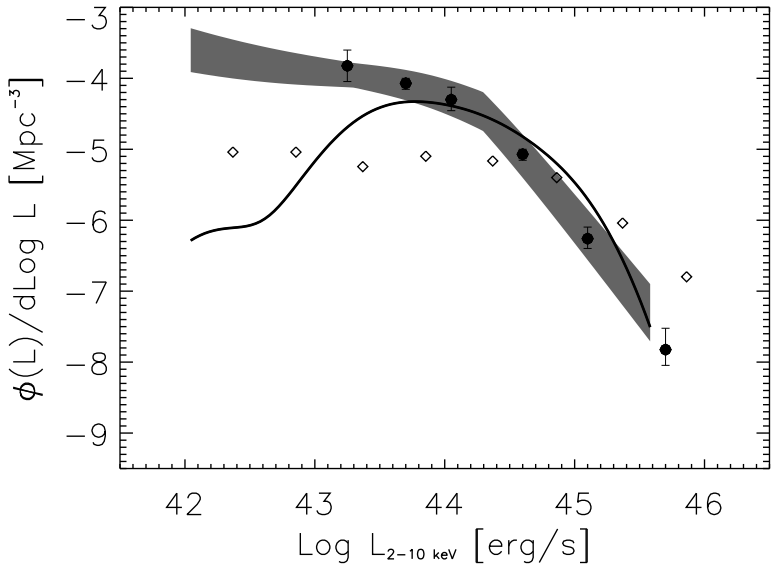

Figure 6.15: Hard-X AGN LF at $z_{\rm sh} = 1.5$. The visibility time is $\tau_{\rm vis} = 3 \times 10^7$ yr. Dots: data from Ueda et al. (2003); diamonds: data from Barger et al. (2005). Gray area: Hard-X LF with its uncertainty region from Ueda et al. (2003) including AGN with $\log N_H \geq 25$.

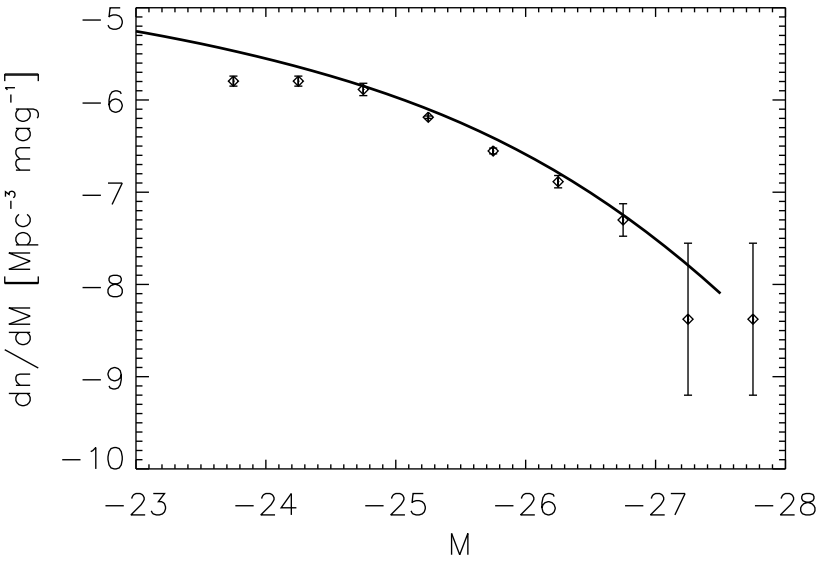

Figure 6.16: Optical AGN LF at $z_{\rm sh} = 1.5$. The visibility time is $\tau_{\rm vis} = 3 \times 10^7$ yr. Data are from Croom et al. (2004).

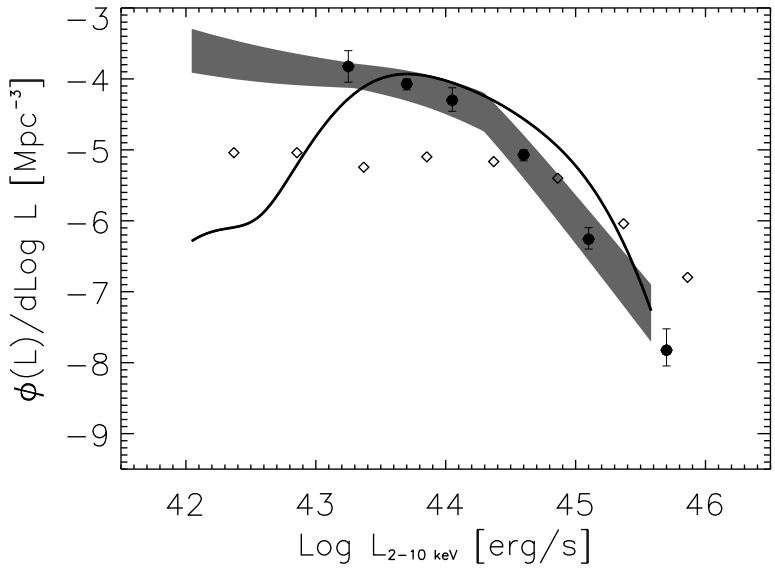

Figure 6.17: Hard-X AGN LF at $z_{\rm sh} = 1.5$. The visibility time is $\tau_{\rm vis} = 8 \times 10^7$ yr. Dots: data by Ueda et al. (2003); diamonds: data from Barger et al. (2005). Gray area: Hard-X LF with its uncertainty region from Ueda et al. (2003) including AGN with $\log N_H \geq 25$.

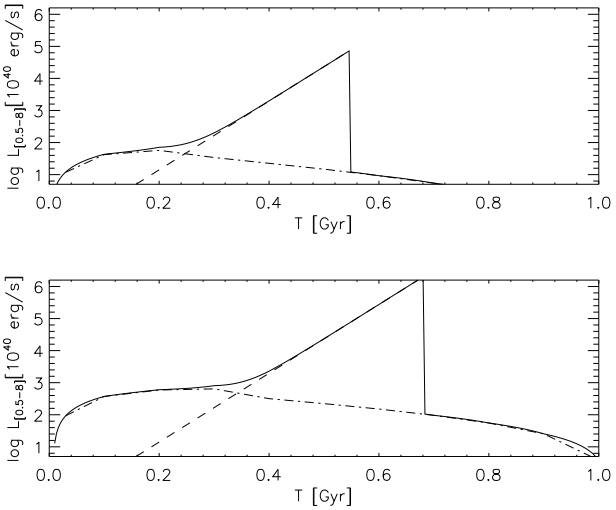

Figure 6.18: Estimated intrinsic X-ray luminosity between 0.5 and 8 keV (rest frame) as a function of galactic age, due to AGN activity (dashed line) and to star formation (dot-dashed line). The top and bottom panel are for a total halo mass of $2.5 \times 10^{12}\, M_{\odot}$ and $2.5 \times 10^{13}\, M_{\odot}$ respectively both virialized at $z_{\rm vir} = 4$. Figure produced by G. Granato.

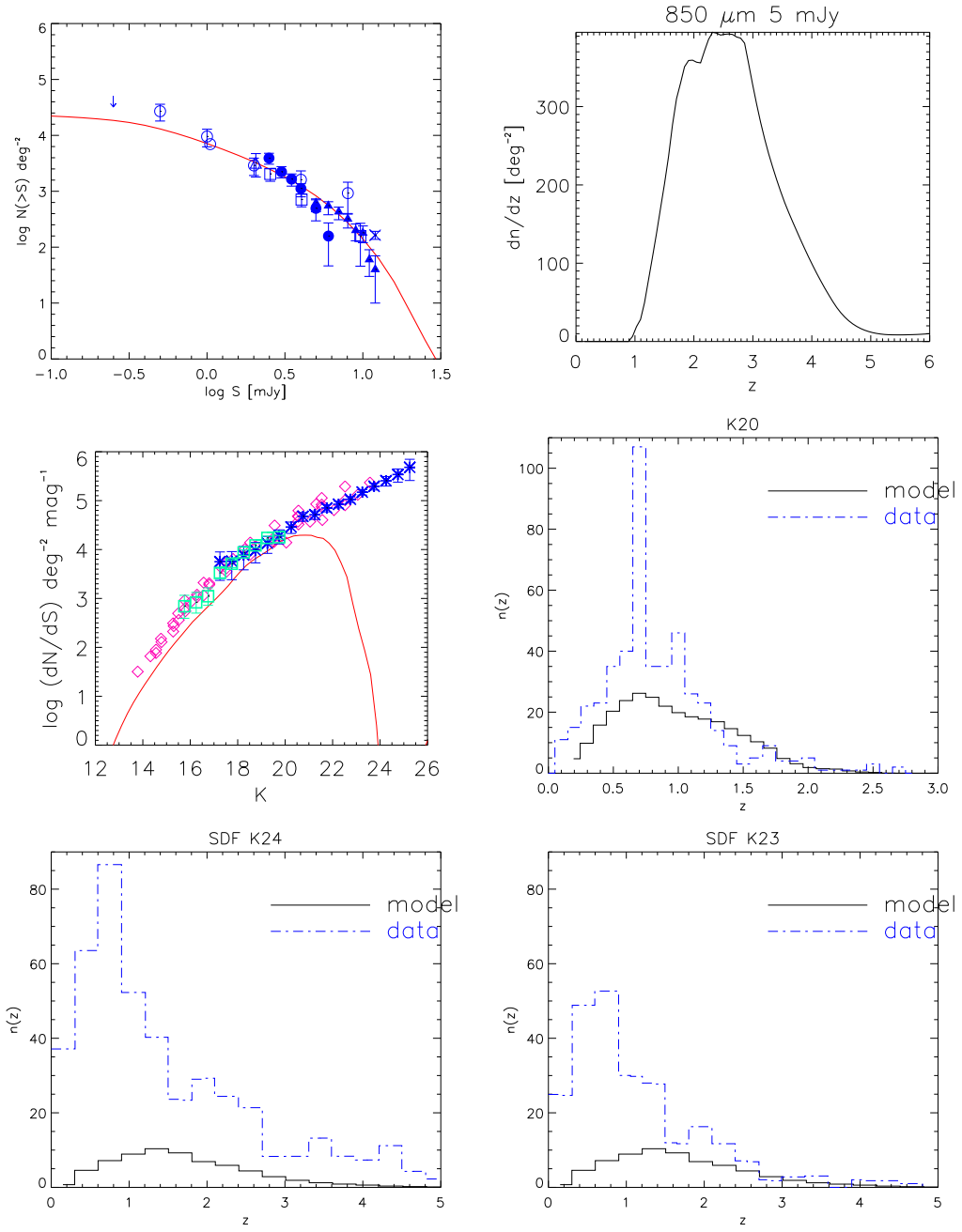

Figure 6.19: Upper panels. Left. Predicted 850 μm extragalactic counts compared with SCUBA counts; data by Blain et al. (1999; open circles), Hughes et al. (1998; asterix and open triangles), Barger et al. (1999; open squares), Eales et al. (2000; filled circles), Chapman et al. (2002; filled triangles) and Borys et al. (2002; filled squares). Right. Predicted differential redshift distribution of 850 μm extragalactic sources. Middle panels. Left. Contribution of Spheroidal galaxies to the K-band number counts. The data for the K-band counts are from Totani et al. (2001) and Cimatti et al. (2002). Right. Redshift distribution of galaxies brighter than K=20. The thin solid histogram is from Cimatti et al. (2002) for $K20$. Lower panels. K-band number counts of galaxies brighter than K=23 and 24. The thin solid histogram is from Kashokawa et al. (2003) for $K23$ and $K24$. Figure produced by G. Granato.

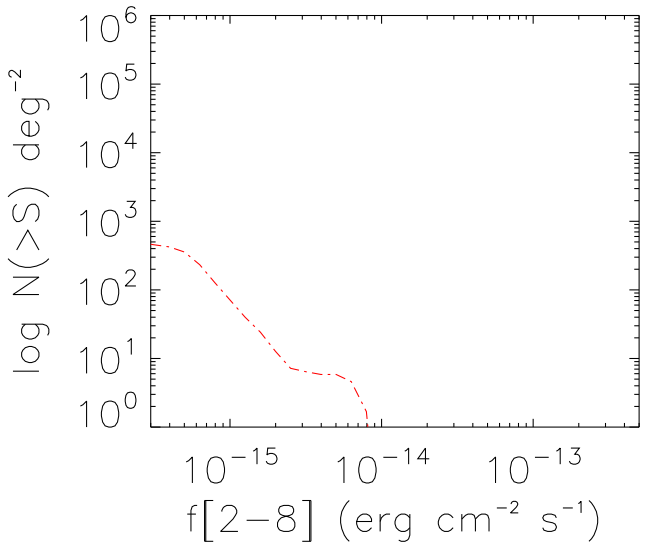

Figure 6.20: Hard-X cumulative number counts. Figure produced by G. Granato.

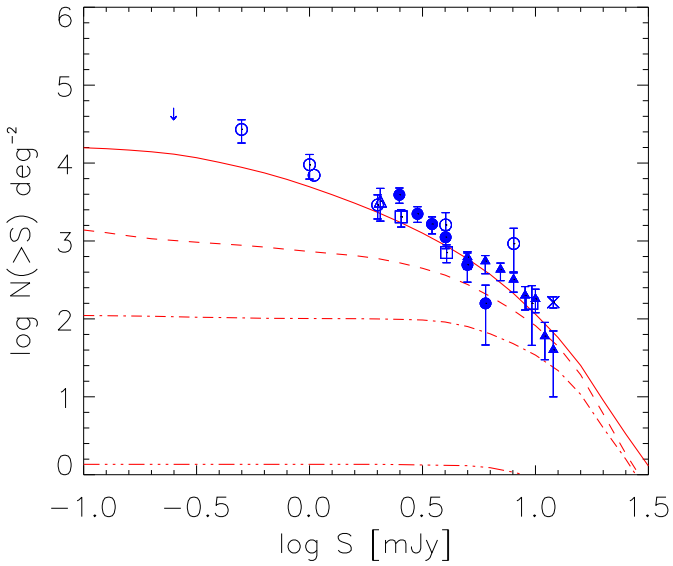

Figure 6.21: Number counts predicted by the model for SCUBA sources with accretion rates greater than several thresholds. Solid line: all sources; dashed line: $\dot{M}_\bullet > 2.3 \times 10^{-3}\, M_\odot\,\mathrm{yr}^{-1} \sim \log L_{2-10\,\mathrm{keV}} = 42\,\mathrm{erg\,s}^{-1}$; dot-dashed line: $\dot{M}_\bullet > 2.3 \times 10^{-2}\, M_\odot\,\mathrm{yr}^{-1} \sim \log L_{2-10\,\mathrm{keV}} = 43 - 44\,\mathrm{erg\,s}^{-1}$; triple-dot dashed line: $\dot{M}_\bullet > 1\, M_\odot\,\mathrm{yr}^{-1} \times \sim \log L_{2-10\,\mathrm{keV}} = 46\,\mathrm{erg\,s}^{-1}$. Data are as in Fig. 6.19. Figure produced by G. Granato.

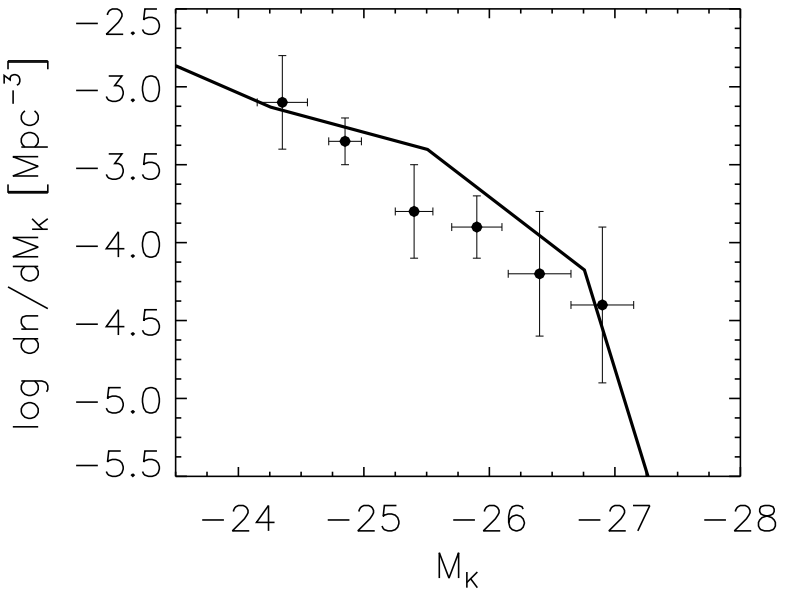

Figure 6.22: Predicted K-band luminosity function of massive spheroids at $z = 1.5$ compared with observational determination by Pozzetti et al. (2003).

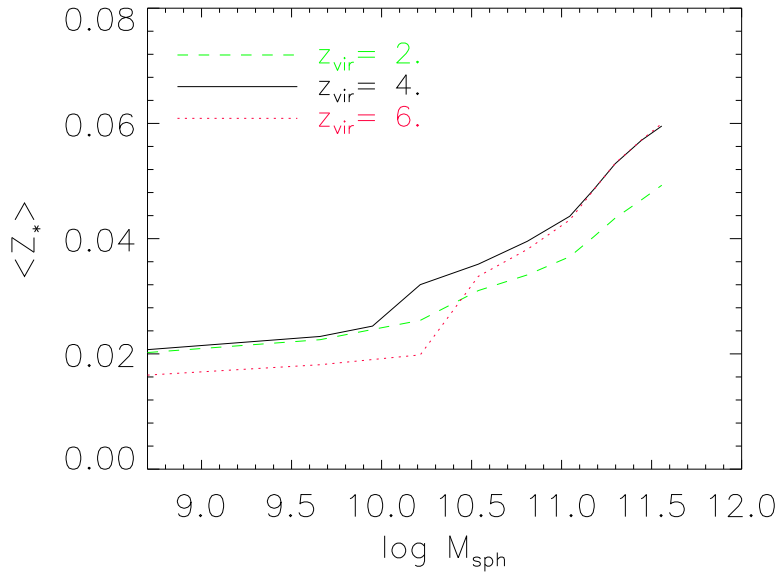

Figure 6.23: Mean stellar metallicity as a function of the present-day stellar mass for three values of $z_{\rm vir}$ as labeled.

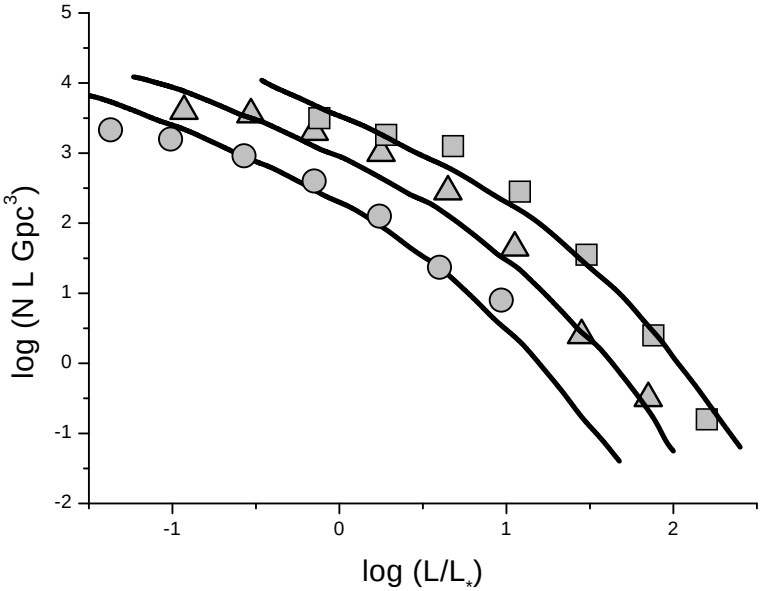

Figure 6.24: Predicted evolution of optical AGN LF from a feedback-constrained model for SMBH accretion. Solid curves: from bottom to top LF at $z = 0.5$, 1 and 2.5. Data are from Boyle et al. (2000) at $z = 0.5$ (circles), from Grazian et al. (2000) at $z = 1$ (triangles) and at $z = 2.5$ (squares).

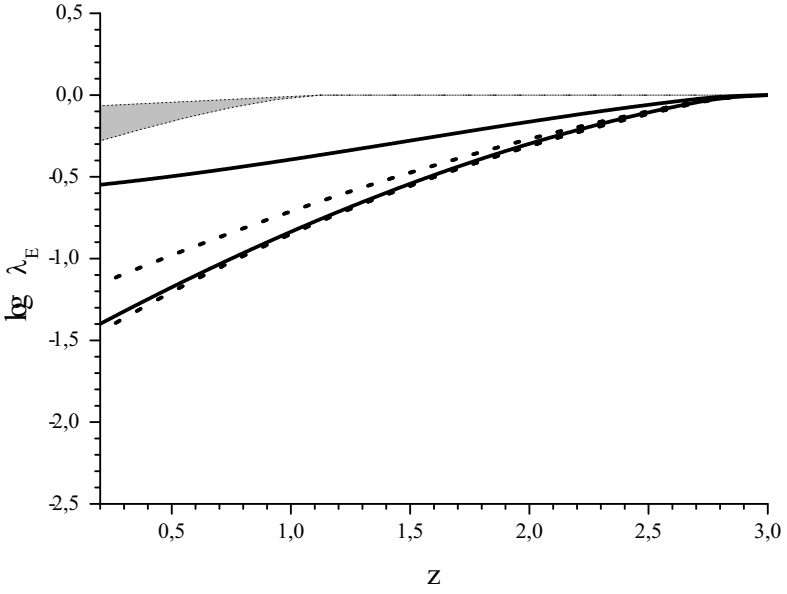

Figure 6.25: Evolution of the Eddington ratio at low-redshift, indicated by λ_E. Solid lines: 95% confidence level corresponding to $\sigma = 400\mathrm{km\,s^{-1}}$; dotted lines: same confidence levels for $\sigma = 100\mathrm{km\,s^{-1}}$. The shaded regions corresponds to galaxies in low-density environments.

Chapter 7

The fundamental plane of E and S0 galaxies

In the previous chapters we have discussed the basic evolutionary regimes regulating SMBH and AGN. Here we further investigate the evolution of SMBH in galaxies and DM halos. After the fast build-up of the DM potential well and rapid baryon collapse, the subsequent mutual feedback among stars and SMBH within the DM host well, are physically traced in the local dynamic and photometric properties of spheroidal galaxies. In this Chapter, using the Granato et al. model, we will reproduce the spheroidal Velocity Dispersion Function (VDF, Sect. 7.1), the luminosity-velocity dispersion relation (Faber & Jackson 1976, Sect. 7.2), the stellar luminosity-effective radius relation (Bernardi et al. 2003, Sect. 7.3), and the SMBH mass-velocity dispersion relation (Ferrarese & Merritt 2000; Tremaine et al. 2002; Onken et al. 2004; Sect. 7.4).

7.1 The Velocity Dispersion Function

As discussed by Loeb & Peebles (2003), the VDF can provide interesting hints on the structure formation process (we remind the line-of-sight velocity dispersion σ is referred to $R_e/8$). Since, given the virialization redshift, $V_{\rm vir}$ depends only on $M_{\rm vir}$ ($V_{\rm vir} \propto M_{\rm vir}^{1/3}$) the $V_{\rm vir}$ distribution function can be straightforwardly derived from the mass distribution

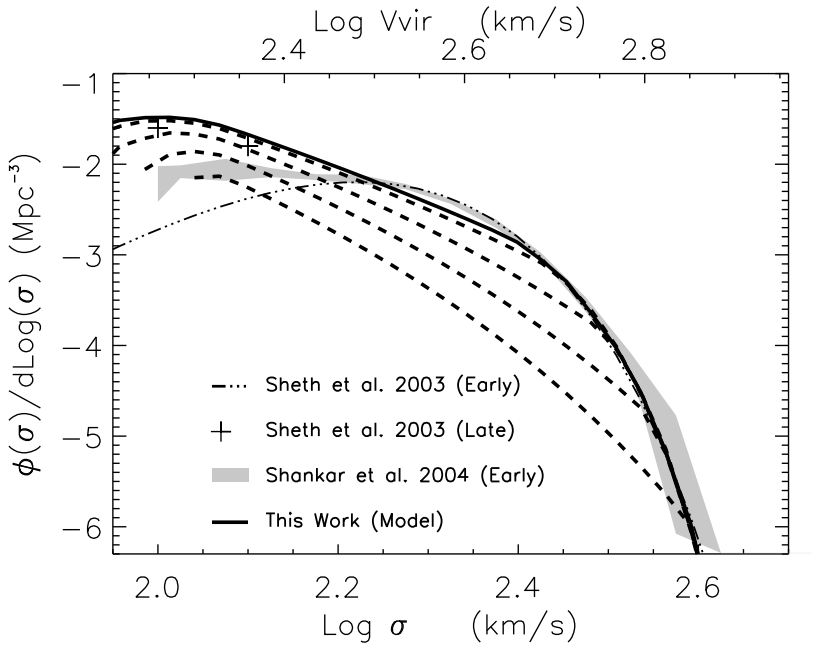

Figure 7.1: Comparison of the virial velocity function of galaxies with $z_{\rm vir} \geq 1.5$ implied by the standard gravitational clustering scenario (solid line, upper scale), with observational estimates of the velocity dispersion function of early-type galaxies computed in Chapter 4, Section 4.2.3 (shaded area) and Sheth et al. (2003) (triple-dot dashed line). The crosses show the contribution of bulges of late-type galaxies, determined by Sheth et al. (2003). The two functions match for $\sigma = 0.55 V_{\rm vir}$. The dashed lines show the virial velocity functions of galaxies for different choices of the minimum $z_{\rm vir}$: from top to bottom, $z_{\rm vir,min} = 2$, 3, 4, 5.

function of spheroidal galaxies, integrated over the virialization redshifts. Following Granato et al. (2004), we assume that all massive halos ($2.5 \times 10^{11} M_\odot \leq M_{\rm vir} \leq 2 \times 10^{13} M_\odot$) virializing at $z \geq 1.5$ yield spheroidal galaxies or bulges of later type galaxies. It may be noted, in passing, that the adopted upper mass limit is close to that inferred by Kochanek & White (2001) from the distribution of gravitational lens image separations.

As illustrated by Fig. 7.1, the derived $V_{\rm vir}$ distribution function (which depends only on the evolution of DM halos) accurately matches the observationally determined VDF (which may be affected by the physics of baryons, and in particular by dissipative processes) if

$$\sigma \simeq 0.55 V_{\rm vir} \, . \tag{7.1}$$

The best fit and the confidence intervals of the $\sigma/V_{\rm vir}$ ratio depend somewhat on the choice of the upper mass limit, $M_{\rm sup}$ (reference value $M_{\rm sup} = 2 \times 10^{13} M_\odot$) and of σ_8 (reference value $\sigma_8 = 0.84$), while the choice of the minimum virialization redshift ($z_{\rm vir,min}$) set at 1.5,

does not affect appreciably the fit. For $\sigma_8 = 0.84$, the 95% confidence interval, determined utilizing the χ^2 statistic with 2 degrees of freedom, is $0.53 \leq \sigma/V_{\rm vir} \leq 0.60$, the upper end corresponding to the smallest value of $M_{\rm sup}$, which is constrained to be $\geq 10^{13}\,M_\odot$ to ensure consistency with the local K-band luminosity function (see Granato et al. 2004 and Chapter 6). The data indicate a constant (independent of virial mass) ratio $\sigma/V_{\rm vir}$. A weak dependence, not steeper than $\sigma/V_{\rm vir} \propto M_{\rm vir}^{0.05}$, is however allowed. The result is affected by the choice of power spectrum used in the calculation by not more than $\Delta(\sigma/V_{\rm vir}) \sim 10\%$.

A linear relationship between the central velocity dispersion, σ, and the maximum circular velocity, $V_c^{\rm max}$ – which, for a concentration $c \simeq 3$ (see below), is essentially equal to $V_{\rm vir}$ – was reported by Gerhard et al. (2001) for a sample of 21 mostly luminous, slowly rotating elliptical galaxies, although the ratio is somewhat higher than found here: $\sigma = 0.66 V_c^{\rm max}$. Very interestingly Pizzella et al. (2004) find a correlation of the type $\sigma \sim 0.7 V_c$, for a sample of 40 high surface brightness galaxies, 8 giant low surface brightness spirals and 24 ellipticals. A weakly non-linear relationship was found by Ferrarese (2002) for a sample of 13 spiral galaxies with rotation curves extending beyond the $B = 25\,{\rm mag/arcsec}^2$ isophote:

$$\sigma/200{\rm km\,s^{-1}} = 0.60 (V_c^{\rm max}/200{\rm km\,s^{-1}})^{1.19}\,. \tag{7.2}$$

According to Ferrarese (2002) this relation can be considered valid also in the σ range populated by elliptical galaxies.

If the stellar velocity dispersion profile is approximately isothermal and stellar velocities are isotropic, adopting the Navarro et al. (1997) density profile we obtain the following relationship between $V_{\rm vir}$ and the velocity dispersion σ:

$$\frac{\sigma}{V_{\rm vir}} = \frac{\{c[3c^2 + 4c - 2c\ln(1+c) - 2\ln(1+c)]\}^{1/2}}{\sqrt{6}[1 + (1+c)\ln(1+c)]}, \tag{7.3}$$

where c, equal to the ratio of $R_{\rm vir}$ to the NFW inner radius r_s, is the "concentration". The N-body simulations by Zhao et al. (2003b) show that halos of mass greater than $10^{11}\,{\rm h}^{-1}\,M_\odot$ at $z \geq 3$ have all a similar median concentration $c \sim 3.5$. For $c = 2$, 3, 4, Eq. (7.3) yields $\sigma/V_{\rm vir} = 0.49$, 0.57, 0.62, respectively. Thus, the value of $\sigma/V_{\rm vir}$ for which we get a match between the local VDF and the $V_{\rm vir}$ distribution function of dark halos is remarkably close to the value expected based on simulations. This is also the value one

expects if $\sigma \sim \sigma_{\rm vir}$ and, following Chapter 3 (Fig. 3.2), $\sigma_{\rm vir} \sim 0.55 V_{\rm circ}(R_{\rm vir})$.

As it will be discussed in more detail below, the tight correspondence between the VDF and the velocity distribution function of dark halos lends support to the dynamical attractor hypothesis (see Chapter 3, Section 3.4.2; Loeb & Peebles 2003; Gao et al. 2004), according to which the total distribution of collisionless matter (dark matter plus stars) keeps essentially constant in the presence of merging and of dissipative settling of baryons, with the dark matter distribution expanding to compensate for the dissipative settling of baryons (but see Gnedin et al. 2004 for a different conclusion). The baryons which fall within the inner regions of the host halo act as effective DM particles, with the same energy which DM particles had in those regions before expansion, and with almost the same dispersion velocity.

The stability of the stellar dynamics in the central regions of dark halos against merging events subsequent to the virialization redshift is also consistent with the results of detailed numerical simulations (see Chapter 3, Sections 3.3.4, 3.3.6 and 3.4.2; Wechsler et al. 2002; Zhao et al. 2003b) showing that the halo circular velocity changes very little after the end of the initial fast accretion process, during which most of the specific binding energy is assembled, even though a large fraction of the halo mass is acquired during the subsequent prolonged slow accretion phase.

Fig. 7.1 also shows the contributions to the VDF of different virialization redshifts and highlights that the highest velocity portion comes from the highest virialization redshifts. This result is nicely consistent with the findings by Loeb & Peebles (2003) who computed the expected cumulative comoving VDF at $z = 4$ for the NFW and the Moore et al. (1999) density profile, and found it consistent with the observational determination by Sheth et al. (2003) for velocity dispersions $\sigma > 300\,{\rm km\,s^{-1}}$, while for lower values of σ the predicted VDF is low compared to the observed one. Our curve for $z_{\rm vir} \geq 4$ has a very similar behavior; but when we allow also for spheroidal galaxies or bulges virializing at lower redshifts we can fully account for the observed VDF. As mentioned above, the contributions to the VDF of sources virializing at $z \leq 1.5$ is small. In Fig. 7.1 it is straightforward to check that, as outlined in Chapter 3, Section 3.4.2, the cumulative virial velocity function (but similar behaviors can be traced in the galaxy/SMBH MF) predicts that *statistically*,

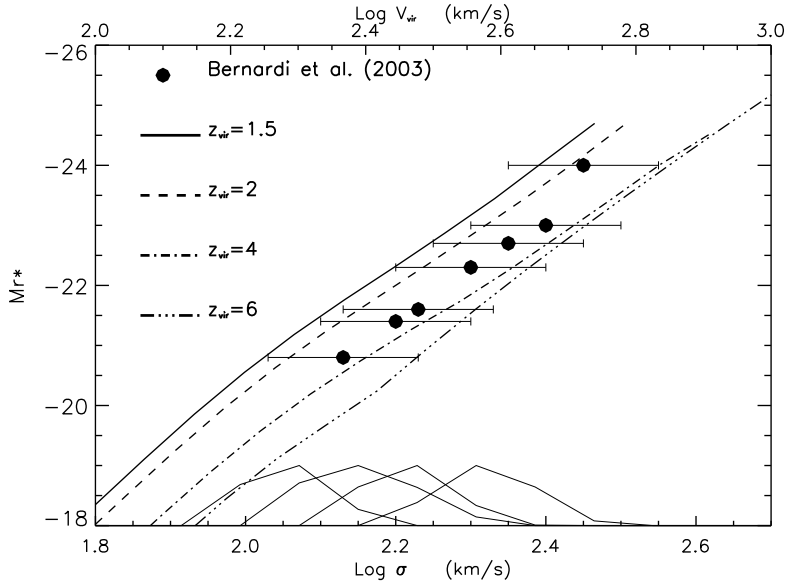

Figure 7.2: Observed FJ relation (filled dots) from Bernardi et al. (2003), compared with our predictions for different virialization redshifts zv. The curves at the bottom of the figure represent the normalized distributions of velocity dispersions of galaxies in 4 absolute magnitude bins 0.5 mag wide, centered at $Mr* = -20.2$, -21, -22, and -23 (from left to right), as predicted by the ABC model. The FWHMs of the predicted distributions are remarkably close to the observed values (FWHM ~ 0.09; Bernardi et al. 2003)

at higher redshifts, the numerical fraction, compared to the number at $z_{\rm vir} = 0$, of the more massive systems, i.e. those residing in deeper potential wells, is much higher compared to the less massive ones.

7.2 The Faber - Jackson relation

Since the first measurements of velocity dispersions of early type galaxies were made, it was recognized that they are correlated with the galaxy luminosities (Poveda 1961; Minkowski 1962). Faber & Jackson (1976) showed that $L_B \propto \sigma^4$ (Faber-Jackson relation). Bernardi et al. (2003), using a sample of ~ 9000 early type galaxies drawn from the Sloan Digital Sky Survey (SDSS) in the redshift range $0.01 \leq z \leq 0.3$, found $L_{r^*} \propto \sigma^{3.92}$, consistent with previous studies (Forbes & Ponman 1999; Pahre et al. 1998). Their data in u, g, i, and z bands show that the relation is roughly independent of wavelength. The distributions of σ at fixed luminosity are approximately Gaussian.

A detailed quantitative analysis can be carried out using the ABC model to follow

the time evolution of the baryonic component, both in the gas and stellar phase, of each halo mass $M_{\rm vir}$ since the virialization redshift $z_{\rm vir}$. Then, the present-day luminosity in bands from UV to radio can be computed with the spectrophotometric code GRASIL (Silva et al. 1998) as a function of $V_{\rm vir}$ at fixed $z_{\rm vir}$. As illustrated by Fig. 7.2, the model predicts the correct normalization, when we use the ratio $\sigma/V_{\rm vir} = 0.55$ found from the analysis of the VDF. Acceptable fits can be obtained with $0.50 \leq \sigma/{\rm V_{vir}} \leq 0.65$ (again, the confidence interval is derived using the χ^2 statistic). The model correctly predicts a slope shallower than the classical Faber-Jackson relation, in particular we find $L \propto \sigma^3$, which, as shown in Chapter 4 (see Fig. 4.8), is the right slope to convert the galaxy LF to the VDF and viceversa (see Chapter 8).

The scatter in the observed relation is interpreted as an intrinsic property of elliptical galaxies, accounted for by different virialization epochs: galaxies with the same spheroidal luminosity, but virializing at lower redshifts, have lower velocity dispersions. The curves at the bottom of Fig. 7.2 show the σ distributions (arbitrary units) of galaxies in four luminosity bins, as obtained from the Granato et al. (2004) model. Such distributions have been computed integrating over cosmic time, for each value of σ, the formation rate of halos with present day luminosities within the considered bin; they turn out to be roughly Gaussian, with the peak close to the σ expected from the best fit relation and FWHM in agreement with that observed by Bernardi et al. (2003).

It is worth noting that the standard scaling of the virial parameters in the hierarchical clustering scenario gives (Bullock et al. 2001) $M_{\rm vir} \propto V_{\rm vir}^3 (1 + z_{\rm vir})^{-3/2}$, which, for a roughly constant $M_{\rm vir}/L$ ratio, would imply a flatter slope than is observed in the FJ relation. However, the slope is steepened in the ABC model which predicts a decrease of the $M_{\rm vir}/M_{\rm sph}$ ratio ($M_{\rm sph}$ being the mass in stars), with increasing $M_{\rm vir}$, whose details depend on the virialization redshift (see Fig. 5 of Granato et al. 2004). This is due to feedback from supernovae, which is increasingly efficient with decreasing $M_{\rm vir}$ in preventing the gas from cooling and forming stars, tempered by the feedback from active nuclei which is more effective in the more massive objects. On average, we have, to a sufficient approximation, $M_{\rm vir}/M_{\rm sph} \propto M_{\rm vir}^{-1/5}$. The ABC model also predicts an essentially constant $M_{\rm sph}/L$ ratio (the observed weak luminosity dependence is attributed to the systematic changes with

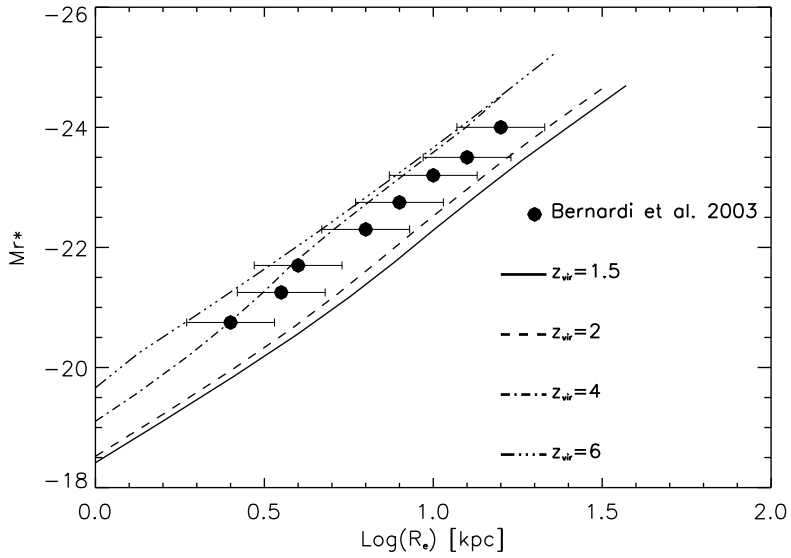

Figure 7.3: Absolute magnitude in the r^* band versus R_e. The data points are from Bernardi et al. (2003) while the lines show our model predictions for different virialization redshifts.

luminosity of the galactic structure, see Sect. 7.3). Therefore, the $M_{\rm vir}$–$V_{\rm vir}$ relation, for $\sigma/V_{\rm vir} = {\rm const}$, translates into $L \propto \sigma^{19/6}(1+z_{\rm vir})^{-9/4}$. A steepening of the $L-\sigma$ relation is expected at low σ values, corresponding to less massive objects where the SN feedback, yielding $M_{\rm vir}/M_{\rm sph} \propto M_{\rm vir}^{-1/2}$, dominates.

In conclusion, the normalization of the "Faber-Jackson relation" is interpreted as providing a quantitative measure of the effect of feedback, and primarily of the effect of the energy injected onto the interstellar medium by supernovae. The close agreement with the predictions of the ABC confirms the correctness of the adopted recipes.

7.3 Completing the Fundamental Plane

An additional check on the physical processes involving baryons in the ABC model is provided by the observed L–R_e relation (see e.g. Bernardi et al. 2003). The effective radius, like the velocity dispersion, is related to the collapse and settling of the baryonic component inside the DM potential well. On the other hand, the model does not give us dynamical information. However, it yields the total mass in stars and dark remnants, while observations ensure that the starlight distribution in spheroids has quite a uniform shape. In fact the surface brightness distribution is well represented by $\log(I(r)) \propto r^{1/n}$ (Sersic

1968); the classical de Vaucouleurs profile has $n = 4$ (de Vaucouleurs 1948).

Borriello et al. (2003), properly taking into account the light distribution, the mass traced by light, and the dark matter, found that the effective radius can be written as:

$$R_e = (k_\sigma + \alpha_{\rm DM})\frac{GM_{\rm sph}}{\sigma^2}, \tag{7.4}$$

where $M_{\rm sph}$ is the total mass traced by light, k_σ is a constant depending on the light distribution (k_σ=0.174 for the de Vaucouleurs profile) and $\alpha_{\rm DM}$ is a function of the DM mass inside R_e and of its density distribution [see Eqs. (13) and (14) of Borriello et al. 2003]. As found by Gerhard et al. (2001) for a sample of about 20 elliptical galaxies and generalized by Borriello et al. (2003) on the basis of the narrowness of the Fundamental Plane, the DM inside the effective radius amounts to only 10-50% of the total mass.

We have checked Eq. (7.4) following Borriello et al. 2003 and improving on it including a generalized Sersic profile for the matter traced by light. The 1-D dispersion velocity of the stars is governed by the hydrostatic Jeans Equation (see Chapter 3). In the case of negligible anisotropy, the dispersion velocity reads as

$$\sigma_r(r)^2 = \frac{G}{\rho_{\rm sph}(r)}\int_r^\infty \frac{\rho_{\rm sph}(r')M(r')}{r'^2}dr' \equiv \sigma_{\rm r;sph}(r')^2 + \sigma_{\rm r;vir}(r')^2 \tag{7.5}$$

where, being $M(r') = M_{\rm sph} + M_{\rm vir}$, we have defined the two contributions by the stellar and halo component to the dispersion velocity. Integrating along a line of sight we get the 'observed' dispersion velocity $\sigma_P(r)$. The luminosity-weighted average σ_P within a given circular aperture of radius, say, $R_e/8$, is instead $\sigma_0(r)$. In Fig. 7.4 it is immediate to notice that the contribution of baryons to the dispersion velocity within the effective radius is up to 80-90%, for realistic values of the NFW (see Chapter 3, Section 3.3.4) scale factor $R_s >> R_e$.

Therefore the contribution of DM in the inner regions is very small, in line with our idea of expansion of the DM after baryonic infall. Moreover, recalling our discussion on the FP in Chapter 2 (Section 2.1.2), we find that most probably the "tilt" of the observed FP could only be due to some changes with luminosity of the stellar mass which is the dominant component in these regions. In particular we recover almost the results of Borriello et al. (2003) that $k_\sigma \sim 0.17$ (see Fig. **??**). We notice however an increase, $k_\sigma \sim 0.3$, depending

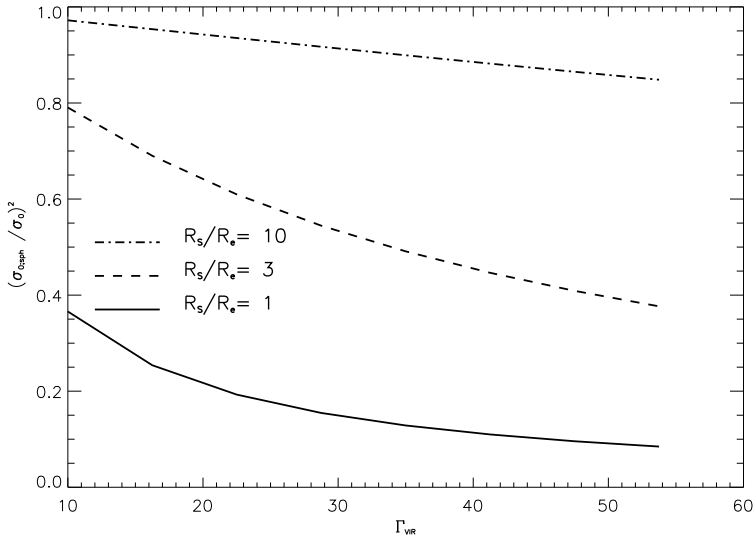

Figure 7.4: The baryonic contribution to σ_0 for different R_s/R_e as a function of $\Gamma_{\rm vir} = M_{\rm vir}/M_{\rm sph}$. R_s is the NFW scale factor and R_e is the effective radius.

on the assumed Sersic index n, in the brightness profiles of Elliptical galaxies, $I(r) \propto r^{1/n}$, which could cause an uncertainty of a factor of 40% in the stellar mass determination.

Due to the fact that the DM amount is so tiny within R_e and its distribution more spread than the baryonic one, $\alpha_{\rm DM}$ results to be almost negligible. Therefore Eq. (7.4) can be rearranged as follows, using the definition of $V_{\rm vir}$ (see Chapter 3, Section 3.3.4):

$$\frac{R_e}{R_{\rm vir}} = (k_\sigma + \alpha_{\rm DM}) \frac{M_{\rm sph}/M_{\rm vir}}{(\sigma/V_{\rm vir})^2} \, . \tag{7.6}$$

The ABC model yields the $M_{\rm sph}/M_{\rm vir}$ ratio and the ensuing $M_{\rm sph}/L$ ratio, whose value depends on the adopted IMF. Using the Salpeter's IMF we get $M_{\rm sph}/L_r \simeq 5\, M_\odot/L_\odot$, with very little dependence on the luminosity in the reference r^* band.

On the other hand, systematic changes with luminosity of the galactic structure, quantified by the Sersic index n, have been reported and found to account for the variation of the M/L ratio with luminosity (Ciotti et al 1996; Graham et al. 2001; Trujillo et al. 2004). As already sketched in Chapter 2, Section 2.1.2, the observed tilt β in the $M_{\rm sph}/L \propto L^\beta$, could be explained for 70% by non-homology effects. Bernardi et al. (2003), exploiting the large sample of early-type galaxies in the SDSS, defined an effective mass $M_0 \equiv 4R_e\sigma^2/G$, and found $M_0/L_r = 3.5(L_r/L_r^\star)^{0.15}$, in solar units, with $L_r^\star = 2 \times 10^{10} L_\odot$. After Eq. (7.4) $M_0 = 4(k_\sigma + \alpha_{\rm DM})M_{\rm sph}$, so that, neglecting $\alpha_{\rm DM}$ and setting $M_{\rm sph}/L_r \simeq 5\, M_\odot/L_\odot$, we

have:

$$k_\sigma \simeq 0.174 \left(\frac{L_r}{L_r^\star}\right)^{0.15}, \tag{7.7}$$

consistent with the findings of Borriello et al. (2003) based on a much smaller sample (221 nearby galaxies) but with more detailed observations. Hence:

$$\frac{R_e}{R_{\rm vir}} \simeq 0.87 \left(\frac{L_r}{L_r^\star}\right)^{0.15} \frac{L_r/M_{\rm vir}}{(\sigma/V_{\rm vir})^2}. \tag{7.8}$$

The ABC model gives, for each value of $z_{\rm vir}$ and for an assumed IMF, $R_{\rm vir}$ and L_r as a function of $M_{\rm vir}$. Using the above equation we can then obtain a relationship between L_r (or the absolute magnitude M_{r^*}) and R_e. The results for a Salpeter IMF and $\sigma/V_{\rm vir} = 0.55$, as implied by the VDF, are compared in Fig. 7.3 with the data of Bernardi et al. (2003). The presence of an average $\sim$30% of DM inside R_e would imply $\alpha_{\rm DM} \leq 0.02$ (see Borriello et al. 2003) and would not modify the fit. The observed M_{r^*}–R_e relation thus constitutes a test for the $L_r/M_{\rm vir}$ ratio predicted by the ABC model, which turns out to be fully consistent with the data.

7.4 The central black hole

The ABC model follows, for any given $M_{\rm vir}$ and $z_{\rm vir}$, the growth of the central BH and gives its final mass. The predicted $M_\bullet$–$V_{\rm vir}$ relation, at fixed $z_{\rm vir}$, is immediately translated into $M_\bullet$–σ using the ratio $\sigma/V_{\rm vir} = 0.55$ derived from the VDF. The scatter of data points is interpreted as reflecting the distribution of $z_{\rm vir}$ (see Fig. 7.5).

The model also predicts a steepening of the relation at low σ values, due to the combined effect of SN feedback – which is increasingly efficient with decreasing halo mass in slowing down the gas infall onto the central BH – and of the decreased radiation drag, due to a decrease of the optical depth (see Chapter 3, Eq. (3.80), Eq. (3.86) and Eq. (3.85)). From an observational point of view, the behavior of the $M_\bullet$–σ relation in the low BH mass and low velocity dispersion regime is still unclear, due to the dearth of data and to the uncertainties on the $M_\bullet$ estimates. In Fig. 7.5 we plot objects found in the literature with estimated BH masses $M_\bullet \leq 10^6 M_\odot$. Dynamical measurements are available only for M33 and NGC 205, while all the other BH masses have been estimated through the

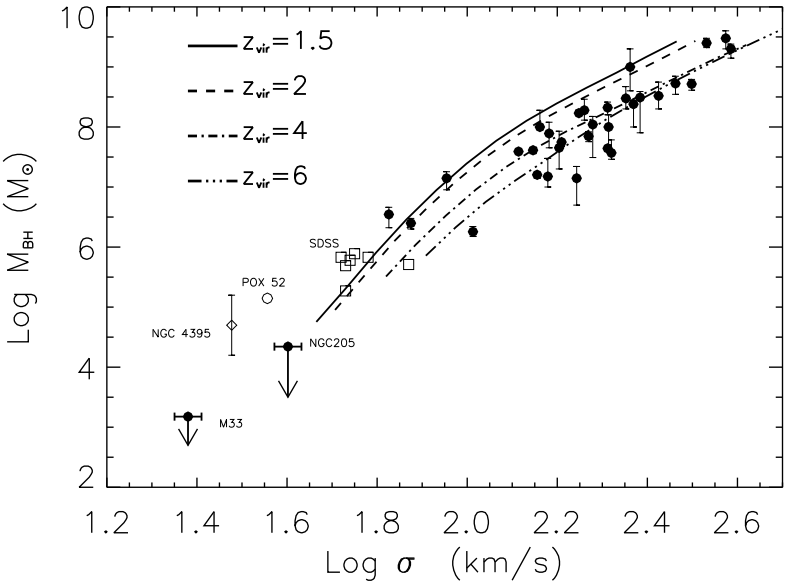

Figure 7.5: The $M_\bullet - \sigma$ relation predicted by the model for different virialization redshifts compared with observational data. Filled circles represent nearby galaxies with dynamical measurements of the BH mass (Tremaine et al. 2002) and the upper limits for M33 (Gebhardt et al. 2001) and NGC 205 (Valluri et al. 2005). Open symbols refer to galaxies with BH masses estimated from the Hβ linewidth-luminosity-mass relation: NGC 4395 (open diamond; Filippenko & Ho 2003), POX 52 (open circle; Barth et al. 2004) and a sample of 7 faint active nuclei drawn from the SDSS, (open squares; Greene et al. 2004).

linewidth-luminosity-mass scaling relation (Kaspi et al. 2000). Therefore the cases of M33 and NGC 205 are particularly interesting, although they are outside the range of masses to which we applied our model up to now. For M33 (see also Chapter 4, Section 4.1.2) the upper limit to the BH mass is $M_\bullet \leq 3000 M_\odot$ (Merritt et al. 2001) or $M_\bullet \leq 1500 M_\odot$ (Gebhardt et al. 2001), while, for NGC 205, $M_\bullet \leq 2.2 \times 10^4 M_\odot$. Both fall below the extrapolation of the mean fit of the $M_\bullet$–σ relation holding at higher σ (Ferrarese & Merritt 2000; Gebhardt et al. 2000; Tremaine et al. 2002; Onken et al. 2004), but still fully consistent with the extrapolation of our model. On the other hand, the BH mass estimates for the faint type 1 Seyfert nuclei in NGC 4395 (Filippenko & Ho 2003), in POX 52 (Barth et al. 2004) and in 7 galaxies drawn from SDSS (Greene et al. 2004) are only marginally consistent with the steepening predicted by our model. More data on the so called intermediate mass BHs ($10^3 M_\odot \leq M_\bullet \leq 10^6 M_\odot$) in the galactic centers (see Chapter 2, Section 2.3 and van der Marel (2003) for a review) are needed to clarify this issue. Of course we should also keep in

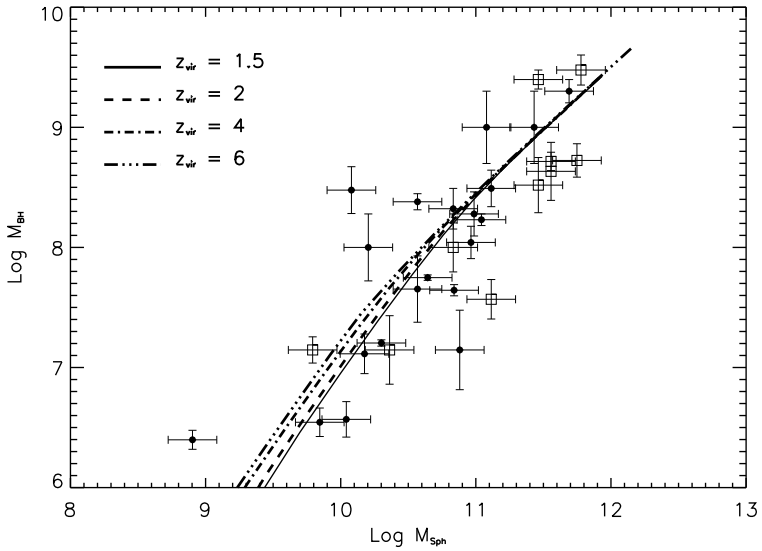

Figure 7.6: Predicted $M_\bullet - M_{\rm sph}$ relation for different virialization redshifts compared with observational data from Häring & Rix (2004). Open squares are sources from their Group 1 and solid circles from their Group 2.

mind that the low BH mass portion of the diagram might just reflect the distribution of BH seeds (see Chapter 2, Section 2.3), possibly created by merging of smaller BHs during the fast accretion epoch, and be only weakly affected by the mass accretion which is controlled by the effects discussed above. For example, Koushiappas et al. (2004) presented a model yielding seed BHs with characteristic masses $\sim 10^5\,M_\odot$.

In Fig. 7.5 we show that the dispersion velocities (and the linked SMBH masses) are imprinted at the moment of virialization of the host DM halo. A simple way to further test this conclusion can be achieved just by comparing, following the method sketched by Ferrarese (2002), the local statistics of SMBH (see Chapter 4) and the statistics of DM halos with which we have reconstructed the VDF.

The starting point of her method is based on a power law fit to the observed BH mass vs. stellar velocity dispersion relationship: $M_\bullet \propto \sigma^{4.58}$. The next step requires inferences on the relationship between σ and the galaxy circular velocity V_c measured at the outermost radius. Then the latter velocity must be linked to the present-day halo velocity $V_{\rm vir}(z=0)$, which eventually yields the halo mass estimate. The study was based on objects spanning a range between $100 \leq V_c \leq 300$ km s^{-1} in circular velocity and $6 \leq \log(M_\bullet/M_\odot) \leq 9$ in BH mass. The fit to the data with a single power law yielded

$M_\bullet \propto M_{\rm vir}^{1.65-1.82}$, depending on the adopted relationship between the circular velocity and the virial velocity. Baes et al. (2003) exploiting the same method, but assuming $M_\bullet \propto \sigma^{4.02}$ and deriving a slightly different $V_c - \sigma$ relation, claimed $M_\bullet \propto M_{\rm vir}^{1.3}$. [1]. The disagreement would become even more striking if $V_c/V_{\rm vir} = 1.8$ is assumed, as suggested by Seljak (2002).

The arguable point in the above procedure is the correlation between the velocity dispersion of the old stellar population and the present-day characteristic velocity of the halo at the virial radius $V_{\rm vir}(z = 0)$. In fact, as suggested by Loeb & Peebles (2003) and shown in details in this thesis, the velocity dispersion of the old stellar population (whose mass is related to the central BH mass) is closely linked to the potential well of the host DM halo at high redshift, when the old stellar population formed. This conclusion is also in agreement with the fact that only minor changes occurred in the spheroidal component of galaxies after redshift $z \sim 1 - 1.5$, as suggested also by recent studies on the Fundamental Plane at $z \approx 1$ (Treu et al. 2002; Treu & Koopmans 2004; van der Weld et al. 2004; see Chapter 3).

Following Ferrarese (2002) we then calculate the $M_\bullet - M_{\rm vir}$ relation from the local observed relation $M_\bullet - \sigma$. We connect σ to the virial velocity $V_{\rm vir}$ (with the assumptions $V_{\rm vir} \sim V_c$) using Eq. (7.2) and finally use the redshift-dependent virial relation $V_{\rm vir} - M_{\rm vir}$ (see Chapter 3, Section 3.3.4). In particular we calibrate the last equation at redshifts $z_{\rm vir} \sim 2.5$, assuming that the early-type galaxies have all formed in halos which virialized at high redshift. We get

$$M_\bullet = 2.6 \cdot 10^7 \left(\frac{M_{\rm vir}}{10^{12}\, M_\odot} \right)^{1.74} M_\odot \,. \tag{7.9}$$

In Eq. (7.9) the dependence of SMBH mass on halo mass is a little steeper than the one inferred at $z_{\rm vir} = 0$ (see Fig. 7.7), and, above all, the normalization is about a factor of 3-4 higher, more consistent with SMBH mass estimates obtained through local statistic comparisons (see Chapter 8, Fig. 8.7).

We now convert the $n(M_\bullet)$ function computed in Chapter 4 to a $n(M_{\rm vir})$ function using Eq. (7.9). In Fig. 7.7 one can check that the statistics of the integrated DM halos (which we have used in Fig. 7.1 to compute the VDF), are well reproduced only using

[1] It is worth noticing that Ferrarese (2002) and Baes et al. (2003) both adopt $V_{\rm vir} \propto (\Omega_M \frac{\Delta_{\rm vir}}{200})^\alpha$ with $\alpha = 1/3$, following Bullock et al. (2001), while the correct value is $\alpha = 1/2$.

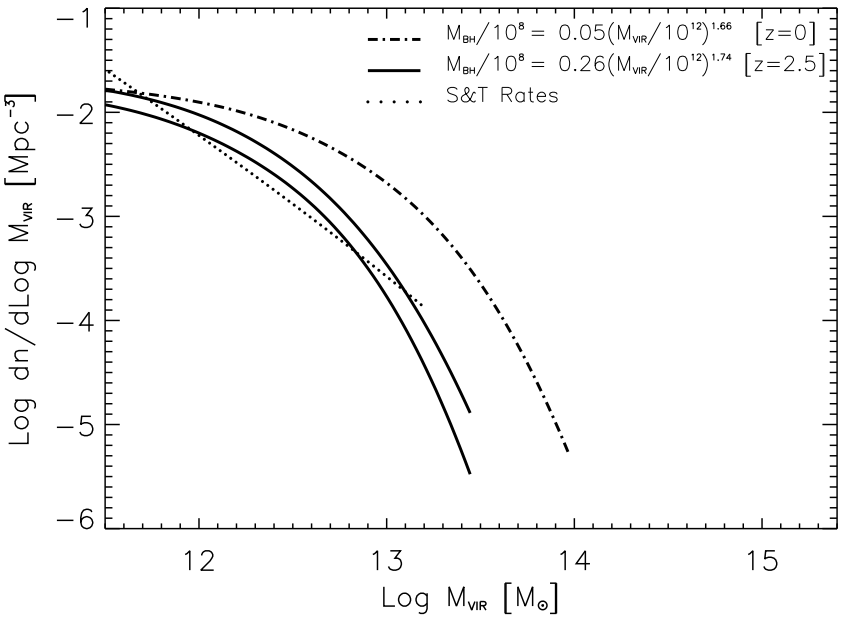

Figure 7.7: Comparison between the mass cumulative rates used in Fig. 7.1 to compute the VDF and the SMBH MF (upper and lower limit) converted into a $M_{\rm vir}$ mass function. The $M_\bullet - M_{\rm vir}$ relation is computed following Ferrarese (2002). Solid line: mass function computed using $V_{\rm vir} - M_{\rm vir}$ at $z = 2.5$. Dashed line: $V_{\rm vir} - M_{\rm vir}$ at $z = 0$.

Eq. (7.7). This result shows that the spheroid population, and therefore their dispersion velocities and potential wells, have been settled, together with their massive BH, at high redshifts.

Another prediction of the ABC model is that the ratio of the BH mass to the mass in stars, $M_\bullet/M_{\rm sph}$, is almost insensitive to variations of $z_{\rm vir}$. Therefore the $M_\bullet$–$M_{\rm sph}$ relation is expected to have a smaller *intrinsic* scatter (see Fig. 7.6) than the $M_\bullet$–σ relation. This is because, as mentioned above, the growth of the BH mass is controlled by the star formation rate through the radiation drag and the SN feedback, and in turn, the feedback from the active nucleus can eventually sweep out the gas thus halting both the star formation and the accretion on the BH. Thus the stellar and BH mass grow (and stop growing) in parallel. The parallelism is not exact, however, since the star formation rate has a twofold effect on the BH growth. As a result, the $M_\bullet$–$M_{\rm sph}$ relation is not strictly linear, but bends down at small masses, and is slightly different for different values of $z_{\rm vir}$. On the other hand, estimates of $M_{\rm sph}$ are somewhat indirect and therefore liable to larger uncertainties than those of σ, that can be directly measured; this may translate in an *observed* scatter around

the mean $M_\bullet$–$M_{\rm sph}$ relation comparable to, or larger than that for the $M_\bullet$–σ relation, in spite of the smaller intrinsic scatter.

In Fig. 7.6 we plot the $M_\bullet - M_{\rm sph}$ relation for objects with reliable bulge mass determinations from Häring & Rix (2004). The agreement between the data, suggesting a slightly non-linear relation ($M_\bullet \propto M_{\rm sph}^{1.12}$), with our predictions is remarkably good. As pointed out by Häring & Rix (2004), a significant fraction of the scatter (which is ≤ 0.3 dex) can be attributed to measurement errors. As mentioned in Chapter 2, Section 2.1.2, Marconi & Hunt (2003) found that the scatter in this relation is reduced to ~ 0.25 dex, when $M_{\rm sph}$ is estimated as a virial mass ($\sim R_e\sigma^2$).

In Fig. 7.8 we report the full predictions of the ABC model in reproducing the "Mass Fundamental Plane" for the system SMBH-Galaxy-DM. The $M_\bullet - M_{\rm vir}$ relation presents a scatter $\Delta_{\rm zvir} \sim 0.3$, deriving for different virialization redshifts, similarly to what is obtained in Fig. 7.5 for the $M_\bullet - \sigma$ relation. It has to be noted that the scatter reported in Chapter 6 in the relation $M_\bullet - M_{\rm sph}$ relation at *fixed* redshift of about $\Delta_{\rm LF} \sim 0.3$ dex, for fitting the AGN LF, has to be quadratically summed to the previous one. The resulting scatter is however small, being $\Delta_{\rm tot} = \sqrt{\Delta_{\rm zvir}^2 + \Delta_{\rm LF}^2} = 0.4$. In the $M_{\rm vir} - M_{\rm sph}$ relation it has to be noted (lower panel in Fig. 7.8) that at virial masses above $M_{\rm vir} \sim 10^{12} M_\odot$, there is an increasing steepening of the usual SN feedback behavior $M_{\rm vir} \propto M_{\rm sph}^{2/3}$ (e.g. Romano et al. 2002; it will be extensively discussed in Chapter 8), due to the more powerful AGN kinetic feedback in removing gas from the host galaxy.

The predicted $M_\bullet - M_{\rm vir}$ relation predicted by the ABC model is close in slope and normalization, to the relation obtained by Baes et al. (2003), $M_\bullet \propto M_{\rm vir}^{1.3}$, assuming the $V_{\rm vir} - M_{\rm vir}$ relation set at $z_{\rm vir} \sim 2.5$.

The very good fits of the observed $M_\bullet$–σ and $M_\bullet - M_{\rm sph}$ relations are additional strong indications that the ABC model properly includes the mutual feedbacks of stars and QSOs. It is worth noticing that the model also correctly predicts the local BH mass function in spheroidal galaxies (see Chapters 4 and 6).

A synoptic view of the effect of feedback on the luminosity-σ relation, on the local r^*-band luminosity function, and on the $M_{\rm bullet}$–σ relation, based on the ABC model, is provided by Fig. 7.9. If we switch off the supernova feedback (central panel row), we

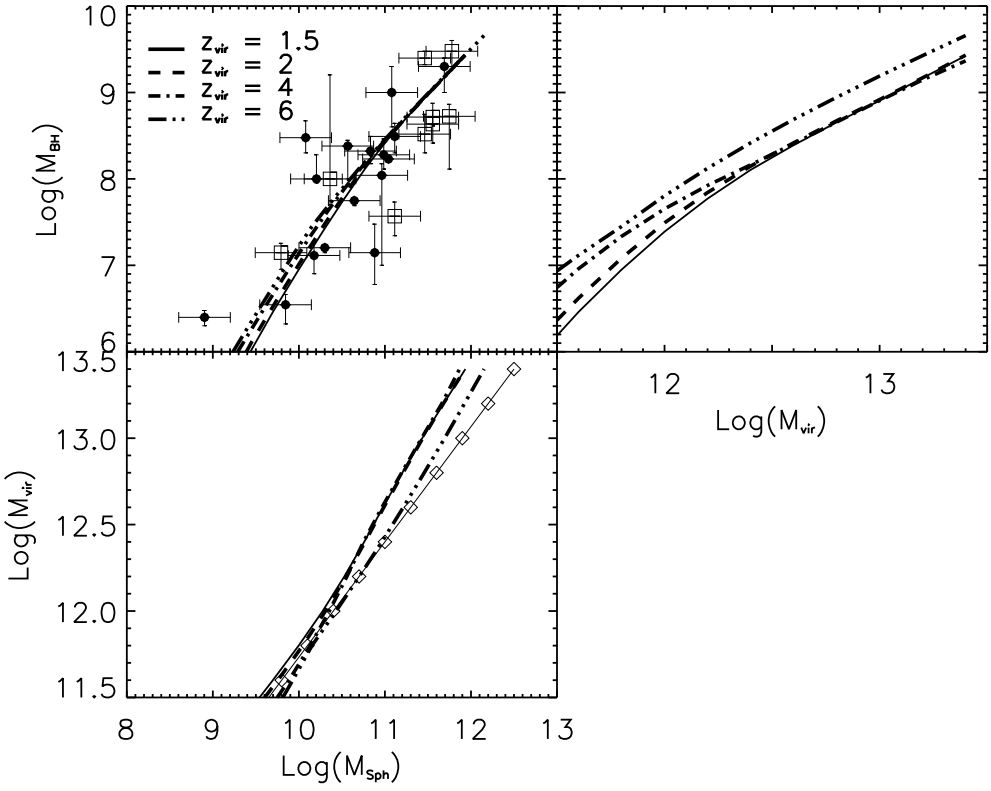

Figure 7.8: Orthogonal projections of the "Mass Fundamental Plane". In the left upper panel the predicted $M_\bullet - M_{\rm sph}$ relation with data by Häring & Rix (2004). The upper-right and lower-left panels show the $M_{\rm vir} - M_\bullet$ and $M_{\rm vir} - M_\bullet$ relations, respectively. Open diamonds connected with a thin solid line represent the scaling relation $M_{\rm vir} \propto M_{\rm sph}^{2/3}$ as suggested by Romano et al. (2002; see also Chapter 8).

get a larger luminosity at fixed virial velocity $V_{\rm vir}$. The increase is of $\simeq 1$ mag. for low luminosity/mass galaxies ($M_{r^*} \simeq -20$), where the stellar feedback is dominating over the QSO feedback, and of 0.5 mag. at high luminosities ($M_{r^*} \simeq -23$). Turning off the QSO feedback (bottom panel row) goes in the same direction, but now the effect is larger for larger galaxies. To fit the observed Faber-Jackson relation with no stellar or QSO feedback, we have to shift by 0.1 dex the $\sigma/V_{\rm vir}$ ratio, but this is inconsistent with the observed VDF.

As shown by the central panel column of Fig. 7.9, the shift to higher luminosities occurring when the feedback is switched off affects only weakly the low luminosity portion of the luminosity function, because of its flat slope. On the other hand, the high luminosity

tail is very sensitive to it, and particularly to the feedback from the active nuclei.

If we were to include in the model also DM halos more massive than $2 \times 10^{13}\, M_{\odot}$ we could still fit the galaxy LF at the bright end at the price of increasing the AGN feedback efficiency. Through this variation our model would inevitably not be able to reproduce the $L_{r^*} - \sigma$ and the $M_{\bullet} - \sigma$ relations anymore, unless a significant decrease in the ratio $\sigma/V_{\rm vir}$ relation is taken into account. However this last solution would worsen the very good match with the VDF provided in Fig. 7.1. Such considerations, together with the observational findings in Chapter 8, reinforce our choice on the value of the upper limit in DM halo mass in our model. As shown in Chapter 6 such findings support the need for introducing an extra scatter in the $M_{\bullet} - M_{\rm vir}$ relation to fit the bright tail of the AGN LF.

On the whole, the local luminosity function of galaxy spheroids and the observed correlations between their properties provide clear evidence that the feedback both from supernovae and from active nuclei plays a key role in the evolution of these sources, and yield rather stringent constraints on the parameters controlling the coupling of the energy injected into the interstellar medium.

7.5 Some physical implications of the $\sigma/V_{\rm vir}$ ratio

At the virialization we consider DM to be distributed with an NFW profile

$$\frac{M_{\rm vir}(< r)}{M_{\rm vir}} = \frac{\ln(1+cs) - cs/(1+cs)}{\ln(1+c) - c/(1+c)} \,, \tag{7.10}$$

where $s \equiv r/R_{\rm vir}$. Moreover we consider the baryons to be distributed as the DM

$$\frac{M_b(< r)}{M_b} = \frac{M_{\rm vir}(< r)}{M_{\rm vir}} \,, \tag{7.11}$$

and that the quantity of baryons is $M_b \approx M_{\rm vir}/6$.

The baryonic binding energy within the DM potential well is (see Chapter 3, Section 3.3.4)

$$E = -\frac{G}{2} \int_0^R dr\, \frac{M_{\rm vir}(< r) + M_b(< r)}{r} \frac{{\rm d}M_b(< r)}{{\rm d}r} \,. \tag{7.12}$$

Through Eq. (7.12) we can set the specific binding energy at the virialization $\epsilon_b \equiv E/M_b$ as

$$\epsilon_b = -\frac{v_v^2}{2} \left(1 + \frac{M_b}{M_{\rm vir}}\right) \int_0^1 \frac{ds}{s} \frac{M_{\rm vir}(< r)}{M_{\rm vir}} \frac{\rm d}{{\rm d}s} \frac{M_b(< r)}{M_b} \,. \tag{7.13}$$

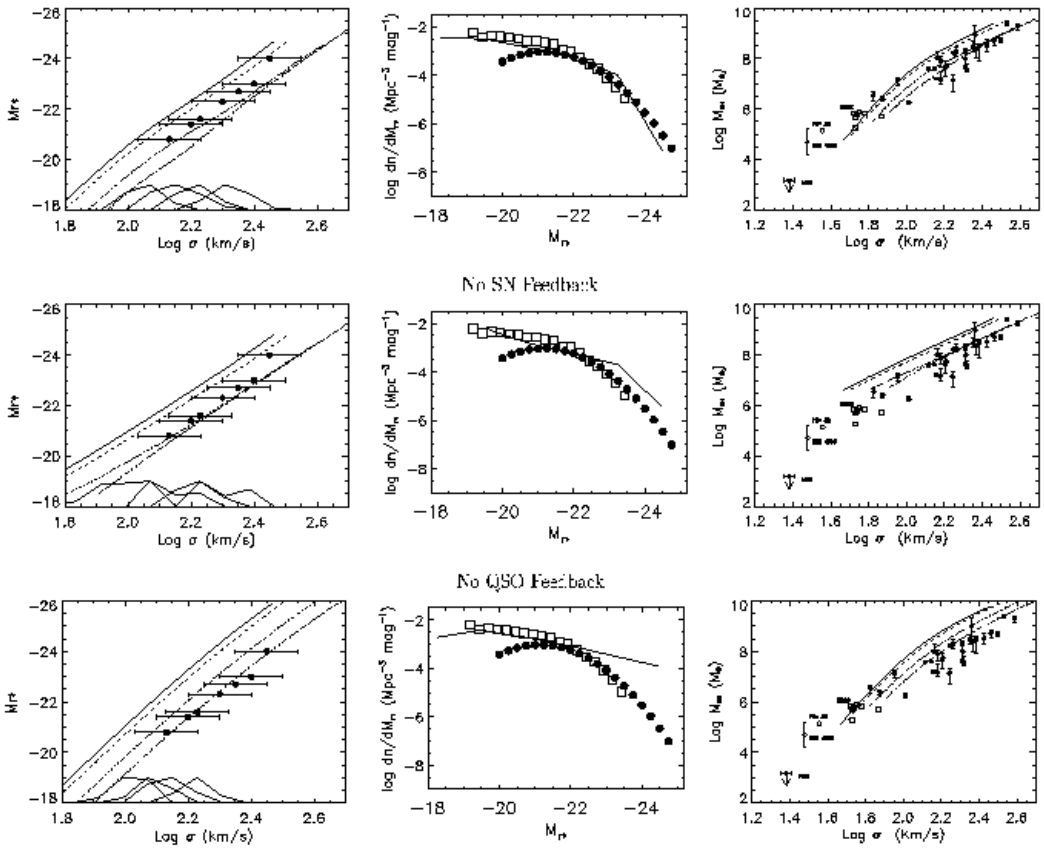

Figure 7.9: Effect of feedback on the Faber-Jackson relation (left panel column), on the local r^*-band luminosity function of spheroidal galaxies (central panel column), and on the $M_{\rm BH}$–σ relation (right panel column), according to the ABC model. The upper, central, and lower panel rows compare with the data the ABC model predictions with feedback fully included and switching off, in turn, the SN and the QSO feedback, respectively. Symbols are as in Figs. 7.2 and 7.5. The observational determinations of the local luminosity function are from Nakamura et al. (2002; open squares), and Bernardi et al. (2003; filled circles).

After infall we suppose the baryons to be distributed as they are observed today. Following the models by Prugniel & Simien (1997) and the above findings and discussions for the $M_{\rm sph}/L$ ratio, the galactic baryons $M_{\rm sph}$ can be described with very good accuracy by a $R^{1/n}$ Sérsic surface brightness profile. The cumulative mass distribution is then given by

$$\frac{M_{\rm sph}(<r)}{M_{\rm sph}} = \frac{\int_0^s dx\, x^{2-\alpha}\, e^{-b\,(\eta\, x)^{1/n}}}{\int_0^1 dx\, x^{2-\alpha}\, e^{-b\,(\eta\, x)^{1/n}}}\ , \tag{7.14}$$

where $1 \leq n \leq 10$, $\alpha = 1 - 1.188/2\,n + 0.22/4\,n^2$ e $b = 2\,n - 1/3 + 0.009876/n$ are the Sérsic profile parameters and $\eta \equiv R_{\rm vir}/R_e$. R_e is simply determined via the fit to the fundamental

plane of Fig. 7.4

$$\log R_e = -0.25\,(M_{r^\star} + 19 - 0.1\,z_{\rm vir} + 0.3) \tag{7.15}$$

where we have also considered the dependence on virialization redshift $z_{\rm vir}$. The specific baryonic binding energy at the present $\epsilon_{\rm sph} \equiv E/M_{\rm sph}$ can then be written as

$$\epsilon_{\rm sph} = -\frac{k_\sigma\,\sigma^2_{\rm sph}}{2}\,\int_0^1 \frac{ds}{\eta s}\,\left[\frac{M_{\rm vir}}{M_{\rm sph}}\,\frac{M_{\rm vir}(<r)}{M_{\rm vir}} + \frac{M_{\rm sph}(<r)}{M_{\rm sph}}\right]\,\frac{\rm d}{{\rm d}s}\,\frac{M_{\rm sph}(<r)}{M_{\rm sph}}\,, \tag{7.16}$$

where the constant $k_\sigma \sim 0.2$ is given in Eq.(7.7).

So we have considered the specific baryonic binding energies at the virialization $\epsilon_b = -V^2_{\rm vir}\,\mathcal{C}_b$ and after infall (at the present) $\epsilon_{\rm sph} = -\sigma^2_{\rm sph}\,\mathcal{C}_{\rm sph}$, in terms of the constants $\mathcal{C}_b$ and $\mathcal{C}_{\rm sph}$ defined in Eq. (7.13) and Eq. (7.16). The specific energy ratio reads as

$$\frac{\epsilon_{\rm sph}}{\epsilon_b} = \left(\frac{\sigma_{\rm sph}}{V_{\rm vir}}\right)^2\,\frac{\mathcal{C}_{\rm sph}}{\mathcal{C}_b}\,. \tag{7.17}$$

Substituting Eq. (7.1) in Eq. (7.17) we find

$$\epsilon_{\rm sph} \sim 1.2 \times \epsilon_b\,, \tag{7.18}$$

showing that, in line with what sketched in Chapter 3, Section 3.4.2, there is *no* significant adiabatic contraction for baryons (at least for spheroids), which just collapse losing energy in favor of DM.

Moreover their final energy is close to the that of DM in the inner regions. As shown in Eq. (7.2) and in Chapter 3, Section 3.3.4 (see Fig. 2, thick solid line), we noticed that the DM dispersion velocity at the virial radius *and* in the inner regions (at about $R_e \sim R_{\rm vir}/100$) is about $\sigma_{\rm vir} \sim (0.5 \div 0.7)V_{\rm vir}$, implying, from Eq. (7.1), that $\sigma_{\rm sph} \sim \sigma_{\rm vir}(R_e) \sim \sigma_{\rm vir}(R_{\rm vir}) \sim 0.55V_{\rm vir}$, which simply shows that the galactic baryons behave kinematically as DM particles in the inner regions.

The cold baryonic clouds in fact in our view, still mostly in gaseous form, settle in the inner regions of the host DM halo, i.e. when they start releasing energy (being the dynamical friction timescale of the order of the collapse timescale, see Mo & Mao 2004 and Chapter 3). At the center the DM particles gaining energy expand and are *replaced* by the baryons which will have their same original energy *and* dispersion velocity (*dynamical attractor* model; see Chapter 3).

Chapter 8

The SMBH-Galaxy-Dark Matter Connection

In the previous chapter we have analyzed the relations occurring among SMBH, stars and host DM halo, as output of the Granato et al. model. Moreover we have derived the basic features of SN and AGN feedback in setting the FP and LF of early-type galaxies and highlighted the imprints of the rapid, non-adiabatic collapse of baryons, imprinted in the $\sigma - V_{\rm vir}$ relation. In this chapter we show that the previous model-dependent results on baryon evolution in DM halos, can be directly inferred from detail analysis of the local data.

We derive the stellar and baryonic MF of galaxy structures from their inner kinematics and their luminosity function. In the following we'll indicate $M_{\rm star}$, the stellar component of a galaxy which, in the case of Ellipticals, coincides with most of its mass $M_{\rm sph}$ (being the gas component negligible). We also estimate the MF of halos hosting one single galaxy, properly taking into account subhalos and galaxy groups and clusters. By comparing local number density distribution of galaxy luminosity, stellar mass, velocity dispersion and black hole mass with the MF of galaxy halos, we obtain the relationships between these characteristic galaxy properties and the galaxy halo mass $M_{\rm vir}$ in the range $3{\times}10^{10}\,M_{\odot} \leq M_{\rm vir} \leq 3{\times}10^{13}\,M_{\odot}$. All the relations involving luminosity, stellar, and central black hole mass are well represented by a double power law, with a break at a characteristic

halo mass $M_{\rm vir}^{\rm break} \approx 3 \times 10^{11}\, M_\odot$, corresponding to a mass in stars $M_{\rm star} \sim 1.2 \times 10^{10}\, M_\odot$, to a r^*-band luminosity $L_r \sim 5 \times 10^9\, L_\odot$ and to a black hole mass $M_\bullet \sim 9 \times 10^6\, M_\odot$. Only the velocity dispersion vs. halo mass relation is well represented by a single power law; the velocity dispersion associated to the break mass $M_{\rm vir}^{\rm break}$ is $\sigma \sim 80$ km s^{-1}. We illustrate how these relations bear the effects produced by SN explosions and AGN activity occurred during the galaxy formation process. In fact, we find that the break of the power laws occurs at a mass which marks the transition between the dominance of the stellar and the AGN feedback. We will show that such findings are indeed very close to the outputs of the Granato et al. model presented in the previous chapters.

8.1 The star and baryon Mass Function of galaxies

The LF is a fundamental statistics for galaxies. Its present form is the result of physical processes involving both baryons and DM. In particular the LFs in the range between about 0.1 to several μm probe the stellar component. In order to derive the mass of stars and baryons associated to galaxies, one considers their LFs and then makes the very reasonable assumption that the starlight and the photons emitted by the interstellar gas are good tracers of the baryon distribution in galaxies. The next crucial step is to estimate the Mass-to-Light Ratio (MLR) of the stellar and gaseous component. As it is well known, the MLR and the fraction of gas depend on galaxy morphology.

As presented in Chapter 4, Nakamura et al. (2002) estimated the LF in the r^*-band for early- and late-type galaxies separately. The separation has been done through light concentrations method. These early- and late-type galaxy LFs are in reasonable agreement with the LFs of red and blue galaxies, respectively, as derived by Baldry et al. (2004). Since the Nakamura LF is well defined only at luminosity brighter than $M_r \leq -18$, we extended the LF at lower luminosity following the findings of Zucca et al. (1997) and Loveday (1998) and translating their results from b_J-band to r^*-band using $(b_J - r^*) \approx 0.33$, as appropriate for star forming irregular galaxies (Fukugita et al. 1995). The resulting LF is well fitted by

$$\Phi(L_r)\, {\rm d}L_r = \left(9.05 \times 10^{-3} x^{-1.14}\, e^{-0.0076\, x} + 4 \times 10^{-5}\, x^{-4.03}\right) {\rm d}x \ , \qquad (8.1)$$

where $x \equiv L_r / 2.4 \times 10^8\, L_\odot$. The fit holds in the range $3 \times 10^7\, L_\odot \leq L_r \leq 3 \times 10^{11}\, L_\odot$.

The MLR pertaining to the star component can be derived by studies of stellar evolution, with uncertainties associated to poor knowledge of details of the IMF (see, e.g., Fukugita et 1998; Bell et al. 2003; Fukugita & Peebles 2004; Baldry et al. 2004; Panter et al. 2004). A more observational and direct approach exploits detailed kinematical and photometric studies of galaxies to estimate the amount of mass traced by light and the mass of the DM component, taking advantage of their different distribution inside the galaxies. This method has been used by Salucci & Persic (1999), who estimated the stellar and gaseous mass as function of the B-band luminosity for late-type galaxies to yield the baryon mass $M_b \approx 1.33 M_{HI} + M_{\rm star}$. We have approximated their results as

$$\log \frac{M_{\rm star}}{M_\odot} = -1.6 + 1.2 \log \frac{L_B}{L_\odot} \ , \tag{8.2}$$

and

$$\log \frac{M_{HI}}{M_\odot} = 0.78 + 0.87 \log \frac{L_B}{L_\odot} \tag{8.3}$$

for stellar and gas component, respectively. Combining these relations and the LF of late-type, we derived the Stellar Mass Function and the Baryonic Mass Function of disk systems (or late-type galaxies).

A similar approach can be followed for early-type galaxies. Following Chapter 7 we use $M_{\rm sph} = c\,\sigma^2\,R_e/G$, setting $c = 2.35$ and rescaling the zero point of the MLR according to Bernardi et al. (2003; see Chapter 7), we obtain the MLR of the stellar component in E/S0 galaxies in the r^*-band

$$\left\langle \frac{M}{L} \right\rangle_{\rm star} = 4.1 \left\langle \frac{L}{L_\star} \right\rangle^{0.15} \ . \tag{8.4}$$

By convolving this result with the r^*-band LF of early-type galaxies of Nakamura et al. (2002), we estimate the Galaxy Stellar Mass Function (GSMF) in $E/S0$ galaxies. This mass function is a fair determination also of the Galaxy Baryonic Mass Function (GBMF), since in early-type galaxies the gas gives a negligible contribution to the baryon mass.

The total GSMF is well fitted by a Schechter Function plus a power law term:

$$\mathrm{GSMF}(M_{\rm star})\,\mathrm{d}M_{\rm star} = \left(2.4 \times 10^{-3} x^{-1.19}\, e^{-0.42\,x} + 3.8 \times 10^{-9}\, x^{-3.16}\right) \mathrm{d}x \ , \tag{8.5}$$

where $x \equiv M_{\rm star}/8.14 \times 10^{10}\,M_\odot$. This fit holds over the mass range $10^8\,M_\odot \leq M_{\rm star} \leq 10^{12}\,M_\odot$. In Fig. 8.1 we show our estimate of the GSMF as a solid line. The upturn at

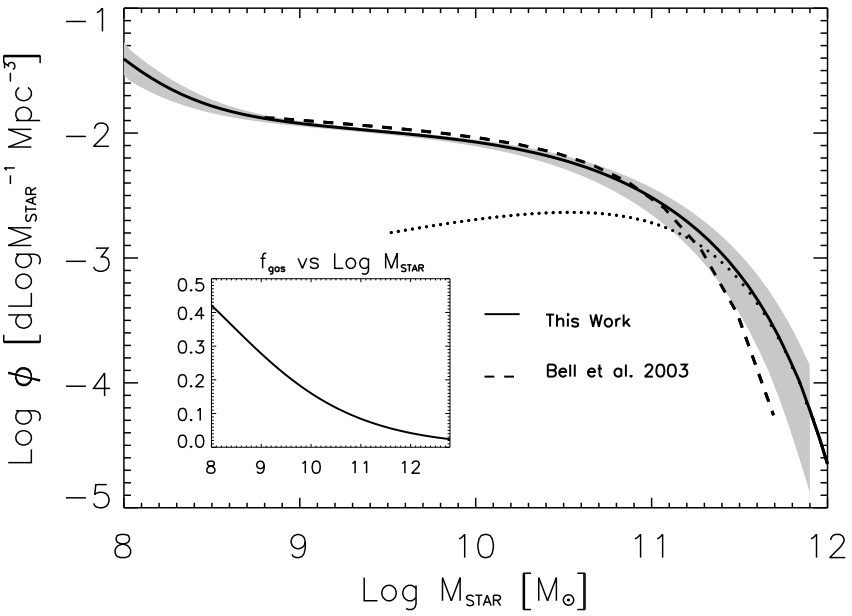

Figure 8.1: Solid line: the galaxy stellar mass function; Dotted line: contribution of early-type galaxies. The shaded area represents the uncertainty of about 30% in the stellar mass to light ratio. The inset illustrates the average fraction of gas as a function of the stellar mass.

$M_{\rm star} \leq 3 \times 10^8\, M_\odot$ corresponds to the appearance of the dwarf galaxy population, i.e. the second term at r.h.s. of the above equation mirrors the second term at r.h.s. of Eq. (8.1). In the inset we have also displayed the gas fraction as function of the stellar mass. The GBMF is easily computed by adding the proper gas mass to the stellar mass. Recent estimates of the GSMF and GBMF have been produced by Bell et al. (2003) and by Baldry et al. (2004), using SDSS and Two Micron All Sky Survey data. Their estimates are quite close, mainly because these authors exploit very similar LFs and MLRs. We have shown the estimate of Bell et al. (2003) as the dashed line in Fig. 8.1. The apparent difference between their and our estimate is mainly due to the difference in the adopted MLR. Bell et al. (2003) have derived their MLR by fitting the broad band SED with stellar population models. As discussed by Bell et al. (2003b) and by Baldry et al. (2004), the uncertainties related to the IMF and star formation history implies about 30% uncertainty in the MLR, to be added to statistical uncertainties of $\sim 20\%$. The MLR adopted by us, based on kinematical determinations, is a factor about 1.3 higher than that used by Bell et al. (2003) at high luminosity, while for very low luminosity objects $L_r \leq 5 \times 10^8\, L_\odot$ is about a factor of 2

lower. At small mass the flatness of the GSMF conceals the difference in MLR, while at large mass the almost exponential decline of the LF amplifies the discrepancy. It is worth noticing that the determination of the MLR in low luminosity objects is hampered by many effects related to the sporadic history of star formation, presence of dust, irregularity of their shapes and DM predominance.

All in all both methods based on kinematical studies and on stellar population synthesis yield GSMFs and GBMFs in reasonable agreement, and establish a sound interval of confidence. The smooth shape over 4 order of magnitude in mass suggests that the galaxy stellar and baryonic mass is not subject to drastic changes with changing morphological type or halo mass. However, it should be noted that while at large mass (dominated by large E/S0 galaxies) baryons are mostly in stars, at the low mass end (dominated by discs and irregular galaxies) a significant fraction of baryons is in the form of diffuse gas.

After integration of the GSMF, the mass density parameter of baryons condensed in stars associated to late-type galaxies turns out to be

$$\Omega^{L}_{\rm star}({\rm KIN}) = (1.3 \pm 0.2) \times 10^{-3} \ , \tag{8.6}$$

where the label KIN indicates that the stellar mass of galaxies has been estimated by using kinematical data. The corresponding neutral gas density amounts to $\sim 20\%$ of this value and it is concentrated in late-type, low mass system with $M_{\rm star} \leq 5 \times 10^{9}\, M_{\odot}$.

The star density parameter associated to early-type galaxies amounts to

$$\Omega^{E}_{\rm star}({\rm KIN}) = (1.8 \pm 0.3) \times 10^{-3} \ . \tag{8.7}$$

It is well known that in early-types the amount of cold gas is negligible. Therefore, the overall local stellar mass density in galaxy structures, with stellar masses in the range $10^{8}\, M_{\odot} \leq M_b \leq 10^{12}\, M_{\odot}$ is

$$\Omega^{G}_{\rm star}({\rm KIN}) = (3.1 \pm 0.4) \times 10^{-3} \ . \tag{8.8}$$

This value is in good agreement with the recent estimates obtained by spectro-photometric galaxy models (Bell et al. 2003; Fukugita 2004; Fukugita & Peebles 2004). The cold gas is only a small fraction $\leq 8\%$ and thus $\Omega^{G}_{b} \approx 1.08 \Omega^{G}_{\rm star}$. This result confirms the well known

conclusion that only a small fraction $\leq 10\%$ of the cosmic baryons is today in stars and cold gas within galaxies.

Is the baryonic matter in galaxies, as measured by the above methods, a reliable cosmological quantity? Have stellar formation processes in galaxies really "not used" $\sim 90\%$ of the available primordial baryonic content? To answer these questions it is worth to investigate whether the density of baryons today detected in stars matches the amount of hydrogen and helium undergone in the past to the cosmological gas-to-stars conversion process. The density of star formation per unit time as function of redshift $\dot{\rho}_*(z)$ can be estimated from observations of the associated IR and UV fluxes. However the conversion from fluxes to $\dot{\rho}_*(z)$ is quite complex and requires assumptions on absorption by dust and on the IMF (the Salpeter IMF is used as a reference). As a consequence the estimates, now extending to z$\approx$ 6, have large uncertainties. Denoting $Y(z) = \log[\dot{\rho}_*(z)]\,(M_\odot \mathrm{yr\,Mpc}^{-3})$, we have approximated the available data (see for a compilation Nagamine at al 2004) as $Y(z) = -1.85 + 0.8z$ for $0 \leq z \leq 1$, $Y(z) = -1.05 + 0.1(z-1)$ for $1 \leq z \leq 3$ and $Y(z) = -0.85 - 0.15(z-3)$ for $3 \leq z \leq 6$. By integrating over the cosmic time and taking into account the dark remnants using a Salpeter IMF extrapolated down to $0.15\,M_\odot$, we get

$$\Omega^G_{\rm star}(SFR) \approx 3.7 \times 10^{-3}\,. \tag{8.9}$$

If, as suggested by a number of arguments (see e.g. Renzini 2004), a flattening of the IMF from 2.35 to 1.35 is allowed below $0.7 - 1\,M_\odot$, then we get $\Omega^G_{\rm star} \approx 3.2 \times 10^{-3}$.

Since there is a general consensus on the fact that the estimated age of the bulk of the stellar populations of spheroidal galaxies is large $T_{\rm sph} \geq 8 - 9$ Gyr (Bernardi et al 1998; Trager et al 2000; Terlevich & Forbes 2002), it is natural to assume that these stars formed in large bursts at redshift $z \geq 1$. On the contrary the stellar populations in discs are younger, mirroring a slower star formation continuing down to the present time (see e.g. Hammer et al. 2005; Heavens et al. 2004). Then, the density of the star formation rate $\dot{\rho}_*(z)$ will be dominated by the contribution of disks for $z \leq 1$. By integrating $\dot{\rho}_*(z)$ we get that the present day density parameter in stars formed at redshift $z \leq 1$ is

$$\Omega_{\rm star}(z < 1) = 1.4 \times 10^{-3} \tag{8.10}$$

while for stars formed at z$\geq$ 1

$$\Omega_{\rm star}(z > 1) = 2.3 \times 10^{-3} \tag{8.11}$$

The excellent agreement of the above values with $\Omega_b^L(KIN)$ and $\Omega_b^E(KIN)$ (see previous section) lends additional substance to the claim that we properly weigh the baryons in galaxies. It is worth to stress that, according to Eq. (8.8), and the assumed SFR, about 60% of the stars today in galaxies were formed at redshift ≥ 1. Moreover the total local SMBH mass density, $\sim 4 \cdot 10^5 M_\odot/{\rm Mpc}^3$ (Chapter 4), is about $1.2 \cdot 10^{-3}$ the amount of star mass density accumulated until $z \geq 1$, very close to the value observed in local galaxies. The ratio of local SMBH mass density and *total* SFR integrated mass density, as given in Eq. (8.9), would yield $\Omega_\bullet/\Omega^G_{\rm star}(SFR) \sim 7 \cdot 10^{-4}$. Such considerations, following Chapter 5 (end of Section 5.3, see Fig. 5.13), highlight the fact that the SMBH accretion history, closely tracks the SFR of spheroidal galaxies.

By subtracting the mass density in groups and clusters $\Omega^{\rm Cls}_{\rm vir} \approx 0.012$ (Reiprich & Bohringer 2002; see lower panel of Fig. 8.2), and in baryons $\Omega_b \leq 0.044$ from the matter density, we obtain the mass density associated with galaxies $\Omega^G_{\rm vir} \approx 0.15$, in excellent agreement with the determination by Fujikawa & Peebles (2004). The average DM-to-baryon (essentially stars) mass fraction in galaxies turns out to be around 60. This value must be compared with the cosmological ratio $R_{\rm cosm} = \Omega_{\rm vir}/\Omega_b \approx 6$. In fact, in rich galaxy clusters the baryon mass, mostly in the form of diffuse gas, and the DM halo have the same relative abundance as the "cosmic" DM to baryon ratio (see, e.g., Ettori, Tozzi & Rosati 2003). This evidences that the ratio between the DM and the baryon component in galaxies decreases on average by a factor about 10 relative to the initial value, due to a number of astrophysical processes occurred during the formation of these objects. In the following we will use the cosmic fraction $f_{\rm cosm} = 1/R_{\rm cosm}$.

8.2 The Galaxy Halo Mass Function and the L, $M_{\rm star}$ and σ vs. halo mass relations

In order to investigate the relationship between the stellar (and baryonic) mass and the DM halo mass in galaxies, the statistics of halos containing one single galaxy, the Galaxy Halo Mass Function (GHMF), has to be estimated. The overall HMF as found by numerical simulations (see, e.g., Jenkins et al. 2001; Springel et al. 2005) is well reproduced with the Press-Schechter (1974) formula as modified by Sheth & Tormen (2002; as discussed in Chapter 3, Sections 3.3.3 and 3.3.5). However, in order to compute the GHMF, we have to deal with the problem of the halo occupation distribution (HOD; Peacock & Smith 2000; Berlind et al. 2003; Magliocchetti & Porciani 2003; Kravtsov et al. 2004; Abazajian et al. 2005). Two effects are mostly relevant: (i) the presence of sub-halos, that are not accounted for by the PS formula and (ii) the fact that a DM halo with mass $M_{\rm vir} \geq 10^{12} \div 10^{13}\, M_{\odot}$ may host a giant galaxy with decreasing probability at increasing halo mass.

To account for effect (i) we use the results by Vale & Ostriker (2004; see their Eqs. [1] and [3]) and we *add* to the HMF the subhalo mass function they have derived; we check that this procedure does not alter substantially the overall mass density in the galactic range. Adoption of van den Bosch et al. (2005) subhalo MF does not alter the final results (see discussion on subhalos in Chapter 3, Section 3.3.7). To account for effect (ii) we *subtract* the halo mass function of galaxy groups and clusters from the HMF. In literature the estimates of the mass function for galaxy groups and clusters have been derived from optical data, using the l.o.s. galaxy dispersion velocity and the virial theorem (Girardi & Giuricin 2000; Martinez et al. 2002; Heinämäki et al. 2003; Pisani et al. 2003; see upper panel of Fig. 8.2). The groups mass functions computed by these authors are in reasonable agreement for $M_{\rm vir} \geq 5 \times 10^{12}\, M_{\odot}$; at lower masses galaxy groups contribute less than 20% to the overall HMF. Therefore large uncertainties in this mass range are tolerable. In this paper we adopt as a reference the determination by Martinez et al. (2002). We stress that a precise determination of the galaxy group and poor cluster mass function is a crucial step toward a sound definition of the GHMF. Observational studies with the aim of increasing statistical samples are strongly needed.

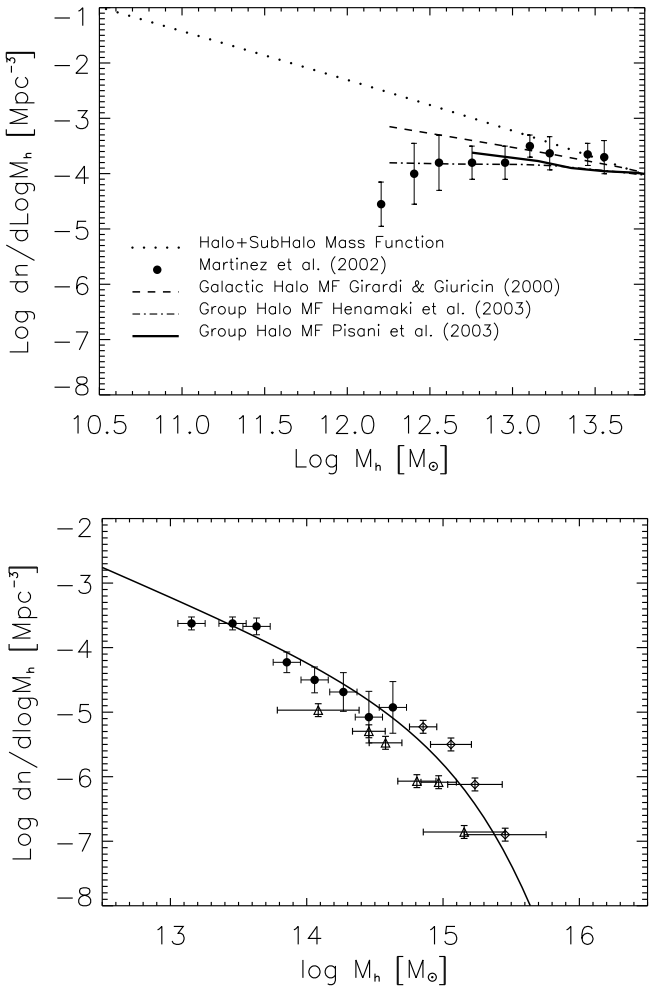

Figure 8.2: Upper panel. Comparison among different observational estimates of galaxy Group mass function. Bottom panel. Thick solid line: S&T mass function computed at $z = 0$; black dots: data from Girardi & Giuricin (2000) of the galaxy Group mass function; diamonds: data from Reiprich & Bohringer 2002 of the galaxy Cluster mass function; triangles: data from Girardi & Giuricin (2000) of the galaxy Cluster mass function.

The resulting GHMF is shown in Fig. 8.3 and it is well fit in the range $11 < \log M_{\rm vir}/M_\odot < 13.2$ by a Schechter function

$$\mathrm{GHMF}(M_{\rm vir})\mathrm{d}M_{\rm vir} = \theta\,(M_{\rm vir}/\tilde{M})^{\alpha}\,\exp[-(M_{\rm vir}/\tilde{M})]\,\mathrm{d}M_{\rm vir}\ , \tag{8.12}$$

with $\alpha = -1.84$, $\tilde{M} = 1.12 \times 10^{13}\,M_\odot$ and $\theta = 3.1 \times 10^{-4}$. The fall off at high mass (where early-type galaxies dominate) mirrors the increasing probability of multiple occupation of mass halos found by Magliocchetti & Porciani (2003) at $M \geq 3 \times 10^{13}\,M_\odot$ (see also Zehavi et al. 2005). Weak lensing measurements also suggest an upper galaxy mass $M_{\rm max} \leq 3 \times$

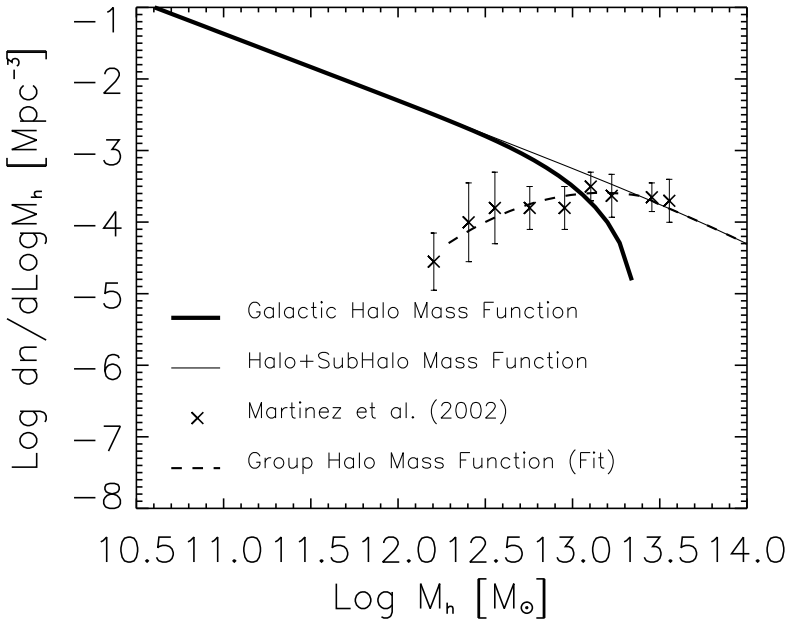

Figure 8.3: Galactic halo mass function.

$10^{13}\,M_\odot$ (Kochanek & White 2001). If we assume that there exists a monotonic relationship between two specific galaxy properties q and p we can write

$$\Phi(p)\frac{\mathrm{d}p}{\mathrm{d}q}\,\mathrm{d}q = \Psi(q)\,\mathrm{d}q\ , \tag{8.13}$$

where $\Psi(q)$ is the number density of galaxies with measured property between q and $q+\mathrm{d}q$ and $\Phi(p)$ is the corresponding number density for the variable p. The solution is based on a numerical scheme that imposes that the number of galaxies with q above a certain value $\bar{q}$ must be equal to the number of galaxy halos with p above a certain $\bar{p}$ (see, e.g., Marinoni & Hudson 2002; Vale & Ostriker 2004), i.e.,

$$\int_{\bar{p}}^{\infty}\Phi(p)\mathrm{d}p = \int_{\bar{q}}^{\infty}\Psi(q)\,\mathrm{d}q\ . \tag{8.14}$$

In the following we will assume $p \equiv M_{\rm vir}$ and $\Phi(p) \equiv \mathrm{GHMF}(M_{\rm vir})$, while the variable q will be luminosity, stellar mass, velocity dispersion, and central BH mass at turns. It is worth noticing that in this way we establish a direct link between the specific galaxy property and the halo mass without any assumption or extrapolation concerning the DM density profile. The result for stellar mass is plotted in Fig. 8.4*a*; we find that its

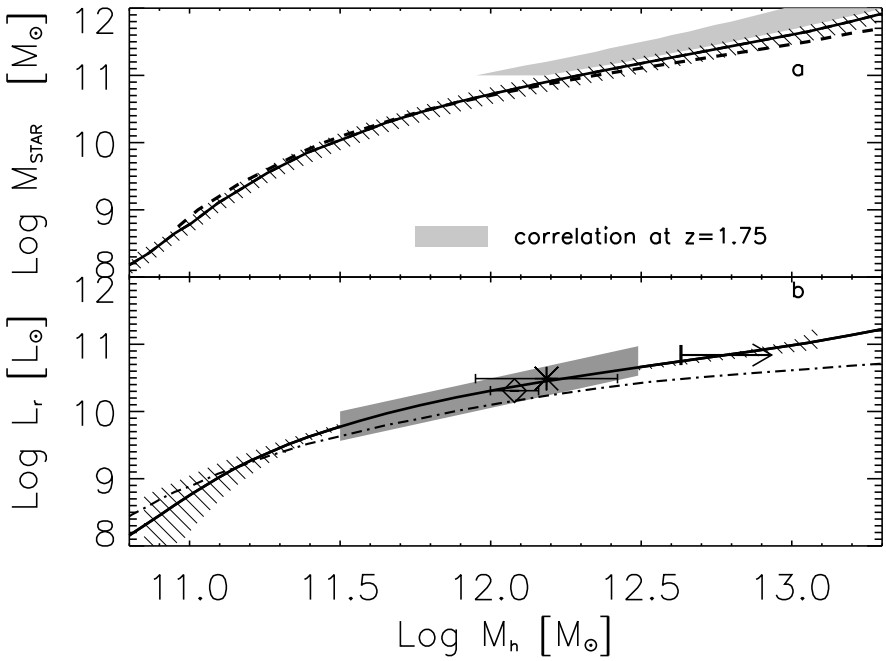

Figure 8.4: Panel *a*. The mass in stars versus halo mass: solid line is the result from this work; dashed line has been obtained by using the GSMF by Bell et al. (2003); the horizontal bars represent the uncertainty associated to the GSMF as shown in Fig. 8.1. Panel *b*. The r^*-band luminosity as a function of halo mass. The shaded region shows the results of Kleinheinrich et al. (2004); arrow: limit set by observations of the galaxy NGC 4555 (O'Sullivan & Ponman 2004); diamond: result of Hoekstra et al. (2004); star: result of Guzik & Seljak (2002); dot-dashed line: $L - M_{\rm vir}$ relation computed by Vale & Ostriker (2004).

relationship with halo mass is well approximated by

$$M_{\rm star} \approx 2.3 \times 10^{10}\, M_\odot \, \frac{(M_{\rm vir}/3 \times 10^{11}\, M_\odot)^{3.1}}{1 + (M_{\rm vir}/3 \times 10^{11}\, M_\odot)^{2.2}} \; . \tag{8.15}$$

The calculations for the baryonic mass is an obvious extension. We also derive the approximated behavior of the luminosity as function of halo mass (Fig. 8.4*b*)

$$L_r \approx 1.2 \times 10^{10}\, L_\odot \, \frac{(M_{\rm vir}/3 \times 10^{11}\, M_\odot)^{2.65}}{1 + (M_{\rm vir}/3 \times 10^{11}\, M_\odot)^{2.00}} \tag{8.16}$$

and, correspondingly, the halo mass as function of luminosity

$$M_{\rm vir} \approx 3 \times 10^{11}\, M_\odot \left(\frac{L_r}{1.3 \times 10^{10}\, L_\odot} \right)^{0.35} \left[1 + \left(\frac{L_r}{1.3 \times 10^{10}\, L_\odot} \right)^{1.30} \right] \; . \tag{8.17}$$

Both stellar mass and luminosity exhibit a double power law dependence on halo mass with a break around $M_{\rm vir} \sim 3 \times 10^{11}\, M_\odot$, corresponding to a luminosity $L_r \sim 6 \times 10^9\, L_\odot$. We

recover the "double power law-behavior" in mass/luminosity as discussed in Chapter 3, Section 3.4.1, which is the clear evidence of a galactic dichotomy. It is worth reminding in fact that the analysis of a huge sample of galaxies drawn from the SDSS shows that around $M_{\rm star} \approx 3 \times 10^{10}\, M_\odot$ and $M_r \sim -20.5$ there is a sort of transition in the structure and stellar ages of galaxies (Kauffmann et al. 2003; Baldry et al. 2004; see also Chapter 3, Fig. 3.14, upper panel).

The method exploited to derive the $L_r - M_{\rm vir}$ relation is quite sensitive to uncertainties in the LF and in the GHMF. Fortunately, in the intermediate range $10^9\, L_\odot \leq L_r \leq 10^{11}\, L_\odot$ the uncertainties in the LF are small. The corresponding uncertainties in the $L_r - M_{\rm vir}$ relation are small in the range $10^{11}\, M_\odot \leq M_{\rm vir} \leq 10^{13}\, M_\odot$. At high mass the results are plagued by the uncertainties in the GHMF; nevertheless the final relation is not much affected, as it is apparent from Fig. 8.4*b*. Much more significant is the uncertainty related to the LF at low mass; in fact, at $L_r \leq 3 \times 10^8\, L_\odot$ the errors rapidly increase bringing the uncertainties in the LF to a factor of about 2. In order to illustrate the consequences on the $L_r - M_{\rm vir}$ relation, we can take as LF in Eq. (8.1) the $1\,\sigma$ upper and lower boundaries given by Nakamura et al. (2003). In the former case, the slope of the $L_r - M_{\rm vir}$ relation flattens from ~ 2.6 to ~ 1.9; in the latter case, an almost exponential decay occurs. Therefore, the extrapolation of the above relationships below $L_r \ll 10^9\, L_\odot$ and correspondingly $M_{\rm vir} \ll 10^{11}\, M_\odot$ must be taken cautiously. This emphasize the need for observations devoted to precise determination of the LF at the low luminosity end.

As an important check, in Fig. 8.4*b* our estimate of the L_r vs. $M_{\rm vir}$ relation is compared with observational evaluations of $M_{\rm vir}$ based on two different methods: (i) X-ray-based mass model of an isolated elliptical galaxy NGC 4555 (O'Sullivan & Ponman 2004), in which the gravitational potential is known up to about 1/8 of the virial radius (the mass within this radius is shown as a lower limit in Fig. 8.4*b*); (ii) weak-lensing observations that provide the shear field around a number of galaxies of average luminosity L, from which it is possible to infer the projected mass density and eventually to extrapolate the virial mass by assuming a DM profile (Guzik & Seljak 2002; Kleinheinrich et al. 2004; Hoekstra et al. 2004). As a further check, our estimate of the ratio $M_{\rm vir}/M_{\rm star}$ is compared with estimates derived by extending to virial radius the inner mass models of a number of giant

ellipticals (Gerhard et al. 2001) and spirals (Persic, Salucci & Stel 1996; Salucci & Burkert 2000). We stress that these results are based on mass extrapolated to the virial radius, by assuming a NFW profile (Navarro, Frenk & White 1996), while our estimate does not need any assumption on DM density profile. It is apparent that these independent results are in nice agreement with our findings.

The dependence of the luminosity on the halo mass has been investigate also by Vale and Ostriker (2004); their result is reported in Fig. 8.4*b*. They exploited the 2dF galaxy luminosity function in b_J-band estimated by Norberg et al. (2002), extrapolating it beyond the range of magnitudes wherein it was defined. The difference in the $L_r - M_{\rm vir}$ relation between our and their estimate is due to steeper slope of the LF adopted by them. At high mass the flattening they found stems from their direct comparison of the galaxy LF to the halo and subhalo number density (cf. their Eq. [9]). As these authors pointed out, in this way the mass term refers to the mass of the entire halo hosting the group or the cluster and not to just the galaxy halo.

It is worth deepening the comparison with the results of Guzik & Seljak (2002), who modelled the galaxy-galaxy lensing trying to separate the central galactic contributions from the surrounding groups and clusters. Their model applied to the SDSS data on galaxy lensing yields $M_{\rm vir}/L_r \approx 50\, M_\odot/L_\odot$ at the characteristic luminosity $3 \times 10^{10}\, L_\odot$ for early-type galaxies, in keeping with our results. They also found a luminosity dependence $M_{\rm vir} \propto L^{1.4\pm0.2}$. From Eq. (8.17) it is apparent that at high luminosity the slope is compatible with their findings. However, at low mass we find that the slope significantly flattens toward a dependence $M_{\rm vir} \propto L^{0.35}$. On the other hand, one starting point of their analysis is the assumption of a single power law relating halo mass and luminosity $M_{\rm vir} \propto L^\beta$. Van den Bosch et al. (2003, 2005) computed the Conditional LF of early- and late-type galaxies, a statistics linking the distribution of galaxies to that of the DM. They concluded that the MLR has a minimum $M_{\rm vir}/L_r \sim 45 - 70\, M_\odot/L_\odot$ at $M_{\rm vir} \sim 2 - 4 \times 10^{11}\, M_\odot$. We also find a minimum around the same position and a rapid increase of the MLR with decreasing halo mass (cf. Eq. (8.17) and Fig. 8.5).

Marinoni & Hudson (2002) investigated the problem of the MLR of the virialized sistems, which include galaxies, groups and clusters. By comparing the luminosity function

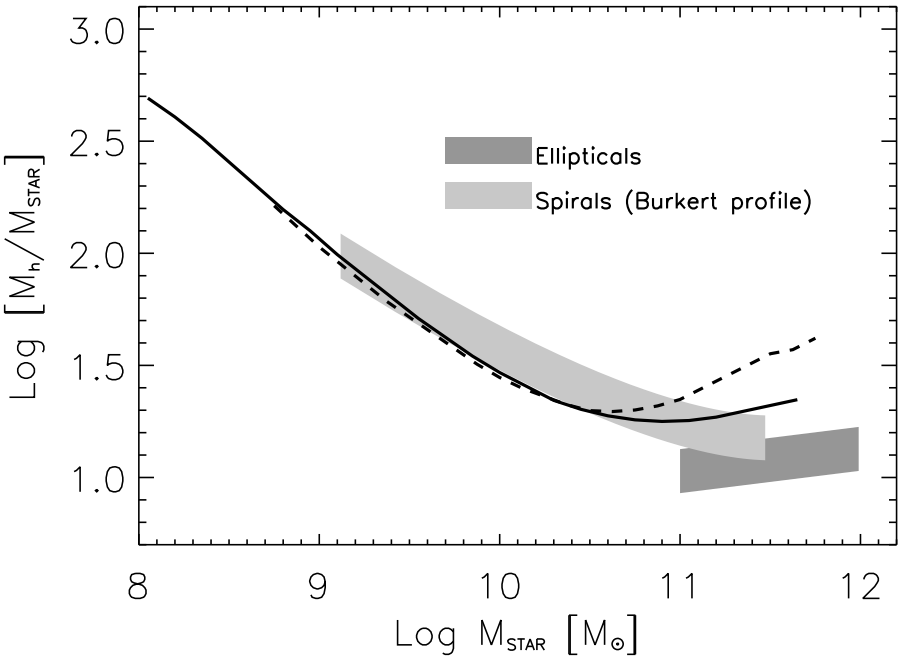

Figure 8.5: Ratio of halo to stellar mass as a function of stellar mass. Solid and dashed lines are as in Fig. 8.1. Data for giant elliptical galaxies are from Gerhard et al. (2001), while data for spirals are from Persic, Salucci & Stel (1996) and Salucci & Burkert (2000).

of virialized systems to the ΛCDM halo mass function, they concluded that the MLR has a broad minimum at around $L_B \approx 2 \times 10^{10}\, L_\odot$. The slopes at low and high luminosity are -0.5 and $+0.5$, respectively. Our slope is similar at low mass, where practically all virialized systems are galaxies and thus the comparison is meaningful.

By comparing the HMF and the LF, as we have done for local galaxies, it is possible to infer the $M_{\rm star} - M_{\rm vir}$ relation even at substantial redshift. For the GSMF we use the linear fit to the data by Fontana et al. (2004) at $\bar{z} = 1.75$. For the GHMF we exploit the HMF computed at the same redshift, assuming the galaxy groups contribution negligible at this redshift; as a consequence the shaded area in Fig. 8.4*a* should be taken as an upper limit. The resulting $M_{\rm star} - M_{\rm vir}$ relation is quite close to the local one. This clearly points to the fact that for large galaxies the relation $M_{\rm star} - M_{\rm vir}$ was already in place at redshift $z \geq 1$ in line with the theoretical modeling of the anti-hierarchical baryon collapse scenario developed by Granato et al. (2001; 2004). Moreover it is interesting to notice that the upper limit in the GSMF, of about $\sim 10^{12}\, M_\odot$ corresponds, in our analysis, to a halo of $\log(M_{\rm vir}/M_\odot) \sim 13.3$ very close to the upper limit for "galactic" halos used in

our code for spheroid evolution.

The VDF computed by Sheth et al. (2003), including the bulges, is defined in the range 80 km $s^{-1} \leq \sigma \leq 400$ km s^{-1}. On comparing the VDF and the GHMF by the same technique presented above (cf. Eqs. (8.13]) and (8.14)), we can derive the relationship $\sigma - M_{\rm vir}$

$$\sigma \approx 126\,{\rm km\,s^{-1}} \left(\frac{M_{\rm vir}}{6.3\times10^{11}\,M_\odot}\right)^b , \tag{8.18}$$

where $b = 0.48$ for $M_{\rm vir} \leq 6.3\times10^{11}$ and $b = 0.26$ for $M_{\rm vir} \geq 6.3\times10^{11}\,M_\odot$. We note that a sufficiently accurate fit (relative errors $\leq 15\%$ in the region of interest) is provided by a single power law $\sigma \sim 117\,{\rm km\,s^{-1}}\,(M_{\rm vir}/6.3\times10^{11}\,M_\odot)^{1/3} \propto V_{\rm vir}$, consistent with the findings of Chapter 7.

One may note that combining the above equation with the high mass asymptote of Eq. (8.16), we obtain a $L_r - \sigma$ relation flatter than the canonical Faber-Jackson relationship. It must be taken into account, however, that such asymptote applies to the mass region populated by groups and clusters of galaxies; confining ourselves to galaxies, we obtain the approximate relation $L_r \propto \sigma^3$, in good agreement with the relation obtained in Chapter 4 (see also Sheth et al. 2003 who used the bisector method).

It is straightforward to compute the fraction $f_{b,\rm coll}$ of the baryon mass left in stars or in cold gas M_b with respect to the initial mass in baryons $M_{b,i} = f_{\rm cosm} M_{\rm vir}$. Fig. 8.6 elucidates the "inefficiency" of baryons in contracting into stars and cold gas, especially in small halo mass. An "adiabatic" and complete contraction would lead to $f_{b,\rm coll} = 1$. Our conclusion is at variance with respect to the claim of Guzik & Seljak (2002) of a high efficiency, up to 75%. However, the claim is based on a MLR $M_{\rm vir}/L_r \approx 15\,M_\odot/L_\odot$ for late-type galaxies, a factor of 3 lower than the value found for early-types. As the same authors point out, the statistical significance of this result is marginal, due to the weak signal of the lensing for the fainter late-type galaxy sample.

8.3 Black hole vs. halo mass

The relation between the central supermassive Black Hole (BH) and the halo mass $M_{\rm vir}$ is fundamental, as described throughout this thesis, in the framework of theories

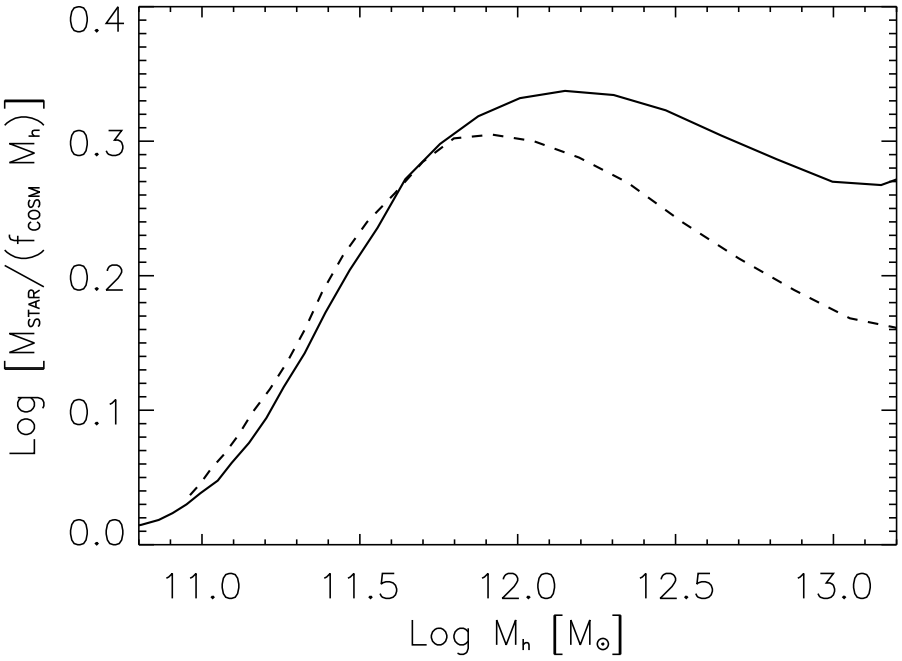

Figure 8.6: Fraction of primordial gas turned into stars as a function of halo mass. Solid and dashed lines are as in Fig. 8.1.

explaining origin and evolution of the central gravitational engine and the associated AGN (Silk & Rees 1998; Monaco, Salucci & Danese 2000; Granato et al. 2001; Ferrarese 2002; Granato et al. 2004). To constrain such a relation we adopt the procedure presented in the previous Section (cf. Eqs. (8.13) and (8.14)), replacing the function $\Psi(q)$ with the local central BH Mass Function (computed in Chapter 4). We assume that each galactic "cusp" hosts just one supermassive BH. Our result is shown in Fig. 8.7*a*, where the barred area illustrates the errors due to the observational uncertainties on the BH mass function. The relationship can be approximated by

$$M_\bullet \approx 1.7 \times 10^7 \, M_\odot \, \frac{(M_{\rm vir}/2.5 \times 10^{11} \, M_\odot)^{3.7}}{1 + (M_{\rm vir}/2.5 \times 10^{11} \, M_\odot)^{2.7}} \; . \tag{8.19}$$

Similarly to the case of luminosity and mass in stars, a double power law with a break at $M_{\rm vir} \sim 3 \times 10^{11} \, M_\odot$ is a very good representation of our result. At the high end, the BH mass is directly proportional to the halo mass $M_\bullet \propto M_{\rm vir}$, while at low mass the relation significantly steepens $M_\bullet \propto M_{\rm vir}^{3.7}$. Moreover, as anticipated in Chapter 7, the relation $M_\bullet - M_{\rm vir}$ we find in Eq. (8.19) is about a factor of 3 higher than what found by means of the $M_\bullet - \sigma$, $\sigma - V_{\rm vir}$ and $V_{\rm vir} - M_{\rm vir}$ relations, if the last one is estimated at $z = 0$ (see

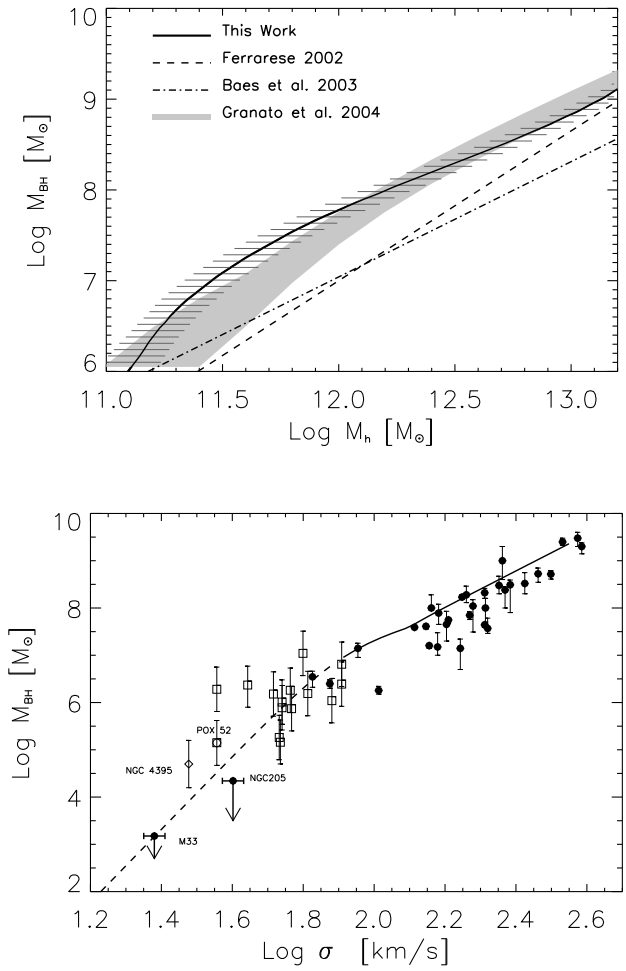

Figure 8.7: Panel *a*. Supermassive BH-halo mass relation: horizontal bars represent the error due to the uncertainty on the BH mass function. Panel *b*. $M_{BH} - \sigma$ relation: Solid line is obtained by replacing the halo mass with σ in Eq. (8.19) through Eq. (8.18); data are as in Chapter 7, Fig. 7.6.

Ferrarese 2002), meaning again that the relationship between SMBH and its halo mass was established at high redshift.

Interestingly a very good fit to the available data (including upper limits) of the black hole mass and velocity dispersion (see Ferrarese 2004 for a review) can be obtained plugging the above $M_\bullet - M_{\rm vir}$ relationship into Eq. (8.18), see Fig. 8.7*b*. It is worth noticing that filled circles represent objects in which the BH mass has been computed through detailed analysis of the stellar and gas motions within the BH influence radius. By the way these galaxies are quite nearby. The open symbols refer to active galaxies, whose BH

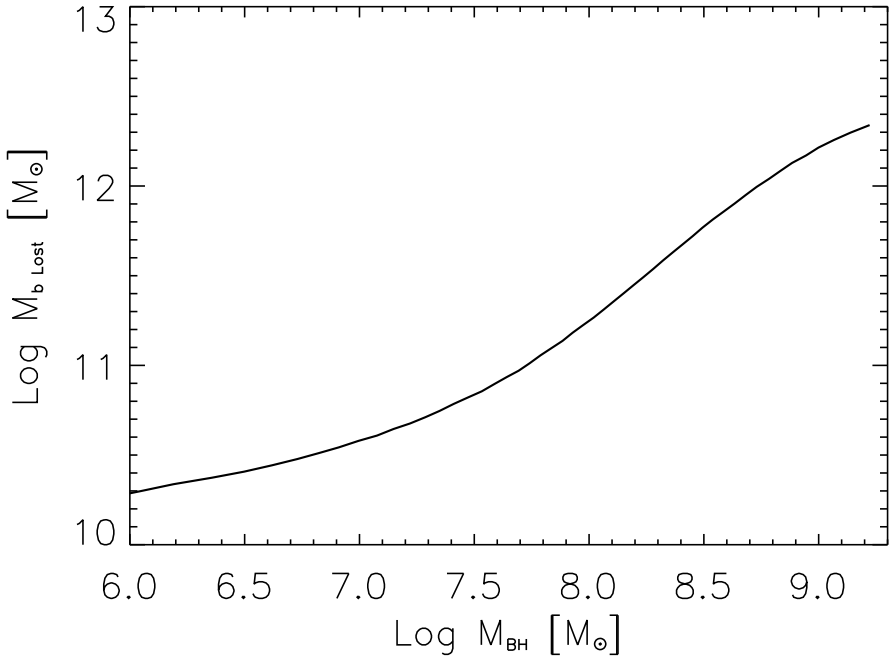

Figure 8.8: Ejected baryonic mass as a function of SMBH mass.

mass has been computed through empirical relationships connecting the widths of emission line, usually H_β, to the BH mass with additional guesses on the radius of the Broad Line Region. Finally in Fig. 8.8 we relate the baryonic mass lost by ellipticals, $M_{\rm b,lost} = M_{\rm vir} \times f_{\rm cosm} - M_{\rm star}$, where $M_{\rm star}$ is given in Eq. (8.15), to the mass of the SMBH. We find a clear steepening of the relation for SMBH with mass higher than $10^8 M_\odot$, meaning that more massive systems have expelled more mass. Such findings are a signature in favor of a *super-linearity* of the feedback output, i.e. a stronger feedback efficiency for more massive SMBH, as theoretical models predict (Murray et al. 1995; Granato et al. 2004; see also Chapter 3, Section 3.4).

8.4 Feedback from stars and AGN

The behavior of star and BH mass as a function of halo mass found in the previous Section, suggests that different physical mechanisms are determining the relations below and above $M_{\rm vir}^{\rm break} \sim 3 \times 10^{11}\, M_\odot$. The corresponding mass in stars is $M_{\rm star} \sim 1.2 \times 10^{10}\, M_\odot$ after Eq. (8.15), while the corresponding r^*-band luminosity is $L_r \sim 5 \times 10^9\, L_\odot$ after Eq. (8.16)

and the corresponding absolute magnitude is $M_r \sim -19.6$.

The efficiency of star formation within galactic halos of different mass is the result of several processes (see Chapter 3, Section 3.4). The most remarkable include: (i) cooling of primordial gas within the virialized halos (White & Rees 1978) (ii) injection of large amounts of energy into the ISM through Supernovae explosions (e.g., Dekel & Silk 1986: White & Frenk 1991; Granato et al. 2001; Romano et al. 2002) and through the activity of a central quasar, (Silk & Rees 1998; Granato et al. 2001, 2004; Lapi et al. 2005). All these mechanisms have been implemented in the model of Granato et al. (2004; see Chapter 3 for details and for the following Eqs.).

So long as the star formation rate obeys Eq. (3.70), the mass in stars at the present time t, assumed to be much longer than the cooling time t_c, is given, after Eq. (3.80), by:

$$M_{\rm star} \propto f_{\rm surv} \frac{f_{\rm cosm} M_h}{1 - R + \alpha} \ , \tag{8.20}$$

where $f_{\rm surv}$ is the fraction of stars that survive up to now. On the other hand, the effect of AGN feedback, that dominates for large masses, is not included in Eq. (3.70). However, the full treatment developed by Granato et al. (2004) shows that it becomes important and stops the star formation in a time of order of few times t_c (see previous Chapters), depending on the halo mass and virialization redshift, so that Eq. (8.20) is a useful approximation even for large galaxies. At high mass, where the stellar feedback is less efficient $\alpha \leq 1$, the quantity $1 - R + \alpha$ is a slowly decreasing function of the halo mass. As a result Eq. (8.20) suggests $M_{\rm star} \propto M_{\rm vir}$, in close agreement with our analysis (cf. Eq. (8.15)) and with the numerical results presented in Chapter 7 (Fig. 7.8). In the same mass range the effective optical depth, which rules the flow of cold gas into the reservoir around the BH (cf. Eq. (3.84)), is large $\tau \geq 1$; therefore from Eq. (3.87) we expect the BH mass to exhibit a dependence on the halo mass very similar to that of the stellar mass, in agreement with Eq. (8.19).

Eq. (3.75) shows that at low masses $M_{\rm vir} \leq 10^{11}\, M_\odot$ the effective SN efficiency ($\alpha \gg 1$) overwhelms the quantity $1 - R \approx 0.7$. Therefore $M_{\rm star} \propto M_{\rm vir}/\alpha$ and taking into account that $\alpha \propto M_{\rm vir}^{-2/3}$, we get

$$M_{\rm star} \propto f_{\rm surv}\, M_{\rm vir}^{5/3} \ . \tag{8.21}$$

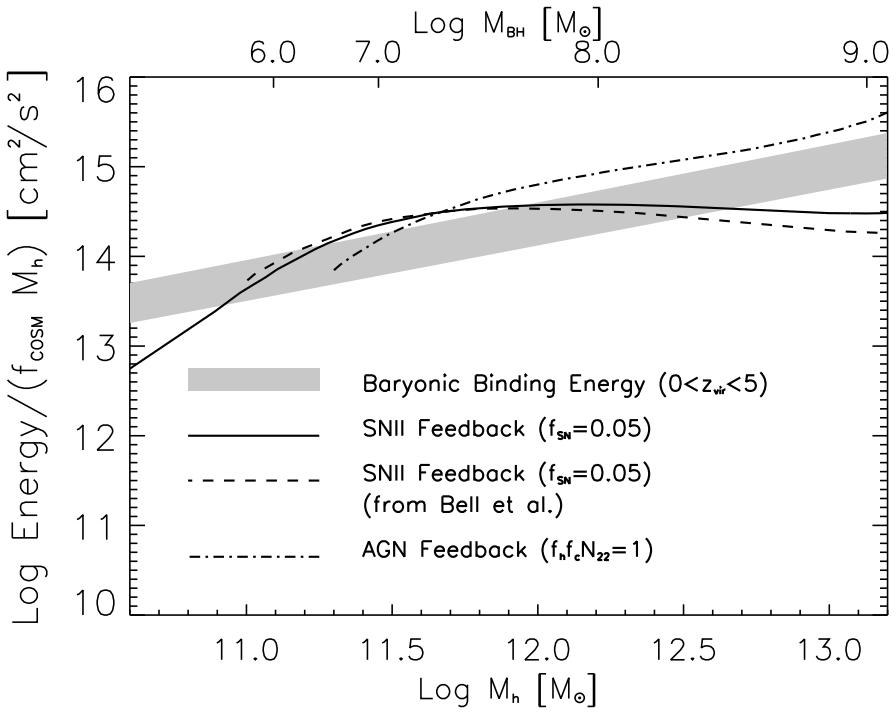

Figure 8.9: Specific energy feedback from stars and AGNs compared to the host DM halo binding energy, as a function of halo mass.

The limiting slope has been derived theoretically also by Dekel & Woo (2003) with similar assumptions. On the other hand, such a slope is significantly flatter than that inferred from data, cf. Eq. (8.15). Possible explanations are: (i) at small mass the SN efficiency may increase with decreasing mass/luminosity; (ii) other processes are at work to remove a significant fraction of the gas and/or to prevent star formation at small masses. However, we recall that at very low mass and luminosity, the slope of the $M_{\rm star} - M_{\rm vir}$ relation is uncertain due to the observational errors in the LF and a limiting slope $M_{\rm star} \propto M_{\rm vir}^{1.9}$ is still permitted by the data (see § 2).

Since in the mass range $M_{\rm vir} \leq 10^{11}\, M_\odot$ the optical depth $\tau \ll 1$ is small, from Eqs. (3.87) and (3.88) we obtain for the BH mass

$$M_\bullet \propto M_{\rm star}\, \tau \propto M_{\rm vir}^{7/3}\ . \tag{8.22}$$

More in general this simple model predicts that the slope of the $M_\bullet - M_{\rm vir}$ relation steepens relative to the slope of the $M_{\rm star} - M_{\rm vir}$ relation, because of the decrease of the optical depth with mass $\tau \propto M_{\rm vir}^{2/3}$, mirroring the decreasing capability of feeding the reservoir around the

BH. Interestingly, such a steepening is also found from our analysis of observational data, cf. Eqs. (8.15) and (8.19).

The impact of stellar and AGN feedback is further illustrated in Fig. 8.9. The DM host binding energy per unit baryonic mass as function of halo mass (cf. Eq. (3.73)) for $0 \leq z_{\rm vir} \leq 5$ is shown as the shaded area. To compute the overall energy per unit bayonic mass injected in the gas by SN ($E_{\rm star}$) and by AGN (E_{AGN}), we use Eqs. (3.81) and Eq. (3.100), respectively, where $M_{\rm star}$ and $M_\bullet$ as functions of halo mass are given by the results of our analysis (Eqs. (8.15) and (8.19), respectively). Then we divide the overall energies by the initial baryon mass $M_{b,i}$ appropriate for the halo mass. From Fig. 8.9 it is apparent that at large mass the stellar feedback falls short with respect to the binding energy; nonetheless the gas can be efficiently removed by the AGN feedback, which overwhelms the binding energy. At small masses, on the other hand, it appears that the star formation rate inferred from the present content in stars is not enough to remove the gas associated to the host halo. This conclusion rephrases the above mentioned problem that the observed $M_{\rm star} - M_{\rm vir}$ relation exhibits a slope steeper than predicted by the simple model of stellar feedback.

The relative value of the two feedbacks depends on their efficiency in transferring the available energy to the gas. In particular the crossing point of the stellar and AGN feedback depends on their relative efficiency. It is interesting that with the efficiencies reported in Fig. 8.9 the crossing point is quite close to the mass of the break of the power laws found above $M_{\rm vir}^{\rm break} \approx 3 \times 10^{11}\, M_\odot$. However, as discussed in Chapters 6 and 7, a more accurate evaluation of the efficiencies can be obtained by fitting statistics of galaxies, e.g., LFs at low and high redshift and the Faber and Jackson relation, and those corresponding for AGN, e.g., LFs as function of redshift and the local mass function of BHs.

Chapter 9

Conclusions

In this thesis we have addressed several topics regarding the evolution of the local SMBH and spheroidal populations. Our main results and conclusions can be listed as follows.

- The local mass function of SMBH can be rather accurately assessed. More in detail, the MF of SMBH hosted in early-type galaxies can be obtained exploiting the velocity dispersion or luminosity functions of host galaxies, coupled with the $M_\bullet$–σ or $M_\bullet$–$L_{\rm sph}$ relationships, respectively. The results obtained in the two ways are in remarkable agreement with small uncertainties up to $M_\bullet \geq 10^9\,M_\odot$ (cfr. Fig. 4.7). The contribution from SMBH hosted by late-type galaxies is more uncertain, and is mostly confined to the low mass end of the MF. The overall SMBH mass density amounts to $\rho^0_\bullet = (4.2\pm1.1)\times10^5\,M_\odot/{\rm Mpc}^3$, with a contribution from SMBHs in late-type galaxies of $\simeq 25\%$. This value of $\rho^0_{\rm BH}$ is higher than those found by Yu & Tremaine (2002), by Aller & Richstone (2002) and by McLure & Dunlop (2004) (who have not considered the contribution from SMBH residing in late type galaxies), but is in excellent agreement with the results by Marconi et al. (2004). The local number density of the SMBH more massive than $10^6\,M_\odot$ is $n(M^0_\bullet > 10^6\ M_\odot) \simeq 1.7\times10^{-2}\,{\rm Mpc}^{-3}$, which corresponds to the number of bulges and spheroids with $M_{\rm sph} > 5\times10^8\ M_\odot$.

- Different methods have been applied in the literature to estimate the final SMBH mass density which give somewhat different results. Moreover also the correlations

found in the literature between SMBH mass and host spheroidal galaxy properties by different groups, present up to 30% of inconsistency, which, according to our analysis, can be ascribed to the inclusion of some, not well-resolved, spirals bulges in the fit.

- The Soltan (1982) argument applied to the hard X-ray selected AGN, allowing for a luminosity-dependent bolometric correction (U03; Fabian 2003), yields, for a mass to radiation conversion efficiency $\epsilon = 0.1$, an accreted mass density of $\rho_{\rm acc}^{HX} \simeq 4.1 \times 10^5 M_\odot/{\rm Mpc}^3$, in close agreement with the local SMBH mass density, indicating that most of the BH masses were accumulated by radiative accretion. Such an estimate includes also those families of very obscured AGN ($\log N_H \geq 25$) which are needed to fit the high normalization of the XRBG. Optically selected QSOs account for only $\simeq 35\%$ of the total SMBH mass density. The dominant contribution comes from Type 2 AGN, mostly missed by optical surveys.

- Not only the mass density, but also the MF of the SMBH and of the accreted mass match remarkably well, if we allow for a decrease of the Eddington ratio $\lambda = L/L_{\rm Edd}$ with redshift, as suggested by observations (McLure & Dunlop 2003; Vestergaard 2003). Optically selected, Type 1 AGNs account for the high mass tail of the AMF, while Type 2 AGNs take over at lower masses, reflecting the strong increase with decreasing luminosity of the Type 2 to Type 1 ratio demonstrated by hard X-ray surveys (see, e.g., Hasinger 2003) and consistent with the outcome of spectroscopic surveys of complete samples of nearby galaxies, without pre-selection (Huchra & Burg 1992; Ho et al. 1997).

- The average accretion history of SMBH, as traced by the Hard-X AGN LF (Fig. 5.13), tracks the average SFR, with a proportionality constant of the order of the local one. This strong link however breaks down at low redshifts ($z \leq 1$), where SMBH growth probably proceeds trough re-activations, at low Eddington rates, and might not be strictly linked with the large scale star formation (possibly occurring in disks).

- The alternative possibility that most of the mass has been accumulated by "dark" accretion (i.e. accretion undetectable by either optical or hard X-ray surveys, as in

the case of BH coalescence), is severely constrained by the above results. In order to make room for this possibility one has to assume that the radiative efficiency during the visible AGN phases is at the theoretical maximum of $\epsilon \simeq 0.3$–0.4. But even in this case (unless the bolometric correction is far lower than currently estimated) the contribution of radiative accretion to the local SMBH mass density is $\geq 25\%$, and one is left with the problem of fine tuning the radiative and non-radiative contributions in order not to break down the match with the local SMBH MF obtained with radiative accretion alone. One would also face the problem of accounting for the tight relationships between BH mass and mass or velocity dispersion of the spheroidal host, naturally explained by feedback associated to radiative accretion. For these reasons it is unlikely that the present day SMBH mass function has been built *mostly* through 'dark' accretion or merging of BHs.

- If indeed the SMBH MF has to be accounted for by radiative accretion, the requirement that it fits with the AMF constrains the radiative efficiency and the maximum Eddington ratio to $\epsilon \simeq 0.09\,(+0.04, -0.03)$ and $\lambda_0 \simeq 0.3\,(+0.3, -0.1)$ (68% confidence errors). The condition that the mean AGN visibility timescale computed via the LF and via the local MF are equal yields an allowed range for ϵ very close to the above ($0.06 \leq \epsilon \leq 0.13$) and looser (but consistent) constraints on λ_0. It has to be noted that the mean estimated value for the Eddington ratio is strongly biased towards low redshifts $z \leq 1$, where most of the faint, more numerous objects, are dominant.

- The analysis of the accretion history highlights that the most massive BHs (associated to bright optical QSOs) accreted their mass faster and at higher redshifts (typically at $z > 1.5$), while the lower mass BHs responsible for most of the hard X-ray background have mostly grown at $z < 1.5$ (see Figs. 5.2 and 5.9). The different evolutionary behaviour of the two AGN populations can be understood if gas accretion is regulated by star formation and by feedback both from SN explosions and nuclear activity (e.g. Kawakatu & Umemura 2002; Granato et al. 2004). In this framework it is expected that the hosts of the most massive BHs have the oldest stellar populations (e.g. Cattaneo & Bernardi 2003).

- The mass-weighted duration of the luminous AGN phase is found to be $\langle\tau_{\rm lum}\rangle \simeq 0.5$–$1.5\times10^8\,{\rm yr}$. Yu & Tremaine (2002), using a similar method, got slightly lower values, because they used in Eq. (5.28) the optical QSO LF and the local MF of SMBHs in early-type galaxies, which, as shown in Chapter 5, is only partly accounted for by optically selected QSOs. Yu & Lu (2004), from a detailed modelling of the luminosity evolution of individual QSO, derived a lower limit $\tau_{\rm lum} \geq 4\times10^7\,{\rm yr}$.

- If the accretion rate per unit BH mass, $\dot{M}_\bullet/M_\bullet$, is constant (as in the case of Eddington limited accretion) during the main accretion phases, the visibility times increase with BH mass [Eq. (5.29)], consistent with the finding by McLure & Dunlop (2004) that the ratio of SMBH in their optically selected sample at $z \simeq 2$ to the corresponding number density at the present day increases with BH mass. These authors estimate, for the most massive BHs ($M_\bullet \geq 10^{9.5}\,M_\odot$), a lower limit to $\tau_{\rm vis}$ (lifetime in their terminology) of $10^8\,{\rm yr}$.

- Setting $\lambda = 1$ and $\epsilon/(1-\epsilon) = 0.1$ and inserting in Eq. (5.29) the value of $\bar{M}_\bullet$ given by Eq. (5.31) with $M_B = -22.5$, we get $\tau_{\rm vis}(10^{9.3}\,M_\odot) \simeq 2\times10^8\,{\rm yr}$. Inserting instead in Eq. (5.29) the value of $\bar{M}_\bullet$ given by Eq. (5.30) with $\log(L) = 42$ we get $\tau_{\rm vis}(10^6\,M_\odot) \simeq 1.2\times10^8\,{\rm yr}$, $\tau_{\rm vis}(10^8\,M_\odot) \simeq 3\times10^8\,{\rm yr}$ and $\tau_{\rm vis}(10^{9.3}\,M_\odot) \simeq 4.4\times10^8\,{\rm yr}$. Such visibility times increase with decreasing redshift for $z < 3$ [Eq. (5.24)]. The amount of time spent above the threshold for inclusion in the LF by objects reaching large luminosities/masses cannot be constrained by the LF themselves since such objects are too rare to contribute significantly to the faint end of the LF.

- On the contrary, Marconi et al. (2004) find mean "lifetimes" increasing with decreasing present day BH masses. For $\lambda = 1$ and $\epsilon = 0.1$ they get $\sim 1.5\times10^8\,{\rm yr}$ for $M_\bullet^0 > 10^9\,M_\odot$ and $\sim 4.5\times10^8\,{\rm yr}$ for $M_\bullet^0 < 10^8\,M_\odot$. However, the latter "lifetime" corresponds to $\simeq 11$ e-folding times, i.e. to a mass increase by a factor 4.5×10^4. But then for a large fraction of their "lifetime" low mass BHs are too faint to be included in actual LF [cf. Eq. (5.30) and Eq. (5.31)]. Short visibility times ($\tau_{\rm vis} \leq 0.02\,{\rm Gyr}$) are also implied by the models of QSO LFs presented by Haehnelt, Natarajan & Rees (1998), Wyithe & Loeb (2003) and Mahmood et al. (2004).

- As also discussed by Hosokawa (2002), in the same general framework, a model which aims at fitting both the QSO LF *and* the relic SMBH mass function, must account for substantially higher values of $\tau_{\rm vis}$. In fact such short visible duty-cycles overproduce the local estimate (see Eq. (6.5) and Fig. 6.1). Also a scatter in the $M_\bullet - M_{\rm vir}$ relation must be taken into account in such models, otherwise too massive dark halos, up to $\sim 10^{14}\, M_\odot$ which host group of galaxies, would be necessary to fit the bright AGN LF tail. Short timescales mainly follow from the assumption of immediate QSO ignition at the virialization of the host DM halo. As shown and discussed by Monaco et al. (2000) and Granato et al. (2001), a delay between virialization and AGN ignition is a key ingredient to understand the QSO LF and the relationship between evolutionary histories of QSOs and of the massive spheroidal galaxies hosting them. Granato et al. (2004) have presented a detailed physical model quantifying such a delay which naturally accounts for the co-evolution growth of SMBH and their host spheroidal galaxies (see Chapter 3).

- Of primary importance is first to define "secure" rates for describing the statistics of DM halos which virialize at any time and that can host a galaxy. We have discussed in Chapter 3 that the S&T mass function and positive derivative term, give the best fits to numerical simulations (e.g. Taffoni et al. 2002, Springel et al. 2005), within a factor of 2 of precision. Through Montecarlo and analytical methods (see Chapter 3) we have then discussed and performed several calculations showing that any virialized halo is built in a fast accretion phase and in the slower accretion phase mass is added mostly in the outer regions.

- Through the use of DM statistics and the Granato et al. model we have then been able to fit AGN LF in Hard-Xray and Optical bands within $1.5 \leq z \leq 6$, assuming visible duty-cycles comparable to the ones found from the statistical analysis in Chapter 5, i.e. $\tau_{\rm vis} \geq 4 \times 10^7 \sim t_{ef}(\epsilon \sim 0.15)$ yr, up to an order of magnitude longer than previously found. We find a modest increase by a factor of $2 \div 3$, in the visibility times at redshifts below 2.5, and in particular we find that the faint, low-redshift Hard-X AGN have visibility times within a factor of 2 higher than the bright Hard-X/optical

AGN. This visibility time wavelength dependence is in perfect agreement with what found from the match between the relic and AMF. To reproduce the AGN LF we have tuned the parameters of the Granato et al. (2004) model in a way to still maintain a good fit to the submillimeter and K-band counts.

- The total mass we accumulate in SMBH up to $z_{\rm vir} \geq 1.5$ is about 60% the local one, in perfect agreement with the Soltan argument. The later evolution of SMBH could then be described by interactions of galaxies, satellite captures or bar instabilities. All such dynamical events trigger gas inflows toward the nucleus by perturbing the symmetry of the host gravitational potential and inducing non-conservation of the integrals controlling the gas equilibrium like the angular momentum (see Chapter 3, Section 3.4.3). On this basis we have computed a formalism to follow the *trend* and the *stochastic* components to the accretion events. We have computed how such events could produce in nearly real time (i.e., within 10^{-1} Gyr) the *shape* of the QSO luminosity functions. Over longer scales of a few Gyrs, their petering out concurs with the exhaustion of the galactic gas reservoirs to produce strong *evolution* in the LF, in fact these dynamical events no longer providing fresh gas to the host, can funnel toward the nucleus considerable fractions of the residual gas left over by previous events.

- We have pointed out an impressively, and unexpectedly, tight correspondence between the virial velocities, $V_{\rm vir}$, controlled by the dynamics of dark halos, and the stellar velocity dispersions, σ, that feel the effect of dissipative baryon loading. A straightforward comparison of the virial velocity distribution, implied by the standard hierarchical clustering scenario in a ΛCDM cosmology, with the observed velocity dispersion function of spheroidal galaxies, shows that the two functions match very well for a constant ratio $\sigma/V_{\rm vir} \simeq 0.55 \div 0.6$. For a NFW density profile, this ratio corresponds to a concentration parameter $c \simeq 3$, noticeably close to that found from N-body simulations (Zhao et al. 2003a) to apply to halos of mass greater than $10^{11}\,{\rm h}^{-1}\,M_{\odot}$ at $z \geq 3$, with no significant dependence on halo mass. Thus the matter density profile at virialization appears to be essentially unaffected by the subsequent

events, including mergers and the dissipative contraction of baryons.

- Such a result poses forward a basic feature of galaxy merging at high redshifts. The baryons within DM halos fall in the form of clouds in a collapse time comparable to their dynamical friction timescale. At the end of their infall, at around 1/10 of $R_{\rm vir}$, which is comparable to R_e, these *gaseuos* clouds, start releasing energy, the DM in those central regions expands and the baryons take the place of the DM (dynamical attractor hypothesis; Loeb & Peebles 2003, Gao et al. 2004). At the center a strong starburst occurs within a few kpc (compatible with observations on the spatial extension of SCUBA galaxies, Greve et al. 2005). Baryons then do not adiabatically contract but rather lose energy and finally replace DM in the inner regions keeping its energy and dispersion velocity (see Chapter 7, Section 7.5). Such a physical picture explains why the baryons posses the dispersion velocity the DM has at the moment of virialization. As a further check of these issues we shown (Fig. 7.7) that following Ferrarese (2002) the local statistics of DM halos can be reproduced only by using the $M_\bullet - M_{\rm vir}$ relation computing the $V_{\rm vir} - M_{\rm vir}$ at $z \geq 2$.

- The $V_{\rm vir}$–σ relation is a key ingredient to connect theoretical predictions with observations. Using the above determination of the $\sigma/V_{\rm vir}$ ratio, we have shown that the observed relationships between photometric and dynamical properties of spheroidal galaxies, defining the Fundamental Plane, carry clear imprints of the feedback processes ruling the early evolution of spheroidal galaxies. The steeper slope of the luminosity-σ (Faber-Jackson) relation compared to the predicted $M_{\rm vir}$–$V_{\rm vir}$ relation is interpreted as due primarily to the heating of the interstellar medium by SN, which increasingly hampers star-formation in smaller and smaller halos, and to winds driven by the active nucleus, that eventually sweep out the residual interstellar gas in the most massive nuclei. A full analysis shows that the treatment of feedback adopted in the ABC model nicely accounts for the normalization of the Faber-Jackson relation (see Fig. 7.2). The model implies that the observed scatter is mostly intrinsic and due to the spread of virialization redshifts. It also predicts a moderate steepening of the relation at low masses.

- The effect of feedback also determines the slope of the luminosity-effective radius relation. As discussed in Sect. 7.2, the feedback yields, approximately, $M_{\rm vir} \propto M_{\rm sph}^{5/6}$. Then, taking into account Eq. (7.6), neglecting $\alpha_{\rm DM}$ and with $k_\sigma \propto L_r^{0.15}$, we get, from $M_{\rm vir} \propto R_{\rm vir}^3$ (for given $z_{\rm vir}$), $R_e \propto L_r^{0.15} R_{\rm vir}^{8/5}$ and $L_r \propto R_e^2$. Weighting with the redshift distributions appropriate for each value of R_e (high-z galaxies contribute more to low R_e's), the mean L_r–R_e relationship flattens towards the observed relation $L_r \propto R_e^{1.58}$ (Bernardi et al. 2003). A further flattening is predicted at low R_e values, where the SN feedback dominates, yielding, approximately, $M_{\rm vir} \propto M_{\rm sph}^{2/3}$, whence $R_e \propto L_r^{0.15} R_{\rm vir}^{5/2}$ and $L_r \propto R_e^{1.4}$. Again, the model correctly reproduces not only the slope but also the normalization of the relation (see Fig. 7.3), implying that it also yields the correct mass-to-light ratio. As in the case of the Faber-Jackson relation, we expect a scatter comparable to the observed one due to the different virialization redshifts.

- The evolution of the stellar component is tied to that of the central black hole, and therefore the $M_\bullet$–σ relation is also shaped by the effect of feedback, primarily from the active nucleus itself in the more massive systems, and from SN in smaller objects. Again, observations are well reproduced (see Fig. 7.5), the dispersion around the best-fit relation is expected to be largely due to the different virialization redshifts, and a steepening of the $M_\bullet$–σ is expected for low BH masses, if these are mostly due to accretion. On the other hand, according to some analyses, seed BH masses may be $\sim 10^5\,M_\odot$, and the low-σ portion of the diagram is testing more the distribution of seed masses than the accretion history.

- We have further pointed out that the $M_\bullet$–$M_{\rm sph}$ relationship is essentially independent of $z_{\rm vir}$ (see Fig. 7.6); its *intrinsic* scatter should therefore be minimum, although this does not necessarily translate in a low *observed* scatter due to the large uncertainties on the $M_{\rm sph}$ estimates (compared to those on σ).

- A synoptic view of the effect of feedback on the luminosity-σ relation, on the local r^*-band luminosity function, and on the $M_\bullet$–σ relation, based on the ABC model, is provided by Fig. 7.9. If we switch off the supernova feedback (central panel row), we

get a larger luminosity at fixed virial velocity $V_{\rm vir}$. The increase is of $\simeq 1$ mag. for low luminosity/mass galaxies ($M_{r^*} \simeq -20$), where the stellar feedback is dominating over the QSO feedback, and of 0.5 mag. at high luminosities ($M_{r^*} \simeq -23$). Turning off the QSO feedback (bottom panel row) goes in the same direction, but now the effect is larger for larger galaxies. To fit the observed FJ relation with no stellar or QSO feedback, we have to shift by 0.1 dex the $\sigma/V_{\rm vir}$ ratio, but this is inconsistent with the observed VDF.

- As shown by the central panel column of Fig. 7.9, the shift to higher luminosities occurring when the feedback is switched off affects only weakly the low luminosity portion of the luminosity function, because of its flat slope. On the other hand, the high luminosity tail is very sensitive to it, and particularly to the feedback from the active nuclei.

- On the whole, the local luminosity function of galaxy spheroids and the observed correlations between their properties provide clear evidence that the feedback both from SN and from active nuclei has a key role in the evolution of these sources, and yield rather stringent constraints on the parameters controlling the coupling of the energy injected into the interstellar medium.

- Our results using M/L ratios for stars and gas derived from galaxy kinematics turn out to be in agreement with previous analysis based on stellar population models. The total baryonic mass density in galactic structures amounts to $\Omega_b^G \approx 3.4 \pm 0.4 \times 10^{-3}$, of which $\sim 40\%$ resides in late-type galaxies. This result confirms the well-known conclusion that only a small fraction $\leq 10\%$ of the cosmic baryons are presently in stars and cold gas within galaxies.

- We have computed the present-day galaxy halo mass function, i.e., the number density of halos of mass $M_{\rm vir}$ containing a single baryonic core, by adding the subhalos to the halo mass function and by subtracting the contributions from galaxy groups and clusters. The subtraction is a crucial step toward a sound definition of the GHMF; we suggest that further observational studies are strongly needed in this field.

- By equating the integrated number density of halos to the corresponding integrated galaxy stellar mass function and r^*-band luminosity function, we have derived the relationships of the stellar mass and the r^*-band luminosity with the halo mass. These are found to be in good agreement with $M_{\rm vir}/L_r$ ratios inferred through X-ray mapping of the gravitational potential and through gravitational lensing. Both relations exhibit a double-power law behavior with a break around $M_{\rm vir}^{\rm break} \approx 3{\times}10^{11}\,M_\odot$, corresponding to $M_{\rm star} \approx 1.2 \times 10^{10}\,M_\odot$ and to an absolute magnitude $M_r \approx -19.6$. A transition at about the same magnitude in the properties of internal structure of galaxies have been evidenced by Kauffmann et al. (2003). An additional interesting outcome of our analysis is that the $M_{\rm star} - M_{\rm vir}$ relation is already set at large redshift $z \approx 1.7$, in line with the theoretical expectation of the ABC model.

- Applying the same technique to the local VDF SMBH MF, we have also computed the $\sigma - M_{\rm vir}$ and $M_\bullet - M_{\rm vir}$ relationships. In the former case the fit is quite close to a single power law $\sigma \propto M_{\rm vir}^{1/3}$. The latter relation is again a double power law breaking at the same $M_{\rm vir}^{\rm break}$ found for the $M_{\rm star} - M_{\rm vir}$ and $L_r - M_{\rm vir}$ relations. As a further cross-check of our analysis, we plugged the $M_\bullet - M_{\rm vir}$ relation (cf. Eq. [8.19]) into the $\sigma - M_{\rm vir}$ relation (cf. Eq. [8.18]) and we found that the resulting $M_\bullet - \sigma$ relation is in very good agreement with the observational data including upper limits (cf. Fig. 8.7*b*).

- The black hole mass associated to the break is $M_\bullet \sim 9 \times 10^6\,M_\odot$ and the associated dispersion velocity is $\sigma \sim 88$ km s^{-1}. The latter value is very close to the first estimate of the critical velocity dispersion for the gas removal by SN explosions given by Dekel & Silk (1986), who found a critical halo velocity $V_{\rm crit} \sim 120$ km s^{-1}, corresponding to a critical velocity dispersion $\sigma_{\rm crit} \sim 80$.

- These results are model-independent and can be interpreted as evidence of the feedback effects of SN and AGN in galactic structures. The Granato et al. co-evolution model, which includes these feedbacks, nicely reproduces (see Chapters 6 and 7 and discussion above) the behavior $M_\bullet \propto M_{\rm star} \propto M_{\rm vir}$ observed in the high mass range, and the break of these relationships at $M_{\rm vir}^{\rm break} \approx 3 \times 10^{11}\,M_\odot$; at low mass we find

$M_{\rm star} \propto M_{\rm vir}^{5/3}$ and $M_\bullet/M_{\rm star} \propto M_{\rm vir}$, which imply stellar masses larger than observed. This suggests that enhanced SN efficiency occurs at low masses or other processes are at work in removing a significant fraction of the gas and/or prevent star formation in dwarf galaxies. However, we have to caution that the uncertainties of the LF at low luminosity are large enough to allow even a flatter slope, closer to the theoretical prediction based on SN feedback. The relationships we find are fundamental to understand the relevance of stellar and AGN feedbacks and to quantify their relative importance. Any galaxy formation and evolution models should eventually comply to them. In fact, we find that the break of the power laws occurs at a mass which marks the transition between the dominance of the stellar and the AGN feedback.

- The stellar feedback is expected to depend on the star formation history of a galaxy and the total energy released to the gas ultimately depends on total mass of formed stars and on the present-day galaxy luminosity. Correspondingly, for the AGN feedback the dependence on the accretion rate is ultimately mirrored by the dependence of the total energy injected on the final central BH mass. The fraction of the gas removed by the feedbacks is expected to also depend on the binding energy of the gas itself, which is determined by the galaxy *virial* mass and by its density distribution. Therefore the missing baryons and the relationships between the DM halo and stellar spheroid with the central SMBH, are expected as a direct result of such processes as predicted by the ABC model.

Bibliography

[1] Abazajian K. et al., 2005, ApJ, 625, 613

[2] Abramowicz M.A., Calvani M. & Nobili L., 1980, ApJ, 242, 772

[3] Abramowicz M.A. & Marsi C., 1987, Observatory, 107, 245

[4] Abramowicz M.A., 2004, Proceedings of the Conference on "Growing Black Holes", Garching, Germany, edited by A. Merloni, S. Nayakshin and R. Sunyaev, Springer-Verlag, series of "ESO Astrophysics Symposia", astroph/0411185

[5] Alexander D.M. et al., 2003, AJ, 126, 539

[6] Alexander D.M. et al., 2005, ApJ, in press

[7] Aller M.C. & Richstone D., 2002, AJ, 124, 3035

[8] Aretxaga I. et al., 2003, MNRAS, 342, 759

[9] Baes M. & Dejonghe H., 2002, A&A, 393, 485

[10] Baes M., Buyle P., Hau G.K.T. & Dejonghe H., 2003, MNRAS, 341, L44

[11] Bahcall J.N., Kirhakos S., Saxe D.H. & Schneider D.P., 1997, ApJ, 479, 642

[12] Baldry I.K., Glazebrook K., Brinkmann J., Ivezic Z., Lupton R.H., Nichol R.C. & Szalay A.S., 2004, ApJ, 600, 681

[13] Ballo L., Braito V., Della Ceca R., Maraschi L., Tavecchio F. & Dadina M., 2004, ApJ, 600, 634

[14] Barcons X., Mateos S. & Ceballos M.T., 2000, MNRAS, 316, L13-L16

[15] Bardeen J., Bond J., Kaiser N. & Szalay A., 1986, ApJ, 304, 15

[16] Barger A.J., Cowie L.L., Capak P., Alexander D.M., Bauer F.E., Brandt W.N., Garmire G.P. & Hornschemeier A.E., 2003, ApJ, 584, L61

[17] Barkana R. & Loeb A., 2005, MNRAS letters, accepted

[18] Barnes J.E., 1992, ApJ, 393, 484

[19] Barnes J.E. & Hernquist L., 1998, 495, 187

[20] Bartelmann M., King L.J. & Schneider P., 2001, A&A, 378, 361

[21] Barth A.J., Ho L.C., Rutledge R.E. & Sargent W.L.W., 2004, ApJ, 607, 90

[22] Barth A.J., 2004, in Carnegie Observatories Astrophysics Series, Vol. 1: Coevolution of Black Holes and Galaxies, ed. L.C. Ho (Cambridge Univ. Press)

[23] Barth A.J., Greene J.E. & Ho L.C., 2005, ApJ, 619, L151

[24] Baugh C.M. et al., 2004, NewAR, 48, 1239

[25] Begelman M.C., 2004, in Carnegie Observatories Astrophysics Series, Vol. 1: Coevolution of Black Holes and Galaxies, ed. L.C. Ho (Cambridge Univ. Press)

[26] Begelman M.C. & Nath B.B., 2005, MNRAS, 361, 1387

[27] Bell E.F., McIntosh D.H., Katz N. & Weinberg M.D., 2003, ApJS, 149, 289

[28] Bennet C.L. et al., 2003, ApJ, 583, 1

[29] Benson A.J., Frenk C.S., Lacey C.G., Baugh C.M. & Cole S., 2003, ApJ, 599, 38

[30] Benson A.J., Kamionkowski M. & Hassani S.H., 2005, 357, 847

[31] Berlind A.A., & Weinberg D.H., 2002, ApJ, 575, 587

[32] Berlind A.A. et al., 2003, ApJ, 593, 1

[33] Bernardi M. et al., 1998, ApJ, 508, 143

[34] Bernardi M. et al., 2003, AJ, 125, 1849

[35] Best P.N. et al., 2005, MNRAS, 362, 25

[36] Binnet L., 2005, contributions to the workshop "SUPERUNIFICATION OF ACTIVE GALACTIC NUCLEI: Black Hole Mass, Spin and Accretion Rate", Elba Island (Italy), May 25-28, 2005

[37] Binney J. & Tremaine S., 1987, "Galactic Dynamics", Princeton Univ. Press

[38] Blain A.W., Smail I., Ivison R.J., Kneib J.-P. & Frayer D.T., 2002, PhR, 369, 111

[39] Blandford R.D. & Znajek R.L., 1977, MNRAS, 179, 433

[40] Blandford R.D., 2004, in Carnegie Observatories Astrophysics Series, Vol. 1: Coevolution of Black Holes and Galaxies, ed. L.C. Ho (Cambridge Univ. Press)

[41] Blandford R.D. & Begelman M.C., 2004, MNRAS, 349, 68

[42] Blanton M.R. et al., 2001, AJ, 121, 2358

[43] Blanton M.R. et al., 2003, ApJ, 592, 819

[44] Blumenthal G.R., Faber S.M., Flores R. & Primack J.R., 1986, ApJ, 301, 27

[45] Bond J., Cole S., Efstathiou G. & Kaiser N., 1991, 379, 440

[46] Bondi H. & Hoyle F., 1944, MNRAS, 104, 273

[47] Borriello A., Salucci P. & Danese L., 2003, MNRAS, 341, 1109

[48] Borys C., Smail I., Chapman S.C., Blain A.W., Alexander D.M. & Ivison R.J., 2005, ApJ, accepted

[49] Boyle B.J., Shanks T., Croom S.M., Smith R.J. Miller L., Loaring N. & Heymans C., 2000, MNRAS 317, 1014

[50] Boylan-Kolchin M. et al., 2005, MNRAS in press, astroph/0502495

[51] Bower, R.G., Lucey, J.R. & Ellis R. S., 1992, MNRAS, 254, 601

[52] Brandt W.N. & Hasinger G., 2005, ARA&A, Vol. 43, in press

[53] Bryan G.L. & Norman M.L., 1998, ApJ, 495, 80

[54] Bullock J.S., Kolatt T.S., Rachel Y.S., Somerville S., Kravtsov A.V., Klypin A.A., Primack J.R. & Dekel A., 2001, MNRAS, 321, 559

[55] Bundy K., Ellis R.S. & Conselice C.J., 2005, astroph/0502204

[56] Burkert A. & Silk J., 2001, ApJ, 554, L151

[57] Burkert A. & D'Onghia E., 2004, in "Penetrating Bars Through Masks of Cosmic Dust: The Hubble Tuning Fork Strikes a New Note", ed. Block, Freeman, Puerari and Groess, Dordrecht: Kluwer, astroph/0409540

[58] Calzetti D. & Giavalisco M., 2000, Summary of the Discussion Session on "Evolution with Redshift" at the Conference on The Evolution of Galaxies. I - Observational Clues, edited by J.M. Vilchez, G. Stasinska and E. Perez, Astrophysics and Space Science (Kluwer, The Netherlands), astroph/0012068

[59] Caputi K.I., Dunlop J.S., McLure R.J. & Roche N.D., 2005, MNRAS, 361, 607

[60] Carr B.J., 1975, ApJ, 201, 1

[61] Cattaneo A. & Bernardi M., 2003, MNRAS, 344, 45

[62] Cavaliere A., Morrison P. & Wood K., 1971, ApJ, 170, 223

[63] Cavaliere A. & Padovani P., 1988, ApJ, 333, L33

[64] Cavaliere A. & Vittorini V., 2000, ApJ, 543, 599

[65] Cavaliere A. & Vittorini V., 2002, ApJ, 570, 114

[66] Cavaliere A., Lapi A. & Menci N., 2002, ApJ, 581, L1

[67] Chartas G., Brandt W.N., Gallagher S.C. & Garmire G.P.. 2002, ApJ, 579, 169

[68] Chartas G., Brandt W.N. & Gallagher S.C., 2003, ApJ, 595, 85

[69] Chokshi A. & Turner E. L., 1992, MNRAS, 259, 421

[70] Cimatti, A. et al. 2002, A&A, 391, L1

[71] Cimatti A., 2004, in the Proceedings of the ESO/USM/MPE Workshop on "Multiwavelength Mapping of Galaxy Formation and Evolution", eds. R. Bender and A. Renzini, astroph/0401101

[72] Ciotti L., Lanzoni B. & Renzini A., 1996, MNRAS, 282, 1

[73] Cole S. et al. 2001, MNRAS, 326, 255

[74] Comastri A. et al., 1995, A&A, 296, 1

[75] Combes F., 2005, review paper for Astrophysics Update 2, astroph/0505463

[76] Cowie L.L., Barger A.J., Bautz M.W., Brandt W.N. & Garmire G.P., 2003, ApJ, 584, L57

[77] Cristiani S. et al., 2003, Proc. of the Meeting Baryons in Cosmic Structures, Monte Porzio (Italy), ASP. Conf. Ser., eds. E. Giallongo, G. De Zotti, N. Menci, in press

[78] Croom S.M. et al., 2004, MNRAS, 349, 1397

[79] Cyburt R.H., Fields B.D. & Olive K.A., 2001, NewA, 6, 215

[80] Daddi E. et al., 2003, ApJ, 588, 50

[81] Dantas C.C. et al., 2003, MNRAS, 340, 398

[82] Dekel A. & Silk J., 1986, ApJ, 303, 39

[83] Dekel A. & Woo J., 2003, MNRAS, 344, 1131

[84] Dekel A. & Birnboim Y., 2004, astroph/0412300

[85] De Lucia G. et al., 2004, MNRAS, 348, 333

[86] de Vaucouleurs G., 1948, Ann. d'Astroph., 11, 247

[87] de Vaucouleurs G. & Olson D.W., 1982, ApJ, 256, 346

[88] Dijkstra M., Haiman Z. & Loeb A., 2004, ApJ, 613, 646

[89] Di Matteo T., Springel V. & Hernquist L., 2005, Nature, 433, 604

[90] Djorgovski S.G. & Davis M., 1987, ApJ, 313, 59

[91] Dressler A., Lynden-Bell D., Burstein D., Davies R.L., Faber S.M., Terlevich R & Wegner G., 1987, ApJ, 313, 42

[92] Drory N. et al., 2003, ApJ, 595, 698

[93] Dunlop J.S. & Peacock J.A., 1990, MNRAS, 247, 19

[94] Dunlop J.S., McLure R.J., Kukula M.J., Baum S.A., O'Dea C.P. & Hughes D.H., 2003, MNRAS, 340, 1095

[95] Dunlop J.S., 2004, in Carnegie Observatories Astrophysics Series, Vol. 1: Coevolution of Black Holes and Galaxies, ed. L.C. Ho (Cambridge Univ. Press)

[96] Duschl W.J., Strittmatter P.A. & Biermann P.L., 2000, A&A, 357, 1123

[97] Dwek E., 2004, in the proceedings of: "The Spectral Energy Distribution of Gas-Rich Galaxies: Confronting Models with Data", Heidelberg, eds. C.C. Popescu and R.J. Tuffs, AIP Conf. Ser., in press, astroph/0412344

[98] Eggen O.J., Lynden-Bell D., & Sandage A., 1962, ApJ, 136, 748

[99] Eke V.R., Cole S. & Frenk C.S., 1996, MNRAS, 282, 263

[100] Ellis, R.S., Smail, I., Dressler, A., Couch, W.J., Oemler, A., Butcher, H., & Sharples R.M., 1997, ApJ, 483, 582

[101] Elvis M. et al., 1994, ApJS, 95, 1

[102] Elvis M., Risaliti G. & Zamorani G., 2002, ApJ, 565, L75

[103] El-Zant A.A., Hoffman Y., Primack J., Combes F. & Shlosman I., 2004, ApJ, 607, L75

[104] Erwin P, Graham A.W. & Caon N., 2004, in Carnegie Observatories Astrophysics Series, Vol. 1: Coevolution of Black Holes and Galaxies, ed. L.C. Ho (Cambridge Univ. Press)

[105] Ettori S., Tozzi P. & Rosati P., 2003, A&A, 398, 879

[106] Faber S.M. & Jackson R.E., 1976, ApJ, 204, 668

[107] Faber S.M. et al., 1989, ApJS, 69, 763

[108] Faber S.M. et al., 1997, AJ, 114, 1771

[109] Fabian A.C., 1999, MNRAS, 308, L39

[110] Fabian A.C., 2004, in Carnegie Observatories Astrophysics Series, Vol. 1: Coevolution of Black Holes and Galaxies, ed. L.C. Ho (Cambridge Univ. Press)

[111] Fabian A.C. & Worsley M.A., 2004, in 'The Obscured X-ray Background and Evolution of AGN', contribution to proceedings of the conference on "Growing Black Holes" held in Garching, Germany on June 21-25, 2004. Edited by A. Merloni, S. Nayakshin, R. Sunyaev, Springer-Verlag

[112] Fan X. et al., 2001, AJ, 122, 2833

[113] Fan X. et al., 2004, AJ, 128, 515

[114] Ferrarese L. & Merritt D., 2000, ApJ, 539, L9

[115] Ferrarese L., 2002, Proceedings of the 2nd KIAS Astrophysics Workshop, Seoul, Korea, astroph/0203047

[116] Ferrarese L., 2002, ApJ, 578, 90

[117] Ferrarese L. & Ford H., 2004, (astro-ph/0411247)

[118] Ferrarese L., 2004, in Supermassive Black Holes in the Distant Universe, Astr. Sp. Sc. Lib. 308, ed. A.J. Barger, (Dordrecht: Kluwer Academic Publishers), 1

[119] Filippenko A.V. & Ho L.C., 2003, ApJ, 588, L13

[120] Fontana A. et al., 2004, A&A, 424, 23

[121] Forbes D.A. & Ponman T.J., 1999, MNRAS, 309, 623

[122] Franceschini A., Vercellone S. & Fabian A.C., 1998, MNRAS, 297, 817

[123] Franceschini A., Braito V. & Fadda D., 2002, MNRAS, 335, L51

[124] Fukugita M., Shimasaku K. & Ichikawa T., 1995, PASP, 107, 945

[125] Fukugita M., Hogan C.J. & Peebles P.J.E., 1998, ApJ, 503, 518

[126] Fukugita M. et al., 2004, ApJ, 601, L127

[127] Fukugita M. & Peebles P.J.E., 2004, ApJ, 616, 643

[128] Fukugita M., 2004, IAU Symp. 220, ed. S.D. Ryder, D.J. Pisano, M.A. Walker, and K.C. Freeman (San Francisco: ASP), 227

[129] Gao L., Loeb A., Peebles P.J.E., White S.D.M. & Jenkins A., 2004, 614, 17

[130] Gebhardt K. et al., 2000, ApJ, 539, L13

[131] Gebhardt K. et al., 2001, AJ, 122, 2469

[132] Gehrels N., 1986, ApJ, 303, 336

[133] Gerhard O., Kronawitter A., Saglia R.P. & Bender R., 2001, AJ, 121, 1936

[134] Gerhard O., 2005, Proceedings to appear in: Planetary Nebulae beyond the Milky Way, ESO Astrophysics Symposia, eds. Stanghellini L. et al., astroph/0502037

[135] Ghez A.M. et al., 2003, ApJ, 586, 127

[136] Giacconi R., Gorenstein P., Gursky H., Usher P.D., Waters J.R., Sandage A., Osmer P. & Peach J.B., 1967, ApJ, 148, L129

[137] Giacconi R. et al., 2002, ApJS, 139, 369

[138] Giavalisco M. & Dickinson M., 2001, ApJ, 550, 177

[139] Gilli R., Risaliti G. & Salvati M., 1999, A&A, 347, 424

[140] Gilli R., Salvati M. & Hasinger G., 2001, A&A, 366, 407

[141] Gilli R., 2004, in "New Results from Clusters of Galaxies and Black Holes", Advances in Space Research, Eds. C. Done, E. M. Puchnarewicz, M. J. Ward. (Amsterdam: Elsevier Science), in press (astro-ph/0303115)

[142] Gilli R. et al., 2005, A&A, 430, 811

[143] Girardi M. & Giuricin G., 2000, ApJ, 540, 45

[144] Gonzalez A.H. et al., 2000, ApJ, 528, 145

[145] Governato F., Tozzi P. & Cavaliere A., 1996, ApJ, 458, 18

[146] Graham A.W., Erwin P., Caon N. & Trujillo I., 2001, ApJ, 563, L11

[147] Graham A.W., 2002, MNRAS, 334, 859

[148] Granato G.L., Silva L., Monaco P., Panuzzo P., Salucci P., De Zotti G. & Danese L., 2001, MNRAS, 324, 757

[149] Granato G.L., De Zotti G., Silva L., Bressan A. & Danese L., 2004, ApJ, 600, 580

[150] Grazian A., Cristiani S., D'Odorico V., Omizzolo A. & Pizzella A. 2000, AJ, 119, 2540

[151] Greene J.E., Ho L.C. & Barth A.J., 2004, in IAU Symp. 222, astro-ph/0406047

[152] Greve T.R. et al., 2005, MNRAS, 359, 1165

[153] Gruber D.E. et al., 1999, ApJ, 520, 124

[154] Guainazzi M., Piconcelli E., Jimenez-Bailon E. & Matt G., 2005 , A& A, 429, L9

[155] Guzik J. & Seljak U., 2002, MNRAS, 335, 311

[156] Haehnelt M.G., Natarajan P. & Rees M.J., 1998, MNRAS, 300, 817

[157] Haehnelt M.G., 2003, Classical and Quantum Gravity, 20, S31, astroph/0307379

[158] Haiman Z. & Loeb A., 1998, ApJ, 503, 505

[159] Haiman Z. & Quataert E., 2004, review for "Supermassive Black Holes in the Distant Universe", Ed. A. J. Barger, Kluwer Academic Publishers

[160] Häring N. & Rix H.W., 2004, ApJ, 604, 89

[161] Hamann F. & Ferland G., 1999, ARA&A, 37, 487

[162] Hasinger G., 2003, in proc. conf. "The restless high energy universe", E.P.J. van den Heuvel, J.J.M. in 't Zand, and R.A.M.J. Wijers (eds.), Nucl. Physics B. Suppl. Ser., in press, astro-ph/0310804

[163] Hasinger G., Miyaji T. & Schmidt M., 2005, A&A, in press

[164] Heckman T.M. et al. 2000, ApJS, 129, 493

[165] Heckman T.M., Kauffmann G., Brinchmann J., Charlot S., Tremonti C. & White S.D.M., 2004, 613, 109

[166] Heinämäki P., Einasto J., Einasto M., Saar E., Tucker D.L. & Müller V., 2003, A&A, 397, 63

[167] Hernquist L., 1992, ApJ, 356, 359

[168] Ho L.C., Filippenko A.V. & Sargent W.L.W., 1997, ApJ, 487, 568

[169] Ho L.C., 2002, ApJ, 564, 120

[170] Hoekstra H., Yee H.K.C. & Gladders M.D., 2004, ApJ, 606, 67

[171] Holland W.S. et al., 1998, 3357, 305

[172] Hopkins P.F., Hernquist L., Cox T.J., Di Matteo T., Robertson B. & Springel V., 2005, ApJ, submitted, astro-ph/0506398

[173] Hosokawa T., 2002, ApJ, 576, 75

[174] Hosokawa T., 2004, ApJ, 606, 139

[175] Huchra J. & Burg R., 1992, ApJ, 393, 90

[176] Hughes S.A. & Blandford R.D., 2003, ApJ, 585, L10

[177] Hui L. & Haiman Z., 2003, ApJ, 596, 9

[178] Inoue S. & Sasaki S., 2001, ApJ, 562, 618

[179] Islam R.R., Taylor J.E. & Silk J., 2004, MNRAS, 354, 427

[180] Jenkins A. et al., 2001, MNRAS, 321, 372

[181] Jørgensen I., Franx M. & Kjaergaard P., 1995, MNRAS, 276, 1341

[182] Kashikawa N. et al., 2003, AJ, 125, 53

[183] Kaspi S., Smith P.S., Netzer H., Maoz D., Jannuzzi B.T. & Giveon U., 2000, ApJ, 533, 631

[184] Kaviani A., Haehnelt M.G. & Kauffmann G., 2003, MNRAS, 340, 739

[185] Kauffmann G., Nusser A. & Steinmetz M., 1997, MNRAS, 286, 795

[186] Kauffmann G. et al., 2003, MNRAS, 341, 33

[187] Kawakatu N. & Umemura M., 2002, MNRAS, 329, 572

[188] Kawaguchi T. et al., 2004, A&A, 420, L23

[189] Kennefick J.D., Djorgovski S.G. & de Carvalho R.R., 1995, AJ, 110, 2553

[190] Kennicutt R.C., 1998, ApJ, 498, 541

[191] King A.R., 2003, ApJ, 596, L27

[192] King A.R., Lubow S.H., Ogilvie G.I. & Pringle J.E., 2005, MNRAS in press

[193] Kitayama T. & Suto Y., 1996, MNRAS, 280, 638

[194] Kleinheinrich M. et al., 2004, A&A, submitted (preprint astro-ph/0412615)

[195] Knop R.A. et al., 2003, ApJ, 598, 102

[196] Kochanek C.S., 2001, in Proceedings of The Dark Universe Meeting at STScI, M. Livio, ed., Cambridge University Press, astroph/0108160

[197] Kochanek C.S. & White M., 2001, ApJ, 559, 531

[198] Kochanek C. S. et al., 2001, ApJ, 560, 566

[199] Kodama T., Arimoto N., Barger A.J. & Arag'on-Salamanca A., 1998, A&A, 334, 99

[200] Kogut A. et al., 2003, ApJS, 148, 161

[201] Komossa S., Burwitz V., Hasinger G., Predhel P., Kaastra J.S. & Ikebe Y., 2003, ApJ, 582, L15

[202] Kormendy J. & Richstone D., 1995, ARA&A, 581

[203] Kormendy J. & Gebhardt K., 2001, in 20th Texas Symposium on relativistic astrophysics, ed. J.C. Wheeler, & H. Martel (AIP Conf. Proc. 586; Melville: AIP), 363

[204] Kormendy J., 2003, in Carnegie Observatories Astrophysics Series, Vol. 1: Coevolution of Black Holes and Galaxies, ed. L.C. Ho (Cambridge Univ. Press), in press, astroph/0306353

[205] Koushiappas S.M., Bullock J.S. & Dekel A., 2004, MNRAS, 354, 292

[206] Kravtsov A.V. et al., 2004, ApJ, 609, 35

[207] Kreysa E. et al., 1998, SPIE, 3357, 319

[208] Krolik J.H., 1999, "Active Galactic Nuclei: From the Central Black Hole to the Galactic Environment", Princeton Univ. Press

[209] Kronawitter A., Saglia R.P., Gerhard O. & Bender R., 2000, A&AS, 144, 53

[210] Kukula M.J. et al. 2001, MNRAS, 326, 1533

[211] Lacey C. & Cole S., 1993, MNRAS, 262, 627

[212] Lacey C. & Cole S., 1994, MNRAS, 271, 676

[213] Lacy M. et al., 2001, ApJ, 551, L17

[214] La Franca F. et al., 2002, ApJ, 570, 100

[215] La Franca F. et al., 2005, ApJ, accepted

[216] Lahav O., Rees M.J., Lilje P.B. & Primack J.R, 1991, MNRAS, 251, 128

[217] Lamers H. & Cassinelli J.P., 1999, "Introduction to Stellar Winds", Cambridge Univ. Press

[218] Laor A., Fiore F., Elvis M., Wilkes B.J. & McDowell J.C., 1997, ApJ, 477, 93

[219] Laor A., 2000, ApJ, 543, L11

[220] Lapi A., Cavaliere A. & Menci N., 2005, ApJ, 619, 60

[221] Loeb A. & Peebles P.J.E, 2003, 589, 29

[222] Lokas E.L. & Mamon G.A., 2001, MNRAS, 321, 155

[223] Loveday J., 1998, in Dwarf Galaxies and Cosmology, proc. XVIII Moriond Astrophys. meeting, ed. Thuan et al. (Paris: Editions Frontieres), astro-ph/9805255

[224] Lynden-Bell D., 1969, Nature, 223, 690

[225] Madau P. et al., 1996, MNRAS, 283, 1388

[226] Madau P. & Rees M.J., 2001, ApJ, 551, L27

[227] Madau P., Rees M.J., Volonteri M., Haardt F. & Oh S.P., 2004, ApJ, 604, 484

[228] Magliocchetti M. et al., 2002, MNRAS, 333, 100

[229] Magliocchetti M. & Porciani C., 2003, MNRAS, 346, 186

[230] Magorrian J. et al., 1998, AJ, 115, 2285

[231] Mahmood A., Devriendt J.E.G. & Silk J., 2005, MNRAS, 359, 1363

[232] Mahmood A. & Rajesh R., 2005, Statistical Mechanics, astroph/0502513

[233] Maiolino R. & Rieke G.H., 1995, ApJ, 454, 95

[234] Maller A.H. & Dekel A., 2002, MNRAS, 335, 487

[235] Maller A.H. & Bullock J.S., 2004, MNRAS, 355, 694

[236] Maraschi L. & Tavecchio F., 2004, in 'Properties of Jets at Different Scales and the Connection with Accretion', contribution to proceedings of the conference on "Growing Black Holes" held in Garching, Germany on June 21-25, 2004. Edited by A. Merloni, S. Nayakshin, R. Sunyaev, Springer-Verlag series of "ESO Astrophysics Symposia"

[237] Marconi A., Hunt L., 2003, ApJL, 589, L21

[238] Marconi A., Risaliti G., Gilli R., Hunt L. K., Maiolino R. & Salvati M., 2004, MNRAS, 351, 169

[239] Marinoni C. & Hudson M., 2002, ApJ, 569, 101

[240] Marshall F.E. et al., 1980, ApJ, 235, 4

[241] Martinez H.J. et al., 2002, MNRAS, 337, 1441

[242] Martinez-Sansigre A. et al., 2005, Nature, in press

[243] Martini M. & Weinberg D.H., ApJ, 547, 12

[244] Martini M., 2004, in Coevolution of Black Holes and Galaxies, L.C. Ho Ed., Cambridge, p. 170.

[245] Mathur S. & Grupe D., 2005, A&A, 432, 463

[246] McKay T.A. et al., 2002, ApJ, 571, L85

[247] Mc Low M. & Ferrara A., 1999, ApJ, 513, 142

[248] McLure R.J. & Dunlop J.S., 2001, MNRAS, 327, 199

[249] McLure R.J., Dunlop. J.S., 2002, MNRAS, 331, 795

[250] McLure R.J., Dunlop. J.S., 2004, MNRAS, 352, 1390

[251] Meiskin A., 2005, MNRAS, 356, 596

[252] Menci N., Cavaliere A., Fontana A., Giallongo E., Poli F. & Vittorini V., 2003, ApJ, 587, L63

[253] Menci N., Cavaliere A., Fontana A., Giallongo E., Poli F. & Vittorini V., 2004, ApJ, 604, 12

[254] Menou K., Haiman Z. & Narayan V.K., 2001, ApJ, 558, 535

[255] Menou K., 2003, Classical and Quantum Graviity, 20, S37, astroph/0301397

[256] Merloni A., Heinz S. & di Matteo T., 2003, MNRAS, 342, 1057

[257] Merloni A., 2004, MNRAS, 353, 1035

[258] Merritt D., Ferrarese L. & Joseph C. L., 2001, Science, 293, 5532, 1116

[259] Milosavljevic M. & Merritt D., 2004, in "The Astrophysics of Gravitational Wave Sources", Ed. J. Centrella, in press, astroph/0211270

[260] Minkowski R., 1962, in IAU Symposium 15, Problems of Extra-Galactic Research, . Ed. G.C. McVittie, 112

[261] Miyaji T., Hasinger G. & Schmidt M., 2000, A&A, 353, 25

[262] Miyoshi M. et al., 1995, Nature, 373, 127

[263] Miralda-Escude J. & Kollmeier J.A., 2005, ApJ, 619, 30

[264] Mo H.J. & White S.D.M., 1996, 282, 347

[265] Mo H.J., Mao S. & White S.D.M., 1998, MNRAS, 295, 319

[266] Mo H.J. & Mao S., 2004, MNRAS, 353, 829

[267] Monaco P., Salucci P. & Danese L., 2000, MNRAS, 311, 279

[268] Morrison R. & McCammon D., 1983, ApJ, 270, 119

[269] Murali C. et al., 2002, ApJ, 571, 1

[270] Murray N., Quataert E. & Thompson T.A., 2005, ApJ, 618, 569

[271] Nagamine K., Cen R., Hernquist L., Ostriker J.P. & Springel V., 2004, ApJ, 610, 45

[272] Nakamura O. et al., 2002, AJ, 125, 1682

[273] Nakamura O., Fukugita M., Yasuda N., Loveday J., Brinkmann J., Schneider D.P., Shimasaku K. & SubbaRao M., 2003, AJ, 125, 1682

[274] Naoz S., Barkana R., 2005, MNRAS, accepted

[275] Narayan R. & Yi I., 1994, ApJ, 428, L13

[276] Nath B.B. & Roychowdhury S., 2002, MNRAS, 333, 145

[277] Navarro J.F. & White S.D.M., 1993, MNRAS, 265, 271

[278] Navarro J.F., Frenk C.S. & White S.D.M., 1997, ApJ, 490, 493

[279] avarro J.F. et al., 2004, MNRAS, 349, 1039

[280] Nipoti C., Londrillo P. & Ciotti L., 2003, MNRAS, 342, 501

[281] Norberg P. et al., 2002, MNRAS, 336, 907

[282] Nozawa T. et al., 2003, ApJ, 598, 785

[283] Oguri M. & Lee J., 2004, MNRAS, 355, 120

[284] Olive K.A., 2002, in Astroparticle Physics, ed. H. Athar, G.-L. Lin, and K.-W. Ng (Singapore: World Scientific), 23

[285] Osmer P. S., 2004, in Carnegie Observatories Astrophysics Series, Vol. 1: Coevolution of Black Holes and Galaxies, ed. L.C. Ho (Cambridge Univ. Press), in press, astroph/0304150

[286] O'Sullivan E. & Ponman T.J., 2004, MNRAS, 354, 935

[287] Padmanabhan T., 2003, "Theoretical Astrophysics, Vol. III", Cambridge Univ. Press

[288] Padmanabhan N. et al., 2004, New Astronomy, 9, 329

[289] Pahre M.A., Djorgovski S.G. & de Carvalho R.R., 1998, AJ, 116, 1591

[290] Panter B., Heavens A.F. & Jimenez R., 2004, MNRAS, 355, 764

[291] Peacock J.A. & Smith R.E., 2000, MNRAS, 318, 1144

[292] Peebles P.J.E., 2000, "The Large-Scale Structure of the Universe", Princeton Univ. Press

[293] Pei Y. C., 1995, ApJ, 438, 623

[294] Persic M. & Salucci P., 1992, MNRAS, 258, 14

[295] Persic M., Salucci P. & Stel F., 1996, MNRAS, 281, 27

[296] Pisani A., Ramella M. & Geller M.J., 2003, AJ, 126, 1677

[297] Porciani C., Magliocchetti M. & Norberg P., 2004, MNRAS, 355, 1010

[298] Portinari L., Moretti A., Chiosi C. & Sommer-Larsen J., 2004, ApJ, 604, 579

[299] Pounds K.A. et al. 2003, MNRAS, 345, 705

[300] Poveda A. 1961, ApJ, 134, 910

[301] Prada F. et al., 2003, ApJ, 598, 260

[302] Press W.H. & Schechter P. 1974, ApJ, 187, 425

[303] Prugniel P. & Simien F., 1997, A&A, 321, 111

[304] Ramella M. et al. 1999, A&A, 342, 1

[305] Rees M.J., 1984, ARA&A, 22, 471

[306] Reiprich T.H. & Böhringer H., 2002, ApJ, 567, 716

[307] Richards G.T. et al., 2005, MNRAS, 360, 839

[308] Rifatto A., Rafanelli P., Ciroi S., Radovich M., Vennik J., Richter G. & Birkle K., 2001, AJ, 122, 2301

[309] Risaliti G. & Elvis M., 2004, Review for "Supermassive Black Holes in the Distant Universe", Ed. A. J. Barger, Kluwer Academic Publishers

[310] Romano D., Silva L., Matteucci F. & Danese L., 2002, MNRAS, 334, 444

[311] Rusin D., Kochanek C.S. & Keeton C.R., 2003, 595, 29

[312] Sadler E.M. et al., 1989, MNRAS, 240, 591

[313] Sadler E.M. et al., 2002, MNRAS, 329, 227

[314] Sadler E.M., 2004, in Carnegie Observatories Astrophysics Series, Vol. 1: Coevolution of Black Holes and Galaxies, ed. L.C. Ho (Cambridge Univ. Press)

[315] Salpeter E. E., 1964, ApJ, 140, 796

[316] Salucci P., Szuszkiewicz E., Monaco P. & Danese L., 1999,MNRAS, 307, 637

[317] Salucci P. & Burkert A., 2000, ApJ, 537, 9

[318] Salucci P. & Persic M., 1999, MNRAS, 309, 923

[319] Sandage, A., & Visvanathan, N., 1978, ApJ, 225, 742

[320] Sasaki S., 1994, PASJ, 46, 427

[321] Sazonov S.Y., Ostriker J.P. & Sunyaev R.A., 2004, 347, 144

[322] Schödel R. et al., 2002, Nature, 419, 694

[323] Scott S.E. et al., 2002, MNRAS, 331, 817

[324] Sersic J.L., 1968, Atlas de galaxias australes, Observatorio Astronomico de Cordoba, Argentina

[325] Setti G., Woltjer L., 1989, A&A, 224, L21

[326] Shakura N.I. & Sunyaev R.A., 1973, A&A, 24, 337

[327] Shakura N.I. & Sunyaev R.A., 1973, A&A, 24, 337

[328] Shankar F., Salucci P., Granato G. L. & Danese L., 2003, http://www.exp-astro.phys.ethz.ch/ETH_Astro_2003

[329] Shapiro S.L., 2005, ApJ, 620, 59

[330] Sheldon E. et al., 2004, AJ, 127, 2544

[331] Sheth R.K., Mo H.J. & Tormen G., 2001, MNRAS, 323, 1

[332] Sheth R.K. & Tormen G., 2002, MNRAS, 329, 61

[333] Sheth R.K. et al., 2003, ApJ, 594, 225

[334] Shimasaku K., 1993, ApJ, 413, 59

[335] Shimasaku K. et al., 2005, PASJ, 57, 447

[336] Shlosman I., Begelman M.C. & Frank J., 1990, Nature, 345, 679

[337] Silk J. & Rees M. J., 1998, A&A, 331, L1

[338] Silk J. & Bouwens R., 2001, New Astronomy Reviews, 45, 337

[339] Silva L., Granato G.L., Bressan A. & Danese L., 1998, ApJ, 509, 103

[340] Silva L., Maiolino R. & Granato G.L., 2004, MNRAS, 355, 973

[341] Silva L., De Zotti G., Granato G.L., Maiolino R. & Danese L., 2005, MNRAS, 357, 1295

[342] Sincell M.W. & Krolik J.H., 1998, ApJ, 496, 737

[343] Small T. A. & Blandford R. D., 1992, MNRAS, 259, 725

[344] Snellen I.A.G. et al., 2003, MNRAS, 342, 889

[345] Soltan A., 1982, MNRAS, 200, 115

[346] Somerville R.S. & Primack J.R., 1999, MNRAS, 310, 1087

[347] Somerville R.S., 2004, in the Proceedings of the ESO/USM/MPE Workshop on "Multiwavelength Mapping of Galaxy Formation and Evolution", eds. R. Bender and A. Renzini, astroph/0401570

[348] Somerville R.S. et al., 2004, ApJ, 600, 135

[349] Spergel D.N. et al., 2003, ApJS, 148, 175

[350] Springel V., Di Matteo T. & Hernquist L., 2005, MNRAS, 361, 776

[351] Springel V. et al., 2005, Nature, 435, 629

[352] Stanford S.A., Eisenhardt P.R. & Dickinson M., 1998, 492, 461

[353] Steed A. & Weinberg D.H., 2004, ApJ, submitted, astroph/03113312

[354] Stiavelli M., Fall S.M. & Panagia N., 2004, ApJ, 610, L1

[355] Stocke J.T., Penton S.V. & Shull J.M., 2003, in "The IGM/Galaxy Connection: The Distribution of Baryons at $z = 0$", Ast. Sp. Sc. Lib. 281, ed. J.L. Rosenberg and M.E. Putman (Dordrecht: Kluwer Academic Publishers), 57

[356] Sugiyama N., 1995, ApJS, 100, 281

[357] Susa H. & Umemura M., 2000, MNRAS, 316, L17

[358] Sutherland R.S. & Dopita M.A., 1993, ApJS, 88, 253

[359] Syer D. & White S.D.M., 1998, 293

[360] Taffoni G., Monaco P. & Theuns T., 2002, MNRAS, 333, 623

[361] Tecza M. et al., 2004, ApJ, 605, 109

[362] Terlevich A.I. & Forbes D.A., 2002, MNRAS, 330, 547

[363] Thomas D., 1999, MNRAS, 306, 655

[364] Thorne K.S., 1974, ApJ, 191, 507

[365] Toomre A. & Toomre J., 1972, ApJ, 178, 623

[366] Trager S.C., Faber S.M., Worthey G. & González J.J., 2000, AJ, 120, 165

[367] Treister E. & Urry C.M., 2005, ApJ, accepted

[368] Tremaine S. et al., 2002, ApJ, 574, 740

[369] Treves A., Maraschi L. & Abramowicz M.A., 1988, PASP, 100, 427

[370] Treu T. & Koopmamns L.V.E., 2002, MNRAS, 337, L6

[371] Treu T., Stiavelli M., Bertin G., Casertano C. & Møller P., 2002, ApJ, 564, L13

[372] Treu T., 2004, in Carnegie Observatories Astrophysics Series, Vol. 3: Clusters of Galaxies: Probes of Cosmological Structure and Galaxy Evolution, ed. L.C. Ho (Cambridge Univ. Press)

[373] Trujillo I., Burkert A. & Bell E.F., 2004, ApJ, 600,39

[374] Ueda Y., Akiyama M., Ohta K. & Miyaji T., 2003, ApJ, 598, 886

[375] Umemura M., 2001, ApJ, 560, L29

[376] Vale A. & Ostriker J.P., 2004, MNRAS, 353, 189

[377] Valluri M., Ferrarese L., Merritt D. & Joseph C.L., 2005, ApJ, in press, astro-ph/0502493

[378] van den Bosch F.C., Yang X. & Mo H.J., 2003, MNRAS, 340, 771

[379] van den Bosch F.C., Tormen G. & Giocoli C., 2005, MNRAS, 359, 1029

[380] van der Marel R. P., 2004, in Carnegie Observatories Astrophysics Series, Vol. 1: Coevolution of Black Holes and Galaxies, ed. L.C. Ho (Cambridge Univ. Press)

[381] van der Wel, A., Franx M., van Dokkum P.G. & Rix H.-W., 2004 ApJ, 601, L5

[382] Vecchi A. et al., 1999, A&A, 349, L73-L76

[383] Vestergaard M., 2002, ApJ, 571, 733

[384] Vestergaard M., 2004, ApJ, 601, 676

[385] Vignali C., Brandt W. N. & Schneider D. P., 2003, AJ, 125, 433

[386] Vivitska M. et al., 2002, ApJ, 581, 799

[387] Volonteri M., Haardt F. & Madau P., 2003, ApJ, 582, 559

[388] Volonteri M., Madau P., Quataert E. & Rees M.J., 2005, 620, 69

[389] Volonteri M. & Rees M.J., 2005, ApJ, accepted

[390] Wada K. & Norman C.A., 2002, ApJ, 566, L21

[391] Walter F. et al., 2004, ApJ, 615, L17

[392] Wandel A., Peterson B.M. & Malkan M.A., 1999, ApJ, 526, 579

[393] Wandel B., 1999, 519, L39

[394] Warren S.J., Hewett P.C. & Osmer P.S., 1994, ApJ, 421, 412

[395] Wechsler R.H., Bullock J.S., Primack J.R., Kravtsov A.V. & Dekel A., 2002, ApJ, 568, 52

[396] White S.D.M. & Rees M.J., 1978, MNRAS, 183, 341

[397] White S.D.M. & Frank C.S., 1991, ApJ, 379, 52

[398] Wolf C. et al. 2001, A&A, 377, 442

[399] Woo J.H. et al., 2004, ApJ, 617, 903

[400] Woosley S.E. & Weaver T.A. 1986, ARA&A, 24, 205

[401] Wyithe J.S.B. & Loeb A., 2003, ApJ, 595, 614

[402] Wyithe J.S.B. & Padmanabhan T., 2005, MNRAS, submitted

[403] Wyithe J.S.B. & Loeb A., 2005, ApJ, submitted

[404] Wyse R.F.G., 2004, ApJ, 612, L17

[405] Yang X., Mo H.J. & van den Bosch F.C., 2003, MNRAS, 339, 1057

[406] Yano T., Nagashima M. & Gouda N., 1996, ApJ, 466, 1

[407] Yu Q., 2002, MNRAS, 331, 935

[408] Yu Q. & Lu Y., 2004, ApJ, 602, 603

[409] Yu Q. & Tremaine S., 2002, MNRAS, 335, 965

[410] Zaldarriaga M., 1997, Phys. Rev. D, 55, 1822

[411] Zehavi I. et al., 2005, ApJ, 621, 22

[412] Zel'dovich Ya.B. & Novikov I.D., 1964, Soviet Phys. Dokl., 158, 811

[413] Zhao H., Haehnelt M.G. & Rees M.J., 2002, NewA, 7, 385

[414] Zhao D.H., Jing Y.P., Mo H.J. & Börner G., 2003a, ApJ, 597, L9

[415] Zhao D.H., Mo H.J., Jing Y.P. & Börner G., 2003b, MNRAS, 339, 12

[416] Zucca E. et al., 1997, A&A, 326, 477

Appendix A

Set of differential equations in the model

Here we define the set of differential equations which have been used in the numerical code by Granato et al. (2004), to follow the evolution of the several baryonic components in a virialized Dark Matter halo. The list of free parameters is given in Table A.

The initial baryon fraction in the halo is given by the cosmological value $f_b = 0.16$

$$M_{\rm inf}(t_{\rm vir}) = f_b M_{\rm vir}. \tag{A.1}$$

The cold gas mass at any instant is computed from the infall divided by the maximum between the cooling and the dynamical times

$$\dot{M}_{\rm cold}(t) = \frac{M_{\rm inf(t)}}{\max[t_{\rm cool}(r_{\rm vir}), t_{\rm dyn}(r_{\rm vir})]}\,, \tag{A.2}$$

where

$$t_{\rm dyn} = \left[\frac{3\pi}{32 G\rho}\right]^{3/2} \tag{A.3}$$

and

$$t_{\rm cool} = \frac{3}{2}\frac{\rho_{gas}}{\mu m_p}\frac{KT}{C\, n^2\, \Lambda(T)}\,. \tag{A.4}$$

We have indicated with ρ, $\rho_{\rm gas}$, $C = \langle n^2\rangle/\langle n\rangle^2$ and $\Lambda(T)$ the total matter density, the gas density, the clumping factor and the cooling function respectively.

The star formation then reads as

$$\psi(t) = \int_0^{r_{\rm vir}} \frac{1}{\max[t_{\rm cool}(r), t_{\rm dyn}(r)]} \frac{dM_{\rm cold}(r,t)}{dr} dr \,. \tag{A.5}$$

We indicate with $M_{\rm gas} = M_{\rm cold} + M_{\rm inf}$ the total gas mass. In the code the fraction of gas mass removed by the feedback is never re-used at successive timesteps, i.e. it is considered that its infall and/or cooling timescales become infinite or it has been swept out of the host halo. The feedback by SN at any instant returns to the hot phase a fraction of cold gas equal to

$$\dot{M}_{\rm cold}^{SN} \sim -\psi(t)\epsilon_{\rm SN} \frac{N_{\rm SN} E_{SN}}{V_{\rm vir}^2} \frac{M_{\rm cold}}{M_{\rm gas}} \,. \tag{A.6}$$

Due to radiation drag the amount of low angular momentum gas which feeds the reservoir around the central SMBH is given by

$$\dot{M}_{\rm inflow} \simeq \dot{M}_{\rm res} = 6.8 \cdot \alpha_{\rm SFR} \cdot 10^{-3} \psi(t)(1 - e^{-\tau})\, M_\odot {\rm yr}^{-1} \,, \tag{A.7}$$

where the optical depth is

$$\tau = \tau_0 \left(\frac{Z}{0.02}\right) \times \left(\frac{M_{\rm gas}}{10^{12}\, M_\odot}\right) \times \left(\frac{10^{13}\, M_\odot}{M_{\rm vir}}\right)^{2/3} \,. \tag{A.8}$$

Here Z is the average metallicity in the system. The seed central SMBH, of mass $M_\bullet^{\rm seed}$, starts then accreting at a rate given by

$$\dot{M}_\bullet = \min[\lambda \dot{M}_{\rm Edd} \,, \dot{M}_{\rm visc}] \sim \lambda \dot{M}_{\rm Edd} \,, \tag{A.9}$$

where the last equality generally holds during the fast initial SMBH growth, due to the generally very short timescales of the viscous accretion. The AGN feedback acts on the cold gas as

$$\dot{M}_{\rm cold}^{QSO} \sim -\frac{L_h}{V_{\rm vir}^2} \frac{M_{\rm cold}}{M_{\rm gas}} \tag{A.10}$$

and on the infall gas

$$\dot{M}_{\rm inf}^{QSO} \sim -\frac{L_h}{V_{\rm vir}^2} \frac{M_{\rm inf}}{M_{\rm gas}} \,. \tag{A.11}$$

Here the kinetic luminosity of the AGN is (see Chapter 3 for details)

$$L_h = \epsilon_{\rm AGN}\, 10^{44}\, L_{\rm Edd,46}^{3/2} \,{\rm erg\,s^{-1}} \,, \tag{A.12}$$

The chemical enrichment of the ISM is computed as

$$\frac{dG_i(t)}{dt} = -X_i(t)\psi(t) + R_i(t) + \left(\frac{dG_i}{dt}\right)_{\rm inf} - \left(\frac{dG_i}{dt}\right)_{\rm reh} . \tag{A.13}$$

$G_i(t) = X_i(t)M_{\rm cold}(t)$ is the cold gas mass in the form of the element i. The quantity $X_i(t)$ represents the abundance by mass of the element i. $R_i(t)$ takes into account the rate at which SNI and SNII as well as single low- and intermediate-mass stars restore their processed and unprocessed material to the ISM. The infalling term in Eq. (A.13) is the primordial chemical composition of the infalling gas while the reheating term gives the amount of cold gas which is heated and subtracted to further stellar processing.

Table A. Free parameters in the numerical code	
$\epsilon_{\rm AGN}$	1.3
$\epsilon_{\rm SN}$	0.05
C	7
$\alpha_{\rm SFR}$	2
$\lambda = \dot{M}_\bullet/\dot{M}_{\rm Edd}$	$1 \quad (z_{\rm vir} < 3)$ $1.7 \quad (3 \geq z_{\rm vir} \geq 5)$ $3,4 \ (z_{\rm vir} \geq 5)$
ϵ	0.15
$M_\bullet^{\rm seed}$	$10^2\ M_\odot$
τ_0	1

Appendix B

Summary of PhD Thesis

Target

The aim of this thesis is to investigate the key points concerning the evolution of the local Super-massive Black Hole (SMBH) population and to understand the origin of the links the SMBH have with their host spheroidal galaxies and dark matter (DM) halos. In fact the tight correlations observed among the SMBH mass, the photometric and dynamical properties of the host galaxy and DM halo, suggest that these systems must have co-evolved during time building up together.

The study of the statistical mass distribution of the local SMBH population and galaxies and their link with the overall AGN statistics are fundamental tools to get important physical insights on the basic average features of SMBH evolution.

Any galaxy formation model must compare with such findings. For this purpose I have worked with the semi-analytical code developed by Granato et al. (2004) to physically model SMBH evolution in galaxies and DM halos, compare model results with empirical derivations and make predictions. In particular, my work has been primarily to tune the parameters and also try to arrange minor modifications, where needed, in order to cope with the variety of the numerous empirical data the model can successfully account for.

Topics on which I have worked

Paper 1: "The Match Between The Local and Accreted Mass Functions"

Shankar F., Salucci P., Granato G.L., De Zotti G. & Danese L., 2004, MNRAS, **354**, 1020

Part I (Chapter 4 of the thesis):

- I have started my work converting local data on the galaxy luminosity and velocity function into a SMBH Mass Function (MF) through the use of the empirical relations $M_\bullet - L_{\rm bulge}$ and $M_\bullet - \sigma$ respectively, and exploiting also available radio data, following Salucci et al. (1999).

- I find that the two MF derived from the $M_\bullet - L_{\rm bulge}$ and $M_\bullet - \sigma$ relations are in reasonable good agreement at variance with most previous works on the topic. I find a SMBH mass density of about $\rho_\bullet \sim 4.2 \times 10^5\, M_\odot/{\rm Mpc}^3$, out of which 25% resides in spiral bulges. Still uncertainties on the basic method through which one computes the statistics of SMBH residing in S0 bulges and on the normalization of the empirical relations can produce an uncertainty of about $\sim 40\%$ in the result.

  Part II (Chapter 5 of the thesis):

- I have then computed the accreted mass function (AMF) summing up the contributions of all the Hard-Xray detected AGN, including those families of very obscured AGN which are needed to fit the most recent data on Xray Background (XRBG) counts and energy spectrum.

- I have sown that the integrated AGN statistics, in the single shot approximation, provides an AMF which matches, at all relevant mass scales, the local SMBH MF if a radiative efficiency of $\sim 10 - 15\%$ is taken into account. Such a result shows that merging must have a minor role in building the relic SMBH population. The statistical comparison between the local SMBH and AGN integrated population, provides, independently of the radiative efficiency, a *lower* limit to the visible timescale for the AGN population of about $(4 - 10) \times 10^7$ yr, higher for the faint X-ray AGN. An estimate of the *total* visible timescale could be provided by the time spent by the SMBH when its mass is above the survey sensitivity limit. Visibility AGN timescales

are of fundamental importance and give constraints on the fact that the duty cycle of these sources depends on wavelength and therefore is not linked with any dynamical quantity of the system as previously claimed by various authors.

Paper II: Fitting AGN Luminosity Functions with the Anti-hierarchical Baryon Collapse model

in preparation

Part I: DM halo 'creation' rates (Chapter 3 of the thesis)

- To face the problem of modeling the actual number of SMBH which form during time and related galaxies, I have first of all studied the actual way of assessing the rate of 'creation' of newly formed DM halos and there survival time as halos harboring a single baryonic core. The statistics of newly formed DM halos at each redshift is better represented, within a factor of two, by the positive derivative of the Sheth & Tormen (2002; S&T) mass function. The generally used Extended Press & Schechter (EPS) formalism underestimates by several factors the numerical simulation results at high redshifts and masses. Analytically implementing a scale-free 'destruction' rate, as in Sasaki (1994), applied to the total S&T mass function derivative, provides 'creation' rates very close to the positive derivative at all relevant redshifts and masses for galactic spheroids formation.

- According to numerical simulations, a single massive halo is usually formed, following a first phase of rapid accretion followed by a longer phase of slow accretion. I have co-written a code for building DM merger trees and compared the outputs with numerical simulations. We have checked that the average accretion history of the main progenitor is actually composed of a two phase step, the first one being faster and during which most of the halo mass is accumulated. Such a result is rather robust and does not much depend on the fraction of the actual accreted mass at each time step.

- I have studied the effect of using different recipes for DM creation rates, power spectrum and variance. All these effects must be taken seriously into account as they can

lead to several factors of discrepancy in the final results when modeling the AGN, SMBH, Galaxy statistics.

Part II: Fitting AGN Luminosity Functions (Chapter 6 of the thesis)

- I have worked in tuning the set of parameters of the Granato et al. (2004) model in order to reproduce the optical and Hard-Xray AGN LF. Assuming a slightly increasing Eddington ratio from 1 to 4 at very high redshifts in the model, and a scatter of at most a factor of two between SMBH and DM halo masses, I was able to reproduce the optical/Hard-X AGN LF evolution from $z \sim 6$ to $z \sim 1.5$. I find a good match imposing that AGN can form only in halos with mass less than $\log M_{\rm vir} = 13.2$, the same limit used to derive the galaxy dispersion velocity function (VDF) and galaxy LF (see below). The maximum SMBH mass I find is almost $\log M_\bullet \sim 9.5$, in agreement with empirical evidence, and at variance with previous models which claimed SMBH of the order of $10^{11}\, M_\odot$ at $z \sim 6$.

- Recent models claim very short visible timescales close to a few 10^6 yr to fit the AGN LF at high redshifts. Moreover these models assess that such timescales are set by the dynamical infall of gas onto a disk during the early stages of galaxy formation. Short timescales mainly could follow from 'wrong' estimates of the details of DM creation, as stated above, and, equally relevant, from the assumption of immediate QSO ignition at the virialization of the host DM halo. As shown and discussed by Monaco et al. (2000) and Granato et al. (2001), a delay between virialization and AGN ignition is a key ingredient to understand the QSO LF and the relationship between evolutionary histories of QSOs and of the massive spheroidal galaxies hosting them. Granato et al. (2004) have presented a detailed physical model quantifying such a delay and can naturally account for the co-evolution growth of SMBH and their host spheroidal galaxies. In this line of research I found that a significant amount of dust in the galaxy is needed to obscure the AGN/galaxy during almost all its growth phase (the galaxy appears as a SCUBA in this phase and the AGN could be in principle detectable in Hard-Xray bands, as actually shown by Alexander et al. 2005). In fact if the AGN

becomes visible only during the last 1-2 e-folding times this gives the right duty-cycle needed to fit the AGN statistics at all relevant redshifts. Moreover the visible times obtained in this way are comparable with those estimated through demographic studies and, at high redshifts, they are about a factor of ten longer than previously estimated. Such results can be physically explained by the fact that the system galaxy/AGN becomes optically visible only during the last e-folding times when the SMBH is enough massive to eventually unbind the residual gas, thus halting both the star formation and the SMBH growth itself.

- I have also taken care to check, using the Granato et al. code, that the new set of parameters used to fit the AGN LF preserves the α-enhancement. To do this I had to tune the parameters to take care that the Star Formation timescales for smaller halos are always longer than for larger halos. I checked that this effect does not produce too much accretion onto the SMBH after the peak of its activity, in order not to overproduce Hard-Xray counts. I have also checked, using the Granato et al. code, that the statistics of SCUBA and K-band counts are preserved and found that about 60-70% of the relic SMBH mass function is produced in this new version of the model, still in agreement with the Soltan argument.

Paper III: The Impact of Energy Feedback on AGN Evolution and SMBH Demography
(Chapter 6 of the thesis)

Vittorini V., **Shankar F.** & Cavaliere A., 2005, MNRAS, accepted

- I have collaborated in a project which aims at reproducing the AGN statistics evolution at low redshifts. At $z \leq 1.5 \div 2$ AGN evolution can be described within a scenario in which SMBH can be *re-activated*, through bar instabilities and/or galaxy interactions and minor merging. Not much mass is however accreted during this phase (up to 30%) as we predict significantly decreasing Eddington ratios with redshift, in accordance with data. In particular I have checked that the low-redshift accretion history evolution, which can be simply described by a source-free second-order conti-

nuity equation, can be analytically solved. I have also contributed in the development of the n-step interaction code for describing the SMBH MF and AGN LF redshift evolution.

Paper IV: Dynamical and photometric imprints of feedback processes on the formation and evolution of E/S0 galaxies

Cirasuolo M., **Shankar F.**, Granato G.L., De Zotti G. & Danese L., 2005, ApJ, 629, 816

Part I: the galaxy Velocity Distribution Function (Chapter 7 of the thesis)

- Following analytical estimates (Oguri & Lee 2004) inspired by numerical results (e.g. Zhao et al. 2003), I have checked that the mass accreted during the slow phase accumulates in the outer edges of the halo, close or slightly beyond the virial radius, preserving the central parts (and relative baryonic core, if present). Such a result is confirmed by the fact that, building the VDF out of the summation in time of the DM 'creation' rates, a very good fit to the Sheth et al. (2003) local VDF is provided if a simple scaling $\sigma/V_{\rm vir}(z_{\rm vir}) \sim 0.55 - 0.6$ between the galaxy dispersion velocity and the host DM halo virial velocity at the moment of virialization is assumed. Such a relation has now been empirically confirmed (Ferrarese 2002; Pizzella et al. 2005; Weatherley & Warren 2005) in the form $\sigma - V_c$, where the circular velocity V_c scales almost constantly with the virial velocity. I checked that this way of reproducing the VDF, uniquely based on the creation rates for DM halos, provides a statistical anti-hierarchical growth of structures, in line with the predictions of the Granato et al. (2004) model.

- I have checked that such a value of $\sigma/V_{\rm vir}$ implies that the energy per particle of baryons and DM is almost the same and $\sigma \sim \sigma_{\rm DM}$. This points to a scenario of *non*-adiabatic contraction of baryons in the host DM wells in which baryonic particles behave dynamically as DM (*attractor hypothesis*; Loeb & Peebles 2003; Gao et al. 2004).

Part II: the early-type fundamental plane (Chapter 7 of the thesis)

- Using the Granato et al. (2004) code and the $\sigma/V_{\rm vir}$ ratio determined above, I have collaborated in reproducing all the projections and tightness of the early type galaxies Fundamental Plane (FP), showing that, properly taking into account the SN and AGN feedbacks, the Granato et al. model is able to reproduce the observed slopes in the FP relations and the spheroid stellar mass function. We find that the $\langle M_{\rm star}/L\rangle_{r^*} \sim 4$ with a slight dependence on galaxy luminosity due to systematic changes with luminosity of the galactic structure.

Paper V: New Relationships between Galaxy Properties and Host Halo Mass, and the Role of Feedbacks in Galaxy Formation (Chapter 8 of the thesis)

Shankar F., Lapi A., Salucci P., De Zotti G. & Danese L., 2005, ApJ, submitted

- I have compared all the available empirical data on the SMBH/galaxy mass and velocity statistical distributions with the total DM "galactic" halo mass function (GHMF), derived adding subhalos and subtracting groups and clusters from the S&T MF at $z = 0$. Through such an operation I have derived the main relationships linking SMBH-galaxy-DM halo. Then I have collaborated in analyzing the previous relations to derive general conclusions on the main processes governing galaxy evolution and in particular I have compared such results with the output of the numerical model.

- The statistical match between the local stellar mass function and the GHMF, provides the $M_{\rm star} - M_{\rm vir}$ relation, while the statistical comparison between the SMBH MF and the GHMF provides the $M_\bullet - M_{\rm vir}$ relation. The former relation is very useful as bypasses any hypothesis on the DM halo profile to compute the DM mass around a galaxy. Moreover I compared the GHMF($z = 1.7$) with the stellar MF by Fontana et al. (2004) at the same redshifts, finding that the $M_{\rm star} - M_{\rm vir}$ relation has similar slope and normalization with respect to the local one. Finally I have collaborated in showing that the $M_{\rm star} - M_{\rm vir}$ relation can be very well fitted with a simple recipe for galaxy evolution which includes feedback from SN and AGN, which seems to be the

most reasonable way for solving the missing baryon problem. In fact I have actively conducted a detailed study on the stellar and gaseous M/L ratios to find the baryons locked up in galaxies at $z = 0$ to build the local baryonic MF, following Salucci & Persic (1999). I find that on average about 10% of the initial baryons, as measured by WMAP data, are left over in galaxies today.

- I have found that the $M_\bullet - M_{\rm vir}$ relation is consistent with a feedback constrained relation and compatible with the output of the numerical model by Granato et al. Furthermore I have computed that the latter relation is compatible with the one derived by Ferrarese (2002), if one assumes that the relation $V_c \propto V_{\rm vir} \propto M_{\rm vir}^{1/3}$ is set at high redshifts.

r